The Dissertation Committee for Rui Xu

certifies that this is the approved version of the following dissertation:

Pore Scale Study of Gas Sorption and Transport in Shale Nanopore Systems

Committee:

Maša Prodanović, Supervisor

Hugh Daigle

Kishore Mohanty

Carlos Torres-Verdín

Farzam Javadpour

Pore Scale Study of Gas Sorption and Transport in Shale Nanopore Systems

by

Rui Xu

Dissertation

Presented to the Faculty of the Graduate School of

The University of Texas at Austin

in Partial Fulfillment

of the Requirements

for the Degree of

Doctor of Philosophy

The University of Texas at Austin

December 2019

Dedicated to my parents.

Acknowledgments

Throughout the writing of this dissertation I have received a great deal of support and assistance. I would first like to thank my supervisor, Dr. Maša Prodanović, whose guidance and support throughout my graduate studies have been invaluable for my academic growth and the completion of this dissertation.

I am grateful to the Equinor Fellows Program at our university that has supported my research for the past three years.

I would like to thank my colleges and friends in my research group. Ayaz and Ali have helped me a lot with the pore network modeling and adsorption work. Chris has saved me considerable effort and time with his expertise in lattice Boltzmann method and SEM image acquisition and analysis. Hasan, Javier, Ningyu, Min, Ying, and Wenhui have been there to discuss problems regarding research, career, and life in general.

Outside our research group, Han and Dr. Daigle have helped me with the collection of nitrogen sorption data. Patrick has trained me to operate SEM machines. Mingyuan, Zhuang, and many other friends that I fail to mention have enriched my graduate life and left unforgettable memories for me to look back several years from now.

I would also like to thank my mentor, Chicheng, during my internship at Aramco Services Company. He provided valuable insight into not only research, but also personal development.

In addition, I would like to thank my parents who are always there for me, understanding and supporting every decision I made. Without them, I would not have made this far.

Finally, I have been fortunate to have Yiting in my life for the past six years. The courage, trust, and happiness she consistently brought to me have accompanied me through ups and downs in either academic or personal life.

Abstract

Pore Scale Study of Gas Sorption and Transport in Shale Nanopore Systems

Rui Xu, Ph.D.

The University of Texas at Austin, 2019

Supervisor: Maša Prodanović

Shale gas production accounts for about 70% of the total natural gas production in the US. Yet it remains a nontrivial task to characterize the petrophysical properties of shale core samples either by experimental analysis or numerical simulations. Shale matrix has low porosity and permeability resulting from nanometer-scale pore sizes. Surface properties of shale can be quite inhomogeneous arising from complex mineralogy and diagenesis. Heterogeneous morphology and topology of the pore structure poses significant challenges on understanding fluid distribution and flow capacity. Pore scale simulations provide insight into the fundamental mechanisms of thermodynamics and hydrodynamics in tight porous materials, and can supplement experimental characterization of shale petrophysical properties (*e.g.* absolute/relative permeability, capillary pressure curves). However, challenges exist in creating representative pore structures tailored for specific simulation tools, incorporating the appropriate and relevant physics for the problems to be simulated, and interpreting, calibrating, or validating the simulation results. In this work, we used two types of pore scale simulation tools, namely pore network modeling (PNM) and lattice Boltzmann method (LBM), to study gas adsorption/desorption and transport behavior in shale matrix.

For the first part of the work, a dual-scale PNM was integrated with lattice density functional theory (LDFT) to study nitrogen adsorption/desorption in mesoporous materials with pore

sizes smaller than 200 nm. Critical pore structure parameters (*i.e.* porosity, pore size distribution, and pore throat connectivity) were characterized by calibrating the simulated nitrogen sorption isotherms to experimental results, and were then used to construct PNMs to study supercritical methane transport. We found that the pore structure characterization results were nonunique and highly dependent on the assumed pore shape. Scanning electron microscope (SEM) images were used to further constrain the description of pore shapes. Advection and diffusion of methane at reservoir conditions were simulated and compared, and suggestions were made regarding the choice of representative pore shape in PNMs for single phase advection/diffusion calculations.

We next used LBM to study two-phase thermodynamic and hydrodynamic problems in nanopore systems in shale. Both 2D and 3D LBM models were developed with consideration of mesoscale fluid-fluid and solid-fluid interactions to model gas adsorption in complex geometries, and phase separation occurs automatically without the need to track the interface. This overcomes the pore shape deficiency of PNMs in cases where nanoporous media reconstruction exists. LBM models were then calibrated to LDFT and validated against experimental adsorption data for both subcritical and supercritical gases for the first time. We studied and compared nitrogen sorption hysteresis in two model nanopore system reconstructions representing the interparticle and intraparticle pores in shale.

As another example of many possible applications of our developed model, we studied water adsorption and condensation in a reconstructed clay pore structure based on SEM image analysis, and explored the effect of surface wettability on adsorbed/condensed water distribution and connectivity. Supercritical methane flow simulations with the existence of condensed water were conducted using a 3D hydrodynamic LBM model that considers nanoscale flow physics for high Knudsen number flow. The relative permeability of methane as a function of water saturation and surface wettability was calculated and compared to available experimental data measured on geosynthetic clay liners. We demonstrated the wide applicability of our model and suggested future applications.

Table of Contents

List of Figures

List of Tables

Chapter 1: Introduction

1.1 Motivation

Shale oil and gas are unconventional resources existing in tight formations that are rich in organic matter and clay minerals. Production of hydrocarbons from shale reservoirs has dramatically increased during the past decade, owing to the technological advances in horizontal drilling and hydraulic fracturing. According to U.S. Energy Information Administration, at the end of year 2018, about 70% of dry natural gas production and 60% of crude oil production in the US were contributed by shale plays. However, rapid production decline (90% loss of the production rate within the first two years [18]) and low recovery factor (10 – 20% [18]) have impaired the economic potential. This is to a great extent attributed to the low porosity and permeability of shale matrix, from which hydrocarbons are produced after the initial depletion from the hydraulic fractures.

Therefore, reliable reserve estimation, production forecasting, and optimal enhanced oil recovery (EOR) design of shale reservoirs highly depend on the knowledge of critical petrophysical properties of shale matrix (*e.g.* mineralogy, total organic carbon (TOC), kerogen maturity, porosity, pore size distribution (PSD), pore throat connectivity, and absolute/relative permeability). However, it is a nontrivial task to characterize these petrophysical properties for shale. The majority of pores in shale matrix are nanopores ($<$100 nm), as revealed by high resolution scanning electron microscopy (SEM) images [1,19] and experimental analysis [20,21]. Low porosity (5 – 10% [22]) and ultra-low permeability (nD – μD scale [1,8]) were reported. The complex mineral composition and diagenetic processes further complicate the inhomogeneous pore structure and surface properties of shale matrix. As a result, conventional experimental techniques or large-scale numerical simulations may no longer provide timely or reliable results. Therefore, special experimental techniques and pore-scale simulations are promising alternatives to supplement conventional experimental measurements, and provide insight into the fundamental mechanisms of thermodynamic and transport behavior of fluid confined in nanoporous media.

Herein, we study two fundamental processes that happen in shale nanopore systems, including gas adsorption/desorption and transport. Due to the dominance of nanopores which have large surface-to-volume ratio, about 20 – 85% of the total gas in shale matrix is stored in the adsorbed state [23]. At reservoir pressure (10 – 50 MPa) and temperature (300 – 400 K), methane, which is the main component of shale gas, is at supercritical state. Knowledge of the adsorption capacity and transport mechanism of supercritical methane is essential for reserve estimation and production analysis. Study of subcritical gas adsorption/desorption in shale has important applications as well. For example, nitrogen adsorption/desorption experiments measured at 77 K provide critical information about nanopore porosity, PSD, specific surface area, and pore throat connectivity of shale core samples [5, 24–27]. Studies also show that subcritical gas desorption curves are quantitatively similar to drainage capillary pressure curves by proper transformations [28]. Water adsorption at different humidity conditions is also widely studied to understand its effect on shale gas adsorption and production [29–32]. Furthermore, capillary condensation might occur in shale mesopores (2 – 50 nm) when there are heavy hydrocarbon gases in the shale gas mixture [33, 34]. It is then necessary to know the distribution and connectivity of the condensed phase to understand its effect on shale gas transport properties.

The mechanism of fluid transport in nanoporous media remains elusive. Because the mean free path of the gas molecules is comparable to the pore size, continuum assumption breaks down when Knudsen number (Kn, which is defined as the ratio between the mean free path of fluid molecule and the characteristic pore size) is above 0.1. Conventional hydrodynamic equations such as Darcy's Law or Navier-Stokes equations are no longer guaranteed to provide reliable results under such conditions. Boltzmann equation, on the other hand, remains valid for the whole range of Kn ($0 - \infty$) theoretically, but it is nontrivial to solve for complex geometries. Therefore, pore-scale or molecular-scale simulations are needed to explore the mechanism of hydrodynamic behavior in nanoporous media.

Thermodynamic and hydrodynamic behaviors are commonly coupled during the production of shale gas. For example, methane desorbs from the pore wall during pressure drawdown of the matrix, and surface diffusion may also arise due to the concentration gradient within the ad-

sorbed gas, both of which contribute to the total production of shale gas. Furthermore, capillary condensation of water vapor within shale matrix and the variation of its saturation and connectivity with complex surface wettability have significant impact on supercritical methane flow properties. Therefore, developing pore-scale models that handle both thermodynamics and hydrodynamics provides invaluable insight into the mechanisms of shale gas production under reservoir conditions.

1.2 Research objectives

In this work, we explore two types of pore-scale modeling methods, including pore network modeling (PNM) and lattice Boltzmann method (LBM), to study two fundamental processes that happen in shale nanopore systems, namely gas adsorption/desorption and transport, for petrophysical characterization purposes. To this end, we formulate the following objectives:

- Establish a workflow to characterize shale nanopore structure (pore shape, PSD, and pore throat connectivity) by integrating nitrogen sorption measurements, SEM image analysis, and PNM.
- Apply nanometer-scale Kn-dependent advection and diffusion models to the constructed PNM to estimate the apparent gas permeability or effective diffusivity of shale core samples.
- Develop novel LBM models that account for the real-gas effect and solid-fluid interactions to study gas adsorption and capillary condensation in different nanopore systems in shale.
- Investigate supercritical methane flow behavior with the existence of adsorbed/condensed water in clay using thermodynamic and hydrodynamic LBM models.

1.3 Dissertation outline

The dissertation is organized into seven chapters. In the first chapter, we introduce the problem, and define our objectives. In the second chapter, we introduce the pore systems and surface properties in shale, and conduct a comprehensive critical literature review on common pore structure characterization methods for shale, and relevant physics and analytical/numerical models

that have been used to describe gas sorption and transport in shale. The third chapter introduces PNM constructions based on nitrogen sorption curves and SEM images analysis to infer the pore structure of shale, and we study methane advection and diffusion properties using the constructed PNMs. In the fourth chapter, we demonstrate a 2D LBM model that considers both rock-fluid and fluid-fluid interactions to study subcritical and supercritical gas adsorption behavior in different nanopore systems in shale. In the fifth chapter we extend the 2D LBM model to 3D, and study nitrogen sorption hysteresis in two model interparticle and intraparticle pore systems in shale. In the sixth chapter, we apply the 3D LBM model to study water adsorption and condensation in a more representative reconstruction of clay pore system based on SEM image analysis, and investigate the subsequent methane transport properties with the existence of adsorbed/condensed water and different surface wettability. Conclusions and future work follow in the last chapter.

Chapter 2: Background and literature review

2.1 Introduction to shale pore systems

Shale or mudrock (sedimentary rocks having a dominant grain size <65 μm) is classified as a type of unconventional rock with low porosity (5 – 10% [22]) and extremely low matrix permeability (nD – μD scale [1, 8]). The mineral composition of shale can be very complex, commonly including quartz, calcite, dolomite, pyrite, smectite, kaolinite, chlorite, illite, mica, and so on, as shown with X-ray diffraction (XRD) mineralogy analysis [22]. Besides the inorganic components, organic matter (OM, *e.g.* kerogen) is also present in shale which hosts most of the hydrocarbons. Pore systems in shale matrix, as a result, are very complex with varying pore sizes, shapes, and types. Most of the pores in shale are nanopores ($<$200 nm) as revealed by SEM images [1, 19], transmission electron microscopy (TEM) [35], small-angle and ultra-small-angle neutron scattering (SANS/USANS) [21], mercury intrusion [36], and gas adsorption/desorption [27, 37].

Here we classify nanopores into three categories based on their pore sizes, namely micropores ($<$2 nm), mesopores (2 – 50 nm), and macropores ($>$50 nm), following the same criterion by International Union of Pure and Applied Chemistry (IUPAC) [38]. Based on high resolution SEM image analysis of shale core samples from around the world, Loucks *et al.* [1] have classified pores commonly observed in shale matrix into three types: interparticle (interP) mineral pores that exist between grain particles, intraparticle (intraP) mineral pores that occur within inorganic grains, and intraP OM pores that are developed within OM.

InterP mineral pores in shale are commonly found between grains and crystals and are generally related to the primary pore network that is reserved after burial and compaction. They may be elongated, rounded or angular in shape [1] (see Fig. 2.1 (A)). IntraP mineral pores are found within grain particles, and they might be moldic pores formed by partial or complete dissolution, preserved intrafossil pores, intercrystalline pores within pyrite framboids, cleavage-plane pores within clay and mica grains and so on [1] (see Fig. 2.1 (B)). IntraP OM pores are developed as a result

of hydrocarbon generation within kerogen during the maturation process [39]. They usually have bubble-like, elliptical, or irregular cross sections and range between 5 and 750 nm in length, and they may or may not form a connected pore network dependent on the maturity and distribution of OM [22] (see Fig. 2.1 (C)). Shale matrix may contain one or more types of the pores defined above. For example, Mississippian Barnett shale in Fort Worth Basin shows mainly OM pores, with limited amount of intraP pores within pyrite framboids; Jurassic Haynesville/Bossier mudrocks contain mostly interP pores; and Cretaceous Pearsall mudrocks contain primarily intraP mineral pores [2].

Furthermore, less commonly observed, there might be micro-fractures with submicrometer to millimeter scale apertures in shale matrix which may or may not contain cements (see Fig. 2.1(D) for a partially cemented example). Since the cements in fractures are considered to be formed by chemical dissolution and precipitation reactions that took place over geologic time scales under subsurface conditions, fractures with cements are considered to exist in-situ [40]. However, it is still controversial whether the fractures without cements exist in the subsurface, and the formation of these fractures during core extraction and handling cannot be ruled out [41]. Direct core observations are needed to differentiate natural and artificial micro-fractures, and core observations have demonstrated that natural fractures in mudrock reservoirs are frequently filled by mineral cement [40, 42]. Cemented micro-fractures are observed particularly in carbonate-rich mudstones, which are thought to block the contribution to flow [43]. However, partially cemented fractures may not completely lose flow capacity and connected nano-grain boundary channels can be found with permeability 1 to 2 orders of magnitude higher than the matrix permeability as shown in the work by Landry *et al.* [40].

2.2 Surface properties of shale

Shale rocks have more complex mineral compositions compared to conventional rocks. Different types of grain particles might have different surface properties, which affects the gas flow or adsorption behaviors. For simplicity yet still capturing the heterogeneity, three types of solid particles (thus three types of surfaces) are considered here, namely clay, OM, and other inorganic particles. Clay usually has bound water attached to it [44] while hydrocarbon gas tends to adsorb

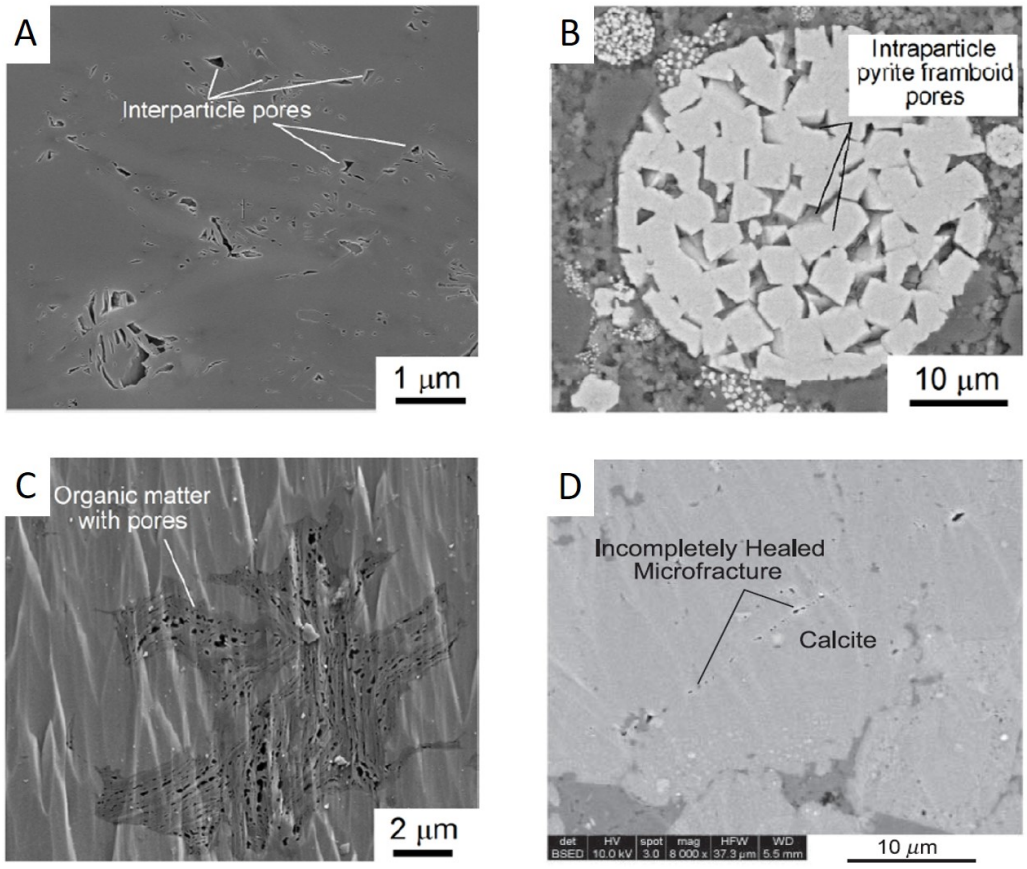

Figure 2.1: Different pore types in shale as classified by Loucks *et al.* [1]. (A) InterP pores between grains. Ion-milled sample of Haynesville/Bossier Shale (12,474 ft) from the East Texas Basin. (B) IntraP pores within a pyrite framboid. Polished thin-section sample of Barnett Shale (7,730 ft) from the Fort Worth Basin. (C) OM pores. Ion-milled sample of Barnett Shale (8,545 ft) from the Fort Worth Basin. (D) Example of a rare natural micro-fracture, approximately 30 μm long, 0.1 μm wide, and partly healed; 10,140 ft Pennsylvanian Atoka interval, Andrews County, Texas. Figures (A) to (C) are reproduced from Loucks *et al.* [2], and (D) is reproduced from Loucks *et al.* [1].

onto the OM [45]. Other inorganic particle surfaces are generally hydrophilic. Understanding the microstructure, distribution, and connectivity of different solid particles and the corresponding surface-fluid interactions is essential for modeling fluid distribution in such media.

SEM images provides direct observation of the microstructure of shale. clay particles are usually elongated and have sheet-like structures, while OM is usually amorphous and abundant with spongy pores [1]. Pyrite particles appear brightest in SEM images and usually contain intraP pores [1]. Energy dispersive spectroscopy (EDS) analysis associated with SEM analysis informs elemental compositions of the imaged surface, which offers supplemental information for mineralogy analysis. XRD can also be used to analyze mineralogy on a much larger sample size.

The surfaces of clay (with bound water), OM, and other inorganic particles interact differently with the confined fluid. Such properties can be referred to as the wall's 'wettability'. Microscopically, it results in different intermolecular potentials between the surface and fluid. Macroscopically, it leads to the occurrence of different contact angles when two fluid phases are present. The microscopic solid-fluid interaction depends on the physical and chemical properties of the surface and the fluid, which may arise in the form of electrostatic forces, vdW forces, hydrogen bonding forces, or hydration forces. The contact angle is a measurement of the affinity of fluid to solid surfaces, and can be measured for a homogeneous surface (*e.g.* sessile drop method), but for heterogeneous surfaces such as shale, the measured value is an averaged representation. Typically, clay and other inorganic grains are hydrophilic (water-wet), and OM is hydrophobic (oil-wet). However, the surface properties are also affected by the saturation history and local heterogeneity. Studies also show that clay particles associated with OM can be hydrophobic, while certain part of the OM can be hydrophilic where hydrogen bondings with water can be formed [46–49].

2.3 Pore structure characterization methods for shale

Gas transport in shale is complicated by the small pore sizes, abundance of OM, and heterogeneous surface properties. As a result, the transport behavior can not be very well studied by flow experiments alone due to the limitation in instruments, resolution, accuracy, and cost. Numerical simulations, on the other hand, are efficient, repeatable, and capable of testing varying conditions,

which greatly supplement the experimental characterization of flow behavior. A reliable understanding of the morphology and topology of the pore systems in shale is prerequisite to conduct numerical simulations. A complete understanding of the pore structure in shale (*e.g.* porosity, PSD, pore throat connectivity) requires a variety of characterization techniques at different scales. Here we critically review several methods commonly performed on core or sub-core scale, including experimental measurements (mercury intrusion tests, nuclear magnetic resonance (NMR) measurements, gas sorption experiments), and direct imaging techniques (micro/nano computerized tomography (CT) scan, and SEM analysis).

2.3.1 Mercury intrusion tests

Mercury injection capillary pressure (MICP) measurement is a standard procedure for determining the pore throat size distribution and flow capacity of conventional rocks. The petroleum industry was first introduced to the use of MICP by Purcell [50] and Rose and Bruce [51]. In MICP experiment, mercury is slowly injected into the core sample and the injected volume is monitored as a function of the intrusion pressure. Pore throat size distribution can be calculated based on the Young-Laplace equation [52]:

$$P_c = \frac{2\sigma \cos\theta}{r}, \tag{2.1}$$

where P_c is the capillary pressure; σ is the interfacial tension between mercury and air with a common value of 0.48 N/m; θ is the contact angle, which is 140° for mercury; and r is the pore throat radii.

For shale rocks, samples have to be crushed and ultra-high pressure has to be applied in order for mercury to penetrate the fine pores. Pressures up to 60,000 psi ($\sim$400 MPa) were reported in the literature, and the smallest pore size that can be detected is 3.6 nm [21, 53] based on Eq. 2.1. Studies on PSD of shale matrix using MICP measurements have reported a very wide range, with the largest pore diameter ranging from hundreds of nanometers to microns, and the smallest pore diameter only a few nanometers [20, 21, 54]. Sigal [55] measured the MICP curves on 92 plugs obtained from two Barnett shale gas wells, and compared the MICP porosity with helium porosity measured on companion samples. It was discovered that MICP porosity is consistently smaller,

which indicates that mercury can not access all the pores. Other issues associated with porosity and PSD characterization from MICP include the 'apparent intrusion' caused by mercury entering the inter-particle spaces of the crushed sample, as well as the compressibility effect caused by the high intrusion pressure [56]. Furthermore, the determination of PSD from MICP measurements depends on the assumption that the pore structure can be represented as a bundle of tubes, thus all the pores are equally accessible to mercury. However, this is seldom the case for any actual rock samples where heterogeneous pore shapes and connectivity are expected.

2.3.2 NMR measurements

NMR tests measure the signal decay after applying an external magnetic field to the water-bearing core samples. They are most sensitive to hydrogen atoms which are mostly present in the formation water, thus providing useful information of the pore structure. NMR tools can directly measure the density of hydrogen nuclei in reservoir fluids. Because the density of hydrogen nuclei present in water is known, data from NMR tools can be directly converted to an apparent water-filled porosity. This conversion can be done without any knowledge of the minerals that make up the solid fraction of the rock. NMR tools can also determine the presence and quantities of different fluids (*e.g.* water, oil, and gas), as well as certain properties of the fluids (*e.g.* viscosity). The magnetic signal decay is a relaxation process which in a porous medium is controlled by the surface properties, pore shapes and sizes. The measured transverse and longitudinal relaxation times (T_2 and T_1) can therefore be used to infer PSD based on the following conversion rule in the fast diffusion limit [57]:

$$\frac{1}{T_2} = \rho \frac{S}{V}, \tag{2.2}$$

where ρ is the surface relaxivity of the sample, and S/V is the surface-to-volume ratio, which is a function of pore size based on the assumed geometry. According to Eq. 2.2, smaller pore sizes correspond to faster T_2 relaxation time. NMR studies on shale samples reported in the literature typically show a bimodal T_2 distribution indicating two scales of pore sizes/systems, with a major T_2 peak below 1 ms (or 100 nm assuming a surface relaxivity of 0.05 μm/ms) [3, 56, 58]. The possible influence of OM or light hydrocarbon on measured T_2 spectrum can be differentiated by using

the $T_1 - T_2$ 2D map [59]. On the other hand, NMR also has limit in detecting small pores when the signal relaxes before the acquisition process starts [59]. Due to the small pore sizes in shale, a fully saturated shale sample may require as many as 10,000 scans for accurate porosity measurements [56]. The surface relaxivity which is critical in determining the PSD from T_2 measurements is dependent on the mineralogy. For example, the surface relaxivity is typically 1.7 μm/s for carbonates compared to 5 μm/s for sandstones. Sondergeld *et al.* [6,56] have reported the use of 0.05 μm/s as a conservative value of surface relaxivity for shale. Typically, the surface relaxivity is determined by calibrating NMR T_2 measurements to MICP pore throat size distributions [46, 60]. However, the average value determined might not be representative of the surface properties in shale where complex mineral compositions, abundance of OM, and complicated pore shapes are expected.

2.3.3 Gas sorption experiments

Use of measured nitrogen (at 77 K) or argon (at 87 K) adsorption isotherms for nanoporous media characterization dates back to the late 1940s [25]. Now, this technique has been widely applied in the chemical, ceramic, and pharmaceutical industries for characterization of materials with fine pores (smaller than 200 nm) [5,25]. In recent years gas sorption measurements have found applications in pore structure characterization of shale samples [36, 61, 62]. To prepare the sample for the experiment, it is first ground into powder (approximately 20 – 40 mesh), then oven-heated at 200 °C and degassed. During nitrogen sorption experiment, the prepared sample is exposed to nitrogen at 77 K at a series of precisely controlled pressures. The adsorbed gas amount is measured by volumetric methods (Boyle's Law) while slowly increasing the pressure up to the saturation pressure (P_0), followed by a desorption cycle as the pressure decreases. The measured sorption data are traditionally reported in the form of adsorption amount normalized by the sample weight (mmol/g) vs. the relative pressure (P/P_0). Two curves are then obtained, namely the adsorption and desorption curves.

Multiple methods have been developed to interpret the measured adsorption isotherms to get pore structure information including porosity, specific surface area, micropore volume, micropore PSD, and mesopore PSD. Details about the sorption mechanism and corresponding mathematical

descriptions can be found in Section 2.4. The specific surface area of the porous medium is usually estimated using Brunauer–Emmett–Teller (BET) method [63]. This method models the adsorption process as a layer-by-layer accumulation based on the construction of the grand canonical partition function. By fitting experimental data to BET isotherm equation, the monolayer capacity (mmol/g) can be obtained and the specific surface area is estimated based on the cross-sectional area occupied by each molecule in a completed monolayer. The micropore volume can be estimated using either the Dubinin adsorption equation or the t-plot method by fitting experimental data at very low relative pressures (usually <0.1) [38]. Micropore PSD can be calculated using the Horvath-Kawazoe (HK) method based on the idea that the relative pressure required for filling of micropores of certain size and shape is directly related to the adsorbate-adsorbent interaction energy [64]. Capillary condensation, which is the complete filling of a pore with condensed liquid phase at a pressure below the vapor pressure, is a unique phenomenon observed in mesopores. It is assumed that, for pores of a given shape and surface chemistry, there exists a one-to-one correlation between the capillary condensation pressure and the pore size [27]. Therefore, adsorption isotherms can be used to quantify PSD of the sample. The most commonly used method for obtaining mesopore PSD is Barret-Joyner-Halenda (BJH) method [65]. This method uses the modified Kelvin equation [66] to relate the capillary condensation pressure with the pore radius. Other advanced approaches use non-local density functional theory (NLDFT) derived adsorption isotherms which are more accurate than BJH method [67, 68]. Based on the size of the hysteresis loop, Seaton and coworkers proposed the earliest method to quantify the average pore throat coordination number (as an evaluation of pore network connectivity) according to percolation theory [26, 69].

Numerous studies have applied nitrogen adsorption measurements to characterize pore texture in shale [20, 36, 61, 62, 70, 71]. Most of the studies show a bimodal pore size distribution which reveals the multi-scale nature of the pore system in shale. Nitrogen sorption experiments are targeted to characterize mesoporous materials with the largest detectable pores below 200 nm, which is the largest pore size where capillary condensation occurs under experimental pressures. Argon is sometimes preferred over nitrogen because its uniform interactions with the surface of the samples, whereas nitrogen might give rise to specific surface interactions due to its quadrapole moments,

which makes the interpretation results dependent on the chemical properties of the characterized solid. Furthermore, nitrogen or argon sorption generally has limited reliability in quantifying micropore size distribution because of the limited instrumental resolution at low pressures, and slow diffusion rate in micropores at low temperatures [5]. CO_2 is another preferred adsorptive for more accurate probe of micropores, since CO_2 sorption measurements are commonly performed at ambient conditions, which enhances diffusion rates in microporous systems, thus making the micropores accessible to CO_2 molecules [72]. Micropores as small as 0.35 nm can be detected [73].

2.3.4 CT scanning

Unlike the indirect experimental measurements introduced above, X-ray computed tomography (CT) provides direct observation of the 3D pore structure. It is a non-destructive imaging technique that uses X-ray signals at different angles to produce a series of 2D slices of the porous media [74]. The strength of the signal is a function of local density and porosity, which can be used to differentiate solid and pore spaces. A 3D reconstruction of the porous media can be obtained by stacking and interpolating between the contiguous 2D slices. Commonly experienced problems with CT scanning include beam hardening, high-frequency noise, scattered X-rays, defective detector pixels or poorly cantered samples, which can not be completely avoided but can be alleviated by careful sample preparation and detector alignment [75, 76].

Conventional CT scanning using medical CT systems has been used to image sandstones or carbonates and the typical spatial resolution is about 200 – 500 μm [77], which is not high enough to differentiate pores in shale rocks. Micro-CT with micrometer scale resolution has recently been used for shale or clay pore system reconstruction [3] (see Fig. 2.2). However, only large fractures, minerals and bedding plane information can be discerned from the images of shale. Nano-CT with resolution down to 65 nm has been used for characterizing shale rocks as well [4, 78]. Although pore structure information at smaller scales can be obtained compared with micro-CT scan, majority of the nanopores remain unrevealed due to the limit of resolution.

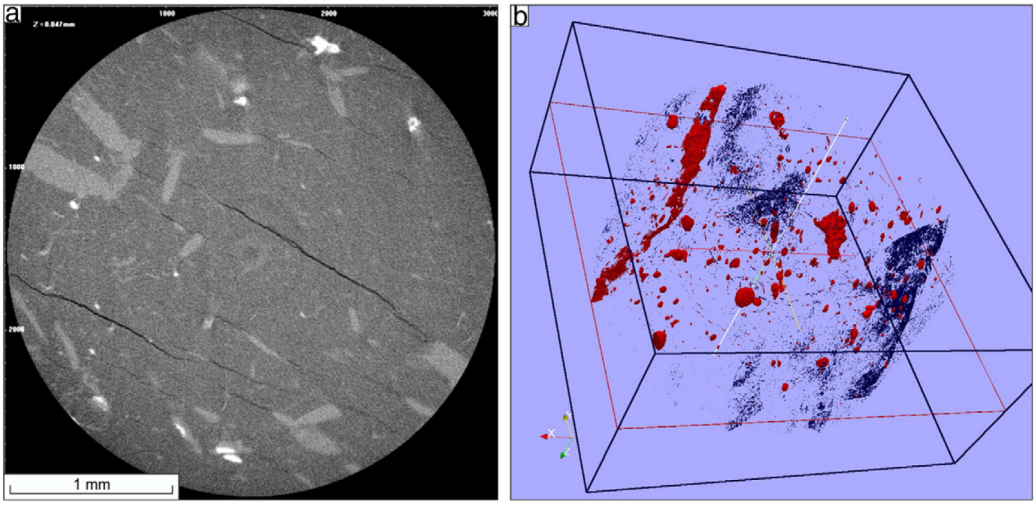

Figure 2.2: Volumetric visualization and rendering of selected regions of shales. a) Attenuation image of a sample of Opalinus Clay acquired using a micro-tomography instrument. b) Volume rendering of pyrite (red) and pore space (blue) distribution in the same sample. The figure is reproduced from Josh *et al.* [3].

2.3.5 SEM images

With much higher resolution (nanometer scale), SEM technique has been used to obtain high quality images of shale samples [1, 19, 45, 53]. By shooting accelerated electrons onto the ion-milled and coated sample, SEM machines detect the returning electrons using detectors such as back scattered electron (BSE) and secondary electron (SE) detectors, and generates an image of the surface of the sample. The grayscale of the images provides qualitative information about the density contrast, based on which pore spaces, OM and other minerals can be segmented and their structure analyzed using image analysis software such as ImageJ [4] (see Fig. 2.3). 2D nanoporous media can be reconstructed based on the segmented SEM images. Broad-ion-beam (BIB) SEM has been used to generate 2D images of wide field of view (sub mm scale) [79]. 3D structures can also be inferred by performing multi-point statistics (MPS) analysis of the 2D images [80]. Recently, advances in focused-ion-beam (FIB) SEM technique allows imaging of consecutive slices of nanoporous shale media in a micrometer scale domain with a resolution as high as 5 nm/pixel [79, 81], and a 3D reconstruction of the characterized sample can be obtained by image segmentation. TEM provides an interior view of a thin (sub μm scale) sample at even higher resolution than SEM, but sample preparation is nontrivial and the field of view is highly limited. Additionally, atomic

force microscopy (AFM) [8] is sometimes used to examine shale nanopores at high resolution, but it is limited to a 2D view.

FIB-SEM honors the 3D true pore structure and connectivity, which is critical for further flow simulations. However, acquiring thousands of images for 3D reconstruction is time-consuming and costly, and the 3D reconstruction process is computationally intensive. Though benefiting from the high resolution to some extent, SEM imaging techniques suffer from the limited image size (nm to μm scale) and imaging artifacts such as curtaining, misaligning, topography-induced contrast and edge charging [79], which deteriorates the imaging quality and impacts image segmentation. Furthermore, the similar grayscale value between OM and pore spaces makes pore differentiation based on simple grayscale value histogram thresholding techniques insufficient [82]. 2D cross sections, which are most commonly acquired by SEM observations, may not represent 3D pore shapes and pore throat connectivity, which are required to obtain credible simulation results.

Another debated subject associated with SEM images is the representativeness of the observation domain. Representative elementary volume (REV) or area (REA) is defined as the smallest sample volume or area over which a measured attribute of it renders a value representative of the bulk sample itself [79]. Shale is usually claimed to be inhomogeneous at every scale ranging from nm to km scale, which makes the explicit determination of a REV/REA to be nontrivial. Characterizations and simulations using FIB-SEM images have reported the size of the studied volume ranging from 4.4 $\mu\mathrm{m}^3$ to 5000 $\mu\mathrm{m}^3$ [47, 79, 83, 84]. Kelly *et al.* [79] conducted a detailed comparison of FIB/BIB-SEM derived geometric, TOC, porosity, and permeability data with core measurements, and concluded that individual FIB-SEM stacks intended for high spatial resolution may not be representative of both local and macroscopic shale geometric properties (although 5000 $\mu\mathrm{m}^3$ stacks lead to better local consistency), while 2D BIB SEM images covering a field of view (about 100 μm across) over ten times larger than a FIB-SEM image show improved agreement with core measurements. BIB-SEM images are promising for characterizing shale geometric properties at the REA scale, but 3D reconstruction is challenging both physically and computationally.

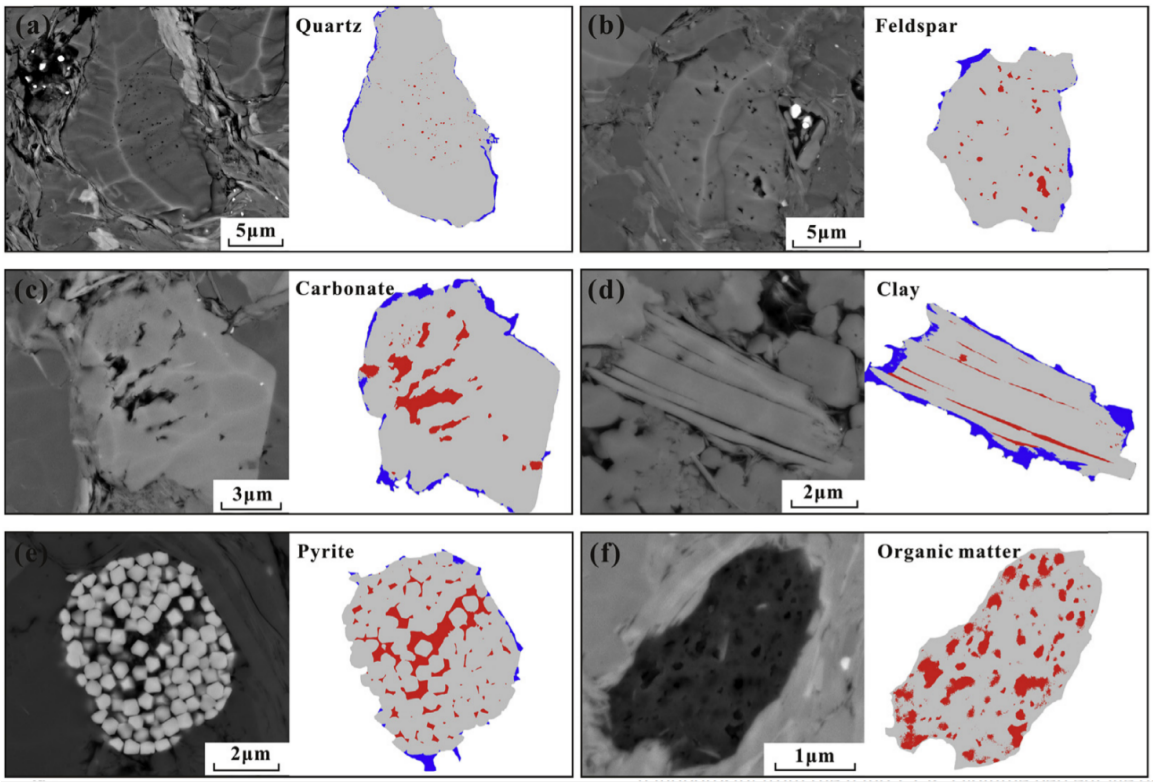

Figure 2.3: Characterization of inorganic pores and organic pores rendered from SEM images using gray scale segmentation. Pores are shown in red. The figure is reproduced from Tang *et al.* [4], see their Fig. 6.

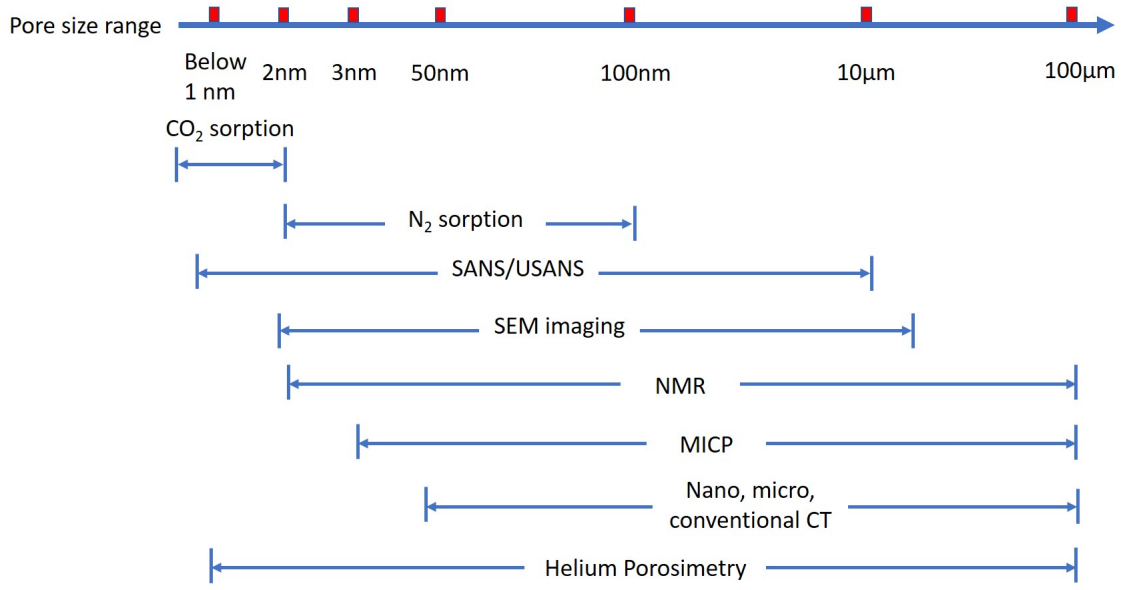

Figure 2.4: Comparison of the detectable pore size ranges of different pore structure characterization methods for shale introduced in Section 2.3.

2.3.6 Comparison of methods

Shale has complex pore structures with pore sizes ranging from nanometer to micrometer scale, and heterogeneity is observed at each different scales. Reliable petrophysical characterization of shale requires a combination of methods. The detectable pore size range for the methods introduced above (with some less commonly used methods including SANS) is compared in Fig. 2.4. The required sample size for the characterization and the applicability to shale of these methods are summarized in Table 2.1.

For the purpose of pore scaling modeling, in this study we focus on nitrogen sorption experiments and SEM image analysis, which provide pore structure information ranging from nanometer to sub-micrometer scale. This range of scales is reasonable for characterization of majority of the nanopores in shale matrix. The characterization results then guide the construction of 3D pore structures, based on which PNM and LBM models will be used to study thermodynamic and hydrodynamic behavior, as will be reviewed in Section 2.5.

Table 2.1: Summary of the nature and scale of pore structure characterization methods reviewed above and their applicability to shale samples

Method	Destructive or not?	Sample size	Properties characterized	Applicability to shale
Mercury intrusion	Yes	Typical core plug size (1 inch diameter)	Pore throat size distribution and accessible porosity	For shale, ultra-high pressure (up to 60,000 psi) needs to be applied to access the smallest porosity. Pores larger than 3.6 nm can be detected. However, high pressure might compress the pore structure.
NMR	No	Typical core plug size (1 inch diameter)	Pore body size distribution and total porosity	High precision instrument is needed to detect T_2 value smaller than 0.1 ms that is associated with micro and mesopores. Surface relaxivity is hard to determine due to complex mineralogy.
Helium porosity	No	Typical core plug size (1 inch diameter)	Accessible porosity	Considered a relatively reliable porosity estimation method for shale, could detect pores larger than the diameter of a helium atom (0.26 nm).
Low pressure gas adsorption	Yes	Ground sample with particle size around 20 – 60 mesh (250 – 840 μm)	Specific surface area, accessible porosity, pore size distribution, micropore volume	Low pressure N_2 sorption can detect pore sizes ranging from about 2 – 200 nm. CO_2 sorption can detect pore sizes ranging from 0.35 – 2 nm. A combination of the two could provide PSD of micro, meso and part of macropores.
SANS and USANS	No	around 20 mm in diameter and 1 mm thick	Pore size distribution and total porosity	Detect pore sizes from 0.5 nm – 10 μm. Not routinely used for shale.
CT scan	No	sample size varies from micrometer to meter based on the resolution needed (nano-CT, micro-CT, medical CT)	Density contrasts which can be used to identify matrix, pore space, and different fluid components.	Resolution for micro-CT and medical CT is too low to differentiate nanopores in shale. Nano-CT typically has a resolution of 50 nm, which can not detect micro and mesopores dominant in shale matrix.
SEM imaging	Yes	About 1 cm^3	2D pore structure, mineralogy and elementary analysis, pore type, shape, porosity	Typically used to analyze shale properties. Need to balance between field of view and resolution. Only provide 2D information about the pore structure, except for FIB-SEM which again is limited by the field of view.

2.4 Gas sorption in shale

2.4.1 Physics of gas sorption in nanopores

Adsorption, in general, is defined as the accumulation of fluid molecules in the vicinity of an interface [5]. In the case of a gas/solid system that we are studying here, adsorption initiates at the solid surfaces. Based on the source of the interaction force, adsorption can be classified into physisorption and chemisorption. In this work, we focus on the physisorption process which occurs mainly as a result of the van der Waals (vdW) forces between solid and gas molecules. Due to strong solid confinement, gas adsorption behavior in nanopores deviates from the bulk state [5], and different behavior is observed for gas adsorption below or above the critical point [85, 86], and in pores of different sizes and shapes [11].

For subcritical gases, according to IUPAC, physisorption isotherms were grouped into six types as shown in Fig. 2.5 [5]. Reversible Type I isotherms are given by microporous ($<$2 nm) solids. The sorption isotherms reaches a limiting value at low relative pressures. The limiting adsorption uptake is controlled by the micropore volume. The difference in the initial adsorption uptake for Type I(a) and (b) isotherms corresponds to different micropore sizes. Reversible Type II isotherms are given by the physisorption of most gases on nonporous or macroporous ($>$50 nm) adsorbents. A sharp knee in the adsorption isotherm (point B) indicates the transition from monolayer to multilayer coverage. The thickness of the adsorbed multilayer generally appears to increase without limit at high relative pressure. For Type III isotherm, there is no point B and therefore no identifiable monolayer formation, which is due to the relatively weak adsorbent-adsorbate interactions. Type IV isotherms are given by mesoporous adsorbents. The initial monolayer/multilayer transition is similar to Type II isotherms, followed by capillary condensation which is the unique behavior for mesopores when the pore space is filled with the condensed liquid phase at a pressure lower than the bulk saturation pressure. The final adsorption uptake then reaches a plateau. For mesopores wider than 4 nm, capillary condensation is accompanied by hysteresis (Type IV(a)). For mesopores smaller than 4 nm and semi-closed mesopores, completely reversible Type IV(b) isotherms are observed. Type V isotherm is very similar to that of Type III at low relative pressures

attributed to relatively weak adsorbent–adsorbate interactions. Capillary condensation is observed at high pressures. Type V isotherms are observed for water adsorption on hydrophobic microporous and mesoporous adsorbents. The reversible stepwise Type VI isotherm is representative of layer-by-layer adsorption on a highly uniform nonporous surface, with the step height representing the capacity of each adsorbed layer. Isotherms commonly observed for shale core samples with pore sizes ranging from micropores to macropores type are Type II and IV.

For mesoporous material such as shale, hysteresis is usually accompanied with capillary condensation, which might occur due to multiple reasons, including the delayed condensation as a result of the metastability of the adsorbed phase, the ink-bottle pore shape which delays the desorption, the network effect arising from the connectivity of the pores, or less commonly the structural change at the end of the adsorption process [5, 27, 38]. For shale with complex pore shape and connectivity, network effect is the major cause of hysteresis. IUPAC [5] classified the sorption hysteresis loops into five types, as shown in Fig. 2.6. Each type is closely related to particular features of the pore structure and underlying adsorption mechanism. The Type H1 loop is found in materials which exhibit a narrow range of uniform mesopores, where network effects are minimal and the steep, narrow loop is a clear sign of delayed condensation on the adsorption branch. Hysteresis loops of Type H2 are given by more complex pore structures in which network effects are important. The very steep desorption branch, which is a characteristic feature of H2(a) loops, can be attributed either to pore-blocking/percolation in a narrow range of pore necks or to cavitation-induced evaporation. The Type H2(b) loop is also associated with pore blocking, but the size distribution of neck widths is now much larger. Type H3 hysteresis has an adsorption branch that resembles a Type II adsorption isotherm and the desorption branch collapses onto the adsorption branch normally at the cavitation-induced relative pressure. This type of hysteresis is commonly observed by particles with plate structures (*e.g.* clays), also by adsorbents with both micro- and macropores. Type H4 hysteresis is similar to H3, with larger adsorption uptake at low relative pressures and finite adsorption uptake at high relative pressures. This indicates a combination of micro- and mesopores. Type H5 hysteresis is not commonly observed, and its distinct form is associated with adsorbents with both open and partially closed mesopores. The sharp desorption knee observed in Type H3, H4 and

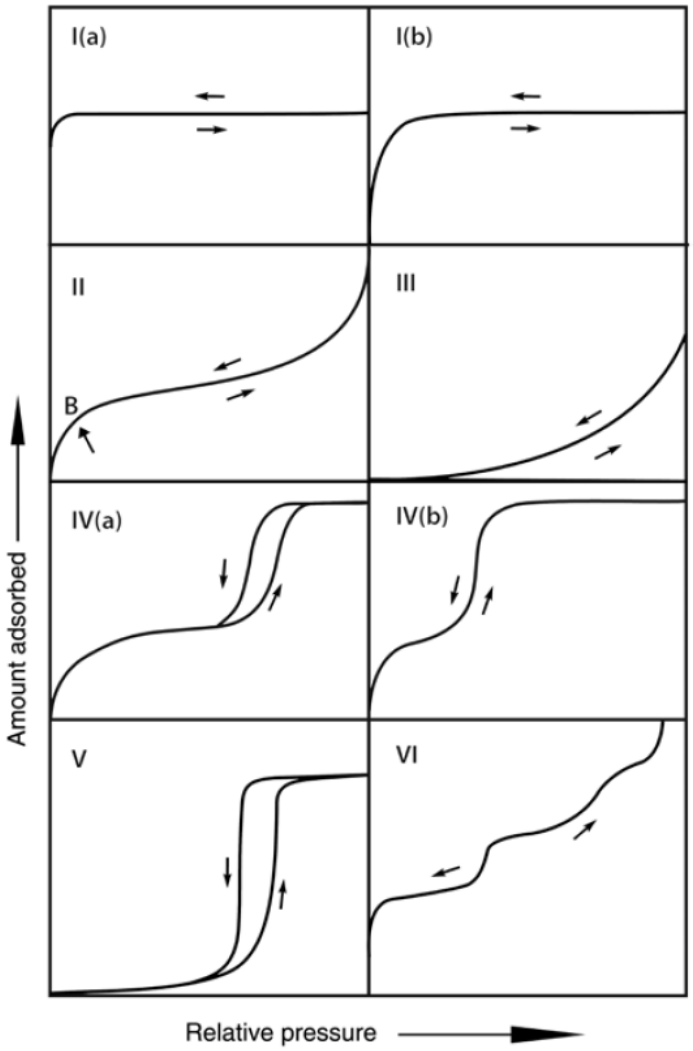

Figure 2.5: Classification of six types of sorption isotherms (I – VI) by IUPAC. Note that on the horizontal axis is the relative pressure which is defined as the absolute pressure normalized by the saturation pressure, and on the vertical axis is the amount adsorbed. The figure is reproduced from Thommes *et al.* [5].

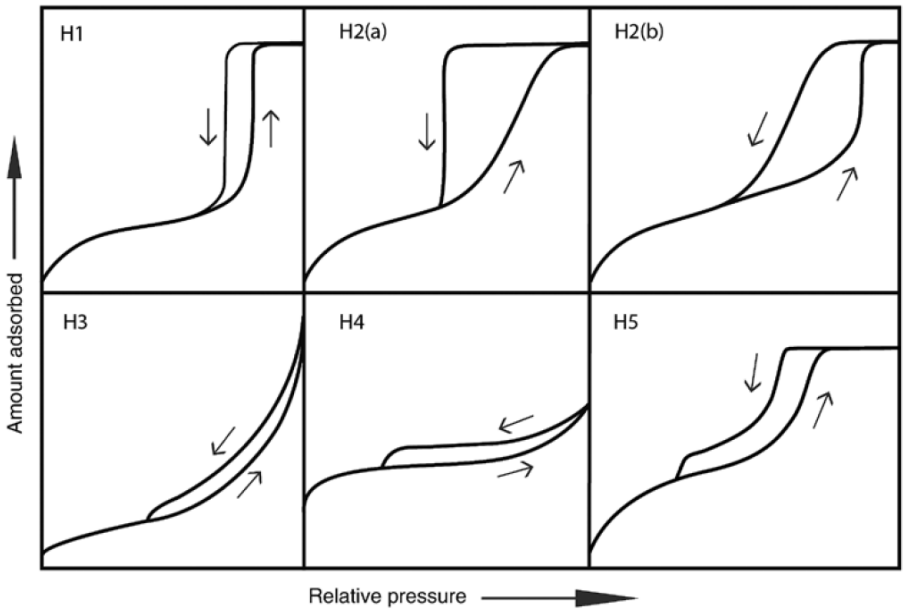

Figure 2.6: Classification of five types of sorption hysteresis loops (H1 – H5) by IUPAC. Note that on the horizontal axis is the relative pressure which is defined as the absolute pressure normalized by the saturation pressure, and on the vertical axis is the amount adsorbed. The figure is reproduced from Thommes *et al.* [5].

H5 hysteresis usually happens at a narrow range of relative pressures for a particular adsorbate and temperature (for nitrogen at 77 K, this corresponds to relative pressure at 0.4 – 0.5).

For supercritical gases (*e.g.* CH_4 at reservoir temperature and pressure), condensation does not occur. The adsorbed phase usually do not extend more than two molecule layers because of the weak intermolecular interactions between gas molecules, and it is the first adsorbed layer that contributes most to the adsorption capacity [87]. The adsorption uptake usually has a concave shape to the horizontal axis which is similar to the Type I adsorption isotherm for subcritical gases (see Fig. 2.5 and the adsorption capacity is dominated by the specific surface area.

2.4.2 Theoretical and numerical models

For subcritical gases, the capillary condensation pressure as a function of pore size can be described by the widely-used modified Kelvin equation:

$$\ln \frac{p}{p_0} = \frac{2\gamma V_m \cos\theta}{(r-t)RT}, \tag{2.3}$$

where p is the absolute pressure, p_0 is the saturation pressure at temperature T, γ is the surface tension, V_m is the molar volume, θ is the contact angle, r is the pore radii, t is the thickness of the adsorbed layer, and R is the gas constant. We can tell from Eq. 2.3 that smaller pores experience earlier capillary condensation, which is due to the stronger solid confinement. The evaluation of the thickness of the adsorbed layer is nontrivial for each individual pore with different shape and size. The commonly used approximation is the Halsey equation developed for nitrogen adsorption at 77 K on a nonporous material [88]:

$$t = 3.54 \left(\frac{5}{2.303 \log \left(\frac{P_0}{P} \right)} \right)^{\frac{1}{3}} \tag{2.4}$$

The adsorption uptake for supercritical gases is commonly described by the Langmuir equation [89]:

$$\theta = \frac{bp}{1 + bp}, \tag{2.5}$$

where θ is surface coverage that ranges from 0 to 1, p is pressure, and b is an equilibrium constant.

Although widely used due to its simplicity, the modified Kelvin equation is not accurate for pores smaller than 7.5 nm when the solid potentials of the opposite pore walls begin to overlap [90]. Determination of constant b in Langmuir equation requires transformation of experimental data reported in the form of excess adsorption amount [87]. These macroscopic theories do not describe the the kinetics of adsorption at the microscale. On the other hand, microscale approaches such as density functional theory (DFT) provide a more comprehensive representation of phase transitions in nanopores than the classical thermodynamic methods, and are applicable over a wide range of pore size, pressures, and temperatures. In the DFT approach, the sorption isotherms are calculated based on the fluid-fluid intermolecular potentials and solid-fluid interactions. The local density of the adsorbate at a given chemical potential is determined by minimizing the grand potential of the system. Due to the difficulty of integrating the surface potentials for complex surface curvatures, DFT sorption isotherms are often limited to simple pore geometries such as slit, cylindrical and spherical.

For adsorption modeling in complex nanoporous media applicable to both subcritical and

supercritical gases, lattice density functional theory (LDFT) and grand canonical Monte Carlo (GCMC) are two common approaches. LDFT is the discretized version of DFT with concepts borrowed from the lattice gas model [85, 86, 91]. The adsorption space is discretized into lattice sites where an adsorbate molecule may or may not reside. The lateral and surface interactions with a certain adsorption site is described by the lateral (E_A) and surface energy (E_0). The possibility of a certain site to be occupied by the adsorbate at equilibrium state is calculated by minimizing the grand potential of the system. The total adsorption amount is then calculated as a function of the site occupation possibilities. Simple 1D lDFT was initially developed for modeling adsorption in a slit pore [85, 86], and was later extended to cylindrical and spherical pore shapes [11]. 3D LDFT has also been developed and applied to study physisorption behavior in complex nanoporous media [92, 93], but certain simplifications have to be made and computational cost is significantly higher.

GCMC is a molecular-scale simulation method based on interaction potentials between fluid and solid molecules [94]. At a certain chemical potential, molecules are inserted or removed from the system until the grand potential is minimized. The adsorption uptake is then calculated by statistical averaging. GCMC provides more accurate results, but it also suffers from statistical noises and high computational cost, thus the simulation domain size is limited to tens of nanometers [92]. Furthermore, neither LDFT or GCMC have been attempted to model flow behavior in nanopores, which limit their applications to thermodynamic studies near equilibrium. Advanced numerical models need to be developed to integrate thermodynamics and hydrodynamics, and handle complex pore geometries at the same time, to fully understand gas sorption and transport in shale.

2.4.3 Water sorption and distribution in shale

Connate water commonly exists within or between clay particles in shale. Pore water in clay materials can be divided into two major categories: bound water and free water, and bound water can be further divided into clay-bound water (CBW) and capillary-bound water [44]. Two recognized mechanisms by which water molecules may be attracted by and oriented to clay surfaces are (1) ionic hydration of the exchangeable ions and (2) sorption phenomena at the clay surface [95]. The

study of clay-water sorption isotherms or water retention curves is important to quantify the amount of bound water and capillary water, and studies have shown that capillary-bound water can be up to 10 times more than CBW [7]. Similar to nitrogen sorption isotherms, water sorption curves are presented in the amount of water adsorbed in clay minerals vs. the relative humidity (the water vapor pressure normalized by the saturated vapor pressure). Other than the sorption isotherms, it is also critical to know the distribution of water in shale under different pressure and temperatures, so as to model shale gas flow accordingly. Wettability was found to influence sorption hysteresis and water distribution in clay materials [96–98]. Therefore, it is necessary to consider wettability heterogeneity when modeling water sorption in shale.

Clay-bound water

Because of the negative charge of the clay particles as a result of cation exchange, it is normal for them to have CBW within interlayer spaces or on the basal surfaces [99] with the presence of water solutions. CBW is normally immobile because of the strong hydrogen bond and electrostatic forces. The thickness of the formed electrical double layer depends on the cation exchange capacity (CEC) and the concentration of the water solution [32]. Generally, the thickness of the CBW is about two to three layers of water molecules (0.56-0.84 nm) under reservoir conditions, beyond which water will have bulk fluid properties [32]. Based on tight rock analysis, CBW could reach 2.63 – 7.19% of the total sample volume [30]. Due to the nanoscale pore size in shale, the influence of CBW is not negligible. Not only the effective pore size is reduced, but the contact interface between the fluid and solid is altered, which affects the surface fluid interactions.

Capillary-bound water

When the relative humidity increases, capillary condensation occurs and liquid water presents in the very small pore spaces between the clay mineral crystals by capillary forces. Water may also be held by capillary forces in pendular rings around the regions of grain-to-grain contacts. Unlike CBW which might only lead to reduced pore sizes for mesopores, capillary bound water may completely block the migration pathway of shale gas, thus significantly reducing the flow capacity.

Characterization of clay-bound and capillary-bound water

Bulk measurements have been used to estimate the volumes of CBW and capillary-bound water in clay. For example, Sondergeld *et al.* [6] performed NMR tests on 'as received' shale core samples, and set T_2 cutoffs of 3 and 33 ms for the determination of CBW ($T_2 < 3$ ms) and capillary-bound water ($3 < T_2 < 33$ ms) respectively for Barnett shale samples (see Fig. 2.7). The relative volume fraction of CBW and capillary-bound water varied sample by sample. However, such cutoffs are not uniformly applicable, therefore only providing an estimation of 'nominal' CBW and capillary-bound water. Water sorption experiments have also been used to quantify the CBW and capillary-bound water content. A water vapour adsorption isotherm for a non-porous oxide material is shown in Fig. 2.8. The amount adsorbed is expressed in terms of a statistical number of monolayers. At relative pressure of 0.55, approximately 2 to 3 layers of water molecules are adsorbed onto the solid surfaces. Based on previous studies by Newman [100], the bound water in clay minerals usually does not extend more than three monolayers. Therefore, the adsorbed water amount at relative pressure of 0.55 can be taken as the bound water content [7]. The amount of capillary water is determined based on the adsorbed amount on relative pressure of 0.9735 [7], corresponding to air/water capillary pressure of 3.63 MPa, which provides a conservative estimation of the capillary water content. Water sorption measurements have shown that CBW accounts up to 2.5% of the total pore volume, while capillary-bound water can hold up to 23% of pore volume [7]. The relative amount of CBW and capillary-bound water is strongly dependent on the type of clay mineral, along with its morphology and location within the pore space. Woodruff and Revil [44] used BET sorption isotherms to study clay-water sorption behavior and normalized the curves by CEC. Limited agreement with experimental data was reported. Most of the studies used the classical thermodynamic models reviewed above in Section 2.4.2 to estimate the water retention curves, yet the distribution and connectivity of the adsorbed water are rarely explored in detail, nor has wettability heterogeneity commonly expected in shale been considered.

Characterization of water distribution

The distribution of water at different humidity conditions has been studied. Li *et al.* performed nitrogen sorption experiments to investigate the size of the pore spaces occupied by water in shale/clay by measuring the samples at different water saturations that are frozen in liquid nitrogen (77 K) before the measurement to preserve the in-situ water [30]. Increasingly larger average pore size was observed with the increase in water saturation for the clay sample, indicating the preference of water to occupy smaller pores. However, for the shale sample, water does not show preference to the smaller pore spaces. Wettability complexity is a possible explanation for such observations. Derjaguin—Landau—Verwey—Overbeek (DLVO) theory was used to model the water adsorption behavior in these two samples. However, the calculations in [30] were based on simplified assumption of pore geometry of clay particles as parallel plates, and the water adsorption process is assumed to happen layer by layer, which oversimplifies the true adsorption behavior in a complex porous medium such as clay. Most importantly, the spatial distribution of the condensed water phase and water/vapor phase connectivity remains illusive, which are critical for understanding shale gas transport with the existence of water.

Direct observations of the fluid distribution in clay/shale have been made as well using CT scanning [101, 102], but the resolution was not enough to resolve the detailed fluid distribution within or between clay particles. Field-emission SEM has been used to directly observe water adsorption/desorption in shale [103]. Cryo-SEM provides another way to directly observe the in-situ fluid distribution at high resolutions by freezing the sample at low temperatures, preserving the fluid in place [104–106]. FIB/BIB-cryo-SEM studies on clay samples in 'as-received' conditions have shown the existence of in-situ water between clay particles [104]. The effect of 'drying' on clay microstructure alteration is observed as well [106]. However, about 10% of the water saturation remain unresolved because of the limited resolution of the cryo-SEM images, and these water mainly exist in clay particle interlayers and small mesoporous interP pores [104]. Understanding the water distribution at such scale require pore scale or molecular scale models that could capture the microscale physi/chemical interactions. On the other hand, the surface wettability of the clay particles affects water adsorption behavior [30, 96, 97], and delayed condensation is observed on non-wetting

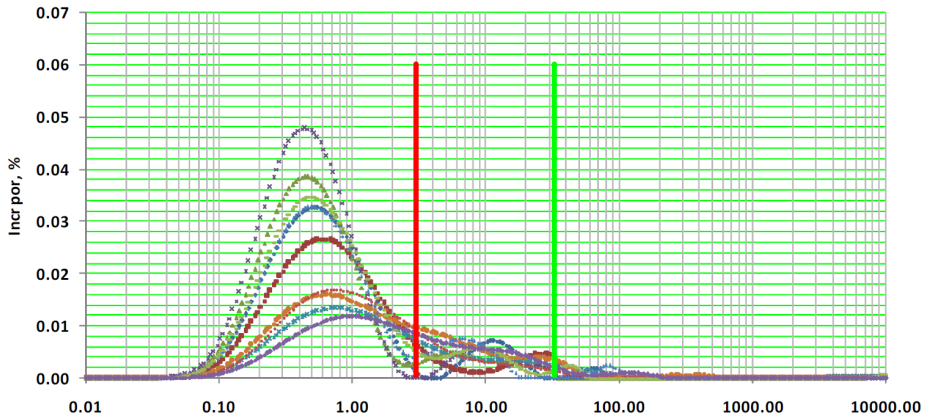

Figure 2.7: NMR T_2 distributions for 'as received' Barnett gas shales. Vertical red and green lines are the 3 ms and 33 ms cutoffs for determination of clay-bound and capillary-bound water. The figure is reproduced from Sondergeld *et al.* [6].

surfaces for relative pressures larger than unity. Previous studies typically assume the clay surfaces to be completely water-wet. However, as revealed by SEM images [1, 45], clay particles may also be associated with OM, which makes their surfaces hydrophobic. The complex saturation history further complicates the surface properties of clay, resulting in mixed wettability [107].

2.4.4 Hydrocarbon gas sorption in shale

Methane is the main component of shale gas. Under reservoir pressure (20 – 50 MPa) and temperature (300 – 400 K), methane is at supercritical state. Methane can be stored underground in shale in three forms, including free gas in the pores and micro-fractures, adsorbed gas on the pore wall, and dissolved gas within kerogen [8] (see Fig. 2.9). Due to the dominance of nanopores which have high surface-to-volume ratio and the abundance of OM, 20 – 85% of the total gas in place is in the adsorbed state [23]. The adsorption capacity is determined by two main factors, namely the specific surface area and the strength of solid/gas interaction. Due to the complex mineral composition in shale, the surface properties are heterogeneous. High pressure methane adsorption experiments are often used to estimate the parameter in Langmuir equation (Eq. 2.5) [13, 108]. Composition studies by XRD or EDS are needed to make reliable estimation of storage capacity.

On the other hand, the composition of shale gas might be a mixture of hydrocarbon gases. When heavy components (such as propane, butane) exist, at reservoir conditions, they may be at

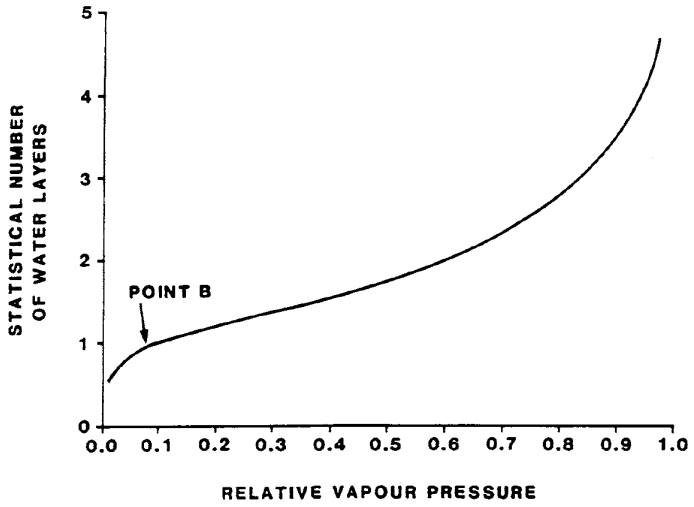

Figure 2.8: A water vapor adsorption curve measured on a nonporous oxide material. The figure is reproduced from Pallatt and Thornley [7].

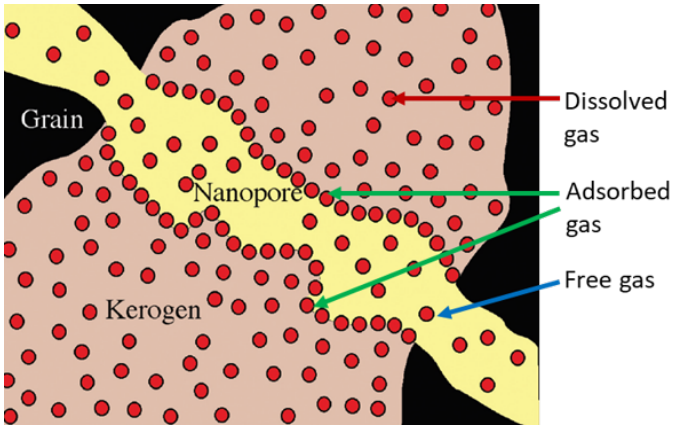

Figure 2.9: A schematic of kerogen pore space in shale and three forms of gases that are stored in shale, including free gas, adsorbed gas and dissolved gas. The figure is modified from Javadpour [8].

subcritical state. In mesopores, capillary condensation of the heavy mixtures will occur, as verified in the laboratory experiments by Chen *et al.* [109], which further complicates the storage and flow conditions. The calculations by Chen *et al.* [110] showed that the hydrocarbon in place can be up to six times larger than the amount estimated by Langmuir equation without considering capillary condensation. Knowledge of the amount and location of the capillary condensation is the key for accurate reserve estimation and production forecasting.

2.5 Pore-scale gas flow

2.5.1 Physics of pore-scale flow

Fluid transport in shale matrix is complicated by the nanometer-scale pore sizes, heterogeneous pore structure and surface properties. Here we focus on single phase gas transport. Knudsen number (Kn), which is defined as the ratio between gas mean free path and characteristic pore size ($Kn = \lambda/L$) is a critical parameter that is used to classify the flow regime. Fig. 2.10 shows the four common flow regimes based on Kn. For conventional reservoirs with micrometer-scale pore sizes, Kn is usually smaller than 0.001, and viscous or continuum flow regime is expected. Under such condition, the slip velocity at the solid boundaries is negligible and fluid flow can be very well described by the Darcy's Law [111]. For tight gas sandstone or macropores in shale gas reservoirs, Kn might be within the range of 0.001 – 0.1, and slip flow can not be neglected any more. Klinkenberg effect is observed for gas permeability measurement under different pressure conditions. The concept of slip velocity or slip length has been proposed to describe the slip flow regime. When Kn further increases, gas flow enters transitional or free molecular flow regimes. Under such condition, the pore size is merely a few molecules wide, and the chance of collision between gas molecules and pore walls is much greater than intermolecular collisions within the gas phase. Knudsen diffusion is expected and gas flow behavior deviates significantly from traditional Darcy flow.

Here we focus on methane transport in shale matrix. Fig. 2.11 shows the calculated Kn as a function of pressure for methane at 400 K within nanotubes of varying radii. At reservoir pressures and temperature, flow of supercritical methane falls within slip flow or early transitional

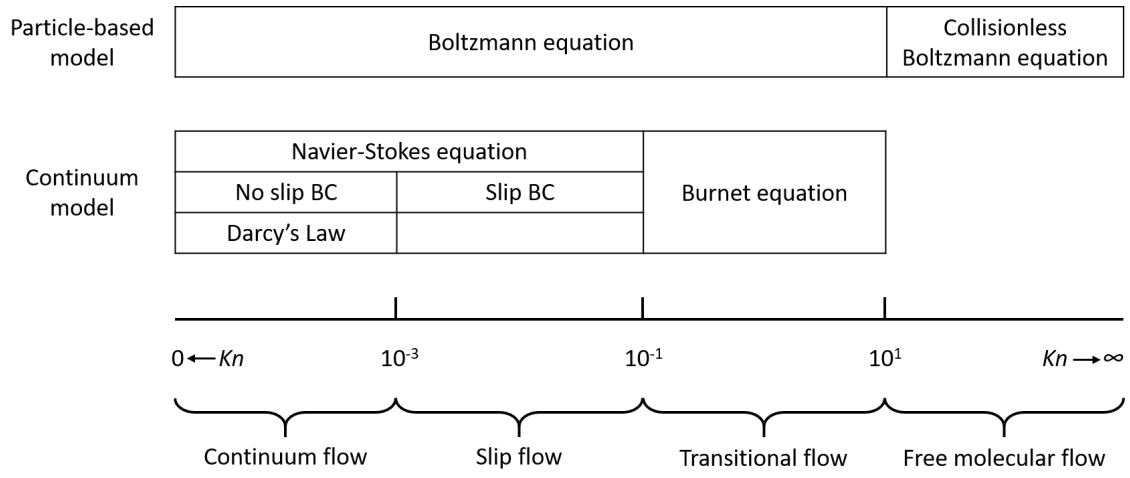

Figure 2.10: Classification of flow regimes based on Kn and corresponding analytical equations that describe each flow regime.

flow regimes ($0.001 < Kn < 1.0$).

For gas flow in nanochannels, the formation of Knudsen layer (see Fig. 2.12) near the wall is not negligible when $Kn > 0.1$. In this layer, the quasi thermodynamic-equilibrium assumption breaks down. When Kn is high, the local mean free path is greatly influenced by the wall boundary. Near the wall, the local mean free path is much shorter than away from the wall, which makes the effective viscosity, a function of mean free path, lower as well. Accurate modeling of the Knudsen layer is required to make reliable estimation of the total flux and apparent permeability.

The transport of shale gas is further complicated by the existence of adsorbed gas. Due to the concentration gradient in the adsorbed gas during the production process, surface diffusion occurs which increases the total mass flux [112–114]. The contribution of gas desorption is also not negligible when the pore pressure draws down. Furthermore, in nanopores diffusion also emerges as an important transport mechanism besides advection. The relationship between diffusion and advection can be described by the Péclet number (Pe), which is defined as the ratio between advection and diffusion transport rates ($Pe = Lu/D$, where L is the characteristic length, u is the local flow velocity, and D is the diffusion coefficient). In nanopores, the diffusion coefficient is different from the bulk and is a function of pore size, pressure, and temperature, and advection is complicated by the emergence of slip or transitional flow. As a result, the contribution of methane diffusion vs.

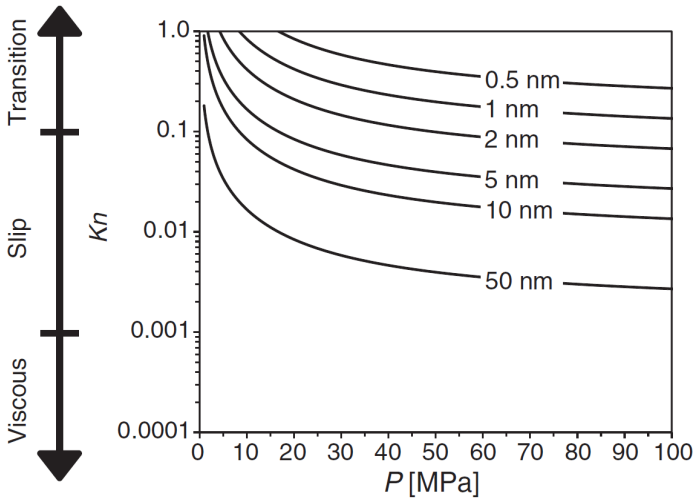

Figure 2.11: Knudsen number as a function of pressure (typical reservoir conditions) for methane confined in pores of varying sizes at 400 K. The corresponding flow regime is shown on the vertical axis. The figure is reproduced from Landry *et al.* [9].

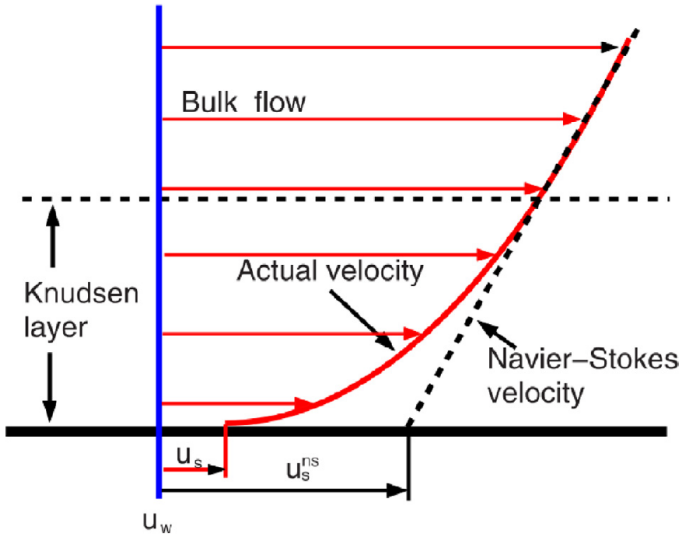

Figure 2.12: A schematic of the Knudsen layer in which the flow velocity deviates from the Navier-Stokes extension. The figure is reproduced from Wang *et al.* [10], see their Fig. 7.

advection in shale with complex pore structure and surface properties remains elusive.

2.5.2 Modeling of pore-scale flow

Single pore model

We first review the analytical flow models developed for a single pore or bundles of tubes model. For continuum low-Reynolds-number flow, Darcy's Law is widely used:

$$Q = \frac{KA\Delta P}{\mu L}, \tag{2.6}$$

where Q is the volumetric flow rate, K is the intrinsic permeability, A and L are the cross-sectional area and length of the flow channel respectively, $\Delta P/L$ is the pressure gradient applied to the channel. For simplified cross-sectional shape of the pore, K can be calculated based on Navier-Stokes equation. For example, for bundle of tubes model with cylindrical channel shapes, K takes the following form:

$$K = \frac{\phi r^2}{8\tau}, \tag{2.7}$$

where ϕ is the porosity of the system, r is the average channel radii, and τ is the tortuosity of the porous medium.

For slip flow regime, a simple correction can be applied to the Darcy permeability as a function of pressure to account for the slip velocity at the pore wall:

$$K = K_0 \left(1 + \frac{b}{\bar{P}}\right), \tag{2.8}$$

where K_0 is the intrinsic permeability, $\bar{P}$ is the average pressure, and b is the Klinkenberg correction factor, which can be determined by fitting experimental data to the equation. The klinkenberg equation is an empirical equation that has limited application to gas flow in shale. Next we review four analytical models that were developed to model high Kn flow, including dusty gas model (DGM) [115, 116], the first-order slip model by Brown *et al.* [117], the model by Javadpour [8], and the Beskok and Karniadakis tube model [118]. These models take the form of Darcy equation

(Eq. 2.6), but the permeability K is no longer a constant, but a function of pore size, pressure, and temperature. The concept of 'apparent permeability' is then used to describe the flow capacity.

The dusty gas model takes the flow as a linear summation of viscous flow and Knudsen diffusion, and the apparent permeability is given by:

$$K_{app} = K_0 \left(1 + \frac{\mu_0 D_{Kn}}{P K_0}\right), \tag{2.9}$$

where μ_0 is the dynamic viscosity of gas, P is pressure, and D_{Kn} is the Knudsen diffusion coefficient, which is described by the following equation [119]:

$$D_{Kn} = \frac{2R}{3}\sqrt{\frac{8R_s T}{\pi}}, \tag{2.10}$$

where R is the tube radii, R_s is the specific gas constant, and T is the temperature.

The tube model by Brown *et al.* [117] applies a slip correction factor F to the mass flux predicted for viscous flow. Using the first order slip-correction to the Navier–Stokes equations, the apparent permeability can be written as:

$$K_{app} = K_0 \left[1 + 4\left(\frac{2}{\alpha} - 1\right) Kn\right], \tag{2.11}$$

where α is the tangential momentum accommodation factor, which is a reflection of the gas-solid interactions. α can have a value ranging from 0 (specular reflection) to 1 (diffusive reflection). A value of 1 is usually used for shale organic pore surfaces due to the surface roughness and heterogeneity [9, 120].

The Javadpour model [8] is a combination of the DGM and the slip flow model by Brown *et al.*, and the apparent permeability is described by:

$$K_{app} = K_0 \left[1 + 4\left(\frac{2}{\alpha} - 1\right) Kn + \frac{\mu_0 D_{Kn}}{P K_0}\right] \tag{2.12}$$

The Beskok and Karniadakis tube model [118] employs a general slip-velocity boundary condition to the Navier–Stokes equations, and a rarefaction coefficient, C_r, which describes the

decrease in the chance of gas–gas collisions compared to gas–wall collisions when Kn increases:

$$K_{app} = K_0 \left[\left(1 + \frac{4Kn}{1+Kn} \right) C_r \right], \tag{2.13}$$

and the rarefaction coefficient C_r was determined by fitting to the solution of the linearized Boltzmann equation:

$$C_r = 1 + Kn \frac{128}{15\pi^2} \tan^{-1}\left(4Kn^{0.4}\right) \tag{2.14}$$

The analytical or empirical models reviewed above are developed for simple geometries (*e.g.* tube, slit), ignoring the complex pore network connectivity, thus they have limited applications in estimating apparent permeability in shale. Next we review several numerical models that either take advantage of these macroscale analytical models or were developed based on mesocale or microscale physics.

Pore network modeling

Pore network models, which represent a porous medium as a network of geometrically simplified pores connected by throats, provide a cost-efficient way of modeling various physical processes at the pore scale. The first PNM was proposed by Fatt [121] in 1956, who exploited the analogy between flow in porous media and a random resistor network. Afterwards, PNMs have grown in sophistication and can deal with irregular lattices, complex pore throat geometries, arbitrary wettability, and have been used to study a variety of physical processes, including gas sorption and condensation, non-Darcy flow, reactive transport, and restricted diffusion [48, 77, 122, 123]. Based on the construction method, PNMs can be classified into three major categories: 1) statistical reconstructions based on a regular network structure with critical morphological and topological parameters informed by experimental measurements reviewed in Section 2.3; 2) image-based methods by extracting PNMs from 3D CT or SEM segmented images; 3) process-based methods by extracting PNMs from grain packs where varieties of diagenetic processes can be modeled.

The statistical reconstructions are usually based on a regular lattice structure onto which porosity, PSD, and pore throat connectivity obtained from experimental sources are populated. The

cubic lattice structure with a constant coordination number (the number of throats connected to a certain pore) of six is commonly used as a simplified 3D PNM [124]. Later more degrees of connectivity (with coordination number up to 26) were added, which however may not be realistic [125]. For statistical reconstruction of shale pore networks, MICP, NMR, and gas sorption results have been used [77,111,126]. The advantage of such reconstruction is that more representative large scale information could be used, however, this method suffers from the fact that not enough pore structure information can be provided, due to the limitation and applicability of the experimental measurements. Therefore, certain assumptions have to be made about the ratio of pore/throat sizes or the connectivity. The reliability of such assumptions needs to be tested by either direct imaging analysis or laboratory flow experiments.

Image-based PNMs are constructed from realistic 3D images of the samples in honor of the true pore/throat locations and connectivity. The pores and throats can be isolated and extracted from the images using either medial axis [74] or maximal ball algorithms [127]. PNMs for shale have also been constructed based on FIB-SEM images with high resolutions, and single phase methane transport properties have been studied in detail [79, 128, 129]. The major problems with image-based PNMs are: 1) the lack of a specific and consistent definition of what is a pore and throat in actual porous media; 2) the difficulty in determining the shape of a pore and throat from voxel-based images with zig-zag features; and 3) the high computational cost and nonuniqueness of PNM construction processes.

The process-based PNM was pioneered by Bryant and co-workers [130–132]. The PNMs were extracted from a close packing of equal-sized spheres with their locations physically measured by Finney [133]. Cementation and compaction were modeled by enlarging the size of the spheres or moving the spheres closer together. They were able to predict absolute and relative permeabilities, capillary pressure curves, resistivity and mechanical properties of sandstones. Later packing of spheres with a distribution of sizes was used for more accurate PNMs construction, and the grain size distribution was quantified from thin section images [134,135]. Previous works could only model a single scale pore network with a unimodal PSD. Mehmani and Prodanović [12,126] further extended the PNM developed by Bryant and co-workers to include two scales of pores explicitly by rescaling

a smaller pore network onto either the pores or grains, forming the so-called 'series' or 'parallel' PNMs. They have then used these models to study diffusion or slip flow in shale matrix [12, 136]. The process-based PNMs have proved to be useful and reliable for flowing modeling in conventional rocks. However, the simplification of grain particles as spheres for shale may be questionable, and the scaling ratio and volume fraction of the smaller-scale pore networks are nontrivial to determine. Furthermore, the representative pore shape and wettability, which control flow properties, are hard to characterize.

Lattice Boltzmann method

LBM is a relatively new method that has been developed since the late 1980s [137]. As a particle-based method, LBM originated from lattice gas cellular automata, but it can also be viewed as a special discretization of the continuum Boltzmann equation [138]. LBM uses discretized fluid particles that moves along discrete directions on a regular lattice, thus avoids solving the complicated Navier-Stokes equation and avoids following each individual molecules as in molecular dynamics (MD) simulations. Several features of LBM make it an ideal method for studying nanoscale thermodynamic and hydrodynamic behaviors: a) the treatment of irregular geometries is straightforward; b) microscale kinetics can be incorporated with ease; c) the local nature of streaming and collision process makes it well suited for parallel computing, which leverages the computational cost.

Slip boundary condition Conventional flow simulation usually assumes no-slip boundary conditions (BC), which can be easily achieved in LBM by applying standard bounce-back BC [137]. However, such assumption breaks down at nanoscale. To capture the slip velocity at the solid boundary, specific BCs are adopted to implicitly consider the solid–fluid interaction. Various treatments of slip boundaries have been proposed in literature, including specular reflection (SR) BC, Maxwellian diffuse reflection BC, and the combination of the former two with standard bounce-back BC [9, 139–141]. The SR BC is motivated by the observation of elastic collisions between a particle and the boundary. The result of such collision is that the velocity component which is orthogonal to the boundary is reversed. Lim *et al.* [142] used the SR boundary condition to investigate

pressure driven and shear driven micro-channel flow. However, the full SR BC overestimates the slip velocity according to Tao and Guo [143]. The Maxwellian diffusive reflection BC was derived from the continuum kinetic theory. The particle distribution functions are redistributed following a Maxwellian distribution. However, work by Chai *et al.* [144] has shown that this boundary treatment also lead to overestimation of slip velocity for flow in a microchannel. To achieve more realistic slip boundary conditions, combination of bounce-back, SR and Maxwellian diffuse BC has been proposed. The combination coefficients are chosen such that the Maxwell-type second order slip boundary is satisfied. The coefficient is also related to the tangential momentum accommodation coefficient (TMAC), which is a reflection of the slip length. Typically, the TMAC can only be inferred from experimental results, rather than direct measurement. As a result, such forms of slip BC are more phenomenological than physical compared to those from MD and Boltzmann equation. To make full use of the kinetic nature of LBM, more physical ways to consider the slip BC has been proposed by directly incorporating the Shan-Chen fluid-solid interaction potential. Zhu *et al.* [145] used an exponentially decaying hydrophobic repulsive force of 4×10^{-3} $\mathrm{dyne/cm^3}$ with a decay length of 6.5 nm to simulate fluid slip in a 3D hydrophobic microchannel and observed good agreement with experimental results. However, this method was not well developed due to more restrictive constraints than the combined form of slip BC [10]. Therefore, phenomenological slip BC remains to be the most widely used in modeling micro-scale gas flow using LBM.

Flow in Knudsen layer For gas flow in nanochannels, the formation of Knudsen layer near the wall is not negligible when $Kn > 0.1$. By introducing an effective relaxation time that correlates with effective viscosity, LBM can be used to model flow in the Knudsen layer. Using this approach, Landry *et al.* [9] presented a local-effective-viscosity (LEV) LBM to simulate supercritical gas flow in the slip flow and early transition flow regimes in complex geometries. The LEV LBM is informed with local effective viscosities at each fluid node to capture the variance of the mean free path of gas molecules in a bounded system (see Fig. 2.13). The authors simulated pure methane flow in digital reconstructions of nanoporous organic matter at reservoir conditions.

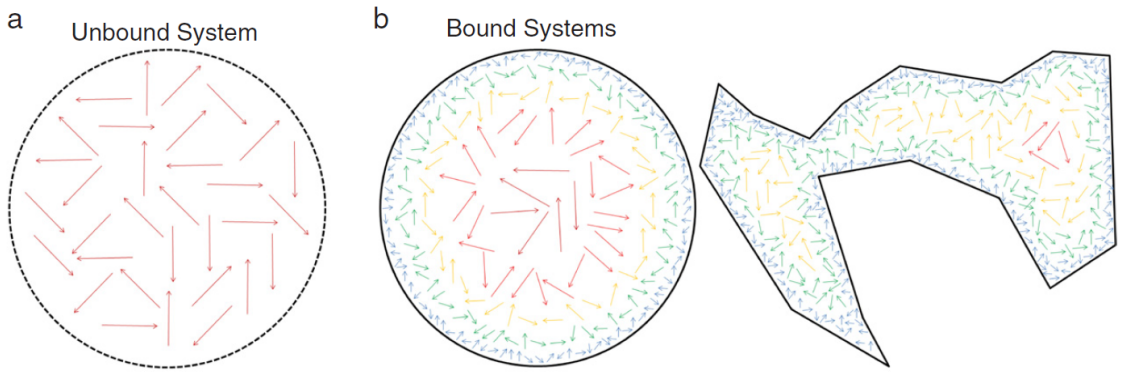

Figure 2.13: (a) Mean free path in an unbound geometry, where the mean free path is constant. (b) Mean free path in a bounded geometry, where the local mean free path is a function of distance from the pore wall. The figure is reproduced from Landry *et al.* [9]. See their Fig. 3.

Gas sorption Gas sorption can be incorporated into LBM implicitly by proper treatment of the boundary conditions. Zhou *et al.* [146] proposed to use a separate concentration distribution function, which is of similar form with the particle distribution function, to describe the concentration variation in the simulation domain due to surface adsorption and intraparticle diffusion. Mass transfer boundary condition is set up on the solid surface and density is updated by concentration variation. Such approach is very appealing as it simplifies the problem from multiphase to single phase simulation, however, because it uses Zou and He bounce-back BC [147] at the solid nodes, the flexibility of application to complex geometries is greatly impaired.

Another approach of sorption modeling is by the use of a single component multiphase (SCMP) LBM model, which explicitly models the adsorbed liquid phase and bulk gas phase at the same time. Several categories of multiphase LBM have been developed so far, including the color-gradient method of Gunstensen *et al.* [148], Shan-Chen method [149, 150], and free energy approach [151, 152]. Method of Gunstensen *et al.* uses two sets of particle (color) distribution functions for two different phases, and the phase interface is maintained via the local color gradient. This method enforces local mass and momentum conservation, but it is nontrivial to introduce realistic equation of state (EOS). Free energy approach defines a pressure tensor inside the equilibrium distribution function that introduces thermodynamic effects through a phenomenological EOS. It conserves local mass, momentum and energy, but it suffers from unphysical Galilean invariance effects, and density ratio achievable is quite limited [153]. Shan-Chen method introduces a phe-

nomenological interparticle force by defining a pseudopotential from a microscale point of view, and phase separation occurs automatically as a result without the need to track the interface [154]. It is easy to implement, computationally efficient, and straightforward for testing different forms of forces. Non-ideal EOS can be explicitly incorporated into the pseudopotential, and as a result, high density ratios can be obtained [155].

Multiphase LBM using the Shan-Chen model has been used to reproduce a variety of phase behaviors such as spontaneous condensation [155], cavitation [138], and adsorption [156]. The majority of LBM adsorption simulations in the literature focus on supercritical or ideal gases. Guo *et al.* [157] used a 1D LBM model to study ideal gas adsorption on a flat surface and observed good agreement with Langmuir equation. They extended their model to a 3D cylindrical pore geometry and incorporated PR-EOS, but did not explore more complex porous media nor attempt comparison to experimental results. Zhao *et al.* [158] used a 2D LBM model with modified Shan-Chen pseudopotential to study supercritical methane adsorption. By benchmarking the adsorption isotherm at different pressures with GCMC simulation, they obtained a specific correlation between solid pseudopotential and pressure. However, this correlation is limited by its calibration to a certain adsorbent/adsorbate pair at a certain temperature. Other researches that study microscale gas flow with adsorbed gas do not provide strict validation of the adsorption isotherm [159]. Fewer studies are performed on subcritical gas adsorption LBM simulations. Sukop and Or [156] used a 2D LBM model with the original Shan-Chen pseudopotential to study subcritical gas adsorption and phase separation in a parallel plate geometry, but their model did not have a well-defined pressure and temperature, and their results did not correlate well with DLVO theory. Because of its kinetic nature, LBM is applicable to thermodynamic behaviors, but the key is to incorporate well-defined EOS and calibrated surface force. Different forms of EOS have been successfully introduced into LBM [155], but the form of surface force that reproduces the correct adsorption physics remains unknown. Developing such an LBM model and establishing correlations with physical parameters is valuable for understanding the mechanism of adsorption and phase separation in nanoporous media with complex geometries.

Molecular-scale methods

Molecular-scale methods provide detailed insight into the kinetic behavior by modeling the individual interactions between gas and solid molecules explicitly. Several commonly used methods to study thermodynamic and hydrodynamic behaviors include GCMC, direct simulation Monte Carlo (DSMC), and MD simulations. A lot of work has been done to explore single component gas adsorption/desorption, multicomponent competitive adsorption, advection and diffusion in nanopores, and a series of gas/solid pairs have been studied in detail [14, 160–164]. The major drawback of molecular-scale methods to study hydrodynamic behavior in shale is the high computational cost as a result of tracking the motion of each individual molecule, thus the simulation domain is limited to tens of nanometer across. Furthermore, usually a homogeneous surface is used which cannot capture the heterogeneity in shale. For low Reynolds number and low Mach number flow which is common in shale nanopores, the flow velocity of gas molecules is usually orders of magnitude smaller than the thermo velocity arising from the Brownian motion, which makes the statistical averaging process of determining macroscale properties quite challenging. Obviously simulations performed at such confined scale has limited implications for large scale behaviors, yet these sets of methods are valuable for understanding the fundamental physics, the cumulative behavior of which controls the large scale thermodynamics and hydrodynamics.

2.6 Summary

In this chapter we introduced the pore structure and surface properties of shale, and critically reviewed the available petrophysical characterization methods for pore structure reconstruction and flow capacity estimation. Two fundamental processes that are important for fluid confined in nanopores in shale, namely sorption and transport, are introduced and the challenges associated with the understanding of these two processes are reviewed in detail. The commonly used analytical and numerical models to study flow behavior at nanometer scale are also critically reviewed.

In this thesis, we will focus on the use of two numerical models: PNM and LBM. For PNM, we develop on the basis of the two-scale process-based PNM proposed by Mehmani and

Prodanović [12] to account for the different types of pore systems and multi-scale pore sizes in shale. We chose to use nitrogen sorption experiments and SEM images to characterize the critical pore structure properties, which will then guide the construction of the PNM. Both advection and diffusion will be studied using the reconstructed PNM.

For LBM, we develop a novel LBM model to model gas sorption from first principles, where adsorbed gas and free gas will be modeled explicitly. The LEV-LBM model developed by Landry *et al.* [9] will then be used to study hydrodynamic behavior with the existence of adsorbed liquid in shale. Both simplified model pore structures and image-based reconstructions will be used to study gas sorption/transport behavior in different pore systems in shale.

Chapter 3: Use of nitrogen sorption isotherms and SEM images to construct PNMs to infer pore structure and flow properties of shale matrix [1]

3.1 Introduction

Nitrogen sorption isotherms have been widely used for surface area, pore size, and pore throat connectivity characterization of nanoporous media [25–27, 37, 69, 165]. A series of adsorption models, such as BET, BJH, and DFT, have been developed to interpret the measured sorption data [5, 25, 27], which have been critically reviewed in Chapter 2. Most of the methods require *a priori* assumption of a simplified pore shape, and representativeness of such shape might be difficult to establish. For example, adsorption curves without a plateau (capillary condensation) are commonly accredited to the existence of slit-shaped pores [24]. However, such behavior may also be reproduced when large macropores are present, not necessarily of slit shape [5]. As a consequence the derived PSD is actually pore shape dependent. Recently, Qajar *et al.* [11] showed that pore geometry has a significant effect on the adsorption curve shape. They applied LDFT to simulate the adsorption curve of a single pore with three different shapes (slit, cylindrical and spherical) but the same size, and observed considerable discrepancy in the simulation results (see Fig. 3.1). Spherical pores have the highest curvature and result in the earliest capillary condensation, because of the strongest surface forces exerted on the fluid molecules in the most confined geometry. In their study, they used an average pore size characterized by BJH method with an assumption of cylindrical pore shape as a representative pore size for all the three pore geometries. However, the

[1] This chapter is modified from our previous publications (the advection and diffusion simulation, however, is the most recent result): (1) Xu, R and Prodanović, M. Effect of pore geometry on nitrogen sorption isotherms interpretation: A pore network modeling study. Fuel, 225:243–255, August 2018. (2) Xu, R, Mehmani, A, Qajar, A, Prodanović, M, Daigle, H, and Nguyen, S. Combination of lattice density functional theory and a multi-scale network model for sorption isotherms study in tight formations. Unconventional Resources Technology Conference, August 2016. My contribution to the two papers includes analyzing experimental data provided by coauthors, improving and integrating the PNMs and LDFT models developed by coauthors, designing and performing the numerical simulation, analyzing the results, and writing the papers.

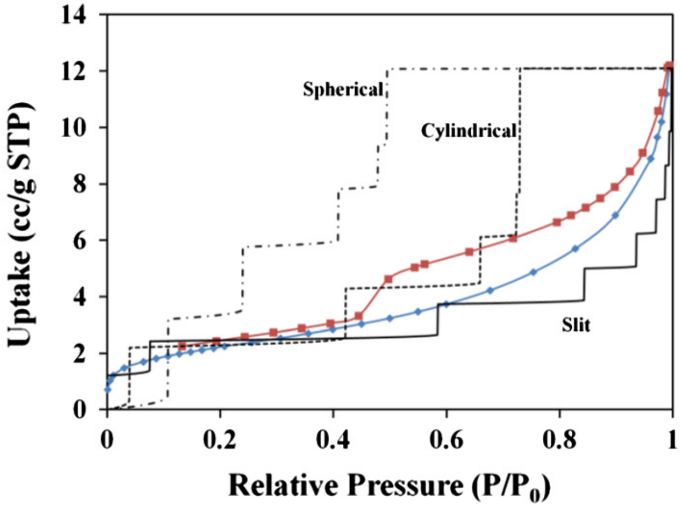

Figure 3.1: Nitrogen adsorption curves at 77 K calculated using LDFT (black curves) for a single pore with the same size (8.6 nm) but three pore shapes (spherical, cylindrical, and slit). The colored curves with symbols are experimental data measured on Cameo coal sample. The figure is reproduced from Qajar *et al.* [11].

actual porous medium presents a bimodal PSD [11]. Significantly different PSD can lead to the same average pore size, but quite different adsorption curves. Moreover, they only focused on the adsorption branch of the sorption isotherms while the desorption branch was not analyzed. The stepwise feature observed in all of their simulation curves as a result of using an average pore size also increases the uncertainty when comparing with the experimental curves.

In this work, we compensated for the above shortcomings by integrating LDFT with a dual-scale PNM developed by Mehmani and Prodanović [126]. The novelty of the PNM in [126] is its capability to include explicitly two scales of pore systems. For shale, this includes both the interP pore system existing between large silt grains (*e.g.* quartz, calcite, and feldspar), and the pores existing within clay particles or OM that are dispersed within the large interP pores. The original PNM in [126] assumed spherical pore and cylindrical throat shapes, which was a reasonable assumption for sandstone, but should be reconsidered for shale. In this work, we made certain geometrical modifications to the original PNM and considered three types of pore/throat shapes (spherical, cylindrical, and slit) to honor the complex pore shape and structure commonly observed by SEM images.

LDFT was applied to each pore in the PNM, and the total adsorption uptake was integrated

based on the PSD. For desorption simulation, pore network effect was explicitly considered to reproduce the sorption hysteresis, and cavitation effect (or tensile strength effect) which causes the forced closure of the nitrogen hysteresis loop was modeled as well. An interpretation workflow was proposed to characterize the PSD and pore throat connectivity of shale core samples by tuning these parameters to match the simulated nitrogen sorption hysteresis loops with experimental data. We studied the effect of pore shape on the interpretation results, which had not been paid enough attention to previously. Nonunique interpretation results were observed with equally good agreement with experimental data. To further constrain the results, we used a combination of the three pore shapes within the same PNM informed by SEM images analysis to match the experimental curves. Such approach had not been attempted in the literature before. Finally, we calculated and compared the apparent permeability for supercritical methane flow through the reconstructed PNMs with different pore shapes, using the hydraulic conductivity model developed by Beskok and Karniadakis [118]. Diffusion of methane was also studied using a unified model which considers both Fick diffusion and Knudsen diffusion [166]. We then studied the apparent permeability and effective diffusivity of these PNMs under different pressure conditions.

3.2 Experiments

Two samples were used for nitrogen sorption characterization in this study, including the organic-rich Woodford shale (Upper Devonian, Oklahoma) and Cameo coal (Cretaceous, Colorado), that have TOC of 17.2 wt% and 69.9 wt%, and vitrinite reflectance of 0.58% $\mathrm{R_o}$ and 0.56% $\mathrm{R_o}$, respectively [11]. We used the same samples as in the work by Qajar *et al.* [11] to compare their results with our model and demonstrate the improvements.

Textural properties of the samples were determined by standard N_2 adsorption at 77 K using a Micromeritics 3Flex Surface Characterization Analyzer instrument. Surface area is estimated using the BET method, and PSD is determined by applying the N_2@77K-Slit-NLDFT model [167] to the adsorption branch of the sorption data. Micropore volumes of the samples were calculated from nitrogen uptake at relative pressure $P/P_0 = 0.14$, corresponding to pore-filling of pores 2 nm in diameter in the HK model [64]. Total pore volume was determined from nitrogen adsorption

uptake at $P/P_0 = 0.99$ [11]. Meso–macro pore volume was obtained by subtracting micropore volume from total pore volume. The surface area and PSD obtained using the above methods were used as reference values for comparison with simulation results. Both adsorption and desorption data were recorded for further usage in the simulation process.

3.3 Numerical modeling

3.3.1 Pore network modeling

In this study, we used a modified version of the dual-scale PNMs developed by Mehmani and Prodanović [12]. A schematic illustration of the two types of dual-scale network is shown in Fig. 3.2. Herein we focused on the pore-filling dual-scale network since this type of pore structure is most commonly observed in SEM images of shale [1, 19], where microporosities are developed within clay or OM dispersed within large interP pore spaces. Grain-filling microporosity has also been observed in calcite or pyrite grains [1]. However, these microposities are most likely not very well connected, therefore not available to nitrogen and has limited contribution to flow capacity [1]. Three types of pore shapes were used in this work with slightly different network structures. 1) PNM with spherical pores, where the sites in the original PNM are treated as pore bodies, and bonds are assumed to be negligible in volume; 2) PNM with cylindrical pores, where bonds are treated as pore bodies, and sites connected by bonds are ignored and their volumes are assumed to be irrelevant; 3) PNM with slit pores, with the same network structure as 2). PNMs with spherical pores are commonly observed for OM pore structure, where a spongy and foamy pore network is formed during the hydrocarbon generation process [1, 53]. PNMs with cylindrical pores can either represent interP pore network or OM pores that are not very well developed [11], while PNMs with slit pores are commonly observed within clay particles [6, 47, 78]. It should be mentioned that the concepts of pores and throats may be obscure for shale with complex pore structure, and therefore will be collectively called 'pores' from here on unless specified otherwise.

To reduce the computational cost while maintaining statistical representation, Mehmani and Prodanović [126] simplified the micropore networks of a pore-filling dual-scale network to be

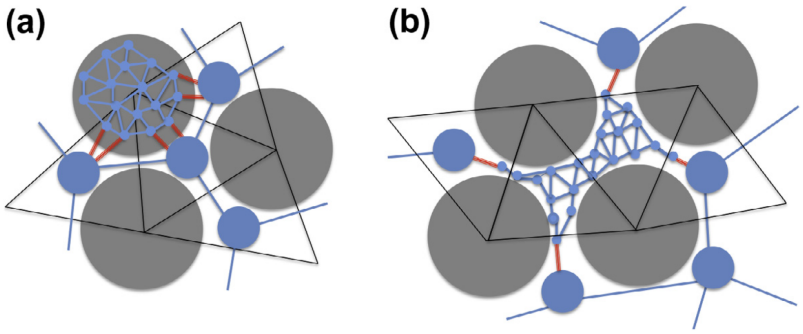

Figure 3.2: 2D schematic of the two types of dual-scale pore network developed by Mehmani and Prodanović [12] for (a) grain-filling, and (b) pore-filling microporosity. InterP pores are shown as larger blue circles. For designated microporous regions, a network is rescaled with an appropriate length ratio and mapped into the microporous region. In (a) grains are microporous, in (b) pores are microporous. Throats connecting the two scales of networks are shown in red. The figure is reproduced from Mehmani and Prodanović [12].

consisting of bundles of tubes of equal radii (mean pore size of the micropore network) occupying the total pore volume of the micropore network. Namely, the interconnectivity within the micropore network was neglected. Such simplification was not found to result in significantly larger error with regard to permeability calculations compared to explicit dual-scale PNMs [126]. In this work we followed the same methodology for simplification. As a result, we have a PNM structure very similar to the single-scale PNM, and the nominal average coordination number (number of bonds connected to a site) is four in this case.

3.3.2 Nitrogen sorption modeling

We modeled the adsorption process in each individual pore using the LDFT approach. LDFT was developed based on statistical thermodynamics [91, 168]. In this theory, the pore space is discretized into a structured lattice of adsorption sites where adsorbate molecules may or may not reside. The probability x of an adsorption site to be occupied by an adsorbed molecule ranges between zero and one. This probability can also be interpreted as the normalized adsorbate density (normalized by the maximum adsorbate density, which is the liquid nitrogen density in this case) at a certain site. The adsorbate molecule interacts with its neighboring sites via a lateral interaction energy term E_0. Molecules close to the solid surfaces are affected by the surface forces in the form of a surface energy term E_A. Several assumptions are made when deriving LDFT for simplified

pore geometries as used in this study:

- The adsorption process is simplified as a 1D process that happens layer by layer. The adsorbate density of a certain layer is the mean value of all the adsorption sites within that layer.
- The mass transfer (diffusion) from the adsorbed phase to the bulk phase is neglected.
- When the adsorption process reaches equilibrium at a certain pressure, it is assumed that the Gibbs free energies of the bulk and adsorbed phases are equal.

Therefore, at equilibrium state, we have:

$$\Delta H = T\Delta S, \tag{3.1}$$

where ΔH is the enthalpy change by removing a gas molecule from the bulk phase to the adsorbed phase, and ΔS is the corresponding entropy change, and T is the temperature which is kept constant during adsorption measurements. ΔH and ΔS can be expressed as a function of the occupation probability x_i of the i^{th} adsorbed layer and its neighboring layers, and Eq. 3.2 shows the series of nonlinear equations that can be solved iteratively to obtain x_i for each layer of a slit pore.

$$RT\ln\frac{x_1(1-x_b)}{x_b(1-x_1)} - \epsilon_A(z_2x_2 + z_1x_1 - z_bx_b) - \epsilon_0 = 0, \tag{3.2a}$$

$$RT\ln\frac{x_i(1-x_b)}{x_b(1-x_i)} - \epsilon_A(z_2x_{i-1} + z_2x_{i+1} + z_1x_i - z_bx_b) - \epsilon_{0i} = 0, \tag{3.2b}$$

$$RT\ln\frac{x_N(1-x_b)}{x_b(1-x_N)} - \epsilon_A(z_2x_{N-1} + z_1x_N - z_bx_b) - \epsilon_0 = 0, \tag{3.2c}$$

where x_b is the normalized adsorbate density for the bulk phase; ϵ_A and ϵ_0 are the lateral and surface energy respectively that have the same unit with RT. Here we define $E_A = \epsilon_A/RT$, and $E_0 = \epsilon_0/RT$ to be the normalized lateral and surface energy. E_{0i} is the surface energy experienced by the i^{th} layer of adsorption sites. E_{0i} is a function of pore shape and $E_{0i} = E_0/i^4$ for a slit pore; z_b is the coordination number in the bulk phase, and for the cubic lattice structure we used here $z_b = 6$ (note that we use the same term 'coordination number' here to represent the number of neighboring adsorption sites that interact with an adsorbate molecule, but it should not be confused

with the coordination number of the pore network); z_1 is the coordination number for an adsorbate molecule interacting with its nearest neighbors within the same layer, and $z_1 = 4$; $z_2 = (z_b - z_1)/2$ is the coordination number for an adsorbate molecule interacting with the adjacent layers. After solving for x_i, the total amount of adsorption for a single pore can be calculated by Eq. 3.3.

$$\frac{\Gamma}{C} = \sum_{i=1}^{N}(x_i - x_b), \tag{3.3}$$

where C is the monolayer adsorption capacity and Γ is the excess adsorption. LDFT was initially developed for slit pores, while for cylindrical and spherical pores, E_{0i} take different forms due to the change in curvature, and C and z are no longer constant for different adsorption layers. The detailed derivations and expressions for the cylindrical and spherical pore geometry can be found in [11].

LDFT has been successfully used to model micropore (<2 nm) filling and capillary condensation in mesopores (2 – 50 nm) [72, 86], but it was developed for a single pore or a pore network with uniform pore size. To extend it to a network pores with dual-scale PSD, we calculated the adsorption amount in every pore in the network using LDFT and integrated the results to obtain the total adsorption amount of the whole network, as is shown in Eq. 3.4.

$$\Gamma_t(P) = \frac{\sum_{i=1}^{N}\Gamma_i(P)V_i}{\sum_{i=1}^{N}V_i}, \tag{3.4}$$

where Γ_t is the normalized total adsorption amount (ranging from zero to unity) at a certain pressure; Γ_i is the adsorbed amount in the i^{th} pore and V_i is the volume of the i^{th} pore. In the adsorption simulation, we tracked the adsorption amount of each individual pore, and capillary condensation pressure was calculated as the lowest pressure at which the normalized adsorbed amount reaches unity). This pressure value was then used in the desorption simulation to judge whether a pore remains filled or not at a certain pressure. As the pressure decreases in the desorption process, the boundary pores are exposed to the bulk vapor outside the pore network. In order for a pore to release the adsorbate, it must lie on a percolating vapor path (*i.e.* a connected path of vapor-filled pores that spans and reaches one of the six sides of the network boundary). However, if its

pathway is blocked by the condensed liquid in smaller pores connected to it, it will not release its adsorbate until the condensed phase in smaller pores is released first. This is the so called pore network blocking effect [28], which is one of the major reasons that lead to the observed hysteresis loop. Metastability of the adsorbed phase has also been argued to contribute to delayed capillary condensation [24, 27], but this is not expected in an inhomogeneous porous medium with complex surface roughness and chemical properties. On the other hand, cavitation effect causes the forced closure of the hysteresis loop at relative pressure around 0.45 for nitrogen [169]. In the desorption simulation, we considered both pore network effect and cavitation effect to create the opening and the forced closure of the hysteresis loop. Note that in our modeling work, adsorption is assumed to be independent of connectivity (which is a common assumption [5, 126]) and is only a function of PSD, surface energy and pore shape, whereas desorption is affected by connectivity of the pore network as well.

3.3.3 Matching sorption curves

As discussed in Chapter 2, nitrogen sorption curves contain useful information about porosity, PSD, and pore throat connectivity. Therefore, we assume that a good match of both adsorption and desorption curves between PNM simulated nitrogen sorption curves and experimental results yields a pore network that is statistically representative of the actual pore structure of the characterized sample. The major goal of this work was then to tune the porosity, PSD, and pore throat connectivity to optimize the matching outcome.

To describe the bimodal PSD that is commonly observed in shale, indicating two scales of pore structure, we used a bimodal Gaussian probability density function (PDF) [170]:

$$p\left(\log_{10} R\right) = \omega_1 \frac{1}{\sqrt{2\pi}\sigma_1} 10^{-\frac{\left(\log_{10} R - \log_{10} \mu_1\right)^2}{2\sigma_1^2}} + \omega_2 \frac{1}{\sqrt{2\pi}\sigma_2} 10^{-\frac{\left(\log_{10} R - \log_{10} \mu_2\right)^2}{2\sigma_2^2}}, \qquad (3.5)$$

where R is the pore radius in Å; ω_1 and ω_2 are the weight coefficients (or volume fractions) of each Gaussian mode, with $\omega_1 + \omega_2 = 1$; $\log_{10} \mu_1$ and $\log_{10} \mu_2$ are the mean values of the logarithmic pore radius of each mode; and σ_1 and σ_2 are the corresponding standard deviations of the logarithmic pore radius. By varying the five parameters $(\omega_1, \mu_1, \mu_2, \sigma_1, \sigma_2)$, we could obtain a wide range of

bimodal PSDs. The cumulative density function (CDF) shown below can be derived by integrating Eq. 3.5 over R:

$$P\left(\log_{10} R\right) = \frac{\omega_1}{2}\left[1 + \text{erf}\left(\frac{\log_{10} R - \log_{10} \mu_1}{\sqrt{2}\sigma_1}\right)\right] + \frac{\omega_2}{2}\left[1 + \text{erf}\left(\frac{\log_{10} R - \log_{10} \mu_2}{\sqrt{2}\sigma_2}\right)\right] \quad (3.6)$$

We began by tuning the PSD and surface energy defined in LDFT to match the simulated adsorption curve with the experimental adsorption branch. Since the adsorption uptake is reported as the normalized value by the total pore volume, porosity was not used as a matching parameter. The physical properties that need to be optimized are the PSD and surface energy E_0, which results in 6 independent parameters. Note that we held the lateral energy term E_A to be constant -1.87 according to the work by Qajar *et al.* [11], since E_A is only a function of gas species and temperature. The relative error E_r between the simulated and experimental curve is calculated using the following equation:

$$E_r = \sum_{i=1}^{n}\left(\frac{Q_{sim_i} - Q_{exp_i}}{Q_{exp_i}}\right)^2, \quad (3.7)$$

where n is the total number of measured data points; Q_{sim_i} and Q_{exp_i} are the normalized adsorption at the i^{th} pressure point for simulation and experimental results respectively. To ensure that we are comparing the same pressure points, the simulation data were extrapolated to the same pressure points as experiments. The best match between simulated and experimental curves is found by minimizing the error function (Eq. 3.7) using a global optimization solver in MATLAB.

After the adsorption curve is matched, the PSD and surface energy E_0 are fixed. The desorption curve is then matched with only one fitting parameter, which is the coordination number of the pore network. We modify the coordination number distribution by randomly deleting a certain fraction of bonds (f_{del}) from the PNM. The larger the f_{del}, the larger the hysteresis will be. The optimized match is found by minimizing the error function between the simulated and experimental desorption curves. The total error of the fit is obtained by summing up the matching errors for both curves.

The above workflow was performed for all three types of pore shapes to acquire the corresponding optimized parameters that describe the pore structure and surface properties. We can

then evaluate the effect of pore shape on the interpretation of nitrogen sorption isotherms. It should be mentioned that the matching procedure is designed based on available data and the result is not necessarily unique.

3.3.4 Advection and diffusion modeling

Methane, which is the main component of shale gas, is stored underground at supercritical state under common reservoir pressure (10 – 50 MPa) and temperature (300 – 400 K) conditions. Two types of transport mechanisms contribute to the flow capacity of tight porous media, namely diffusion and advection. Their relative contributions can be described by the Péclet number (Pe), which is the ratio between the advective transport rate and diffusive transport rate. Pe is a function of pressure, temperature, pore size and shape. To compare the flow capacities of the constructed PNMs with different pore shapes, we conducted both advection and diffusion simulations, and calculated the apparent permeability k_a and effective molecular diffusivity D_e of methane. The relative contribution of diffusion and advection to total mass flux as a function of pressure and temperature was compared as well.

As discussed previously, we made certain geometric modifications to the PNMs to include different pore shapes to calculate nitrogen adsorption uptake. For advection and diffusion simulations, bonds (throats) of the PNMs dominate the transport properties rather than sites (pores). PNMs with slit and cylindrical pore shapes remain unaltered here. For PNMs with spherical pore shapes, we assume that spherical sites are connected by cylindrical bonds, forming the so-called ink-bottle pore structure as is commonly observed for OM pores. The site/bond size ratio varies sample by sample as a function of kerogen type and maturity, and for convenience we used a common value of two. On the other hand, for PNMs with slit pores, we assumed that the cross sections of all the slit pores have an aspect ratio of one.

For hydraulic advection modeling in cylindrical and slit pores, we used the Darcy-type equations established by Beskok and Karniadakis [118], which were fitted to the solutions of linearized Boltzmann equation, and were shown to agree well with DSMC data over the entire range

of Kn. The free gas volumetric flow rate q for a cylindrical pore of radii r can be expressed as:

$$q = f(Kn)\frac{\pi r^4}{8\mu}\frac{\Delta P}{L}, \tag{3.8}$$

where μ is the dynamic viscosity, $\Delta P/L$ is the pressure gradient, and $f(Kn)$ is a correction function which is written as [118]:

$$f(Kn) = (1 + \alpha_{cyl} Kn)\left(1 + \frac{4Kn}{1 - \beta Kn}\right), \tag{3.9}$$

where β is the slip coefficient and $\beta = -1$ by fitting to the velocity profiles from DSMC and linearized Boltzmann equation [171]. α_{cyl} is the rarefaction coefficient which is a function of Kn:

$$\alpha_{cyl} = \frac{128}{15\pi^2}\tan^{-1}\left(4Kn^{0.4}\right) \tag{3.10}$$

The hydraulic conductance of a cylindrical pore $g_{a_{cyl}} = q/\Delta P$ can then be written as:

$$g_{a_{cyl}} = \frac{\pi r^4 f(Kn)}{8\mu L} \tag{3.11}$$

For a slit pore, the volumetric flow rate q can be written as [171]:

$$q = C(1 + \alpha_{slit} Kn)\left(1 + \frac{6Kn}{1 - \beta Kn}\right)\frac{wh^3}{12\mu}\frac{\Delta P}{L}, \tag{3.12}$$

where w and h are the width and height of the slit pore and for a slit pore with unity aspect ratio, $w = h$, C is a correction factor as a function of aspect ratio AR [172]:

$$C = 1 - \frac{192(AR)}{\pi^5}\sum_{i=1,3,5,\ldots}^{\infty}\frac{\tan(i\pi/2(AR))}{i^5}, \tag{3.13}$$

and the rarefaction coefficient α_{slit} is expressed as [171]:

$$\alpha_{slit} = 1.7042\frac{2}{\pi}\tan^{-1}(8Kn^{0.5}) \tag{3.14}$$

The hydraulic conductance of a slit pore can then be written as:

$$g_{a_{slit}} = C(1 + \alpha_{slit} Kn) \left(1 + \frac{6Kn}{1 - \beta Kn}\right) \frac{wh^3}{12\mu L} \tag{3.15}$$

In this study, the effect of adsorbed gas on flow capacity is ignored. The existence of adsorbed gas reduces the effective pore size for hydraulic advection, but surface diffusion as a result of the concentration gradient of the adsorbed gas on the pore wall, or diffusion from the adsorbed phase to the bulk phase may arise as additional sources of mass flux. Therefore, the overall contribution of adsorbed gas to flow capacity varies as a function of pressure, temperature, and surface properties. Here we mainly focus on the comparison between advection and diffusion without considering the adsorption induced flow physics.

The molecular diffusion process in nanopores can be divided into three regimes based on Kn, including Fick diffusion for $Kn \leq 0.1$, transitional diffusion for $0.1 < Kn < 10$, and Knudsen diffusion for $Kn \geq 10$ [166, 173, 174]. For unconventional tight rocks with multiscale PSDs, Kn may vary widely within the pore system. As a result, the diffusion mechanism is often a mixture of the three, and the effective molecular diffusivity is a function of pressure, temperature, PSD, and pore throat connectivity. Therefore, we consider here the local diffusivity within each individual pore. The determination of local diffusion coefficient is crucial for accurate modeling of gas diffusion across the whole regime. The molecular (Fick) diffusion coefficient D_b depends on the gas type, temperature, and pressure. Speedy [175] proposed an expression for D_b that considered the real gas effect under the high-pressure condition, which was shown in the work by Yin *et al.* [166] to agree well with experimental data for a wide range of pressures (10 – 200 MPa).

$$D_b = \frac{3}{8nd_m^2}\sqrt{\frac{k_B T}{\pi m}} \left(1 - \frac{n^*}{1.09}\right) \left[1 + n^{*2}(0.4 - 0.83n^{*2})\right], \tag{3.16}$$

where n is the number density of gas molecules, d_m is the molecular diameter, k_B is Boltzmann constant, T is temperature, m is the molecular mass, and n^* is the reduced number density, and $n^* = nd_m^3$ [166].

On the other hand, the Knudsen diffusion coefficient D_{Kn} only depends on the local pore

size, gas type, and temperature. D_{Kn} has been derived in the kinetic theory of gas [176]:

$$D_{Kn} = \frac{4d}{3}\sqrt{\frac{k_B T}{2\pi m}}, \tag{3.17}$$

where d is the local pore size.

The empirical Bosanquet formula has been proposed in the previous work to calculate the gas diffusivity D_t in the transition regime, which takes the harmonic mean of D_b and D_{Kn} [177, 178]:

$$\frac{1}{D_t} = \frac{1}{D_b} + \frac{1}{D_{Kn}} \tag{3.18}$$

The local Kn is calculated as the ratio between the gas mean free path λ and local pore size d, and λ can be calculated as:

$$\lambda = \frac{1}{\sqrt{2}\pi n d_m^2} \tag{3.19}$$

Then the choice of appropriate formula for diffusivity depends on Kn calculated locally in each pore.

The molar flux of diffusion J_d within the pore is defined as a function of the concentration gradient:

$$J_d = D_t \frac{dC}{dL} \tag{3.20}$$

Therefore the volumetric flow rate caused by diffusion for either cylindrical or slit pores is expressed as:

$$q_d = \frac{MA}{\rho} D_t \frac{dC}{dP}\frac{dP}{dL}, \tag{3.21}$$

where M is the molar mass, ρ is the gas density, and A is the cross-sectional area of the pore, for cylindrical pores with radius r, $A = \pi r^2$, and for slit pores with width w and aspect ratio of one, $A = w^2$, $\frac{dC}{dP}$ can be solved numerically with the use of PR-EOS. Then the diffusion conductance for a cylinder and slit pore is calculated as:

$$g_{d_{cyl}} = \frac{M\pi r^2}{\rho L} D_t \frac{dC}{dP} \tag{3.22}$$

$$g_{d_{slit}} = \frac{Mw^2}{\rho L} D_t \frac{dC}{dP} \tag{3.23}$$

For steady state advection and diffusion, the cumulative mass flow rate into and out of a site i of the PNM should be zero. Therefore, based on mass balance:

$$\sum_{j=1}^{N} \rho(\frac{P_i + P_j}{2}) g_{ij}(\frac{P_i + P_j}{2})(P_i - P_j) = 0, \tag{3.24}$$

where N is the total number of bonds connected to a site i. Applying Eq. 3.24 to all the sites in the PNM renders a series of nonlinear equations of P_i, which can be solved iteratively to get the pressure distribution within the PNM. The apparent flow permeability of methane can be calculated based on the following equation:

$$k_a = \frac{q_{avg} \mu_{avg} L}{A(P_{in} - P_{out})}, \tag{3.25}$$

where q_{avg} is the average volumetric advective flow rate across a cross section perpendicular to the flow direction, and μ_{avg} is the average dynamic viscosity calculated by the average pressure of the system, which for a small pressure drop (*e.g.* a pressure gradient of 0.1 MPa/m across a domain size of 10 μm renders a pressure drop of only 1 Pa across the inlet and outlet) can be approximated as the arithmetic mean of the inlet and outlet pressures (P_{in} and P_{out}).

The effective diffusivity of methane can be calculated in a similar way:

$$D_e = \frac{\sum_i J_{di} A_i L}{A(C_{in} - C_{out})}, \tag{3.26}$$

where J_{di} and A_i are the diffusion molar flux and cross-sectional area for i^{th} pore at the inlet, and C_{in} and C_{out} are the inlet and outlet methane concentrations, A and L are the total cross-sectional area and length of the PNM.

3.4 Results and discussion

3.4.1 Experimental results

The measured nitrogen sorption isotherms for Cameo coal and Woodford shale samples are shown in Fig. 3.3. Note that on the vertical axis we plot normalized adsorption, which is defined as the ratio between the quantity adsorbed and the maximum adsorption amount, for easier comparison with simulation results. For Cameo coal sample, there is a significant hysteresis loop compared with Woodford shale sample, which indicates the difference in connectivity and shape/size of the pores. The PSDs for the two samples obtained by NLDFT approach using the analysis software associated with the experimental instrument are shown in Fig. 3.4 with assumption of slit pore shape by default. Both samples show roughly a bimodal PSD with nanoscale pore sizes below 200 nm, if the smaller local peaks are ignored. The other pore structure information characterized by nitrogen sorption measurements are shown in Table 3.1. The mean pore size for Woodford shale is about seven times larger than Cameo coal. There is considerably larger microporosity in Cameo coal sample. The surface areas analyzed using the BET method are 7.87 and 1.95 m^2/g for Cameo coal and Woodford shale respectively, and the total pore volumes are 0.0187 and 0.0099 cm^3/g respectively.

Table 3.1: Textural properties of Cameo coal and Woodford shale determined by nitrogen adsorption isotherms at 77 K.

Sample	Mean pore size (nm)	BET surface area (m^2/g)	Micropore volume (cc/g)	Total pore volume (cc/g)
Cameo coal	9.3	7.87	0.0032	0.0187
Woodford shale	68.5	1.95	0.0008	0.0099

3.4.2 Pore structure characterization results

Pore network models with uniform pore shape

To test the reliability of LDFT on a network of pores, we used PNM with slit-shaped pores to match the experimental sorption curves of Cameo coal and Woodford shale samples. The optimized simulation curves are shown in Fig. 3.5 in good agreement with experimental measurements. We

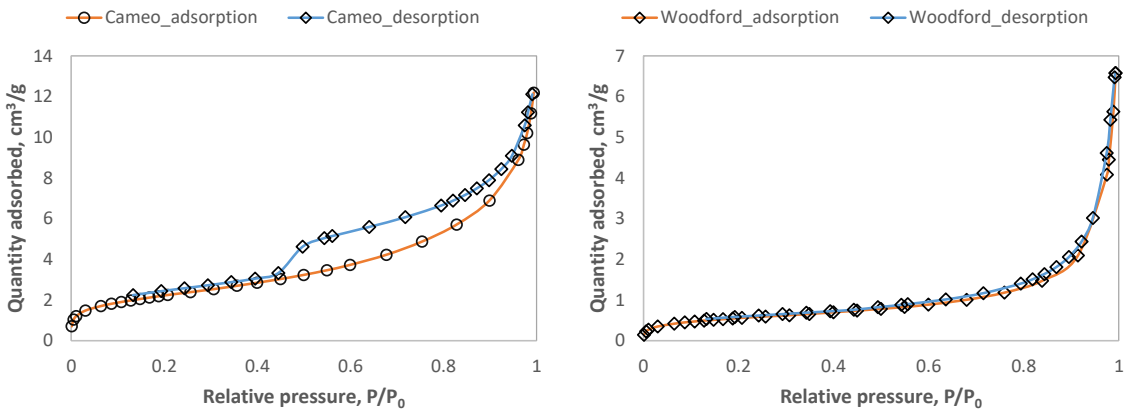

(a) (b)

Figure 3.3: Measured nitrogen sorption isotherms for (a) Cameo coal and (b) Woodford shale samples.

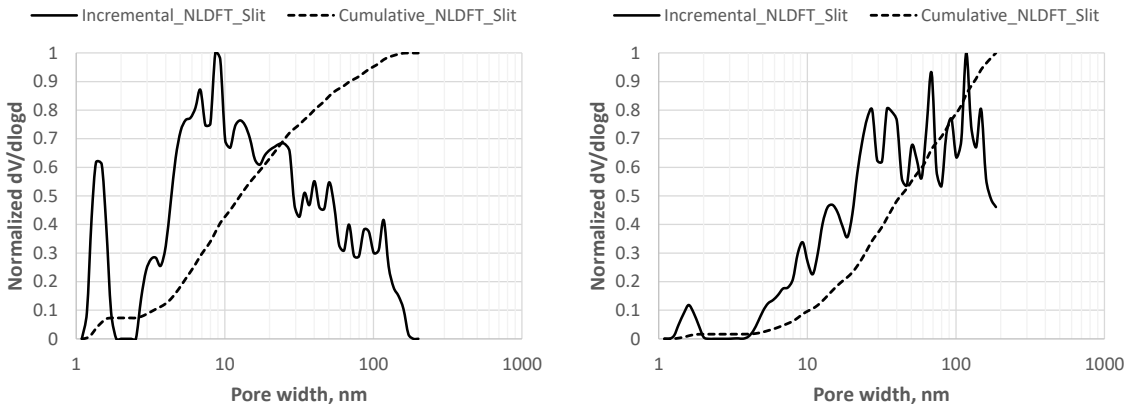

(a) (b)

Figure 3.4: Incremental (solid line) and cumulative (dashed line) PSD for (a) Cameo coal and (b) Woodford shale samples, acquired by applying the NLDFT method to analyze the adsorption curves.

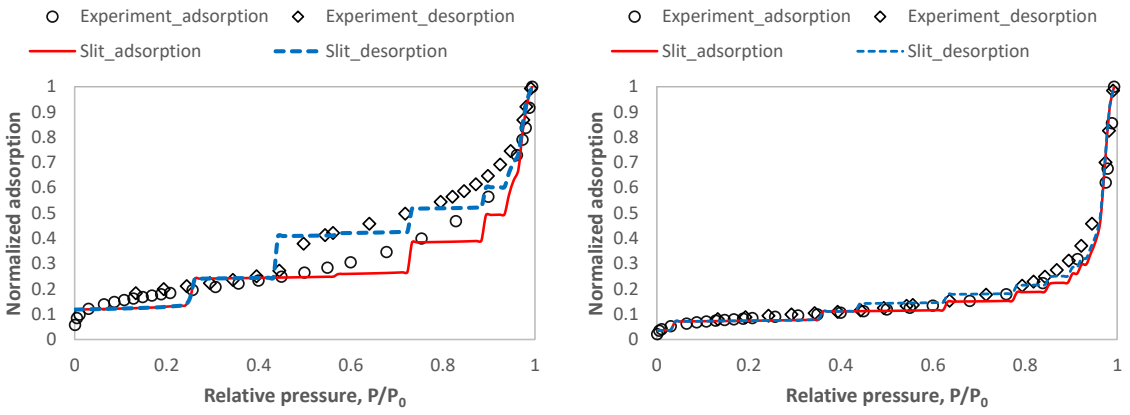

(a) (b)

Figure 3.5: Optimized simulation sorption curves using PNMs with slit pores compared with experimental results. (a) Cameo coal results (E_r = 0.1035); (b) Woodford shale results (E_r = 0.0522).

also observed similar peaks in the incremental PSD obtained by LDFT and NLDFT approaches, and the cumulative PSD shows close match as well (see Fig. 3.6).

We then used PNMs with cylindrical and spherical pore shapes to match the experimental sorption curves and the optimized curves for Cameo coal and Woodford shale are shown in Fig. 3.7 and 3.8. PSDs and the coordination number distributions based on the use of three pore shapes are compared in Fig. 3.9, 3.10 and 3.11, and a comparison of the optimized parameters is shown in Table 3.2 and 3.3.

Interestingly, neither a qualitative visual examination (see Figure 3.5, 3.7, and 3.8) nor a quantitative error comparison (see Table 3.2 and 3.3) of the matching results is able to deterministically choose the best match among PNMs using three types of pore shapes. Therefore, it is possible to achieve reasonably good matches with sorption curves regardless of the pore shapes, and the optimal match is not a unique function of pore shape. However, the resulting PSD, surface area, surface energy, and connectivity of the pore networks are considerably different. We then examined the differences among these parameters and tried to provide physical explanations for such discrepancies.

As shown in Fig. 3.9 and Table 3.2, as the pore shape changes from slit, cylindrical to spher-

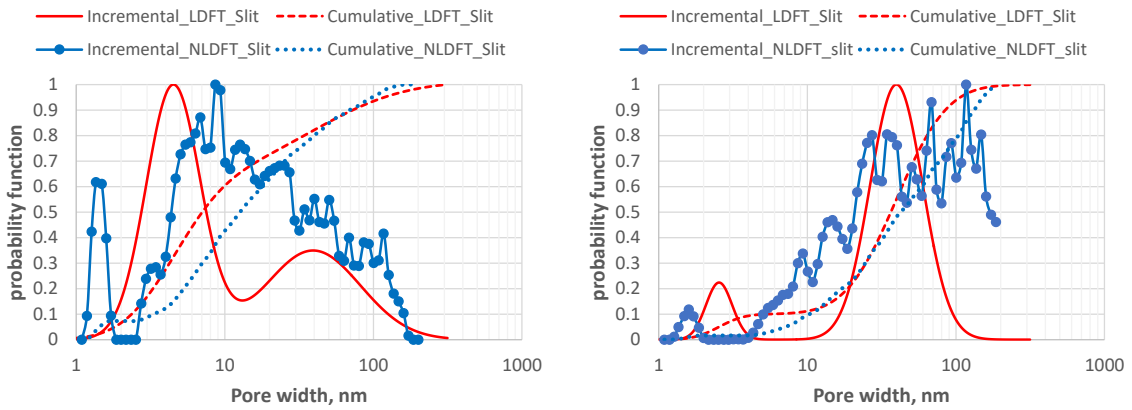

(a) (b)

Figure 3.6: PSD predicted by simulation (red lines) for slit pore shape compared with NLDFT results (blue lines). (a) Cameo coal results; (b) Woodford shale results.

ical, the average pore size increases, with an increasingly wider distribution of the microporosity peak (larger σ_1) and an increasingly narrower distribution of the mesoporosity peak (smaller σ_2). The variation in the predicted pore sizes as a function of pore shape is as expected, because as is shown in Fig. 3.1, for a single pore with the same size, spherical pore predicts the fastest adsorption uptake, followed by cylindrical and slit geometries due to the decrease in the curvature of the pore space. As a result, in order to achieve the same adsorption uptake, pores with spherical geometry have to be the largest in size, either for a single pore or a network of pores. The change of standard deviation of PSD shows the collective effect of pore shape for a distribution of pore sizes.

The connectivity of the pore network also increases with the curvature of the pore spaces (Fig. 3.10 and 3.11). However, another common approach to predict the network connectivity (reported as the average coordination number) based on the percolation theory tends to give the same result regardless of pore shapes as long as the size of the hysteresis stays the same [26]. The dependence of connectivity on pore geometry can be interpreted as follows: at a certain relative pressure during the desorption process, larger fraction of pores in a network of spherical pores tend to be filled with liquid nitrogen as the capillary condensation pressure is much lower, which potentially blocks the migration pathway of the desorbed gas. As a result, in order to achieve the

hysteresis loop of the same size, better network connectivity is needed for spherical pores to release their adsorbate through alternative pathways.

A further examination of the surface energy reveals that spherical pore geometry requires the highest surface energy to match the measured sorption curves due to the largest pore sizes, while slit and cylindrical pores result in similar surface energy even though they have quite different PSD, which indicates that surface energy has a larger effect on adsorption in spherical pores. The surface area of the sample is not a fitting parameter. It can be calculated based on the measured pore volume and the predicted PSD for different pore geometries using the following equation:

$$S_r = V_t \sum_{i=1}^{n} kp(r_i), \tag{3.27}$$

where S_r is the specific surface area of the sample, m^2/g; V_t is the measured total pore volume in the sorption experiment, m^3/g; n is the total number of pores in the network; k is the surface to volume ratio of the specific pore shape used, which is $2/W$ for slit pore, where W is the pore width, and $2/r$ for cylindrical pore, where r is the pore radius, and $3/r$ for spherical pore; $p(r_i)$ is the probability function (Eq. 3.5) value at $r = r_i$, which can be interpreted as the volume fraction of pores of size r_i.

Based on Eq. 3.27, the surface areas of the pore networks generated using different pore shapes are calculated as shown in Table 3.2 and 3.3. For Cameo coal sample, slit geometry predicts the largest surface area (6.172 m^2/g) among the three types of pore shapes (4.489 and 2.750 m^2/g for cylindrical and spherical geometries), and it is also closest to the BET result of 7.87 m^2/g. For Woodford shale sample, slit and cylindrical geometries give quite similar results (0.96 m^2/g), much closer to BET result of 1.95 m^2/g than the result given by spherical geometry (0.581 m^2/g). The general underestimation of the surface area calculated from simulation is due to the existence of micropores which are not captured in the bimodal PSD. On the other hand, BET method tends to overestimate the surface area when samples have large amount of micropores [179, 180]. Due to the limited availability of experimental data, it is hard to deterministically characterize pore shape from nitrogen sorption experiments alone. However, if a certain pore shape is to be chosen to be

statistically representative of the actual sample, it should be the one with the closest match of surface area, given that all shapes are able to provide a reasonably good match with the measured sorption curves. In this case, the dominant pore shapes for Cameo coal and Woodford shale are determined to be slit and cylindrical respectively, which is consistent with the findings by Qajar *et al.* [11] reported on the same samples.

In this work, we only used slit, cylindrical and spherical pore shapes in our simulation. While triangular-shaped pore cross-sections are very common in pore network modeling, there are significant difficulties modeling adsorption in such shaped pores using our 1D LDFT approach. 1D LDFT assumes layer by layer adsorption, either in an open pore or with closed boundary. For cylindrical or spherical pores, the layer geometry is well-defined (circular or spherical), which makes it relatively easy to derive the coordination number and monolayer adsorption capacity of each layer. However, for triangular pore shape, nitrogen condenses preferentially at the corners, and the geometry of the open pore space changes from triangular to circular as adsorption accumulates, which results in a varying monolayer capacity and the coordination number is not constant even in a single layer. This complex feature cannot be modeled using 1D LDFT, which is the reason why it is only extended to cylindrical and spherical pore shapes.

Table 3.2: Optimized pore structure parameters based on different pore shapes for Cameo coal sample

Cameo coal	ω_1	$\log \mu_1$	σ_1	$\log \mu_2$	σ_2	E_0/RT	f_{del}	E_r	S_r, m^2/g
Slit	0.619	1.653	0.277	2.594	0.485	-20.474	0.200	1.035×10^{-1}	6.172
Cylinder	0.507	1.744	0.393	2.715	0.300	-20.262	0.146	2.766×10^{-2}	4.489
Sphere	0.468	2.199	0.591	3.067	0.260	-29.408	0.100	1.031×10^{-2}	2.750

Table 3.3: Optimized pore structure parameters based on different pore shapes for Woodford shale sample

Woodford shale	ω_1	$\log \mu_1$	σ_1	$\log \mu_2$	σ_2	E_0/RT	f_{del}	E_r	S_r, m^2/g
Slit	0.200	1.906	0.114	2.599	0.269	-25.279	0.040	5.220×10^{-2}	0.961
Cylinder	0.256	1.925	0.423	2.881	0.114	-26.055	0.020	3.250×10^{-2}	0.962
Sphere	0.134	2.194	0.585	3.139	0.137	-33.129	0.018	1.970×10^{-2}	0.581

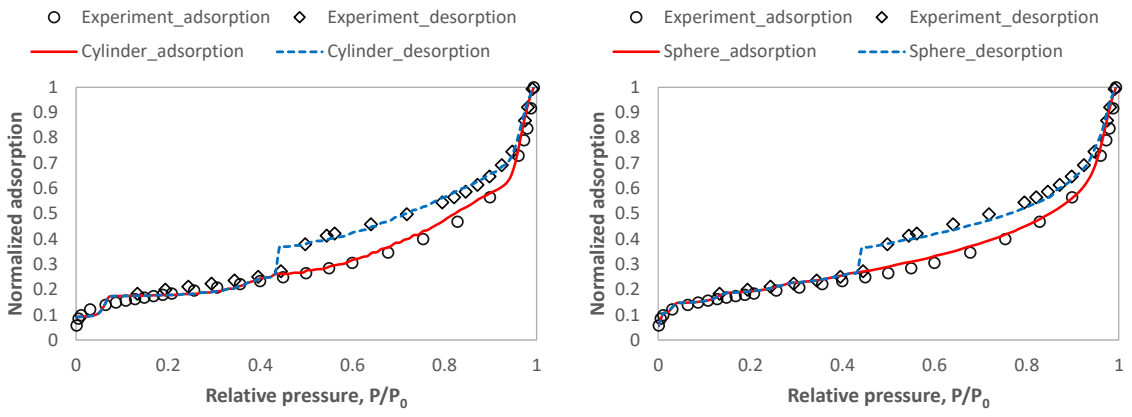

(a) (b)

Figure 3.7: Optimized simulation sorption curves for Cameo coal sample based on (a) cylindrical pore shape (E_r = 0.0274); and (b) spherical pore shape (E_r = 0.0103). Data points in both graphs are measured experimental results.

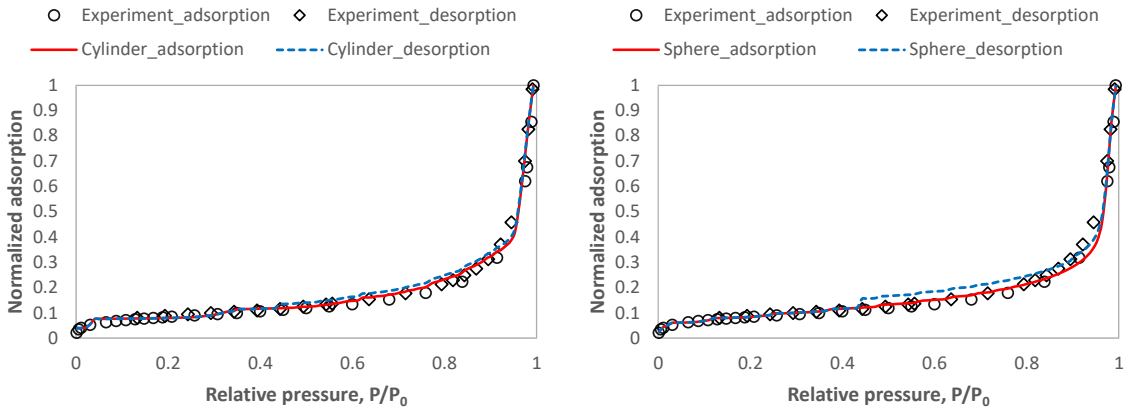

(a) (b)

Figure 3.8: Optimized simulation sorption curves for Woodford shale sample based on (a) cylindrical pore shape (E_r = 0.0325); and (b) spherical pore shape (E_r = 0.0197). Data points in both graphs are measured experimental results.

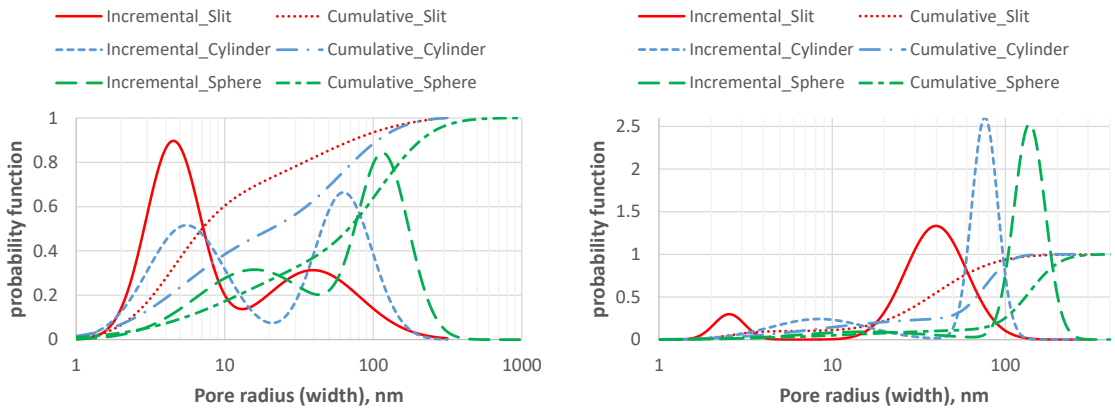

Figure 3.9: PSD obtained based on different pore shapes for (a) Cameo coal sample; and (b) Woodford shale sample.

Pore network model with combination of three pore shapes

Given that actual porous media can seldom be described using only one specific pore geometry, we investigated the limitation of our single pore shape assumption by combining three types of pore shapes within the same PNM to match the sorption curves. In order to determine the fractions of pores with each pore shape (*i.e.* slit, cylindrical, and spherical), we took SEM images of the two samples at different resolutions (Fig. 3.12 and 3.13). Pore spaces are extracted by image segmentation and shape factors G (ratio between 2D area and squared perimeter, $G = A/P^2$) [123] are quantified by image analysis. Generally, the larger the shape factor, the more circular the shape is, with circular disk cross-sections pores having a G of 0.08. For the upper limit of a slit pore with square cross section, $G = 0.0625$. Ovals (cross sectional shape for cylinders cut by a plane at a random angle to the cylinder axis) with aspect ratio close to 1 have a G between 0.07 and 0.08. For simplicity, we assign $G < 0.06$ to be slit pores, $0.06 < G < 0.08$ to be cylindrical pores and $G = 0.08$ to be spherical pores ($G > 0.08$ results from resolution issue and is discarded here). We also note that there is no way to distinguish between a circular cross-section that results from cutting a sphere and cutting a cylinder perpendicular to the cylinder axis, but the probability of the

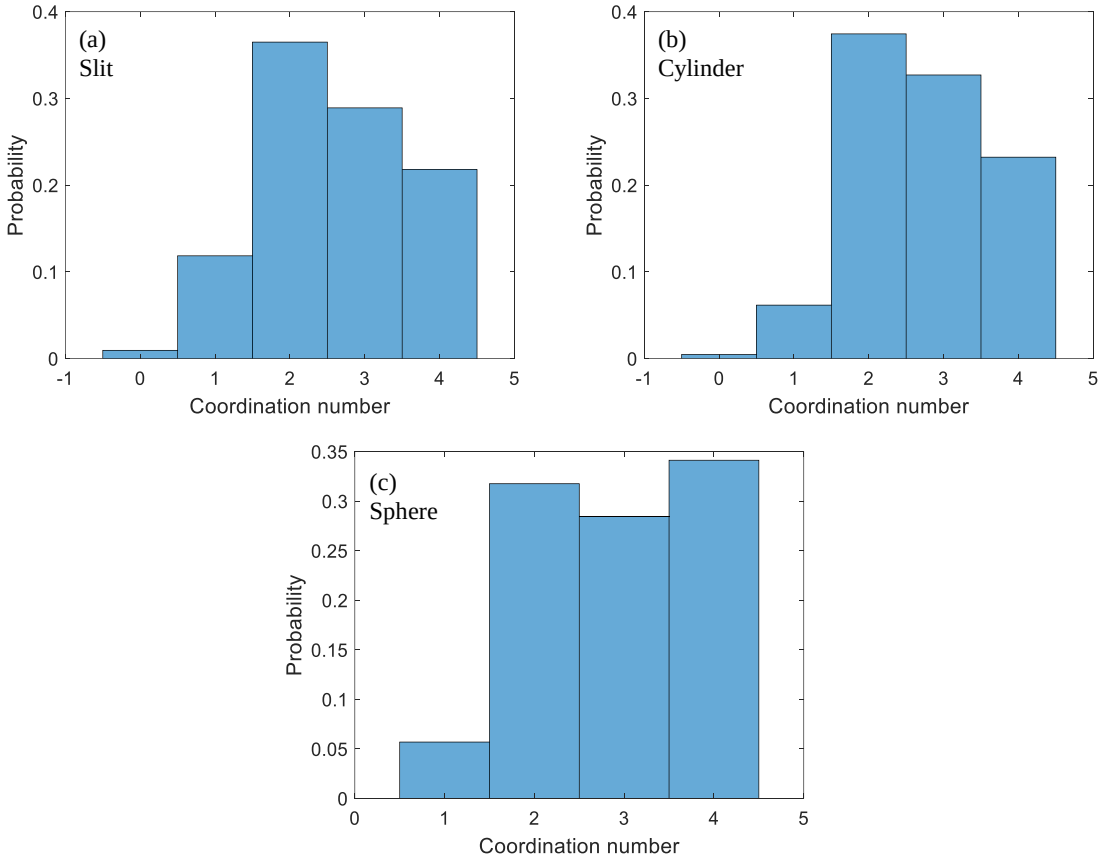

Figure 3.10: Comparison of pore network coordination number distribution for Cameo coal sample based on different pore shapes. (a) Slit pore shape; (b) cylindrical pore shape; and (c) spherical pore shape.

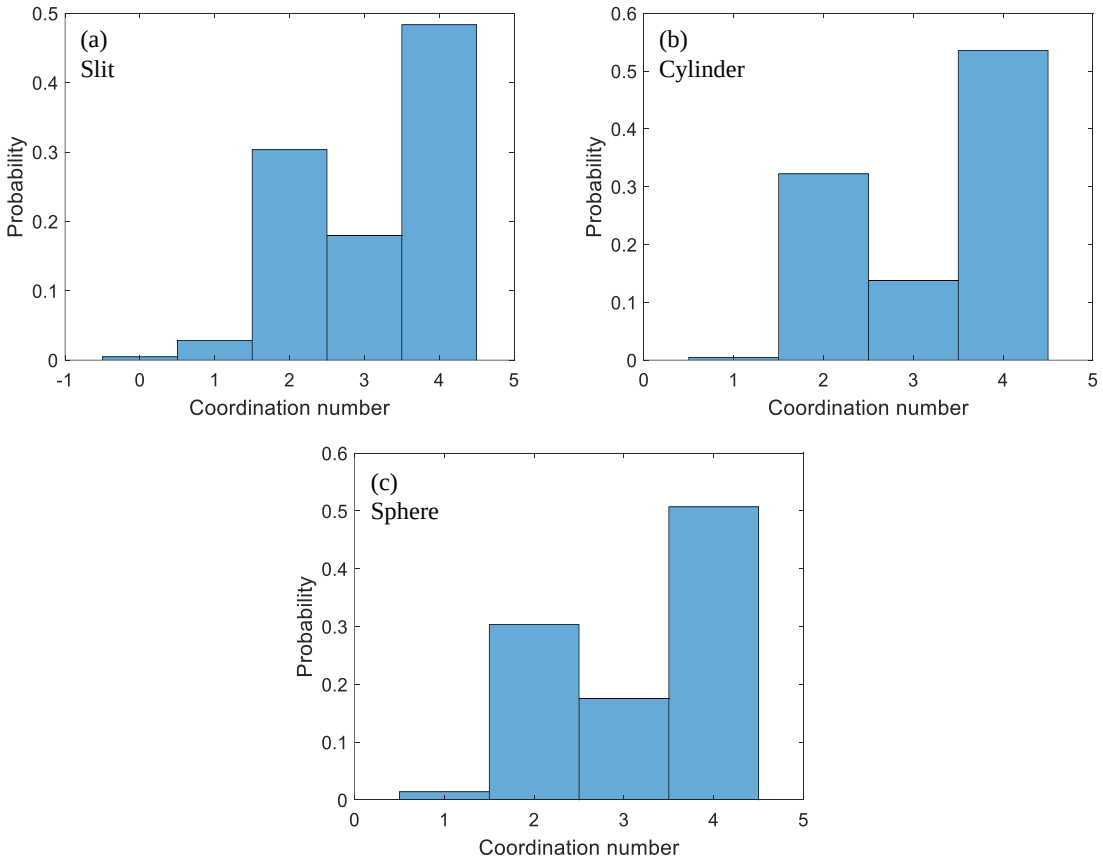

Figure 3.11: Comparison of pore network coordination number distribution for Woodford shale sample based on different pore shapes. (a) Slit pore shape; (b) cylindrical pore shape; and (c) spherical pore shape.

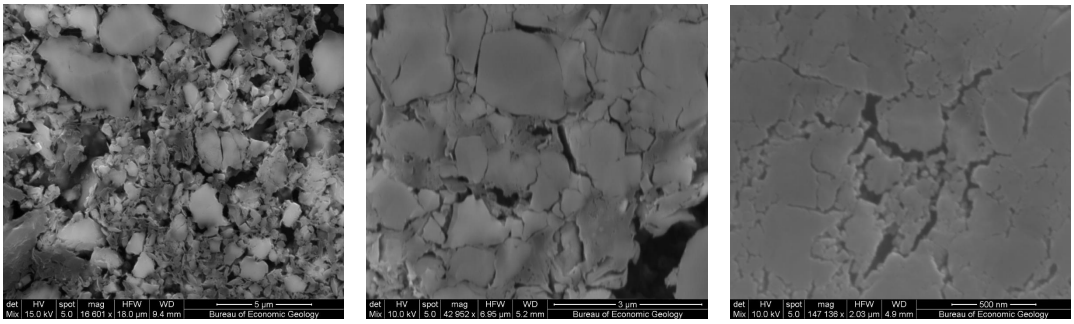

(a) (b) (c)

Figure 3.12: SEM images of Cameo coal sample at different resolutions.

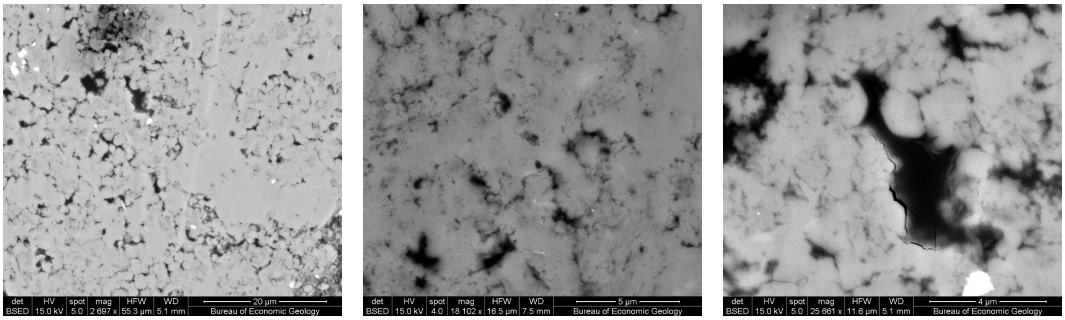

(a) (b) (c)

Figure 3.13: SEM images of Woodford shale sample at different resolutions.

latter is rather low. For Cameo coal sample, by averaging the information from images of different resolutions, we obtain a distribution of G shown in Fig. 3.14, based on which we find the number fraction of slit, cylindrical and spherical pores to be 0.49, 0.42 and 0.09 respectively. However, for Woodford shale sample, majority of the pores are below the resolution of the images, which prevents us from extracting useful information on pore geometries. Given the abundance of organic matter, we assume most of the pores are within the organic matter and thus tend to be spherical or cylindrical. For simulation purpose, we assign the number fraction of slit, cylindrical and spherical pores to be 0.2, 0.4 and 0.4 respectively.

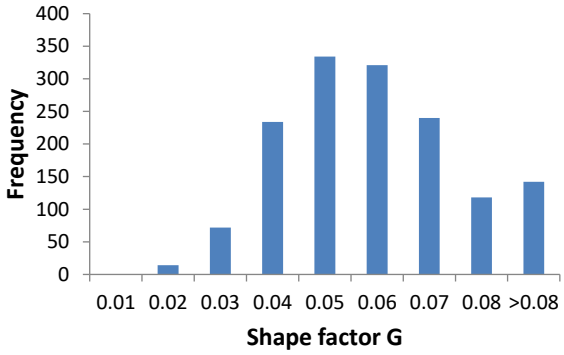

Figure 3.14: Shape factor distribution quantified based on SEM image analysis of the Cameo coal sample.

We further assume each type of pore shape has the same PSD as determined by matching the adsorption curve using that specific geometry, since SEM images with 2D limited field of view are not appropriate for 3D pore size quantification. In the multi-shape pore network, the nodes are assigned spherical shapes, while the bonds can be either cylindrical or slit in shape. The location of a bond with a specific shape is assigned randomly. The average surface energy E_0 is determined by matching the adsorption curve. The coordination number distribution is then obtained by matching the desorption curve. Following the above procedure, we obtain reasonably good matches with experimental results (see Fig. 3.15), which are much better than using only slit pore shape. The average surface energy E_0 for Cameo coal and Woodford shale samples are 20.5 and 28 respectively, quite close to the weighted averages of the results given by each specific pore shape, which are 21.14 and 28.73 respectively. However, the fractions of disconnected throats optimized using the combined pore shapes are 0.21 and 0.04 respectively, which are close to the maximum value given by using a specific pore shape (see Table 3.2 and 3.3). By combining multiple pore shapes into the pore network model based on SEM image analysis, we obtain much smoother sorption curves than using 100% slit pores, even though for Cameo coal sample about half of the pores are slit in shape.

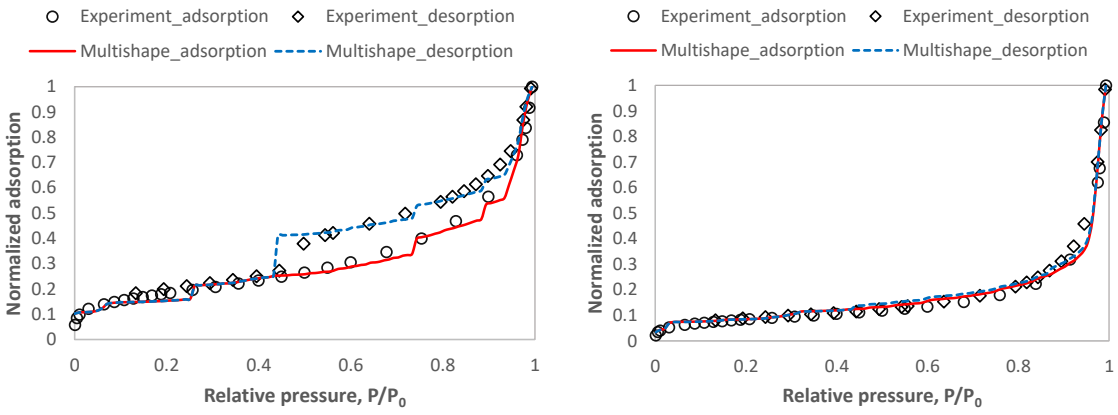

Figure 3.15: Optimized nitrogen sorption curves using a combination of three types of pore shapes for (a) Cameo coal sample and (b) Woodford shale sample, in comparison with experimental measurements.

3.4.3 Advection and diffusion simulation results

Advection and diffusion in a single nanopore with different geometries

We first studied advection and diffusion of supercritical methane in a single nanopore of cylindrical and slit shapes. The calculated advective and diffusive mass flow rate (kg/s) of methane at 400 K and average pressure of 10 MPa with a pressure gradient of 0.1 MPa/m (typical reservoir condition) as a function of pore radius ranging from 1 – 50 nm (assuming the ratio between pore length and effective radius is constant 10) is shown in Fig. 3.16. Generally, the mass flow rate increases with pore radius r. Below $r = 10$ nm, the flow rate increases dramatically, while for $r > 10$ nm, the flow rate roughly scales log-linearly with pore size for both advective and diffusive flows. Slit pores result in slightly higher mass flow rate than cylinder pores. The ratio between advective and diffusive flow rate (q_{adv}/q_{diff}) is shown in Fig. 3.17 along with the Kn as a function of pore size. At reservoir conditions, advective flow dominates for a wide range of pore sizes. q_{adv}/q_{diff} varies up to three orders of magnitude for pore size ranging from 1 to 50 nm, and for a 50 nm pore, advective flow rate can be 700 times larger than the diffusive flow rate. The trend remains the same for both cylinder and slit pores. In micropores (<2 nm), because of the large

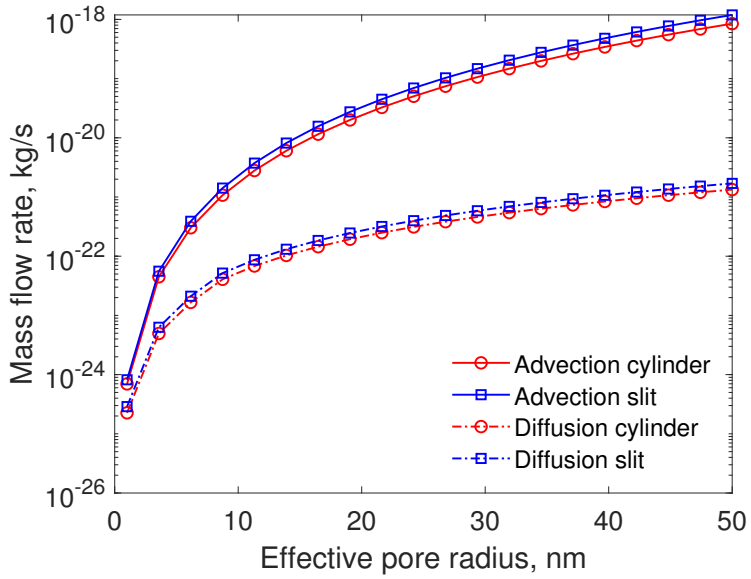

Figure 3.16: The calculated advective and diffusive mass flow rate (kg/s) of methane at 400 K and 10 MPa with a pressure gradient of 0.1 MPa/m (typical reservoir conditions) as a function of pore radius ranging from 1 – 50 nm (assuming the ratio between pore length and effective radius is constant 10) for a cylinder and slit pore.

Kn (>0.4), transitional diffusion occurs which is a combination of Fick and Knudsen diffusion. In this case, diffusive flow rate becomes nonnegligible, accounting for at least 15% of the total flux (superposition of advection and diffusion).

Fig. 3.18 shows the ratio between the advective and diffusive mass flow rate of methane in a cylinder pore at 400 K as a function of average pressure while keeping the pressure gradient a constant (0.1 MPa/m). Since similar behavior is observed for the slit pore, therefore we did not show the results here for the sake of clarity. The contribution of advective flow increases with pressure. In micropores or small mesopores, q_{adv}/q_{diff} is not sensitive to the change in pressure when $P < 1$ MPa. When $P > 10$ MPa, q_{adv}/q_{diff} scales exponentially with pressure. Diffusive flow accounts for up to 25% of the total flux in micropores at reservoir conditions, while its contribution can be neglected at reservoir pressure conditions (10 – 50 MPa) for mesopores/macropores larger than 10 nm compared with advective flow, if a threshold ratio of $q_{adv}/q_{diff} = 10$ is used.

Fig. 3.19 shows the ratio between the advective and diffusive mass flow rate of methane in a cylinder pore at 20 MPa as a function of temperature while keeping the pressure gradient a constant

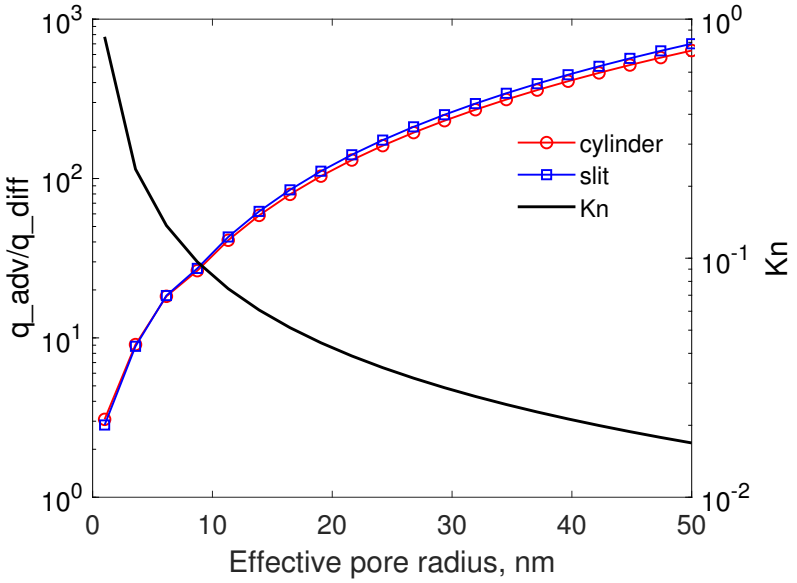

Figure 3.17: The ratio between the calculated advective and diffusive mass flow rate of methane at 400 K and 10 MPa with a pressure gradient of 0.1 MPa/m (typical reservoir conditions) as a function of pore radius ranging from 1 – 50 nm (assuming the ratio between pore length of pore effective radius is constant 10) for a cylinder and slit pore, also shown on the right vertical axis (black curve) is the corresponding Kn.

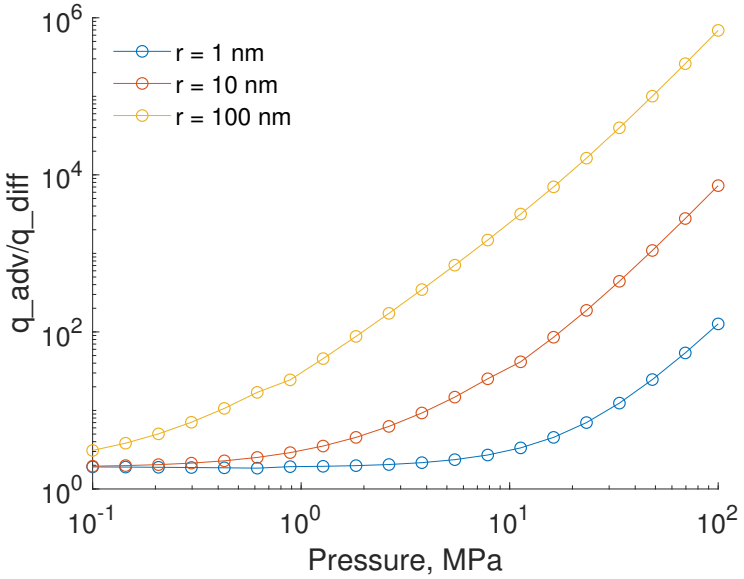

Figure 3.18: The ratio between the calculated advective and diffusive mass flow rate of methane at 400 K with a pressure gradient of 0.1 MPa/m (typical reservoir condition) as a function of average pore pressure ranging from 0.1 – 100 MPa for a cylinder pore (slit pore behaves similarly and for the sake of clarity is not shown). Results for three pore sizes (1, 10, 100 nm) are shown.

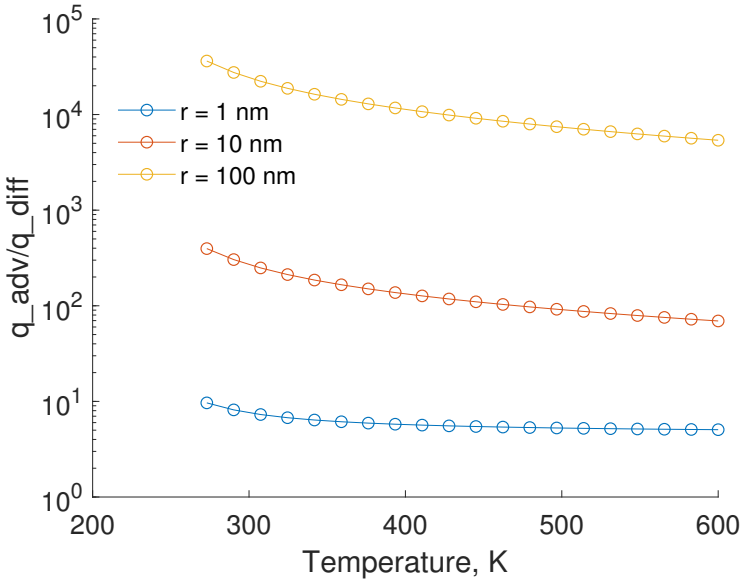

Figure 3.19: The ratio between the calculated advective and diffusive mass flow rate of methane at 20 MPa with a pressure gradient of 0.1 MPa/m (typical reservoir condition) as a function of temperature ranging from 273 – 600 K for a cylinder pore (slit pore behaves similarly and for the sake of clarity is not shown). Results for three pore sizes (1, 10, 100 nm) are shown.

(0.1 MPa/m). The contribution of diffusive flux slightly increases with temperature, because of the accelerated Brownian motion of the gas molecules. The effect of temperature on q_{adv}/q_{diff} is not as significant as pressure.

Advection and diffusion in PNMs

As is shown in Fig. 3.9, the PSDs of the reconstructed PNMs show a bimodal feature with pore sizes ranging from 1 – 300 nm, and the average pore size is consistently larger than 10 nm. Therefore, it is reasonable to conclude based on the results shown for a single pore that advective flow dominates the gas transport. To understand the extent of difference in flow capacities among PNM reconstructions based on different pore shapes, we calculated the effective apparent permeability and effective diffusivity of supercritical methane at 400 K with a pressure gradient of 0.1 MPa/m as a function of average pressure for the characterized two samples. Fig. 3.20 shows the calculated k_a for Cameo coal and Woodford shale samples. k_a decreases with pressure for all types of pore shapes, which is as expected and illustrated broadly in the literature [12, 172]. k_a calculated

using PNMs with slit and cylindrical pore shapes are consistently similar for both samples, while PNMs with spherical pores result in k_a that can be up to two times larger than the results given by slit/cylindrical pores. The PNM using a combination of three pore shapes does not always result in k_a values within the ranges set by individual pore shapes, but the values are quite close to the predictions using slit/cylindrical pore shapes.

Similar trend is observed for the effective diffusivity D_e as shown in Fig. 3.21, except for a much wider variation in D_e for the same range of pressures, indicating that diffusion is more sensitive to pressure than advection. However, pore shape has limited effect on diffusion and contradictory to advection, PNMs with slit pores result in the largest D_e, indicating that the micro/mesopores make the most contribution to the effective diffusivity of a porous medium.

Based on the comparison of the surface area calculated by PNMs and nitrogen sorption measurements, we have ruled out the choice of PNMs with uniformly spherical pore shapes, even though they resulted in satisfactory match with experimental sorption curves. However, ambiguity still exists between the choice of slit vs. cylindrical pore shape. According to our flow simulation results here, it is then safe to conclude that the choice of slit v.s. cylindrical pore shape for PNMs does not lead to significantly different results regarding k_a or D_e for flow or diffusion that occurs at common reservoir conditions. However, because the simulated sorption curves using PNMs with slit pores have the 'step' features, consistently larger matching errors are observed for slit pores (see Table 3.2 and 3.3). As a result, larger uncertainty is expected regarding the resulting pore structure parameters. Therefore, we suggest that unless the pore shape is well characterized (such as slit pores in clay), cylindrical pore shape can be used in general to interpret the nitrogen sorption curves for tight porous media with complex pore space morphology. This is because: 1) spherical pores generally underestimate the surface area and overestimate the permeability; 2) slit pores result in larger uncertainties when calibrating to experimental sorption curves; 3) cylindrical pores lead to smooth sorption curves, and the flow properties (permeability and diffusivity) do not vary much with the results predicted by PNMs with combined pore shapes.

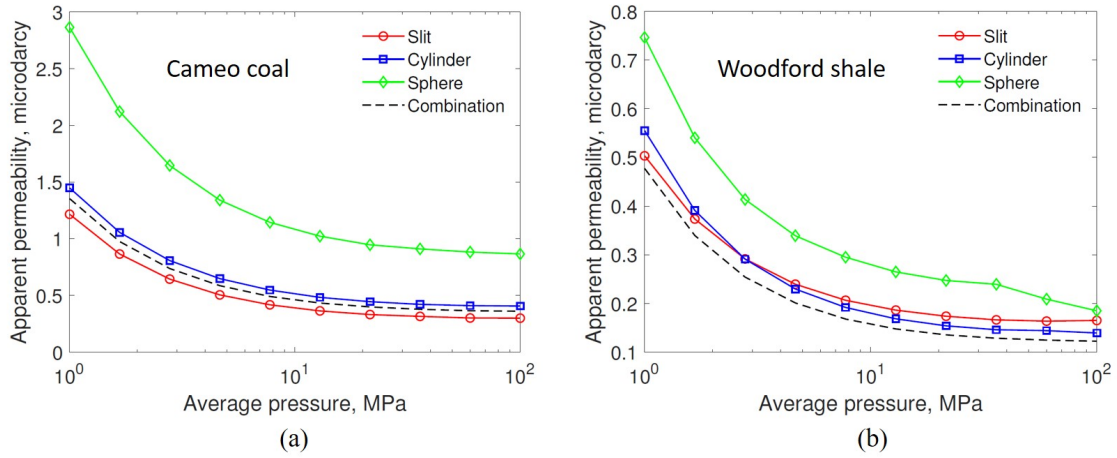

Figure 3.20: The calculated apparent permeability of methane as a function of average pressure at 400 K with a pressure gradient of 0.1 MPa/m for (a) Cameo coal sample (b) Woodford shale sample. The results using PNMs with uniform spherical, cylindrical and slit pore shapes and a combination of three pore shapes are shown together.

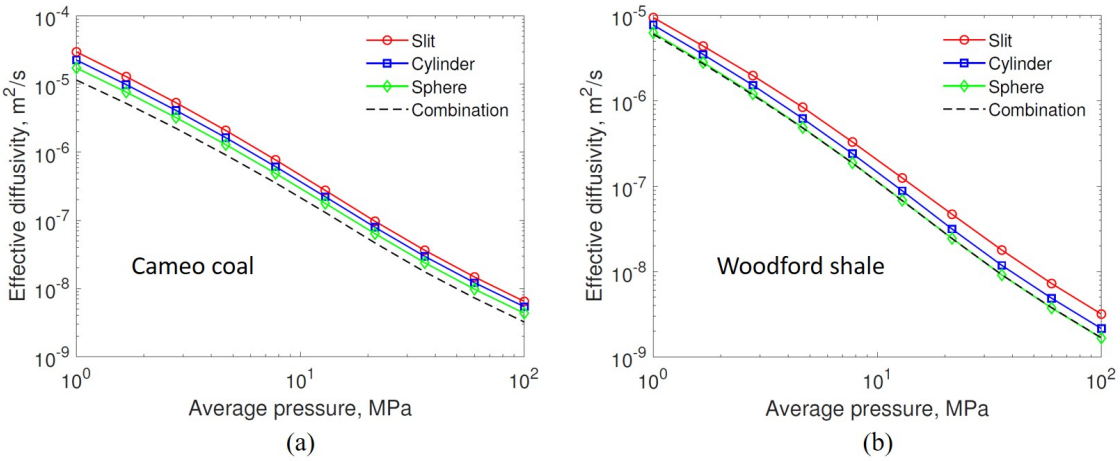

Figure 3.21: The calculated effective diffusivity of methane as a function of average pressure at 400 K with a pressure gradient of 0.1 MPa/m for (a) Cameo coal sample (b) Woodford shale sample. The results using PNMs with uniform spherical, cylindrical and slit pore shapes and a combination of three pore shapes are shown together.

3.4.4 Error and uncertainty assessment

Representativeness of PNM

The capability of performing simulation at the REV scale is essential for reliable thermodynamic or hydrodynamic properties estimation. However, there has to be a compromise between the computational cost and the desired size of the simulation domain. For the dual-scale PNM used this study, the average linear size of the model (a 3D cube) is about 5 μm, with about 1000 pores and 1800 throats. Even though the size of the PNM is below REV (hundreds of microns across) commonly assumed for shale or coal samples [79], its pore structure properties (*e.g.* PSD, pore throat connectivity) are informed by nitrogen sorption experiments which are measured on about 1 gram of powdered samples with average particle size of about 400 μm at the REV scale. A statistically representative pore structure at the REV scale is then mapped onto the PNM. Therefore, it is reasonable to conclude that the simulation results using our PNM are also statistically representative at the REV scale.

Error and uncertainty associated with nitrogen sorption experiments

Nitrogen sorption experiments characterize the pore structure of nanoporous media with pore sizes below 200 nm [5]. The maximum pore size that can be detected depends on the final pressure at the end of the adsorption stage. The total pore volume determined by the highest adsorption uptake is therefore a nominal value. In case large macropores ($>$200 nm) exist in the sample, the use of this value for PNM reconstruction underestimates the actual total porosity.

Before the experiment, about 1 gram of the sample is powdered (20 – 60 mesh), oven heated (at 200 °C), and degassed. Sample preparation might affect the resulting pore structure properties to some extent. For example, size and shape of the particles might affect the interpretation of the PSD and connectivity. The removal of clay-bound water after the heating process might alter the microstructure of clay in the sample, therefore exposing larger fraction of micropores to nitrogen during the experiment.

In nitrogen sorption experiments, carefully-dosed nitrogen vapor is introduced into a closed

system containing the sample, the equilibrium bulk pressure is recorded and the adsorbed amount is determined based on Boyle's Law. The diffusion of nitrogen molecules from the adsorbed phase to the bulk phase might affect the equilibrium density and pressure, even though at low experimental temperature (77 K) the diffusion rate is low. The largest error and uncertainty occurs at the beginning and end of each measurement cycle, which corresponds to the regions where micropores and macropores are detected. As a result, the largest uncertainty of the resulting PSD characterization is associated with the lower and upper limits of the pore sizes.

Error and uncertainty associated with numerical interpretation

In this study, we assume a maximum coordination number of 4 in our pore network model as a result of the simplification of dual-scale PNMs. Sands and sandstones typically have an average coordination number of 4, but this assumption might not always be true for other porous media. To further address the effect of this assumption on the results of the simulation, we simulated the desorption process using an average coordination number of 3, 2.72, and 1.94 respectively with the same PSD and shape (cylinder) for the Cameo coal sample and the results are shown in Fig. 3.22. Obviously, smaller coordination number leads to larger hysteresis. Average coordination number higher than 4 (pores with higher degree of connectivity than sandstones) is not a realistic assumption for any porous medium with relatively homogeneous pore sizes (and in such a medium our simulations would yield less hysteresis than it is experimentally observed). Coordination number higher than 4 could result from heterogeneous samples with both pore-filling and grain-filling microporosities [12], and we would need explicit treatment of micropores in such cases.

The repeatability of the optimization process is also a major concern. Since the PNMs we used in this study are large enough to have about 1000 pores and 1800 throats, the repeatability of our optimization is quite high. We repeated the optimization process 30 times with different initial guesses for the parameters for Cameo coal sample using a PNM with cylindrical pore shape, and the maximum, minimum, average values and standard deviation of each of the optimized parameters are shown in Table 3.4. For the adsorption curve match, we get almost the same results with accuracy up to 2 decimal digits, and the maximum standard deviation is below 0.02. For the desorption curve

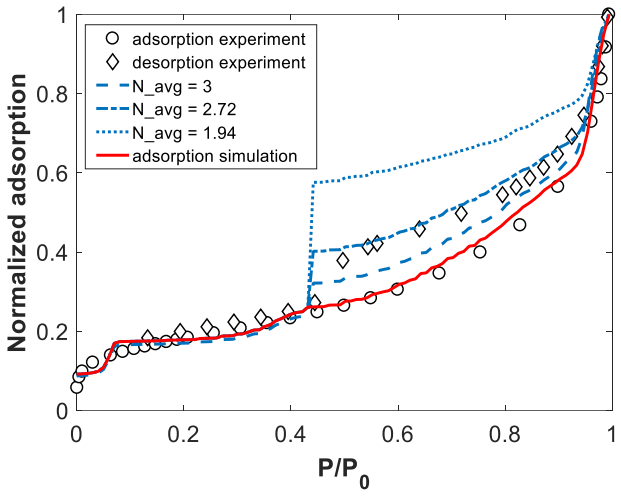

Figure 3.22: Desorption curves obtained using different average coordination numbers (N_{avg}) with PSD and pore shape being the same. As an example, the calculations are done using the PNM with cylindrical pores for the Cameo coal sample.

match, due to the randomness in the creation of the pore network and the deletion of throats, we get a relatively wider distribution of results, but the standard deviation is still quite small (0.225). Since we applied exactly the same procedure for each pore shape, we were confident that this repeatability test result applies to all of our simulations.

Table 3.4: Repeatability test using 30 optimizations on Cameo coal sample with cylindrical pore network elements

Statistics	ω_1	σ_1	σ_2	$\log \mu_1$	$\log \mu_2$	E_0/RT	f_{del}	E_r
Min	0.5009	0.3901	0.2906	1.7401	2.7105	-20.1886	0.1152	0.0273
Average	0.5065	0.3929	0.2996	1.7444	2.7154	-20.2615	0.1457	0.0278
Max	0.5198	0.4086	0.3148	1.7611	2.7231	-20.6033	0.1806	0.0283
Standard deviation	9.75×10^{-3}	1.46×10^{-2}	1.65×10^{-2}	3.49×10^{-3}	1.10×10^{-3}	6.45×10^{-3}	2.25×10^{-1}	1.88×10^{-2}

Further evaluation of LDFT

Regarding nitrogen sorption simulation using LDFT, one may notice the step feature of the simulated sorption curves for slip pore geometry whereas the curves are much smoother for cylindrical and spherical pores. In fact, for a single pore, LDFT always predicts a stepped adsorption curve regardless of pore shapes due to the simplified layer-by-layer pore filling assumption (see Fig.

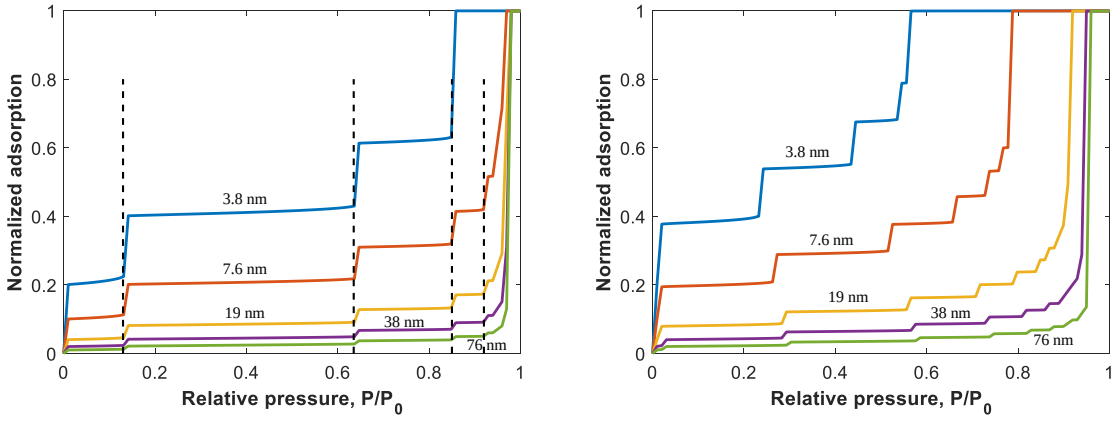

Figure 3.23: Adsorption curves predicted for a single pore with different sizes ranging from 3.8 nm to 76 nm using (a) slit pore shape and (b) cylindrical pore shape. Dashed vertical lines in (a) demonstrate that two-dimensional capillary condensation occurs at the same relative pressure regardless of pore sizes for slit pores. However, for cylindrical pores in (b), the 'steps' of the adsorption curves occur at different relative pressures for different pore sizes.

3.23). However, we expected to see smooth curves for all three types of pore shapes since we believed a distribution of pore sizes would attenuate the step feature. Obviously, this is the not the case for slit pores. A further examination of LDFT method reveals that the two-dimensional layer filling process (namely the 'steps') occurs at the same relative pressure regardless of pore sizes for slit pore geometry (see Fig. 3.23(a)). This is because the parallel pore walls lead to uniform coordination number (as in LDFT definition) across different layers regardless of the pore size and abate the effect of surface energy on thermodynamic behavior, so that the adsorption process becomes less sensitive to pore sizes. However, the nonzero curvature of cylindrical and spherical pores results in a varying coordination number across different layers, so that the 'steps' are dependent on pore sizes (see Fig. 3.23(b)). As a result, a distribution of pore sizes reduces the step size in the sorption curves.

3.5 Conclusions

In this chapter, we applied LDFT developed for a single pore with slit, cylindrical or spherical shapes, to a modified dual-scale PNM to simulate the nitrogen adsorption and desorption processes with consideration of bimodal lognormal PSD, varying surface energy and network connectivity. Via optimizing the match between simulated and experimental nitrogen sorption curves, we obtained corresponding PSD, surface energy and network connectivity using three types of pore shapes. We applied the above workflow to analyze the sorption curves measured on Cameo coal and Woodford shale samples. Results show that all three types of pore shapes demonstrate reasonably good match with the experimental results, but with considerable discrepancies in the optimized pore structure parameters. A network of spherical pores always predicts a larger pore size, higher surface energy, better connectivity yet smaller surface area than cylindrical pores, while slit pores show the opposite. The step feature of the sorption curves predicted using network of slit pores leads to relatively larger fitting errors. This occurs due to the fact that LDFT predicts adsorption as a layer by layer process with assumption of infinite long plates. We found that based on the sorption curves matching results alone, we cannot provide deterministic characterization of pore shape. However, further examination of surface areas predicted by PNMs ruled out the choice of spherical pore shapes as unphysically low surface area was reported. To further reduce the uncertainty in the results and remove pore shape as a fitting parameter, we took SEM images of both samples and quantify the fraction of each pore shape based on shape factor analysis of extracted pore spaces via image processing. By combining all three pore shapes into the same PNM, we achieved much better matching results than using only slit pores. The repeatability of our optimization process was also tested and validated by running the optimization process 30 times.

The subsequent advection and diffusion simulations showed that at reservoir pressure and temperature conditions, diffusion contributes to mass flux (above 10%) only in micropores and small mesopores ($<$ 10 nm). The calculated results of k_a and D_e using PNMs as a function of average pressure are very close for cylindrical and combined pore shapes, suggesting that cylinder could be used as the representative pore shape for PNM reconstruction to obtain reasonable estimation of

single phase flow/diffusion properties, without the necessity of analyzing SEM images to constrain the detailed pore shape distribution. However, we do not imply that this conclusion holds true for multiphase problems, as the configuration of the complex phase interfaces that need to be tracked for solving multiphase flow problems highly depend on the morphology and topology of the pore space.

Herein, the surface energy term is used as a fitting parameter in our simulation, whereas it can be measured experimentally by conducting sorption measurements at two different temperatures [11]. However, our results showed that surface energy can not differentiate between slit and cylindrical pores. Another assumption that was made to facilitate the simulation process is the neglect of the interconnectivity within the micropore networks, which matters the most when large volume fractions of microporosity is observed. We defer simulations with explicit treatment of micropore clusters to future work after parallelizing the simulation codes to improve efficiency. In this study we focused on the pore-filling dual-scale network since it is a commonly observed pore structure in shale. However, we do not deny the existence of grain-filling porosities and their possibility of forming a connected pore network. Currently, the grain-filling PNM can only be treated explicitly, and we defer to future work the exploration of different types of PNM as defined in [12] to interpret nitrogen sorption isotherms.

Chapter 4: 2D LBM modeling to study subcritical and supercritical gas adsorption in shale [1]

4.1 Introduction

In shale, two common types of pore systems are present, which we refer to as the interP and intraP pores. They differ in terms of pore sizes, shapes, connectivity and surface properties. One of the critical difference in these two pore systems is the surface curvature of the pore space. For interP pores, if the particles can be simplified as spheres, the pore space consists of the outside of the spheres, where the curvature is positive (convex). On the other hand, since OM intraP pores usually have a spongy structure as revealed by SEM images [1,81], the pore space can be simplified as the inside of spheres, where the curvature is negative (concave). Understanding gas adsorption behavior in the two types of pore systems is essential for petrophysical characterization, reserve estimation, and production forecast, but it is a nontrivial task because of the complex pore structure and surface chemistries.

DFT and GCMC are two common methods for studying phase behavior in nanopores. We have introduced a 1D LDFT model in Chapter 3. However, it is limited to simple pore shapes (*i.e.* spherical, cylindrical, and slit) which might not be representative of the actual pore geometries, because of the theoretical difficulty of dealing with complex curved surfaces. Improved 3D LDFT models [92, 93] have recently been used to study subcritical and supercritical gas adsorption in more complex geometries at substantially greater computational cost than the LBM methods used here. GCMC is a molecular scale method for adsorption modeling which is more accurate, but it is also computationally intensive thus is limited to small simulation domains on the scale of several

[1] This chapter is modified from our previous publications: (1) Xu, R, Prodanović, M, and Landry, C. J. Study of subcritical and supercritical gas adsorption behavior in different nanopore systems in shale using lattice Boltzmann method. International Journal of Coal Geology, 212:103263, August 2019. (2) Xu, R, Prodanović, M, and Landry, C. J. Simulation of gas adsorption and capillary condensation in shale nanopores using lattice Boltzmann modeling. Unconventional Resources Technology Conference, August 2018. My contribution to the two papers includes developing the codes, designing and performing the numerical simulation, analyzing the results, and writing the papers.

nanometers. **Neither LDFT nor GCMC have been used to model flow and adsorption at the same time.**

On the other hand, LBM has the potential to model thermodynamics and hydrodynamics at the same time. In this study, we developed and quantitatively validated a 2D LBM model that incorporates both rock-fluid and fluid-fluid interactions for subcritical and supercritical gas adsorption modeling in shale nanopore systems. For subcritical gas, here we focused on nitrogen sorption, since in Chapter 3 the simplification of pore shapes and the assumption that adsorption happens independently in each pore led to nonunique interpretation of the pore structure based on nitrogen sorption isotherms. By building more realistic pore structures and performing direct numerical simulations using LBM, we aim to reveal the difference in the nitrogen adsorption behavior in two representative pore systems in shale, namely the interP and intraP pore systems, thus guiding the selection of representative pore shapes when building PNMs. For supercritical gas, we focus on methane, which is the main component of shale gas. Understanding methane adsorption as a function of pore geometries provides insight into shale gas storage capacity. The 2D LBM model developed in this study could be treated as a numerical exercise since surface tensions are not very well defined in 2D, and morphology and topology of the pore space in 2D might not be representative of 3D. However, the 2D model serves as a prototype, which is extended to 3D in Chapter 5, and nanoscale flow physics can be further incorporated to model the coupled thermodynamic and hydrodynamic behavior in nanoporous media as will be shown in Chapter 6.

The remaining of this chapter is organized as follows. In Section 4.2 we provide a brief introduction of the LBM model used in this study and the methodology of incorporating interparticle and surface forces. In Section 4.3 we establish the correlation between parameters used in our LBM model and physical properties for both subcritical and supercritical gases, followed by validation of our model against experimental data. In Section 4.4, we simulate and compare nitrogen and methane adsorption behavior in two model nanoporous media which represent the interP and intraP (OM) pore systems typically found in mudrocks, as well as a synthesized polyethylene porous medium with more complex and realistic pore structure.

4.2 Lattice Boltzmann method

4.2.1 Governing equations

LBM originated from lattice gas cellular automata [137], and it can also be treated as a discretization of the continuous Boltzmann equation. It is a mesoscopic model based on microscopic dynamics with locally defined hydrodynamic moments. Fluids are simulated as swarms of particles which flow on a discrete lattice, represented by particle distribution functions (f_i, where i refers to the discretized i^{th} velocity direction). Here we use the D2Q9 (two dimensional nine velocity) discrete velocity model [138], wherein the particle distribution functions are limited to nine discrete velocities (eight advecting, one at rest, see Fig. 4.1). Each discrete particle distribution contains the value of the density of the particles moving in its respective direction. During a single time iteration the LB equation is carried out in two steps, streaming of the particle distribution function to the neighboring lattice nodes, and collision of the particle distribution function [9]. The streaming and collision processes can be described by the following equation:

$$f_i\left(\mathbf{x}+\mathbf{e}_i\Delta t, t+\Delta t\right) = f_i\left(\mathbf{x}, t\right) + \Omega_i, (i = 1, 2, \ldots, N), \tag{4.1}$$

where f_i and $\mathbf{e}_i$ are the particle distribution function and velocity along the i^{th} direction respectively; N is the total number of velocity directions, and here N = 9; and Ω_i is the collision operator. For the widely-used D2Q9 LBM model applied in our study,

$$\mathbf{e}_i = \begin{cases} (\cos\left(\frac{\pi}{2}\left(i-1\right)\right), \sin\left(\frac{\pi}{2}\left(i-1\right)\right)) & \text{for } i = 1, 2, 3, 4 \\ \sqrt{2}(\cos\left(\frac{\pi}{2}\left(i-1\right)+\frac{\pi}{4}\right), \sin\left(\frac{\pi}{2}\left(i-1\right)+\frac{\pi}{4}\right)) & \text{for } i = 5, 6, 7, 8 \\ 0 & \text{for } i = 0 \end{cases} \tag{4.2}$$

Different forms of the collision operator in LBM have been proposed, including the popular lattice Bhatnagar–Gross–Krook (LBGK) [181], two-relaxation time [182], and multi-relaxation time (MRT) [183] collision operators. Lu *et al.* [184] used a TRT LBM to study solid-liquid phase change and to eliminate unphysical numerical diffusion. Kuzmin and Mohamad [185] used a multi-

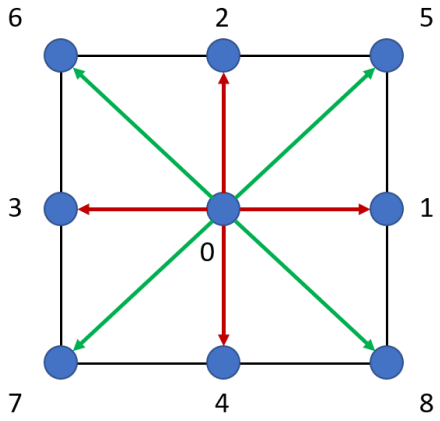

Figure 4.1: A schematic of the velocity direction and magnitude used in D2Q9 LBM models.

range MRT LBM which improved the gas-liquid density ratio achievable by Shan-Chen model and decoupled the surface tension and EOS. Although TRT or MRT may increase the numerical stability and provide more degrees of freedom, LBGK is widely used due to its simplicity. Moreover, MRT LBM models usually use the forcing scheme introduced by Guo *et al.* [186], which was found in a comprehensive comparison study by Huang *et al.* [187] to be unstable when the reduced temperature drops below 0.8. This unfortunately affects simulation of nitrogen adsorption in 77 K where the reduced temperature is about 0.61. Thus in our work we use LBGK model to maintain consistency for both subcritical and supercritical gas adsorption modeling, in which the collision operator Ω_i is defined as:

$$\Omega_i = \frac{1}{\tau}\left(f_i - f_i^{eq}\right), \tag{4.3}$$

where τ is the relaxation time, and f_i^{eq} is the equilibrium distribution function, which is defined as:

$$f_i^{eq} = \omega_i \rho \left[1 + 3\mathbf{e}_i \cdot \mathbf{u} + \frac{9}{2}\left(\mathbf{e}_i \cdot \mathbf{u}\right)^2 - \frac{3}{2}u^2\right], \tag{4.4}$$

where ρ is the particle density, $\mathbf{u}$ is particle velocity and ω_i is the weighting factor for different

velocity directions:

$$\omega_i = \begin{cases} \frac{4}{9} & i = 0 \\ \frac{1}{9} & i = 1, 2, 3, 4 \\ \frac{1}{36} & i = 5, 6, 7, 8 \end{cases} \tag{4.5}$$

The macroscopic properties such as density ρ and velocity $\mathbf{u}$ are defined as moments of the particle distribution function:

$$\rho = \sum_{i=1}^{N} f_i \tag{4.6}$$

$$\mathbf{u} = \frac{1}{\rho} \sum_{i=1}^{N} f_i \mathbf{e}_i \tag{4.7}$$

4.2.2 Fluid-fluid and solid-fluid interactions

To account for the vdW forces between fluid particles which contribute to the non-ideal behavior of real gases, Shan and Chen [150] introduced a pseudopotential ψ of the fluid particles as a function of density. Here we adopt the same methodology (we define ψ later in this section) and limit the interparticle interactions within the nearest neighbors since the multirange interactions are nontrivial to implement for the solid boundaries. The interaction force $\mathbf{F}_{ff}$ between pairwise fluid particles surrounding position $\mathbf{x}$ is calculated as a function of their pseudopotentials:

$$\mathbf{F}_{ff}(\mathbf{x}, t) = -G_{ff}\psi(\mathbf{x}, t) \sum_{i=1}^{N} \omega_i \left[1 - I(\mathbf{x} + \mathbf{e}_i \Delta t, t)\right] \psi(\mathbf{x} + \mathbf{e}_i \Delta t, t) \mathbf{e}_i, \tag{4.8}$$

where G_{ff} is a temperature-like constant that determines the strength of fluid-fluid interaction, and I is an index function that is 0 for fluid nodes and 1 for solid nodes.

For solid-fluid interactions, we adopt two forms of surface forces for subcritical and supercritical gases respectively, which lead to quantitative agreement with LDFT and adsorption measurements as will be shown later in Section 4.3. For subcritical gases, we extend the previously defined pseudopotential to solid nodes by defining a constant solid pseudo-density, which is equivalent to defining a new solid-fluid interaction parameter G_{fs}. The surface force then takes the following

form:

$$\mathbf{F}_{fs}(\mathbf{x},t) = -G_{fs}\psi(\mathbf{x},t)\sum_{i=1}^{N}\omega_i I(\mathbf{x}+\mathbf{e}_i\Delta t,t)\mathbf{e}_i \tag{4.9}$$

For supercritical gases, since adsorption is usually limited to the first two molecular layers adjacent to the solid wall, we adopt a different form of the surface force, in which the solid pseudopotential is defined as a function of the pseudopotential of the first adsorbed layer:

$$\mathbf{F}_{fs}(\mathbf{x},t) = -G_{fs}\psi(\mathbf{x},t)\sum_{i=1}^{N}\omega_i I(\mathbf{x}+\mathbf{e}_i\Delta t,t)\psi(\mathbf{x},t)\mathbf{e}_i \tag{4.10}$$

The total interaction force $\mathbf{F}$ is the summation of F_{ff} and F_{fs}, and is incorporated into LBM by modifying the velocity $\mathbf{u}$ in the equilibrium distribution function f_i^{eq} (Eq. 4.4) with an equilibrium velocity $\mathbf{u}^{eq}$:

$$\mathbf{u}^{eq} = \mathbf{u} + \frac{\tau\mathbf{F}}{\rho} \tag{4.11}$$

Different forms of the pseudopotential function ψ have been proposed in literature which might lead to different EOS. In this study, we use a modified version of the Shan-Chen model by incorporating Peng-Robinson (PR) EOS, following the work by Yuan *et al.* [155]. For PR-EOS, we have:

$$p = \frac{\rho RT}{1-bp} - \frac{\alpha(T)a\rho^2}{1+2b\rho-b^2\rho^2}, \tag{4.12a}$$

$$a = 0.45724\frac{R^2T_c^2}{p_c}, \tag{4.12b}$$

$$b = 0.0778\frac{RT_c}{p_c}, \tag{4.12c}$$

$$\alpha(T) = \left[1+\left(0.37464+1.54226\omega-0.26992\omega^2\right)\left(1-\sqrt{\frac{T}{T_c}}\right)\right]^2, \tag{4.12d}$$

where p is the pressure, ρ is the molar density, R is the gas constant, T is the temperature, and subscript c indicates the critical point, here ω is the acentric factor. Since we only focus on the reduced properties in implementing the PR-EOS, the choice of T_c and p_c in lattice units is relatively arbitrary except for stability considerations. Following the recommendation of Yuan *et al.* [155], we use $a = 2/49$, $b = 2/21$ and $R = 1$, which leads to $T_c = 0.073$ and $p_c = 0.060$. The acentric factor

ω for different gases can be found in look-up tables [188]. For example, for nitrogen $\omega = 0.038$ and for methane $\omega = 0.011$. The D2Q9 BGK LBM leads to an EOS that has the following form:

$$p = \frac{\rho}{3} + \frac{G_{ff}}{6}\psi^2(\rho), \tag{4.13}$$

from which the pseudopotential function $\psi(\rho)$ is derived as:

$$\psi(\rho) = \sqrt{\frac{6}{G_{ff}}\left(\frac{\rho RT}{1-bp} - \frac{\alpha(T)a\rho^2}{1+2b\rho-b^2\rho^2} - \frac{\rho}{3}\right)} \tag{4.14}$$

Note that G_{ff} here after incorporating PR-EOS is not a temperature-like parameter anymore, and it merely maintains the sign of the expression within the square root of $\psi(\rho)$ to be positive. Temperature is explicitly defined within Eq. 4.12 by PR-EOS. Here we set $G_{ff} = -1$.

4.2.3 Correlation with physical parameters

Since we are interested in the density evolution in the adsorption process, it is imperative to correlate PVT properties between lattice and physical units. In this study, we use the concepts of reduced properties:

$$T_r = \frac{T}{T_c}, p_r = \frac{p}{p_c}, \rho_r = \frac{\rho}{\rho_c}, \tag{4.15}$$

where the subscripts 'r' and 'c' represent 'reduced' and 'critical'. Based on the law of corresponding states, the reduced properties for lattice and physical units should be the same. Therefore, we have $T_r = \frac{T^{lu}}{T_c^{lu}} = \frac{T^{phy}}{T_c^{phy}}$, which gives $T^{lu} = \frac{T^{phy}T_c^{lu}}{T_c^{phy}}$, where superscripts '$lu$' and '$phy$' represent 'lattice units' and 'physical units'. Similarly, we can derive the relationship between lattice and physical units for pressure p and density ρ.

We set the lattice resolution equal to the hard sphere diameter of nitrogen and methane molecules ($\sim$0.4 nm), such that we have a similar lattice construction with LDFT that is also developed based on lattice theory [11], therefore facilitating comparison between the two. In LDFT the probability of gas occupation in the first layer of adsorption sites is a function of the surface and lateral interaction energies E_0 and E_A(see Eq. 3.2 in Chapter 3) [86, 91].

In LDFT, E_A is determined by the gas species and temperature and is introduced into LBM by incorporating PR-EOS. E_A for nitrogen adsorption at 77 K ($T_r = 0.6$) can be calculated based on the following equation according to the approximations in LDFT [85]:

$$E_A = \frac{4}{z_0 T_r}, \tag{4.16}$$

where z_0 is the volume coordination number, here taken as 6 for a cubic lattice, and T_r is the reduced temperature. For nitrogen at 77 K, E_A = 1.87.

E_0 (a function of isosteric heat of adsorption) is an important parameter that is determined by the physical properties of the adsorbate and adsorbent [189]. Physisorption of non-polar molecules such as nitrogen and methane on microporous carbons at their normal boiling points typically release heats of adsorption of 5 – 25 $\mathrm{kJ/mol}$ ($E_0 \sim 1 - 5$ for methane, and $1 - 30$ for nitrogen) [108]. Adsorption of methane on graphene releases heat of adsorption of $\sim$15 $\mathrm{kJ/mol}$ ($E_0 \sim 3$) [85]. Moreover, the heat of adsorption for a particular adsorbate/adsorbent pair (*e.g.* nitrogen/methane and shale) can be calculated using two adsorption isotherms measured at different temperatures [108]. It is then imperative to establish the relationship between G_{fs} and E_0 (and therefore calibrating G_{fs} to the isosteric heat of adsorption). However, this correlation is not straightforward to derive theoretically. Here we determine this correlation numerically by fitting LDFT adsorption isotherms to LBM results at a series of G_{fs} values, as will be shown later in Section 4.3.

The relaxation time, τ, is typically set to 1 to achieve the optimal numerical stability [190–192]. Here the relaxation parameter is set to reflect changes in the kinematic viscosity as a function of nanoconfinement. The shortening of the mean free path due to nanoconfinement results in a decreasing kinematic viscosity. By keeping Knudsen number (Kn) the same between lattice and physical units, we ensure the simulation is performed under the same extent of nanometer scale confinement. Guo *et al.* [193] proposed a correlation between relaxation time τ in LBM model and Kn for microscale gas flow:

$$\tau = \frac{1}{2} + \sqrt{\frac{6}{\pi}} N Kn \Psi(Kn), \tag{4.17}$$

where N is the characteristic length in lattice units, and $\Psi(Kn)$ is a correction function for Kn accounting for the solid confinement at the nanometer scale, which is defined in Eq. 4.18. For a certain Kn, we calculate the relaxation time τ based on the lattice resolution we choose (0.4 nm/lu), and in this study τ was set to 1.

$$\Psi(Kn) = \frac{2}{\pi} \arctan\left(\sqrt{2} Kn^{-3/4}\right) \tag{4.18}$$

4.3 Model validation

4.3.1 Phase diagram

To test the reliability of our LBM model in reproducing the correct phase behavior, we simulated the phase separation of nitrogen at 77 K. The PR-EOS of nitrogen at 77 K is shown in Fig. 4.2. In our simulation, we set up a 100×100 lattice with initial fluid density of 1 at each lattice node. A random perturbation in density is introduced to initialize the phase separation process. Because the system is unstable, as time proceeds, phase separation occurs spontaneously, and Ostwald ripening effect is observed until a final liquid droplet is formed (see Fig. 4.3). Phase separation simulations were conducted at a series of temperatures, and the resulting phase diagram agrees very well with the Maxwell equal area construction [138] based on PR-EOS (see Fig. 4.4). The gas and liquid densities at 77 K are determined to be 0.0205 and 8.24 respectively from LBM simulations. Here the densities are in lattice units, and the following reported values are all in lattice units unless specified otherwise. The theoretical values of gas and liquid densities calculated using Maxwell construction on PR-EOS gives gas and liquid densities of 0.0400 and 8.20, respectively, which are close to our simulation results. The deviation of gas density from theoretical value is because LBM simulation achieves mechanical rather than thermodynamic stability, which has been discussed broadly in the literature [194, 195]. Therefore, we use the average liquid density normalized by the maximum achievable density (or the probability of an adsorption site to be occupied by a nitrogen molecule) as an approximation of the pressure in this study, which is a common assumption for LDFT as well.

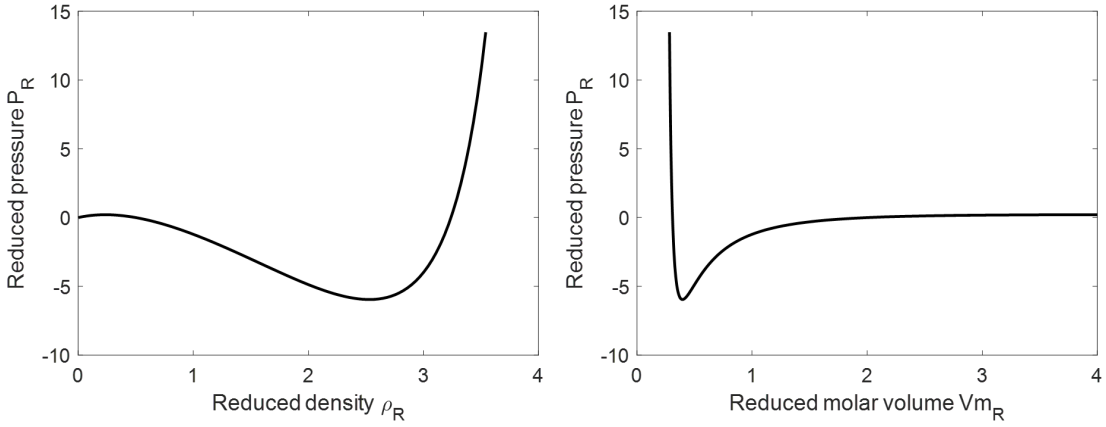

Figure 4.2: PR-EOS of nitrogen at 77 K with p_c = 3.396 MPa and T_c = 126.15 K. (a) Relationship between reduced pressure and density; (b) Relationship between reduced pressure and molar volume.

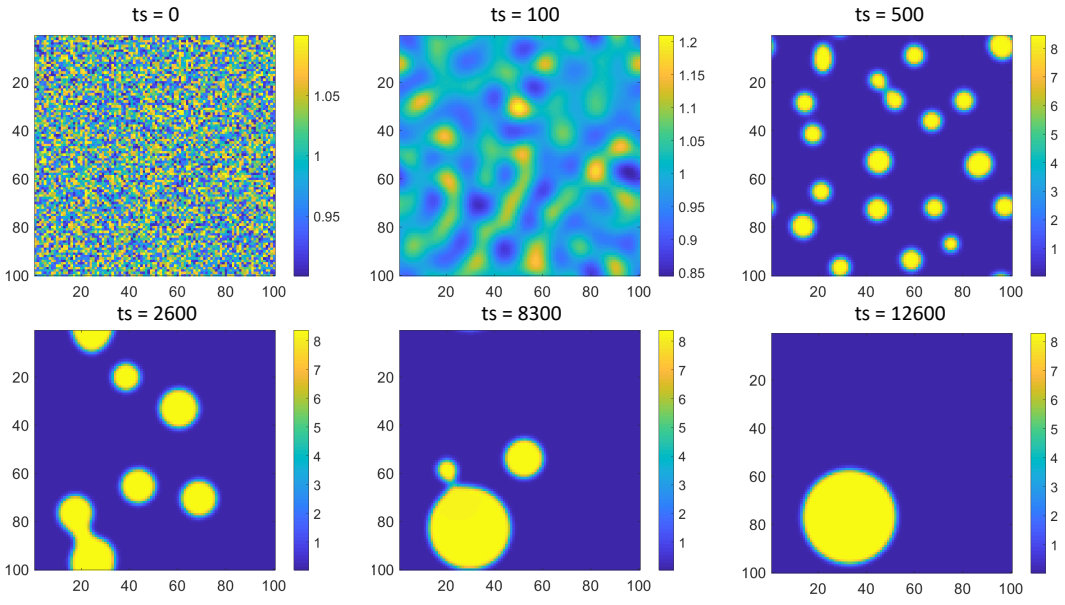

Figure 4.3: Evolution of the density profile at different time steps (ts) in the phase separation simulation of nitrogen at 77 K. Yellow is the condensed phase and blue is the gas phase. Density values on colorbar are in lattice units.

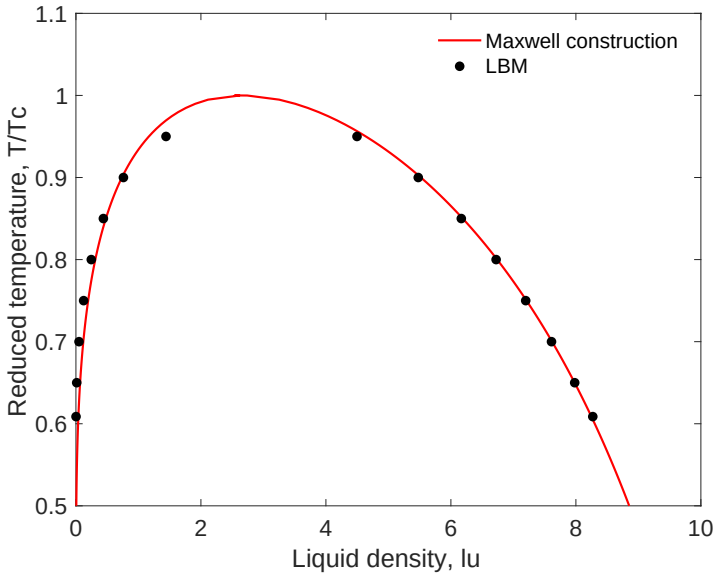

Figure 4.4: Phase diagrams constructed by LBM simulations (points) and Maxwell equal area constructions of PR-EOS (curve). Gas and liquid densities are shown in the left and right branches respectively.

4.3.2 Calibrating G_{fs} to E_0 for subcritical gases

We then establish the correlation between G_{fs} and E_0 for subcritical gases by simulating nitrogen adsorption at 77 K in a 10 nm slit pore, and fit LDFT calculations to the data. The problem setup is as follows: a 27×80 lattice is generated with the top and bottom layers as solid nodes. The fluid nodes are initialized with a uniform density of 0.1 and periodic boundary conditions are applied. Then we slowly inject gas into the system, resulting in a relative density increase ($\Delta\rho/\rho$) of 10^{-4} at each time step. Such density variation is small enough to be treated as quasi-equilibrium state. The density profile is recorded every 1000 time steps until bulk condensation occurs when the pore is filled with liquid nitrogen (at about 70000 time step). Due to the smooth density transition between gas and liquid phases, we determine the normalized adsorption amount at each pressure point to be the fraction of fluid nodes with density larger than $(\rho_g + \rho_l)/2$ [156], where ρ_g and ρ_l are gas and liquid nitrogen densities respectively. We calculated 8 nitrogen adsorption isotherms at 77 K for G_{fs} ranging from 2 to 4. LDFT results calculated based on the same geometry and temperature (E_A = 1.87 [11]) are fitted to LBM curves by varying E_0, and the optimal E_0 is determined by

minimizing the relative fitting error E_r:

$$E_r = \frac{1}{N}\sum_{i=1}^{N}\left[\left(n_i^{LBM} - n_i^{LDFT}\right)/n_i^{LBM}\right]^2, \tag{4.19}$$

where N is the total number of data points from LBM simulations, and n_i is the normalized adsorption amount for the i^{th} data point. Note that LDFT data are interpolated to the same relative pressures as LBM data so as to compare the two. The average fitting error for the 8 cases is about 4%. For detailed LDFT calculations please refer to Chapter 3. For the sake of clarity, we only show 3 adsorption curves and fitted results in Fig. 4.5. Our LBM model accurately predicts the occurrence of two-dimensional condensations (the sudden jumps in the adsorption uptake, or the 'steps') which indicates the filling of an adsorption layer, and the final condensation pressure is captured precisely. The correlation between G_{fs} and E_0 from the fitting is shown in Fig. 4.6. To generalize the relationship, dimensionless parameters (G_{fs}/G_{ff}, E_0/E_A) are used. A linear relationship is observed with the two parameters negatively correlated. As shown in Fig. 4.5, higher surface energy leads to earlier two-dimensional condensation. However, by examining the total effective force exerted on the first adsorbed layer as a function of its density (see Fig. 4.7), we see that it alters from attraction force to the wall to repulsive force, and higher surface energy leads to earlier occurrence of the repulsive force, which facilitates the capillary condensation process. This explains the negative correlation between G_{fs} and E_0. The correlation between G_{fs}/G_{ff} and E_0/E_A can be approximated by a straight line (R^2 = 0.9872, see Fig. 4.6):

$$\frac{G_{fs}}{G_{ff}} = -0.1465\frac{E_0}{E_A} + 4.2062 \tag{4.20}$$

4.3.3 Calibrating G_{fs} to E_0 for supercritical gases

For supercritical gas adsorption, we simulate methane adsorption isotherm at 323 K in the same geometry used above. In the simulation, the pore space is initialized with uniform density of 0.01 (0.1 MPa), and the gas density is increased by a factor of 10^{-4} at each time step until the system pressure reaches 20 MPa (or gas density reaches 2.44). Since the adsorbed gas usually does

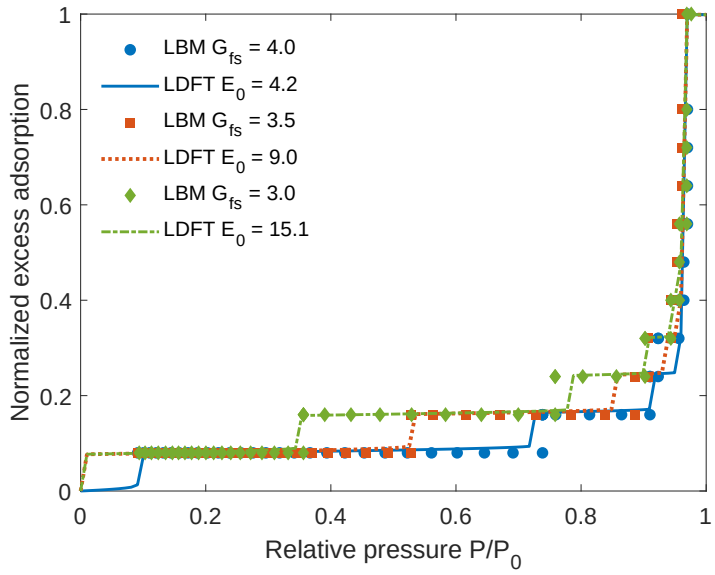

Figure 4.5: Simulated nitrogen adsorption curves (symbols) at 77 K using our LBM model at three different G_{fs} values (4.0, 3.5, and 3.0), and LDFT results (lines) at three corresponding E_0 values (4.2, 9.0, and 15.1) are fitted to LBM curves.

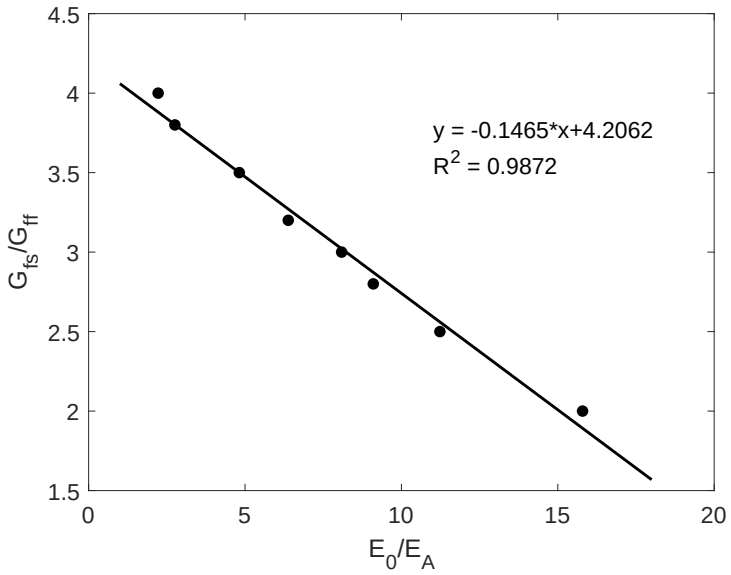

Figure 4.6: Correlation between dimensionless parameters G_{fs}/G_{ff} from LBM and E_0/E_A from LDFT for subcritical gases (nitrogen). Dots represent simulation data, and the straight line is fitted to the data points.

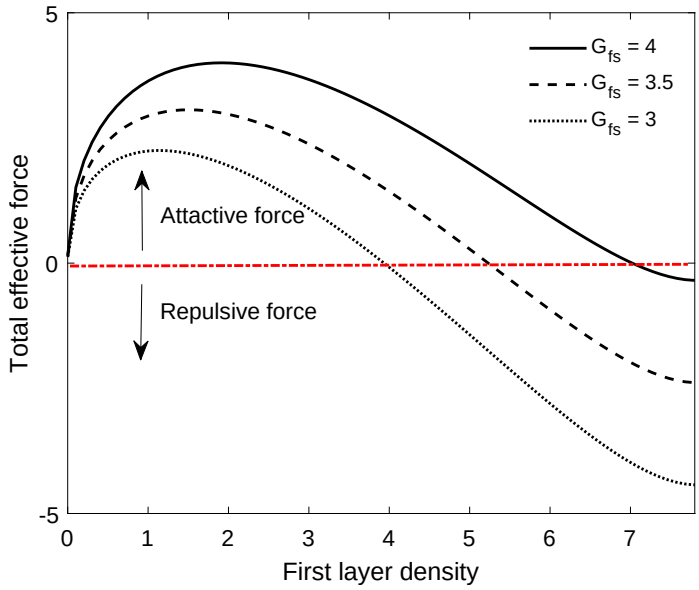

Figure 4.7: The total effective force exerted on the nitrogen molecules adsorbed at the first monolayer as a function of its density at three different G_{fs} values (4.0, 3.5, and 3.0). Here positive values represent attractive forces and negative values represent repulsive forces.

not extend more than two molecular layers as shown by LDFT or GCMC calculations [108, 162], and it is the first adsorbed layer that contributes most to adsorption, here we define adsorption uptake to be the monolayer density, normalized by the maximum monolayer capacity (25.52 mol/L), which is calculated by vdW co-volume factor [196]. The bulk pressure is calculated from the gas density in the system based on PR-EOS. Again LDFT adsorption curves are fitted to LBM results calculated at 7 G_{fs} values ranging from 1 to 4, with average fitting error below 1%. For the sake of clarity, we show in Fig. 4.8 three of the fitted results. For G_{fs} = 2.0 (E_0 = 1.16) we show in Fig. 4.9 the density profile of LBM (symbols) and LDFT (lines) at three pressures (5, 10, and 20 MPa) that extends from the first adsorbed layer to the eighth. Good agreement between LBM and LDFT further validates our model, and justifies our focus on the first adsorbed layer density. The fitted correlation between G_{fs}/G_{ff} and E_0/E_A is shown in Fig. 4.10. A linear correlation is observed (R^2 = 0.9986):

$$\frac{G_{fs}}{G_{ff}} = 0.2336\frac{E_0}{E_A} + 0.8759 \tag{4.21}$$

However, unlike subcritical gases, here the two parameters are positively correlated. Since

there is no phase separation observed for supercritical gases, higher surface energy leads to larger effective forces exerted on the monolayer as shown in Fig. 4.11. For $G_{fs} > 1$, only attractive forces are observed and the maximum force occurs when the average monolayer density is around 5. The total force reduces to 0 when maximum adsorbate density is reached. Using Eq. 4.21, we show in Fig. 4.12 the simulated methane adsorption curves that agree very well with experimental measurements by Zhang *et al.* [13] on three unconventional rock samples, including Woodford shale, isolated kerogen from Woodford shale, and Cameo coal. Note that the surface energy parameter E_0 is calculated based on measured isosteric heat of adsorption provided by Zhang *et al.* [13], and then converted to corresponding G_{fs} used in our LBM model based on Eq. 4.21. From LBM simulations we get the normalized monolayer density, which is then transformed to the excess adsorption (Γ, mmol/g) measured experimentally using the following equation:

$$\Gamma = C(\rho_m - \rho_b), \tag{4.22}$$

where C is the monolayer capacity which is a function of the specific surface area, and ρ_m and ρ_b are the normalized monolayer and bulk density respectively. Values of C are not reported in Zhang *et al.* [13] and is tuned in our simulation to match the experimental data.

4.4 Results and discussion

4.4.1 Gas adsorption in two model pore systems in mudrock

Simulation domain setup

Real porous media such as mudrock have more complex pore shapes other than slit, therefore the ability to perform direct simulation on more realistic geometries is essential for providing results more representative of an actual rock. In this study, we use 2D slices of a 3D Finney sphere pack [133] (available from Digital Rocks Portal [197]) to mimic pore structures with varying pore shapes and sizes in mudrock (see Fig. 4.13). For silty mudrock with coarse grains, the interparticle pores are dominant. Therefore, in our simulation the grains are simplified as the circular disks whereas the interparticle pores are the spaces between them (domain 1, see Fig. 4.13(b)). For

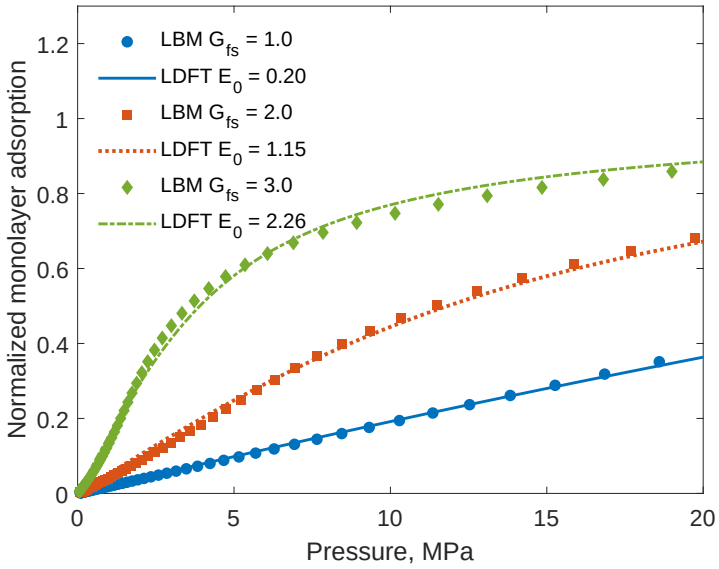

Figure 4.8: Methane adsorption isotherms calculated at 323 K with G_{fs} = 1.0, 2.0, and 3.0. The adsorption amount is determined by the monolayer density normalized by the maximum monolayer capacity. LBM results are shown in symbols, and fitted LDFT results are shown in lines.

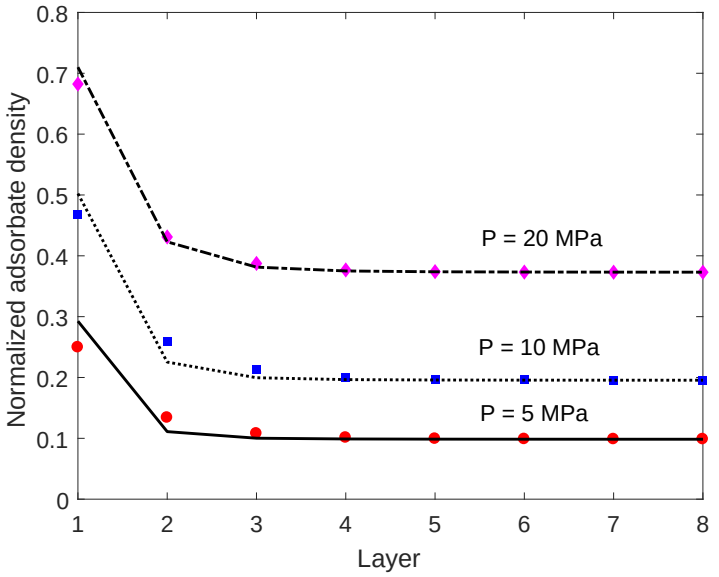

Figure 4.9: Methane density profiles calculated by LBM (symbols) and LDFT (lines) for adsorption layers ranging from 1 (closest to the solid wall) to 8. Calculations at three pressures (5, 10, and 20 MPa) are shown with G_{fs} = 2.0 (E_0 = 1.16) and T = 323 K.

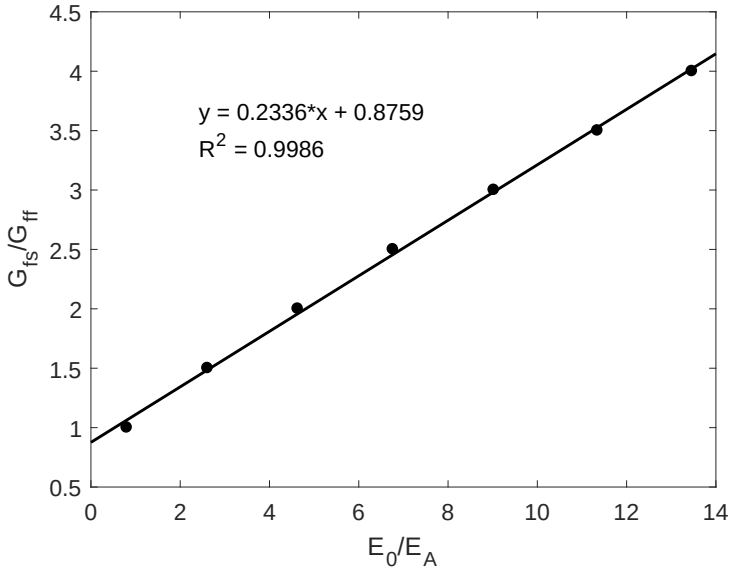

Figure 4.10: Correlation between dimensionless parameters G_{fs}/G_{ff} from LBM and E_0/E_A from LDFT for supercritical gases (methane). Dots represent simulation data, and the straight line is fitted to the data points.

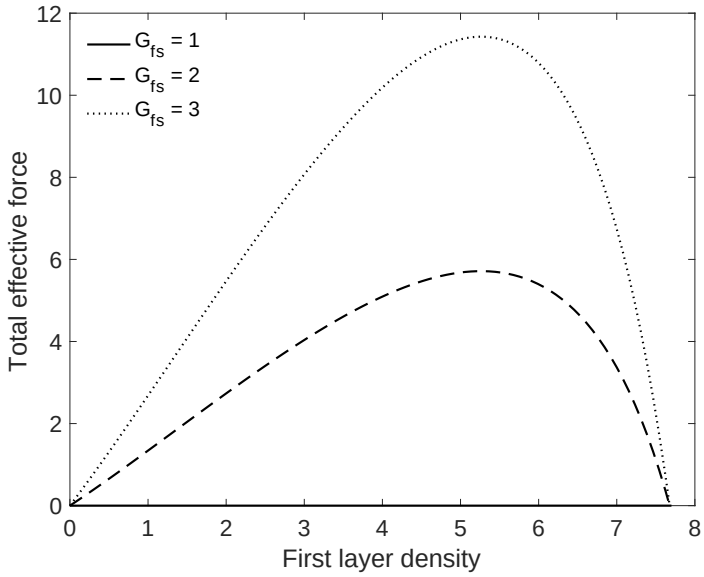

Figure 4.11: The total effective force exerted on the nitrogen molecules adsorbed at the first monolayer as a function of its density at three different G_{fs} values (1.0, 2.0, and 3.0). Here only attractive forces are observed for $G_{fs} > 1$.

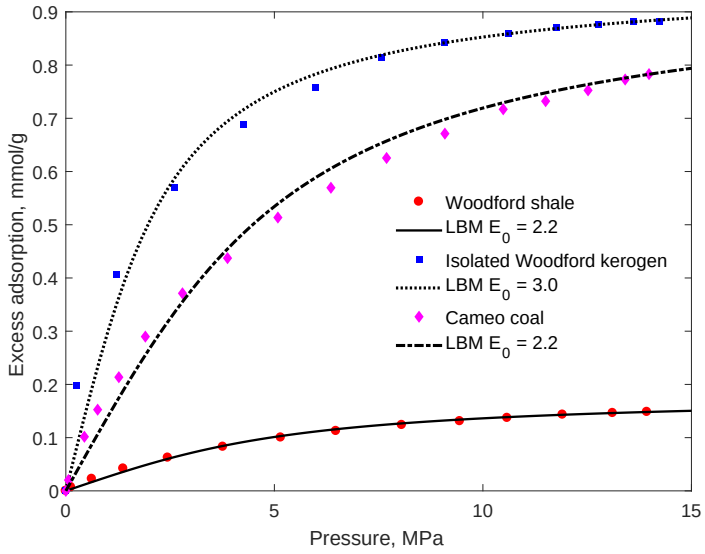

Figure 4.12: Experimental methane adsorption data at 323 K from Zhang *et al.* [13] (symbols) for three unconventional rock samples, including Woodford shale, isolated kerogen from Woodford shale, and Cameo coal, and LBM simulated adsorption isotherms (lines) based on experimentally determined surface energy values and correlation Eq. 4.21.

organic-rich mudrock, the dominant connected pore space occurs within the organic matter. Since most of the OM hosted pores are spherical in shape and form a spongy structure as revealed by SEM images [1, 19], we invert the 2D disks to be pore spaces and dilate them until they form a connected structure (domain 2, see Fig. 4.13(c)). Note that for all the simulation domains, we close the boundaries (adding a layer of solid nodes to the boundaries) to make sure mass balance is conserved in the simulation. For each type of domain, we extract 10 2D slices and report all adsorption curves for comparison.

Pore structure characterization

We first characterize the pore structure of the two domains including pore size distribution, pore shape, porosity, specific surface area and pore network connectivity. Individual pores are extracted and labeled, and their equivalent pore sizes and shapes are analyzed using the watershed algorithm in ImageJ software. Specific surface area is calculated as the length of grain boundaries normalized by the total area of solids. The pore network connectivity is quantified by calculating the

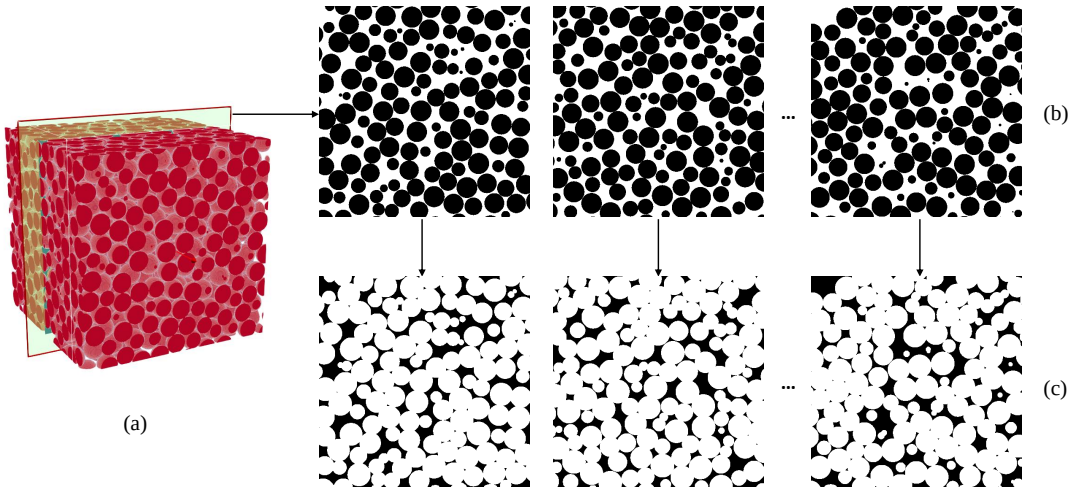

Figure 4.13: (a) 3D Finney sphere pack; (b) 2D slices extracted from (a) which are used as the simulation domains representing interparticle pore spaces that are dominant in coarse-grain silty mudrock (domain 1). (c) Model organic matter hosted pore space in organic-rich mudrock (domain 2). For both domains the solid is in black and pore space in white. Note that (c) is obtained by reverting the pore and solid spaces in (b) and dilating the pore spaces using a circular disk with radii = 4.

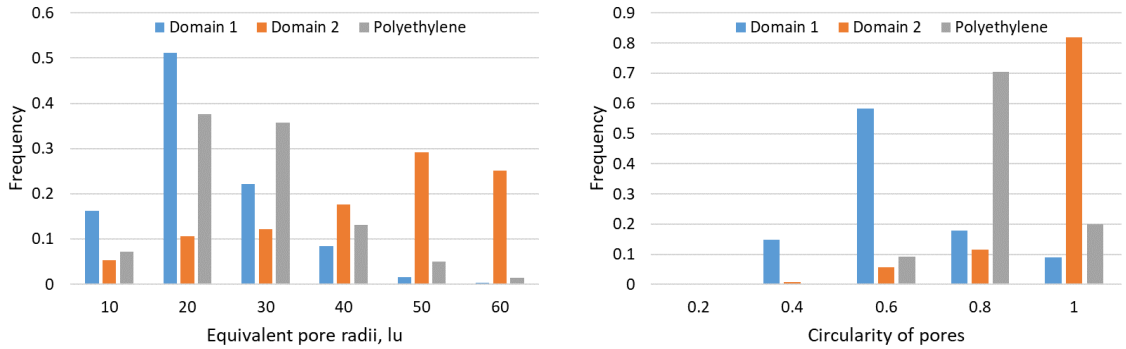

Figure 4.14: Comparison of (a) pore size distribution and (b) pore shape distribution for three types of domains. Domains 1 and 2 are described in Section 4.4.1, and polyethylene geometries are described in Section 4.2

Euler characteristic [198] using the BoneJ [16] plugin in ImageJ. Euler characteristic χ is a number that describes a topological space's shape or structure, and it is defined as $\chi = V - E + F$, where V, E and F are the numbers of vertices (corners), edges and faces in the given polyhedron, with more negative Euler characteristic representing better connectivity. As is shown in Fig. 4.14(a), the average pore size of domain 1 (18 lu, 7.2 nm) is about half of domain 2 (38 lu, 15.2 nm), and majority of the pores in domain 1 are below 12 nm. Shown in Fig. 4.14(b) is the circularity of pores for both domains. Note that in Fig. 4.14 we also show the comparison with the polyethylene geometry, which will be discussed later in Section 4.2. Circularity here is defined to be $4\pi A/P^2$, where A and P represent the area and perimeter of a certain geometry. A circularity value of 1 indicates a perfect circle. As the value approaches 0, it indicates an increasingly dispersed shape. Obviously, domain 2 has pore shapes closer to circular than domain 1. The calculated average porosity and specific surface area for domain 2 (0.81 and 0.21) is much larger than domain 1 (0.35 and 0.08). Moreover, the average Euler characteristic for both domains (-64.3 and -97.0 for domain 1 and 2) shows that domain 2 has better-connected pore spaces.

Sensitivity analysis of the representative elementary area

To ensure that simulations are performed at the REA scale and to eliminate the boundary effect, we first perform a sensitivity analysis on the representative domain size. As shown in Fig.

4.15, we extract three sets of domain sizes, including 125×125, 250×250 and 500×500 lu^2 with the same lattice resolution of 0.4 nm/lu, and the smaller domain is chosen as a subset of the larger one. For each domain size, 10 slices are extracted from the 3D Finney sphere pack. We then perform nitrogen adsorption simulations on all extracted geometries. Here we set G_{fs} = 3.5 (E_0 = 9.0) which is a common value for non-polar gas surface energy [108]. The resulting adsorption curves are shown in Fig. 4.16 and Fig. 4.17. Here for nanoporous media with a distribution of pore sizes, we observe smooth adsorption curves instead of the 'step' feature for a single slit pore. The mean standard deviation of the 10 adsorption isotherms calculated at 100 data points linearly interpolated between relative pressure 0.4 and 0.9 for each domain size is shown in Fig. 4.18. We observe that at domain size 250×250 the divergence of the adsorption curves is significantly smaller than the smaller domain yet comparable to the larger one. While there is no doubt it would be best to use the largest domain, it is reasonable to conclude that the REA is satisfactorily achieved at a domain size of 250×250 lu^2 or 5 – 7 pores/grains across. As a result, all following analysis is based on simulations performed on this domain size. In Fig. 4.19, we show a comparison of the nitrogen adsorption curves for both geometries of size 250×250 lu^2.

Since methane adsorption at reservoir temperatures is predominantly monolayer adsorption, the REA to study methane adsorption should be much smaller than the case for nitrogen. For convenience, we only perform methane adsorption simulation on the domain size of 250×250 lu^2 at temperature 323 K (E_A = 0.25) and pressures between 0.1 and 20 MPa. We set G_{fs} = 2 (E_0 = 1.15) which is also a common value for non-polar gas surface energy. The resulting adsorption curves for both domains are shown in Fig. 4.20. Here we show for each domain the min, max, and mean values of the normalized first adsorbed layer density as a function of pressure.

Nitrogen adsorption analysis

For nitrogen adsorption, as an example, we show the evolvement of the density profile of one of the ten geometries at four adsorption stages in Fig. 4.21 and Fig. 4.22 for domain 1 and 2 respectively. For domain 1, our LBM model accurately predicts the early capillary condensation at pore throats with smaller sizes that accumulates in the form of pendular rings, which is consistent

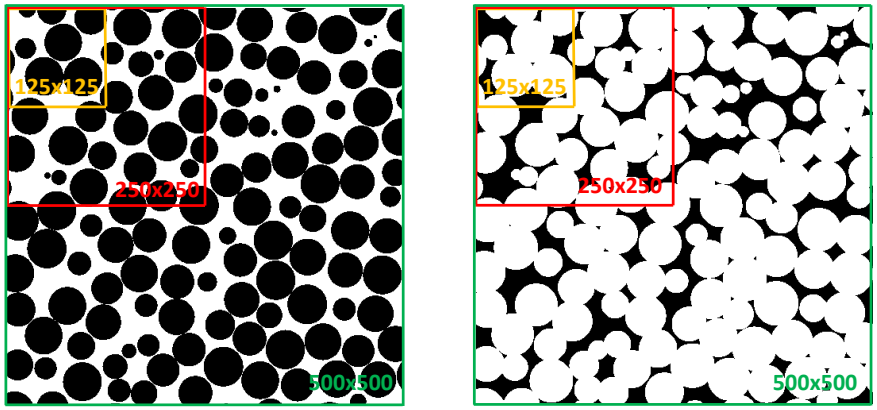

Figure 4.15: Simulation domain of three different sizes (125×125, 250×250 and 500×500 pixels) used in the sensitivity analysis. Note that the smaller domain is a subset of the larger one, and solid is in black while pore space is in white.

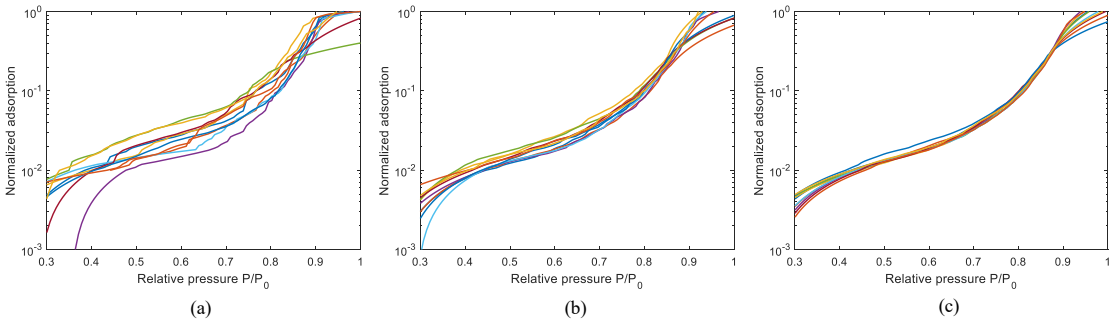

Figure 4.16: Simulated nitrogen adsorption curves for 10 2D slices extracted from domain 1. (a) domain size 125×125 lu; (b) domain size 250×250 lu; (c) domain size 500×500 lu. Note that all domains have the same resolution of 0.4 nm/lu.

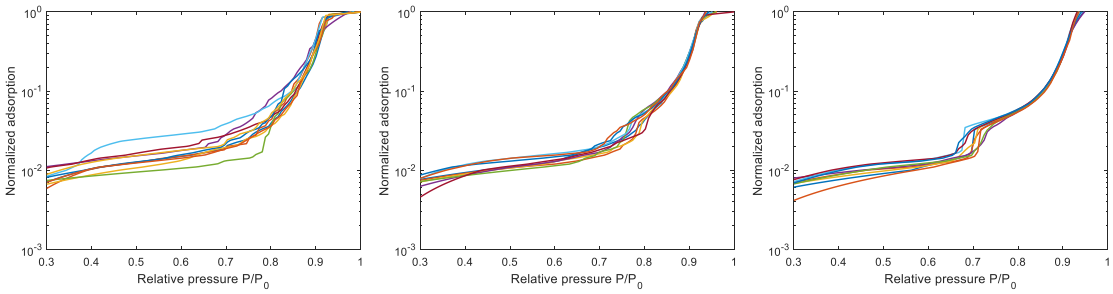

Figure 4.17: Simulated nitrogen adsorption curves for 10 2D slices extracted from domain 2. (a) domain size 125×125 lu; (b) domain size 250×250 lu; (c) domain size 500×500 lu. Note that all domains have the same resolution of 0.4 nm/lu.

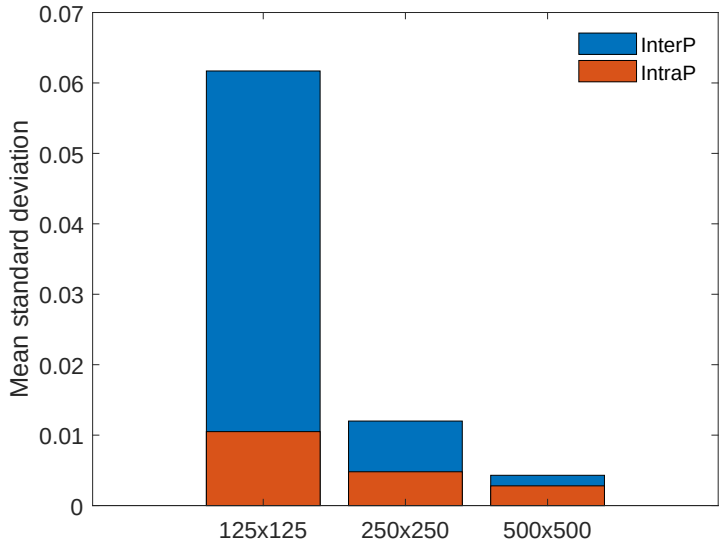

Figure 4.18: Mean standard deviations of the simulated 10 adsorption isotherms for each domain size, calculated based on 100 data points linearly interpolated for relative pressure ranging from 0.4 to 0.9. Blue and orange bars represent interP and intraP geometries respectively.

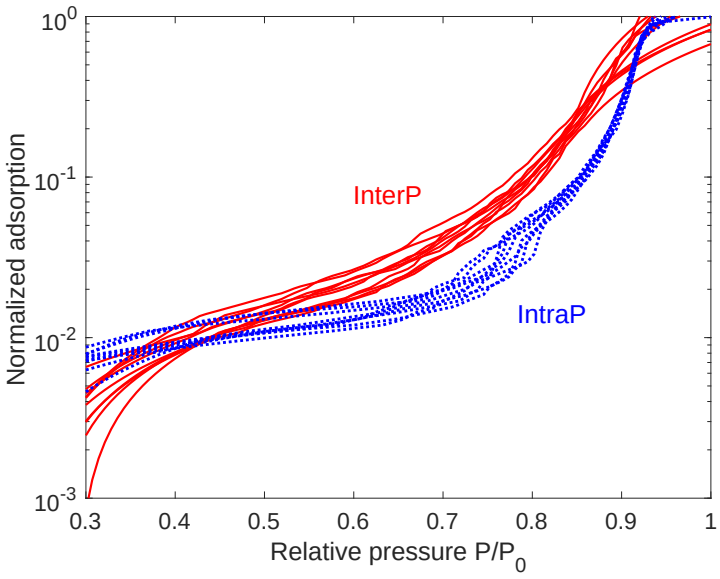

Figure 4.19: Comparison of nitrogen adsorption curves at 77 K in interP (red lines) and intraP (blue dotted lines) geometries. For each type of geometry, results for the 10 2D slices of size 250×250 are shown.

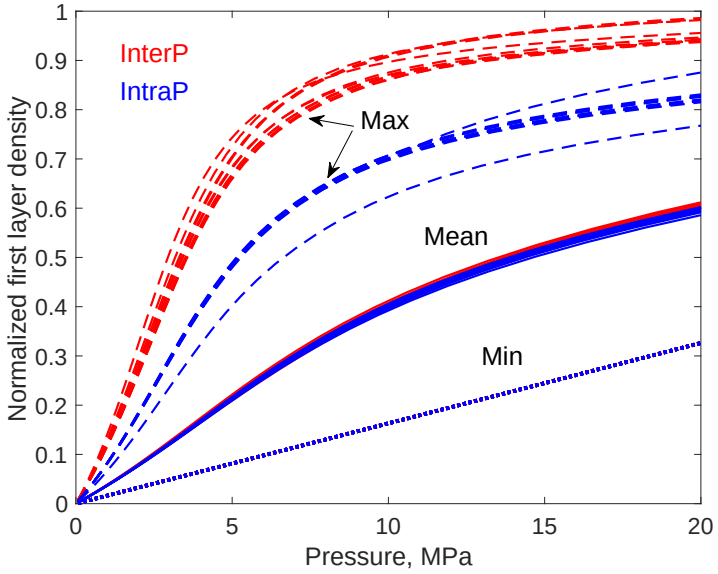

Figure 4.20: The simulated methane adsorption curves for domain 1 (interP, red curves) and 2 (intraP, blue curves) at the domain size of 250×250 pixels. All simulations are performed at temperature 323 K and E_0 = 1.15.

with Kelvin equation [199], as well as experimental studies of nitrogen adsorption in a packing of spherical nanoparticles [200]. As pressure increases, we observe the isolated pendular rings growing, moving and merging as a result of ongoing phase condensation, leaving the relatively larger pores unfilled. The adsorption behavior is strongly dependent on the adsorption history and the pore structure plays an important role in the phase condensation process. Both the effective pore size and shape change along the adsorption process, which can not be properly captured by the theoretical models. In the last adsorption stage (P_r = 0.90), the condensed phase forms a fully connected structure with isolated gas bubbles randomly spreading between the grains, before bulk condensation occurs. For domain 2 we observe multilayer adsorption adjacent to solid walls, followed by early phase condensation which occurs close to the sharp corners where strong solid confinement is present rather than uniform multilayer accumulation, which is different from the adsorption behavior for a single pore. As pressure increases, the adsorbed phase grows into the pore space, forming circular gas-liquid interface due to the balance between gas-liquid and liquid-solid surface tensions. Similar to domain 1, in the last adsorption stage, isolated gas phases exist within the well-connected condensed phase.

The corresponding nitrogen adsorption curves are shown in Fig. 4.19. For domain 1, lower adsorption uptake is observed for relative pressure below 0.4, and final capillary condensation pressure is slightly higher than domain 2, which is a result of the convex solid surface that delays the adsorption process. However, for relative pressure between 0.4 and 0.9, we observe higher adsorption uptake for domain 1 due to the sequential capillary condensation in the range of pores/throats below 20 nm (see Fig. 4.14(a)), and the adsorption amount increases smoothly. This indicates that pore size has a major effect on adsorption behavior for medium relative pressures, whereas at the early and late adsorption stages, the adsorption uptake is mainly controlled by the pore shape. For domain 2, the adsorption uptake is generally lower for relative pressure between 0.4 and 0.9. However, an obvious adsorption upshot ('a step') is observed for relative pressure around 0.75, which we do not observe for domain 1. As shown in Fig. 4.22(b), we attribute this signature behavior to the initiation of abrupt phase condensation following multilayer adsorption, which is a result of the concave solid surfaces that facilitates the adsorption process to some extent.

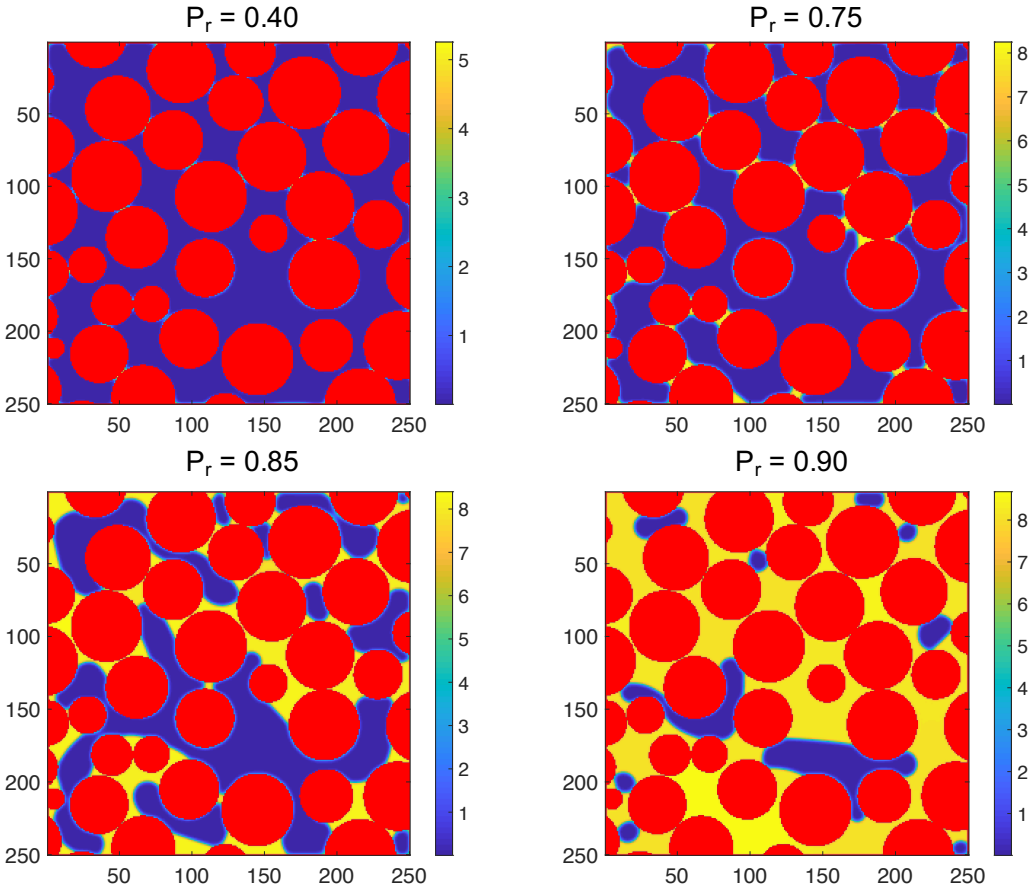

Figure 4.21: Density profiles of adsorbed nitrogen at different relative pressures for domain 1 (interP pores). The colorbar represents the density of nitrogen in lattice units, and the solid is in red. P_r is the relative pressure.

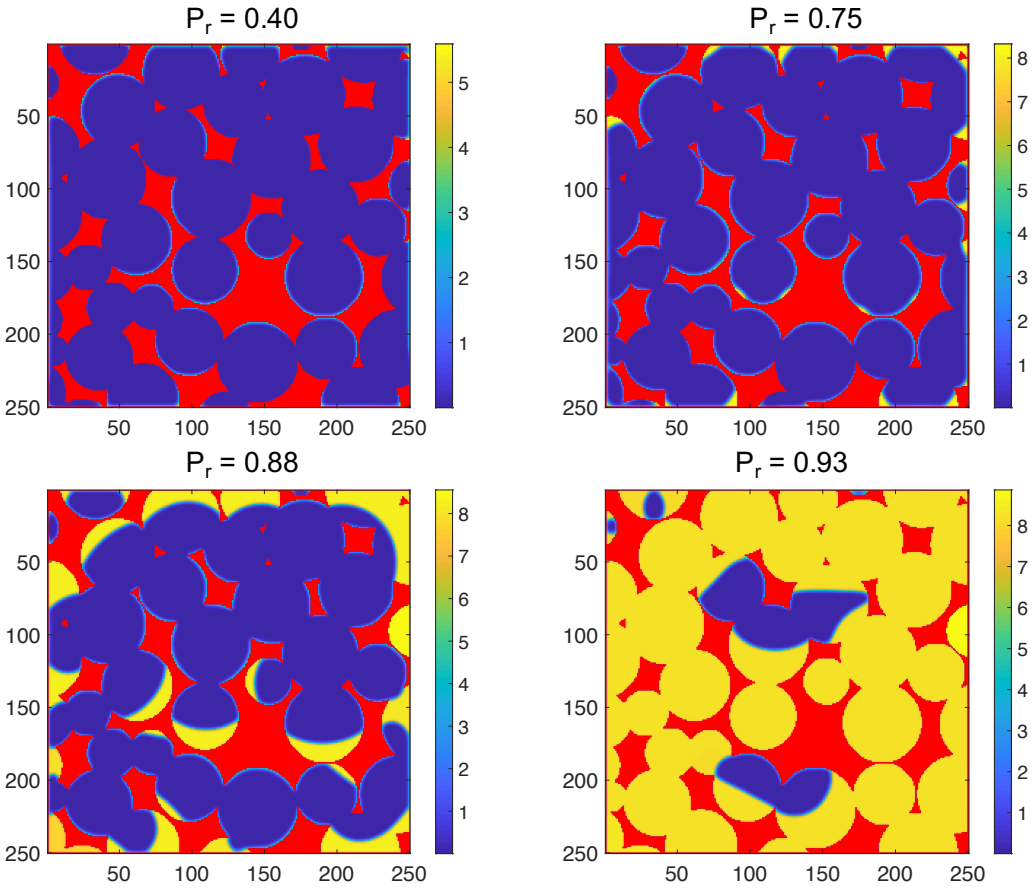

Figure 4.22: Density profiles of adsorbed nitrogen at different relative pressures for domain 2 (intraP pores). The colorbar represents the density of nitrogen in lattice units, and the solid is in red. P_r is the relative pressure.

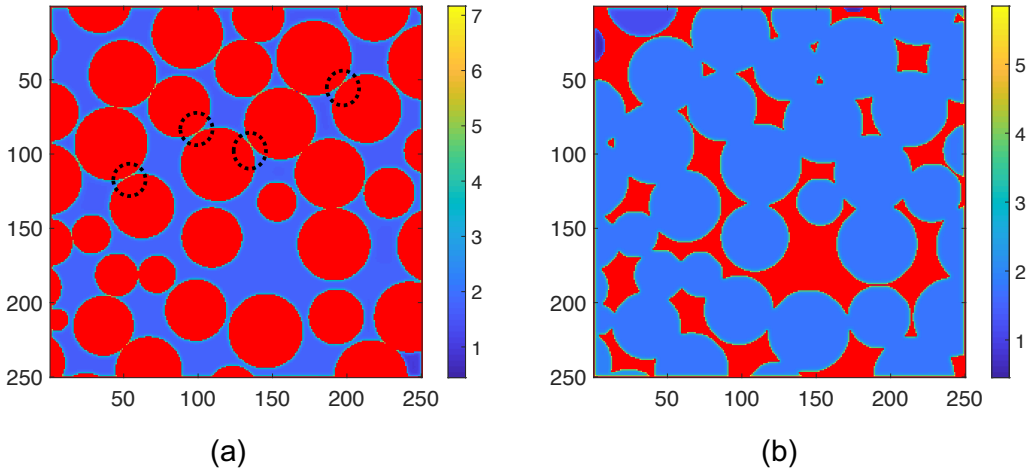

Figure 4.23: Density profiles of methane at 14 MPa in two example geometries from (a) Domain 1 (InterP) and (b) Domain 2 (IntraP). The black dotted circles label some of the grain contact regions where high densities are observed for Domain 1.

Methane adsorption analysis

For methane adsorption, the normalized first layer density for both domains as a function of pressure is shown in Fig. 4.20. The average monolayer density for both domains is almost the same for a wide range of pressures, which indicates that pore shape (solid surface curvature) has minor effect on supercritical gas adsorption in mesoporous materials. Since the adsorption uptake is mostly contributed by the first monolayer, supercritical gas adsorption is mainly a function of specific surface area, temperature, and surface energy. However, due to the variation of pore size and shape in both domains, the monolayer density is not a uniform value. Although the lower limits for both domains are bounded by the bulk density at a certain pressure, the upper limits are significantly different. The maximum achievable monolayer density for domain 1 can be up to 1.5 times larger than domain 2. As is shown in Fig. 4.23, we can see that those high density regions exist between grain contacts where the solid confinement effect is strong. These pore throat regions, by definition, belong to micropores. This indicates that for microporous materials the adsorption uptake will also be affected by pore sizes, rather than just surface areas.

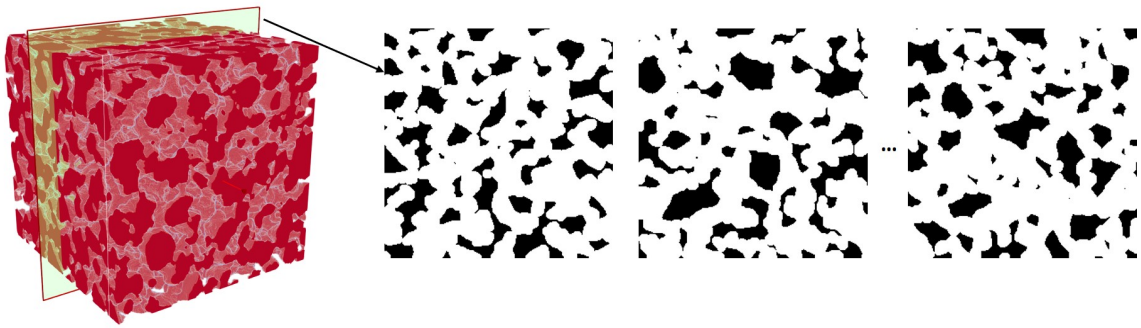

Figure 4.24: 3D polyethylene porous medium (256×256×256 voxels, grains are in red), and 2D slices (256×256 pixels or 128×128 nm^2, 10 slices in total) which are used as the simulation domains. The solid is in black and pore space is in white.

4.4.2 Gas adsorption in a complex polyethylene porous medium

We next study gas adsorption in a synthetic polyethylene porous medium with heterogeneous pore shapes and connectivity. Similarly, 10 different 2D slices (256×256 lu^2 with a lattice resolution of 0.4 nm/lu) were extracted from the 3D X-ray microtomography images [74] (see Fig. 4.24). Due to the poor connectivity of the pore space in 2D, we dilate the pore space using a circular mask with radii = 4 pixels and perform nitrogen adsorption simulation. Note that we have done a similar sensitivity analysis of the representative domain size and determined that the size we chose is at the REA scale. We then perform a pore structure characterization and the pore size and shape distribution are shown and compared together with domain 1 and 2 in Fig. 4.14. The average pore size and circularity is between the values for domain 1 and 2. The simulated average nitrogen and methane adsorption curves for the 10 slices are shown in Fig. 4.25, in comparison with the averaged results for domain 1 and 2. As shown in Fig. 4.25, the nitrogen adsorption curve for a complex pore structure is between the results for the simplified interP and intraP pore systems, while the methane adsorption curve almost overlaps with the results for intraP pore system due to large pore sizes. This indicates that the two simplified interP and intraP pore systems are two extreme cases for subcritical and supercritical gases adsorption. Real porous media with complex pore geometries have intermediate adsorption behavior.

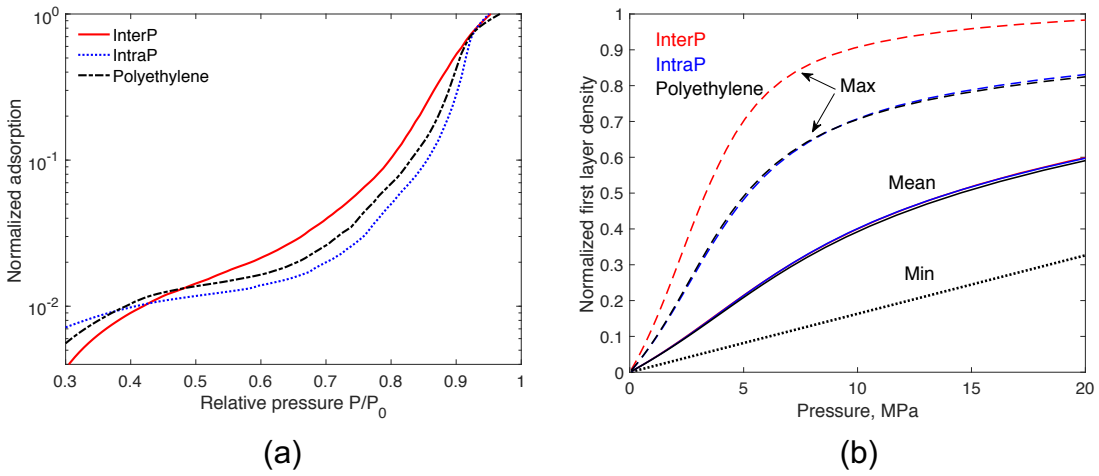

Figure 4.25: The simulated average (a) nitrogen and (b) methane adsorption curves for the three types of domains used in this study.

4.4.3 Error and uncertainty assessment

In this study we define a REA of 250×250 pixels (or 100×100 nm^2) for nitrogen adsorption simulation for these two particular types of 'model' pore systems. The representativeness of REA is established by observing the divergence of the simulated nitrogen adsorption curves. However, this should not be confused with the actual REA or REV in shale with much more complex pore structure, where we would expect a REV at least hundreds of microns across in size.

It should be mentioned that in LBM the fluid particles residing on the lattice are statistical ensembles instead of actual fluid molecules. We constrain the interparticle forces between the nearest neighbors along the velocity directions as is commonly done in the literature, neglecting long-range forces. The interparticle forces are defined as a function of local fluid density and solid-fluid interactions are incorporated by defining solid pseudopotential either as a constant or as a function of the density of the first adsorbed layer. Either fluid-fluid or solid-fluid interaction forces are phenomenological rather than physical, and the correlation between simulation and physics is established by tuning the numerical parameters to match with physical ones. This is one caveat associated with LBM modeling in general. However, once calibrated, LBM could reproduce a wide range of thermodynamic behavior as shown in this work.

Here adsorption is simulated by increasing the fluid density by a small factor ($\Delta\rho/\rho = 10^{-4}$), assuming pseudo-thermodynamic equilibrium is reached at each time step. The smaller this factor, the closer simulation reproduces equilibrium states. However, the choice of this factor has to be balanced with the computational cost. As a result, at certain time steps when local capillary condensation occurs, longer simulations are required for local thermodynamic equilibrium to be reached. This explains the varying contact angles and phase interface shapes (not at apparent equilibrium state) as shown in the nitrogen adsorption density profiles in Fig. 4.21 and 4.22, as a result of the inconsistent local capillary condensation. Furthermore, the location and extent of the sudden increase in the nitrogen adsorption uptake for intraP pore systems (see Fig. 4.20) might be affected by this factor. However, since we consistently observe this behavior for ten different geometries, such behavior can be considered to be unique for intraP pores.

The gas phase density calculated from the simulation is off by about 50% and therefore we determined the bulk pressure based on liquid density instead. This is due to the fact that the LBM model used here is not strictly thermodynamically consistent. Modifications of EOS and the way forcing term is incorporated into LBM have been suggested in the literature and good agreement of the simulated phase envelope with Maxwell construction results has been obtained [195]. Such inconsistency is eliminated in our 3D LBM model which will be introduced in Chapter 5.

On the other hand, 2D pore shape and connectivity might not be representative of 3D, and the surface tension, which is a dominant factor in capillary condensation, is not very well defined in 2D. The 2D simulations conducted in this study served as numerical exercises where boundary conditions, numerical stabilities, and convergence criteria are throughly explored, which eases the 3D model development and implementation as will be discussed in Chapter 5.

4.5 Conclusions

In this study, we developed a LBGK D2Q9 LBM model that incorporates both rock-fluid and fluid-fluid interactions to study subcritical (nitrogen) and supercritical (methane) gas adsorption behavior in mudrock nanopore systems with complex pore geometries. The main benefit of developing an LBM model over existing adsorption modeling approaches (such as LDFT and GCMC) is the

applicability to pore structure of arbitrary complexity which has a first-order impact on multiphase thermodynamics, while conducting simulations at the REA scale at relatively low computational cost. A modified Shan-Chen pseudopotential model with incorporation of PR-EOS was used to achieve automatic phase separation without the need to track the phase interface, and to maintain thermodynamic consistency which is lack in most LBM models using the unmodified Shan-Chen pseudopotential model [149,150]. The novelty of this work was the introduction of two phenomenological forms of surface forces for subcritical and supercritical gases respectively. For the first time, we validated the LBM model against theoretical (LDFT) and experimental data for both subcritical and supercritical gas adsorption. Application of our LBM model to nitrogen adsorption simulation in reconstructed interP and intraP mesoporous media reveals three adsorption stages with distinct features. The simulated adsorption curves for intraP pores show a unique adsorption upshot at relative pressure around 0.8 which occurs due to the abrupt phase condensation following multilayer adsorption. Further study of methane adsorption in these two domains show that supercritical gas adsorption is not sensitive to pore shape, but rather surface area. However, the existence of micropores significantly affects the monolayer density. Extension of our model to a complex polyethylene geometry reveals that subcritical and supercritical gas adsorption for real nanoporous media is bounded by the limits given by the two model interP and intraP pore systems.

The 2D reconstruction of porous media used in this study provides a preliminary understanding of adsorption behavior in complex pore structures under nanometer scale confinement. Yet we are aware that the 2D pore shape and size might not be representative if extended to the third dimension. With the recent development of direct imaging techniques such as FIB-SEM, it is possible to reconstruct high resolution 3D image stacks of pore structures, and simulation in such 3D images can provide more realistic results. In this chapter, we mainly focused on the adsorption branch of the isotherm. For subcritical gas sorption experiments, desorption is also an important process and usually sorption hysteresis is observed as a function of pore shape and pore network connectivity. We will address these problems in Chapter 5 by using a 3D LBM model.

Chapter 5: 3D LBM modeling for nitrogen sorption hysteresis study in different shale pore systems [1]

5.1 Introduction

In Chapter 4, we used a D2Q9 LBM model incorporated with PR-EOS to study both subcritical and supercritical gas adsorption behavior [201, 202] in shale. Two different forms of surface forces were proposed which led to quantitative agreement with LDFT and experimental data. This was the first time that LBM models had been validated against theoretical and experimental data for both subcritical and supercritical gases. A unique characteristic of the simulated nitrogen adsorption curve was observed for the intraP pore system which differentiates with the interP one. On the other hand, for supercritical methane adsorption, we found that the average adsorption uptake is dominantly controlled by the specific surface area rather than pore shape/curvature.

The previous work was conducted in 2D, which has limited representation of the pore shape/connectivity in 3D. We also limited our study to the adsorption branch. In this study, we focused on subcritical gas sorption which is more sensitive to pore shape and connectivity. We extended our 2D model to 3D using a LBGK D3Q19 (three dimensional 19 velocity) LBM model. The model was first calibrated to LDFT calculations, then validated against GCMC simulations. We studied both nitrogen adsorption and desorption processes in more representative 3D pore structure reconstructions, to further evaluate the capability of nitrogen sorption hysteresis measurements to differentiate the dominant pore type/shape in shale matrix, as a supplement to the workflow introduced in Chapter 3. As far as we know, this is the first time that 3D LBM models has been validated against LDFT or molecular-scale simulations for subcritical gas adsorption/desorption. Furthermore, sorption hysteresis was produced in complex 3D geometries using LBM for the first time. The 3D LBM model developed here served as a prototype based on which complex nanoscale

[1] This chapter is currently under preparation for publication.

flow physics can be incorporated for coupled adsorption/flow simulations, as will be discussed in the next chapter.

For the remaining of this chapter, we first make a brief introduction to the D3Q19 LBM models developed and used here in Section 5.2. Then in Section 5.3, we show calibration of the model parameters to physical properties. Several validation cases of our model regarding reproducing the phase diagram, visualizing the adsorbate distribution in irregular geometries, and reproducing sorption curves by GCMC simulations are shown in Section 5.4. Applications of our models to study nitrogen sorption hysteresis in two 3D model pore systems (interP and intraP pores as used in Chapter 4) are introduced in the last section.

5.2 Numerical method

5.2.1 Lattice Boltzmann equation

In this study, we used a D3Q19 LBM model with the lattice structure and velocity directions (18 advecting, 1 at rest) shown in Fig. 5.1. This lattice is the most common choice for 3D [137, 193, 203]. The corresponding 19 discrete velocities are defined to be:

$$\mathbf{e_i} = \begin{cases} (0,0,0) & i = 0, \\ (\pm 1,0,0),(0,\pm 1,0),(0,0,\pm 1) & i = 1,2,\ldots,6, \\ (\pm 1,\pm 1,0),(\pm 1,0,\pm 1),(0,\pm 1,\pm 1) & i = 7,8,\ldots,18 \end{cases} \tag{5.1}$$

For subcritical nitrogen sorption modeling, we used the LBGK collision operator [204] due to its simplicity and stability under low reduced temperatures and high density ratios as discussed in Chapter 4. Appropriate implementation of the body force term is especially necessary in phase separation simulations because forces (and velocity changes) inside the liquid/vapor transition layer are not small. For incorporating external forces into LBM, herein we used the exact difference method (EDM) [195]. EDM is considered superior over the simple forcing scheme (changing equilibrium velocity) we used in Chapter 4 because EDM removes the dependency of equilibrium gas/liquid densities on viscosities (relaxation times) and achieves better thermodynamic consistency [195].

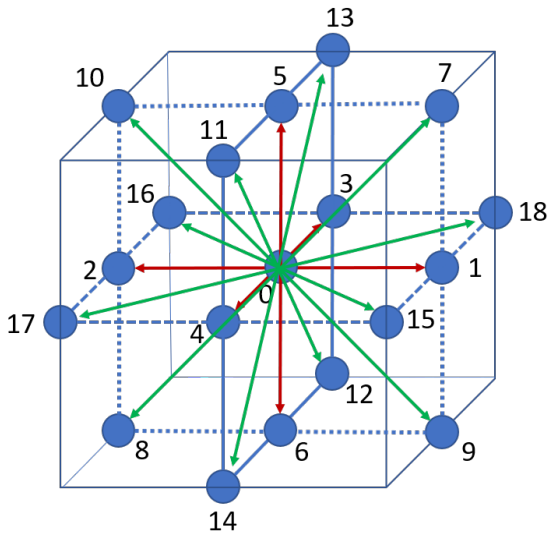

Figure 5.1: Schematic of the lattice structure and velocity directions and magnitude for D3Q19 LBM models.

EDM was derived directly from the Boltzmann equation by adding an extra forcing term Δf_i into the governing equation which was introduced in Chapter 4 Eq. 4.1, and we get:

$$f_i(\mathbf{x} + \mathbf{e}_i \Delta t, t + \Delta t) - f_i(\mathbf{x}, t) = -\frac{1}{\tau}(f_i - f_i^{eq}) + \Delta f_i, \tag{5.2}$$

where f_i is the particle distribution function, and $\mathbf{e}_i$ is the particle velocity. The terms on the left hand side describe the particle streaming process, whereas the first term on the right hand side represents the collision process. Δf_i is the variation in the particle distribution function caused by the external forces:

$$\Delta f_i = f_i^{eq}(\rho, \mathbf{u} + \Delta \mathbf{u}) - f_i^{eq}(\rho, \mathbf{u}), \tag{5.3}$$

and $\Delta \mathbf{u} = \mathbf{F}\Delta t/\rho$. The interparticle force $\mathbf{F}$ is expressed as a gradient of the potential field U which is the nonideal part of the EOS [205]:

$$\mathbf{F} = -\Delta U = -\Delta \left[P(\rho, T) - \rho\theta \right], \tag{5.4}$$

where $\theta = 1/3$ for D3Q19 LBM models.

Unlike the Shan-Chen force model which is based on the mean-value approximation of the

interparticle forces [150], Kupershtokh *et al.* [195] proposed a general way of calculating $\mathbf{F}$ by taking a weighted average of the local approximation and mean-value approximation, providing an additional tuning parameter A for the surface tension or equilibrium densities, which will be shown later in Section 5.3 to result in better thermodynamic consistency. Eq. 5.5 shows the expression of $\mathbf{F}$ [195]:

$$\mathbf{F} = \frac{1}{3h}\left[A\sum_{a=1}^{N} G_i\psi^2(\mathbf{x}+\mathbf{e}_i)\mathbf{e}_i + (1-2A)\psi(\mathbf{x})\sum_{i=1}^{N} G_i\psi(\mathbf{x}+\mathbf{e}_i)\mathbf{e}_i\right], \tag{5.5}$$

where A is a weighting factor which can be used to adjust the contribution of local and mean-value approximation in order to tune the LBM model for better thermodynamic consistency, G_i is the weighting factor of forces for each velocity direction i, and $G_i = 1$ for nearest neighbors ($a = 1-6$), $G_i = 1/2$ for the next nearest neighbors ($i = 7-18$), and $\psi = \sqrt{-U}$.

5.2.2 EOS in LBM

Incorporating realistic EOS to calculate the interparticle forces leads to quantitative consistency with the phase behavior expected for fluid below the critical temperature. Various types of EOS, such as vdW, PR, Carnahan-Starling, and Redlich–Kwong EOS, have been integrated into LBM [150, 155, 157, 201] to reproduce varieties of phase behaviors. However, due to the deficiency of the Shan-Chen forcing scheme used in [155] for establishing thermodynamic consistency, even though realistic EOS is incorporated, the simulated phase diagram does not necessarily agree well with theoretical results based on Maxwell equal area constructions [195], especially at the gas branch. Fine-tuning the forcing scheme improves the thermodynamic consistency as shown by Kupershtokh *et al.* [195], which is critical for studying subcritical phase separation and determining the bulk pressure of the system. A tuning parameter A was introduced by Kupershtokh *et al.* [195] to adjust the contribution of local and mean-value approximation of the interparticle forces (Eq. 5.5), therefore providing the possibility of tuning the equilibrium gas and liquid densities. By setting $A = -0.152$, they observed improved agreement with experimental data. However, in their study they did not use PR-EOS, which is a common choice for describing phase behavior, but a modified Kaplun-Meshalkin (mKM) EOS which was also fitted to experimental data. There is no superiority

regarding the choice of one form of EOS over the other. However, since the parameter A was tuned based on mKM-EOS in the work by Kupershtokh *et al.* [195], to maintain consistency, herein we also used mKM-EOS with A setting to -0.152 to model subcritical gas sorption and condensation. When expressed in the reduced state, mKM-EOS can be written as:

$$P_r = c\rho_r T_r \left(1 + \frac{d}{1/\rho_r - b}\right) - a\rho_r^2, \tag{5.6}$$

where a, b, c and d are constants which are determined based on critical state analysis:

$$a = \frac{1}{3-c}, b = 3 - c, d = \frac{12c - 6c^2 + c^3 - 8}{c(3-c)}, \tag{5.7}$$

where c is a free parameter which was set to 2.78 for best agreement with the experimental data on the coexistence curve (see Fig. 1 in [195]).

5.2.3 Surface forces

We define surface forces for D3Q19 models in the same way as D2Q9 models. For subcritical gases, the potential field ψ of fluid particles is extended to the solid nodes by defining a solid pseudodensity ρ_s which is calibrated to surface energy E_0 (see Section 5.3) in a similar way as was described in Chapter 4 for the D2Q9 model.

5.3 Correlation with physical parameters

The PVT properties obtained from LBM simulations are dimensionless reduced properties defined directly by mKM-EOS in the reduced state (Eq. 5.6), which can be correlated with physical parameters through the corresponding state principles as introduced in Chapter 4. For nitrogen adsorption modeling, we calibrated ρ_s to surface energy E_0 to reproduce physical surface forces using LBM models.

Based on mKM-EOS, the equilibrium gas and liquid nitrogen reduced densities at $T_r = 0.6$ are 0.02 and 3 respectively in lattice units, and all the parameters hereafter are in lattice units unless specified otherwise. For stability reasons, the choice of solid pseudodensity is bounded by the lower

and upper limits given by the gas and liquid nitrogen densities. Here we performed adsorption simulations in a slit pore (infinitely long parallel plates) of width 7 nm at $T_r = 0.6$ at five values of ρ_s (3, 2.5, 2, 1.8, 1.5). The adsorption process is simulated in a similar way as introduced in Chapter 4 by uniformly increasing the system density by a factor of 2×10^{-5} at each time step, assuming the system reaches pseudo-equilibrium state, until the average density reaches the maximum density (3) as an indication of final condensation. The system is initialized with a uniform density of 0.1 and the equilibrium density profiles are recorded every 10,000 time steps. Final condensation is reached at approximately 180,000 time steps. The relative pressure here is taken as the gas density of the confined system normalized by the bulk gas density, which is defined in the same way as in LDFT calculations [11, 86]. Note that after capillary condensation occurs, there is no apparent 'gas' phase in the system, and the mean density approaches liquid density. The relative pressure at which gas density dramatically increases is then taken as the capillary condensation pressure. LDFT calculations were performed using $E_A = 1.87$ and varying E_0 to match with the LBM results. For the sake of clarity, only three out of the five matched adsorption isotherms are shown in Fig. 5.2 and the resulting correlation between ρ_s and E_0 is shown in Fig. 5.3. Note that to generalize the relationship, we normalized ρ_s by subtracting the bulk gas density (0.02) and then divided by the difference between bulk liquid and gas density, so that the normalized ρ_s ranges between 0 and 1. E_0 is also normalized by the lateral interaction energy E_A. The average fitting error (defined in the same way as in Chapter 4) between LBM and LDFT results is 0.088. In 3D cases, we observed a positive correlation between ρ_s and E_0, which is contrary to our findings using D2Q9 LBM models in Chapter 4. We attribute such conflicts to the lattice structure, the difference in the EOS and forcing scheme, and the way relative pressure is defined. This is not to claim that 2D results are not credible, but different correlations should be used for 2D and 3D lattices. The correlation between $(\rho_s - \rho_g)/(\rho_l - \rho_g)$ and E_0/E_A can be approximated by a straight line passing the origin ($R^2 = 0.99$):

$$\frac{\rho_s - \rho_g}{\rho_l - \rho_g} = 9.415 \frac{E_0}{E_A} \tag{5.8}$$

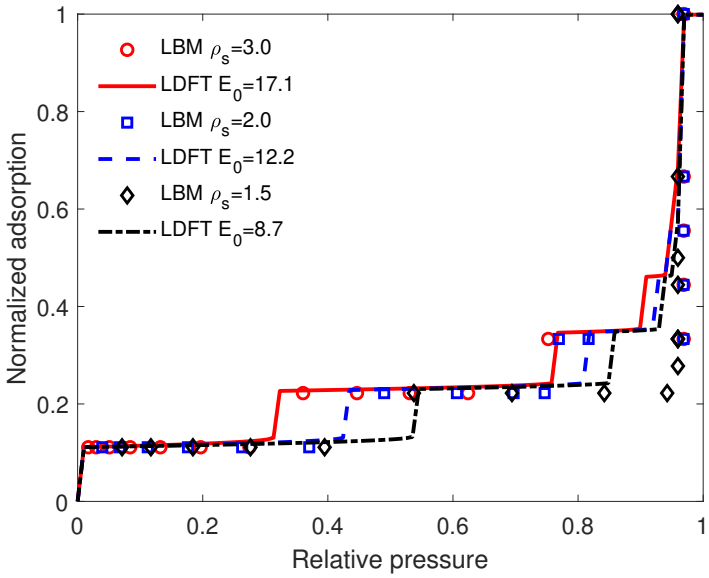

Figure 5.2: LBM simulated nitrogen adsorption curves at 77 K for a slit pore of width 7 nm at three values of solid pseudodensity ($\rho_s = 3, 2, 1$), and LDFT calculations that are fitted to LBM results ($E_A = 1.87$) using different values of E_0 ($E_0 = 17.1, 12.2, 8.7$).

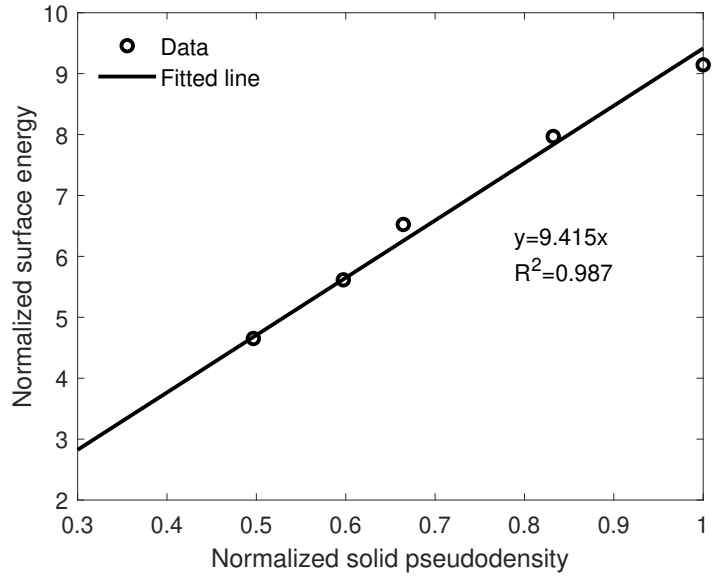

Figure 5.3: Correlation between solid pseudodensity defined in LBM and surface energy defined in LDFT. Note that ρ_s is normalized by subtracting the bulk gas density (0.02) and then divided by the difference between bulk liquid and gas density. E_0 is also normalized by the lateral interaction energy E_A.

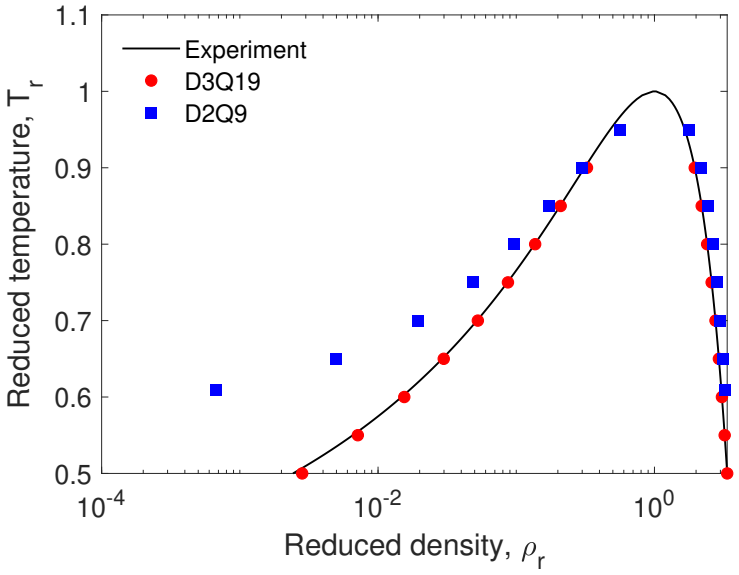

Figure 5.4: Simulated phase envelope of nitrogen/water at a series of reduced temperatures. The results of D3Q19 and D2Q9 models are shown in filled circles and squares respectively, and the experimental data are shown in line. Note that the reported densities here are normalized by the critical densities.

5.4 Model validation

We first show the thermodynamic consistency of our model by reproducing the phase envelope, namely quantifying the equilibrium gas/liquid densities at a series of reduced pressures, in a similar procedure as introduced in Chapter 4. The simulated phase envelope is shown in Fig. 5.4 compared with the result using the D2Q9 LBM model in Chapter 4, and experimental data. Improved thermodynamic consistency is observed by using the combined forcing scheme proposed by Kupershtokh *et al.* [195] (Eq. 5.5), especially at the gas density branch.

We then test the capability of the model to reproduce the physical phase interface and surface tension, which is typically done by running the so-called 'bubble test' [195]. In the test, a series of spherical liquid droplet of increasing radius are initiated at the center of a cubic domain surrounded by the gas phase at $T_r = 0.6$. The gas and liquid density and the corresponding liquid droplet radii were recorded after the system reaches equilibrium. The equilibrium pressure difference between the gas and liquid phase, which is the capillary pressure P_c, can be calculated using mKM EOS. The plot of P_c and equilibrium liquid droplet radii is shown in Fig. 5.5. A linear re-

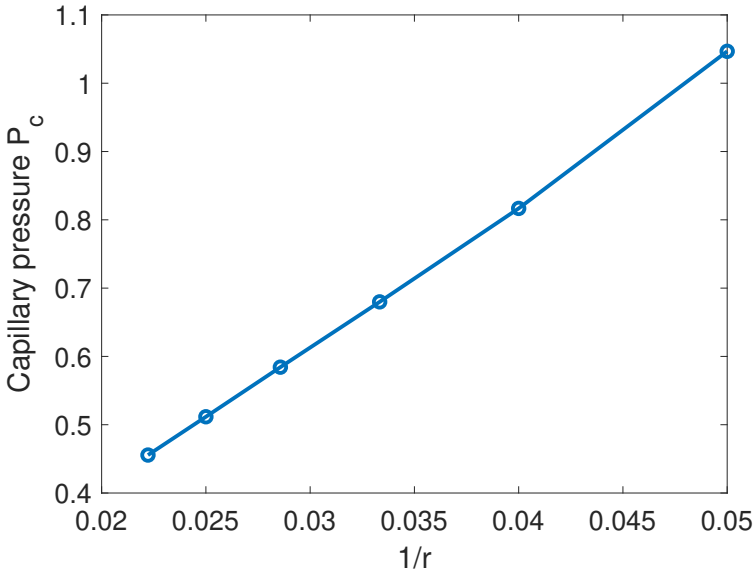

Figure 5.5: Plot of calculated capillary pressure and the reciprocal of the equilibrium liquid droplet radii. The circles are from the simulation and the straight line is fitted to the simulation data. All reported values are in lattice units.

lationship between the two was observed which agrees well with the Young-Laplace equation. The surface tension was then determined to be 10.58.

Furthermore, to demonstrate the reliability of our model in reproducing the adsorbate density distributions in both regular and irregular geometries, we simulated argon adsorption and desorption at 87 K ($E_A = 1.4$) in an open slit pore and semi-closed slit pore (pore width = 3 nm, length = 20 nm). For the open slit pore, 10 layers of pore space nodes were added to the two boundaries respectively and periodic boundary conditions were used to introduce the finite length effect. For the semi-closed slit pore, 10 layers of pore space nodes were added to the open boundary to minimize the influence of the closed boundary on the open side of the pore space. We carefully calibrated the parameters used in LBM with GCMC simulations with the same setup conducted by Fan *et al.* [14]. The lattice resolution was set to be 0.4 nm/lu (molecular diameter of argon). The solid-fluid interaction energy E_0 is calculated by integrating the vdW forces between an infinite 2D solid basal plane and a fluid molecule of distance z from the plane, based on the parameters from

GCMC simulations following the Bojan-Steele equation [206, 207]:

$$E_0(z) = 2\pi\rho\epsilon_{gs}\sigma_{gs}^2\left[\frac{2}{5}\left(\frac{\sigma_{gs}}{z}\right)^{10} - \left(\frac{\sigma_{gs}}{z}\right)^{4}\right], \tag{5.9}$$

where z is the distance of the gas molecule from the plane and since we only focus on the nearest neighbor interaction, z is taken as the lattice resolution (0.4 nm). ρ is the in-plane density of carbon atoms ($0.0262\ \mathrm{nm}^2$) and ϵ_{gs}, σ_{gs} are the well-depth and size parameters for the gas atom carbon site Lennard-Jones potential, which can be determined by the Lorentz–Berthelot mixing rule with $\sigma_{gg} = \sigma_{ss} = 0.34$ nm, and $\epsilon_{gg}/k = 119.8$ K, $\epsilon_{ss}/k = 28$ K. E_0 was then calculated and normalized with regard to the Lennard-Jones potential of argon atoms interaction (E_A), and we get $E_0/E_A = 8$ in this case, corresponding to $\rho_s = 2.5$ based on Eq. 5.8 which was then used in our LBM calculations.

Adsorption simulation was conducted by gradually increasing the system density by a factor of 2×10^{-5} at each time step as introduced in Section 5.3. For desorption simulation, the pore space of the system was initiated with a uniform liquid density (3). Reduction of the system density by a same factor of 2×10^{-5} was conducted at each time step to mimic the gradual drawing-down of the pressure. Pseudosteady state was again assumed for such a small pressure variation and the density profile was recorded every 10,000 time steps until the average density reaches the bulk gas density.

The simulated adsorbate density profiles along the sorption processes for the two slit geometries are shown in Fig. 5.6a and 5.6b. The results are in qualitative agreement with GCMC simulation results by Fan *et al.* [14] (see Fig. 5.8). Moreover, the simulated sorption curves as shown in Fig. 5.7 are in quantitative agreement with GCMC results (see Fig. 5.8). For the semi-closed slit pore, capillary condensation initiates at the corners where solid confinement and surface force is the largest. After the gas/liquid interface from the two corners merges, a constant curvature meniscus is formed, extending to the open boundary. For the open slit pore, condensation accumulates along the two separate planes until the two opposite interfaces bridge, forming two constant curvature meniscus which are drawn to the open boundaries. Because of the change in the curvature of the meniscus during adsorption and desorption process, we observed considerable hysteresis for the open slit pore. On the other hand, there is negligible hysteresis for the closed slit pore since the meniscus does not change shape during the adsorption and desorption processes.

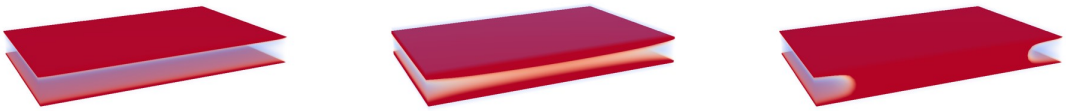

(a)

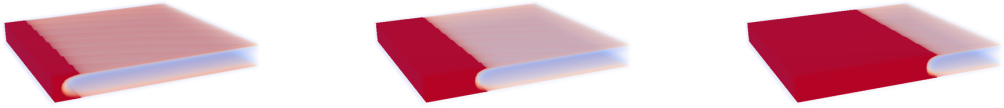

(b)

Figure 5.6: Evolution of density profile during the adsorption process for (a) an open slit pore and (b) semi-closed slit pore. The adsorbed/condensed phase is shown in red. The visualization was done using ParaView software.

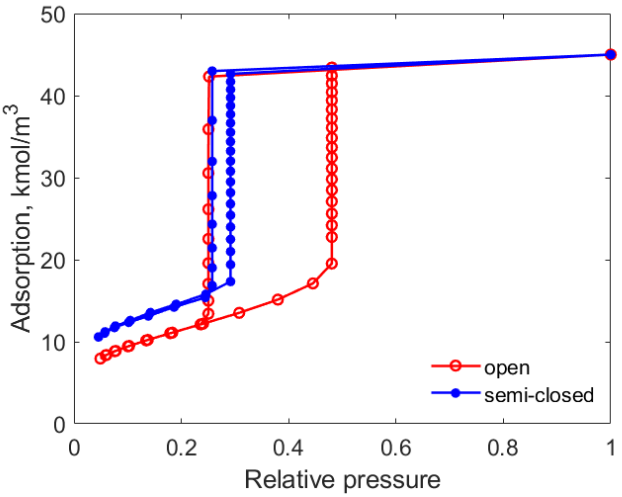

Figure 5.7: Simulated argon adsorption and desorption curves at 87 K for an open and semi-closed slit pore with pore width = 3 nm

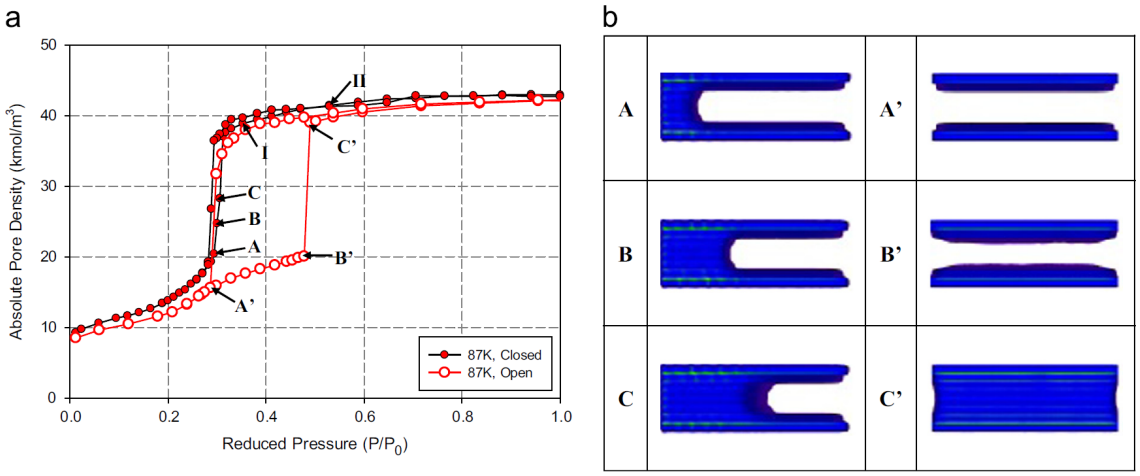

Figure 5.8: GCMC simulation results by Fan *et al.* [14] of argon adsorption and desorption at 87 K for an open and semi-closed slit pore with pore width = 3 nm and pore length = 20 nm. (a) Sorption hysteresis curves. (b) Density profiles of the adsorbed phase at three adsorption stages for the semi-closed slit pore (A, B, C) and open slit pore (A', B', C'). The figure is reproduced from Fan *et al.* [14].

5.5 Shale pore systems reconstruction

Here we use a 3D subset ($200 \times 200 \times 200$ voxels) of the Finney sphere packing [133, 197] for a simplified reconstruction of the interP and intraP pore systems in shale, as we did in Chapter 4. For interP pores, grains are simplified as spheres of equal size, and pore spaces exist between them (Fig. 5.9a). For intraP pores, we invert the solid and pore spaces of interP pore system and dilate the spheres several times so that they form a connected and spongy structure as is commonly observed in OM pores [19] (Fig. 5.9b). We set the lattice resolution to be 0.4 nm/lu, which is approximately the hard sphere diameter of nitrogen molecules in order to correlate explicitly with LDFT.

We conducted a routine pore structure analysis of the two pore systems. Porosity and specific surface area (solid surface voxels normalized by total solid voxels) were calculated. A 3D watershed algorithm available in ImageJ software was used to identify individual pores, and the equivalent pore radii was calculated based on the Euclidean distance map. The corresponding incremental and cumulative PSD are shown in Fig. 5.10. The calculated pore space statistics are shown in Table 5.1.

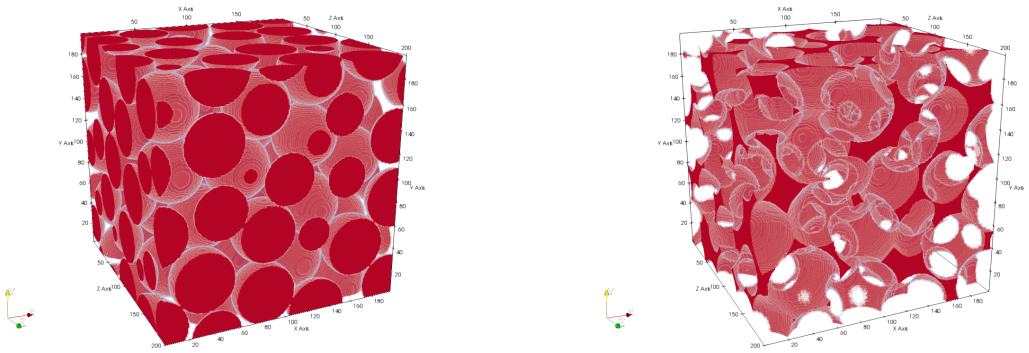

(a) InterP pore system

(b) IntraP pore system

Figure 5.9: Reconstruction of two types of pore systems in shale using a subset of 3D Finney sphere packing. Solids are in red. The slight difference in solid color is due to shading when visualizing using the ParaView software.

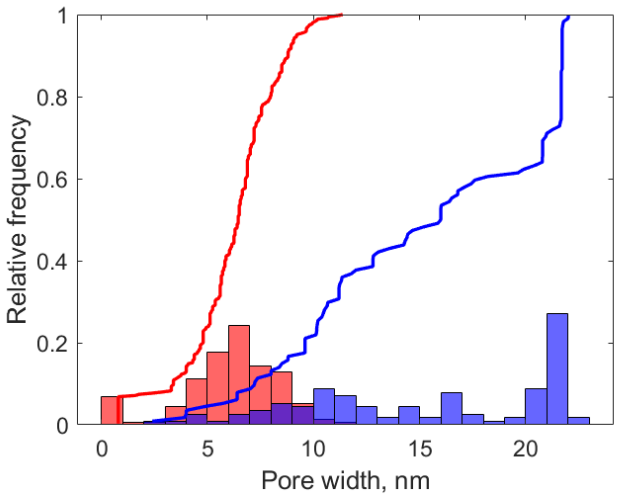

Figure 5.10: Incremental and cumulative PSD of the reconstructed interP and intraP pore systems

Table 5.1: Pore structure statistics of the interP and intraP pore systems

Pore structure statistics		interP pore system	intraP pore system
Pore size, nm	mean	6.15	15.25
	min	0.80	2.40
	max	11.37	22.01
	std	2.20	5.83
Porosity		0.37	0.83
Specific surface area		0.17	0.46

5.6 Results and discussion

5.6.1 Sorption hysteresis in interP and intraP pores

The simulated nitrogen adsorption and desorption curves for the interP and intraP pore systems are shown in Fig. 5.11. To visualize the adsorption process, we also show both 3D and 2D slices of nitrogen density profiles at 3 adsorption stages ($P_r = 0.20, 0.57, 0.65$, labeled as point A, B, and C) and their counterparts (same relative pressures) during the desorption process (labeled as A$'$, B$'$, and C$'$) in Fig. 5.12 to 5.15. As shown in the normalized sorption curves, the interP pore system has higher monolayer adsorption capacity because of the larger surface area to volume ratio due to smaller pore sizes. At middle range of relative pressures ($P_r = 0.2 - 0.6$), the adsorption uptake for the interP pore system increases smoothly because of the successive capillary condensation that occurs at the narrow grain contact regions as a result of the strong solid confinement (see Fig. 5.12 A1 and B1). However, adsorption uptake for the intraP pore system does not change much due to relatively larger pore sizes which prevents the merging and growing of the randomly nucleated condensed phase on the solid surface (see Fig. 5.14 A2 and B2). As pressure further increases, the condensed phase forms quasi-spherical interfaces to minimize the interfacial energy. Up to this point, the adsorption uptake is not only a function of the equivalent pore size, but also highly dependent on pore shape and the connectivity of the adsorbed phase. Obviously, due to the complex pore structure of the porous medium, the adsorption no longer accumulates uniformly along the solid surfaces, therefore conventional adsorption theories developed for a simple pore shape have limited applicability in such cases. Bulk capillary condensation happens at higher relative pressure (around

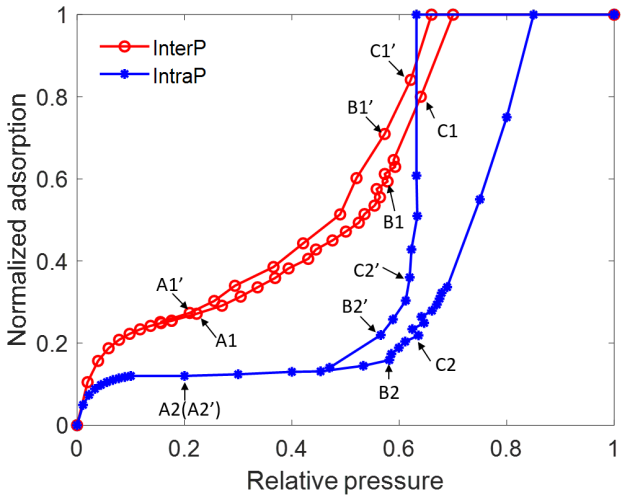

Figure 5.11: Simulated nitrogen adsorption and desorption curves for the interP and intraP pore systems. The 2D and 3D density profiles at the numbered points are shown in Fig. 5.12 to 5.15

0.85) for intraP pore system. Although the convex curvature of the pore space might facilitate the adsorption process to some extent [208], our simulation shows that pore size has a larger effect on capillary condensation. During the desorption process, delayed release of the condensed phase (hysteresis) is observed for both pore systems at regions labeled in the yellow dotted boxes in Fig. 5.12 to 5.15. The intraP pore system shows more significant hysteresis, which is not related to the connectivity of the pore space in this case since both pore systems are very well connected. This indicates that the sorption hysteresis we observed is dominantly controlled by the pore shape, with higher curvature (more convex) of the pore space leading to larger hysteresis. The shapes of the sorption hysteresis curves for interP and intraP pore systems resemble type H5 and H2(a) as defined by IUPAC [5], which indicates that the measured nitrogen sorption curves at 77 K can be used to distinguish the dominant pore system in shale.

5.6.2 Error and uncertainty assessment

By extending the 2D LBM developed in Chapter 4 to 3D, more realistic pore structure can be used to generate more physical sorption simulation results. In this case, surface tension is very well defined and validated against Young-Laplace equation. Much smaller density increment is used in this study to model the adsorption process since the codes are efficiently parallelized for optimal

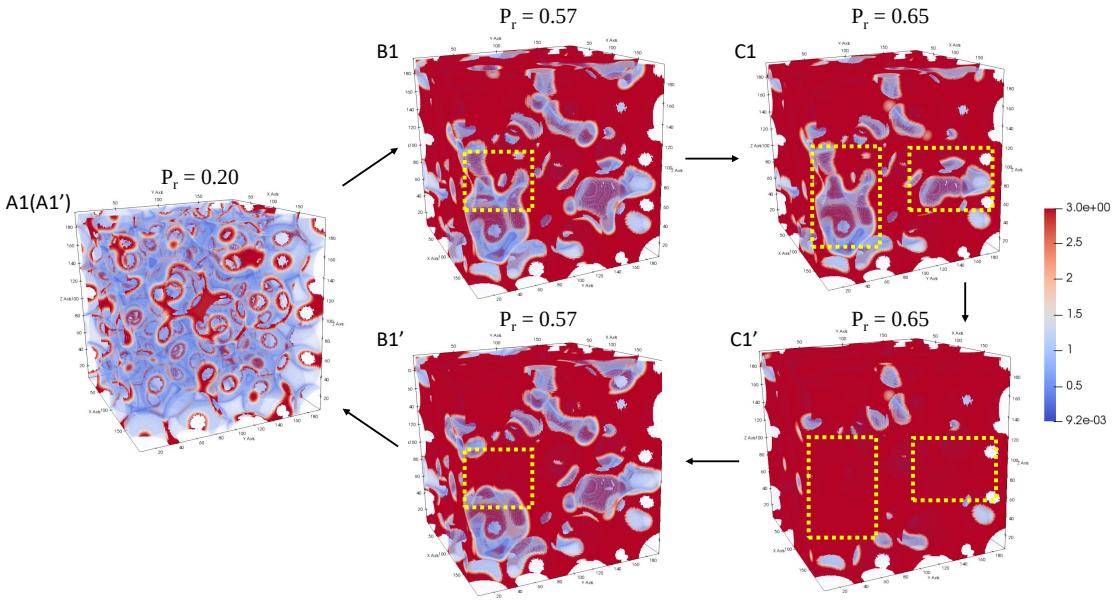

Figure 5.12: The evolution of 3D nitrogen density profile for interP pore system. The upper track shows the adsorption process and the lower track shows the desorption process. Regions where trapping of the condensed phase occurs during desorption are labeled in the yellow dashed boxes.

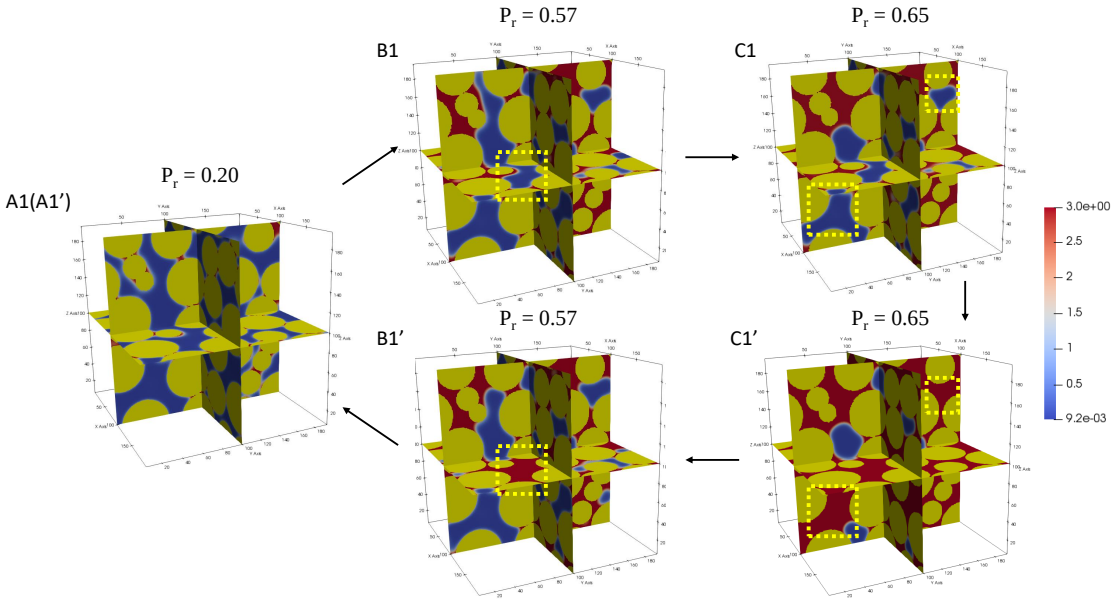

Figure 5.13: Three 2D orthogonal slices extracted from the 3D density profiles shown in Fig. 5.12. The upper track shows the adsorption process and the lower track shows the desorption process. Regions where trapping of the condensed phase occurs during desorption are labeled in the yellow dashed boxes.

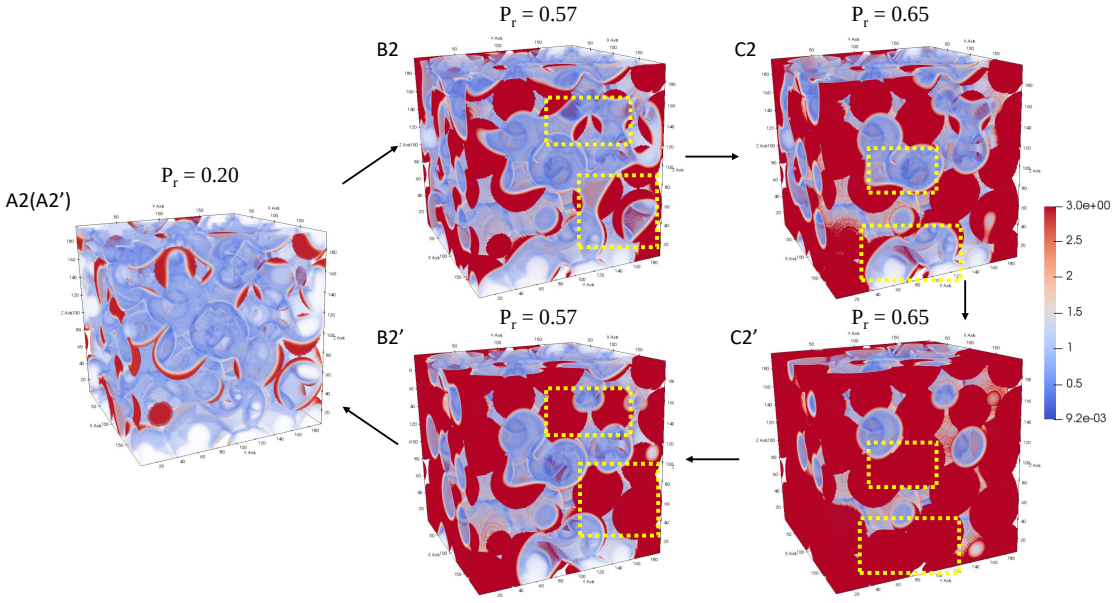

Figure 5.14: The evolution of 3D nitrogen density profile for intraP pore system. The upper track shows the adsorption process and the lower track shows the desorption process. Regions where trapping of the condensed phase occurs during desorption are labeled in the yellow dashed boxes.

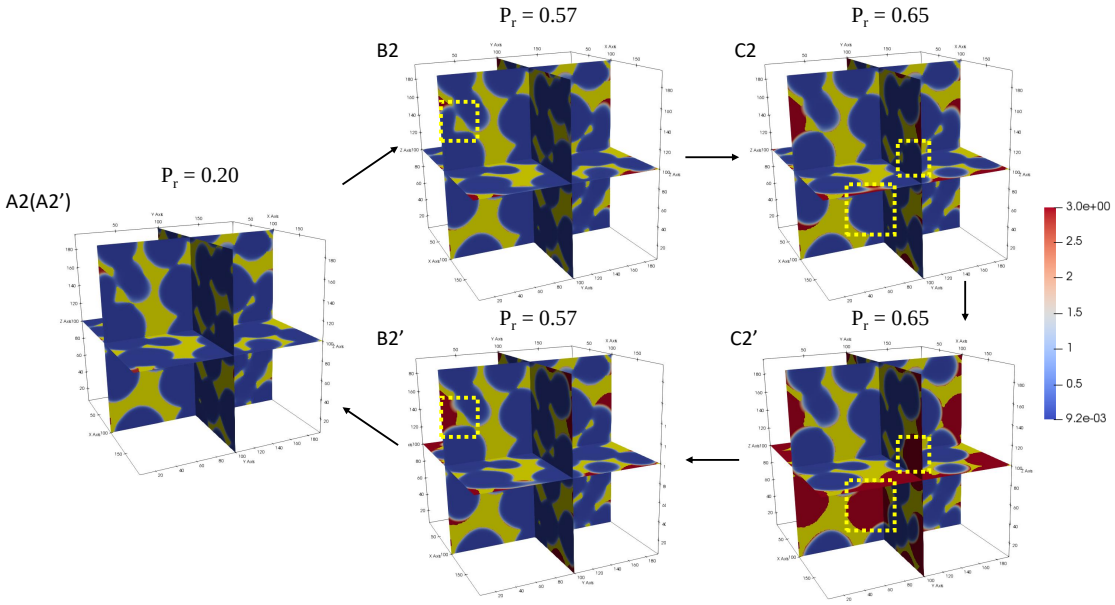

Figure 5.15: Three 2D orthogonal slices extracted from the 3D density profiles shown in Fig. 5.14. The upper track shows the adsorption process and the lower track shows the desorption process. Regions where trapping of the condensed phase occurs during desorption are labeled in the yellow dashed boxes.

computational performance, therefore thermodynamic equilibrium is more likely to be reached in 3D simulations than 2D at each time step. Furthermore, better thermodynamic consistency is observed compared with the 2D model, especially for the gas density. Validation against GCMC on irregular geometries shows that the 3D LBM used in this study could accurately reproduce the correct physics, and therefore could supplement GCMC calculations in much larger domain sizes. Possible error and uncertainty associated with this model include the determination of the bulk pressure by averaging the gas density, identification of the phase interface based on simple thresholding of the density profile, and the representativeness of the simulations at the REV scale.

5.7 Conclusions

In this study, we extended the improved forcing scheme (EDM) proposed by Kupershtokh *et al.* [195] in 2D to 3D using a LBGK D3Q19 LBM model. A weighted average of mean-value and local approximation of the interparticle forces proposed in [195] with incorporation of mKM-EOS was found to result in better thermodynamic consistency than the D2Q9 model discussed in Chapter 4. Similar form of the surface force as introduced in Chapter 4 was applied to the D3Q19 model, which was calibrated again with LDFT and validated against GCMC simulations for the first time. Two types of pore systems that are commonly observed in shale, namely the interP and intraP pores were constructed in 3D by extracting/modifying a subset of the Finney packing of spheres, similar to what was shown in Chapter 4 where we used 2D slices of the 3D geometries. Both the adsorption and desorption processes were simulated and nitrogen sorption hysteresis were successfully reproduced. For interP pore system, a smooth adsorption curve is observed due to a wider range of pore sizes spanning from mesopores to macropores. However, the final capillary condensation pressure is slightly higher as a result of the concave curvature of the pore space which delays the adsorption process. Moreover, the shape of the hysteresis loop is highly dependent on the pore shape, with convex curvature of the pore space resulting in larger hysteresis. Type H5 and H2(a) hysteresis loops as defined by IUPAC are observed for interP and intraP pore systems respectively, which indicates that the experimentally measured nitrogen sorption curves could help distinguish between interP dominated or intraP dominated pore systems in shale. Furthermore, the

desorption process is not only qualitatively similar to the drainage process, but also has been shown to correlate with capillary pressure curves quantitatively [28]. Therefore, desorption simulations can be used as an alternative and more efficient way of estimating drainage behavior, for which typically a two-component LBM model with two explicit sets of particle distribution functions is used, limited by the low density ratio for stability considerations as well as the high computational cost doubling the work compared with our single-component LBM model.

In this study we set constant pseudo-density of the solid for the two pore systems since we focus on the effect of pore structure on sorption behavior. In reality, however, due to the difference in diagenesis and mineralogy compositions, it is highly likely that the surface properties of the pore systems are inhomogeneous. Usually, shale exhibits mixed pore types and mixed wettability, leading to complex fluid distributions and connections. The effect of surface wettability on sorption behavior will be studied in the next chapter. Moreover, we are aware that the simplified sphere packing geometry might not be representative of the complex pore structure in shale. Advanced 3D imaging techniques such as nano-CT [78] and FIB/BIB SEM [79, 209] have been used for more realistic reconstruction of the nanoporous media. A more realistic 3D reconstruction of the clay structure in a shale sample based on BIB-SEM image analysis will be used for water sorption study and flow simulations in the next chapter.

Chapter 6: Effect of wettability on water adsorption, distribution, and resulting methane flow properties in clay [1]

6.1 Introduction

Fine-grained sedimentary rocks such as shale and mudstone account for about 2/3 of the total sedimentary rocks in mass on Earth [210]. The understanding of hydraulic conductivity or seal capacity of such rocks has applications in shale gas production [3], carbon capture and sequestration [211], and nuclear waste disposal [212]. Yet it remains a challenging problem which requires characterization of these tight porous media at multiple scales. Clay minerals are abundant in such rocks, characterized by a lamellar structure and dimensions smaller than a micron, giving rise to nanometer scale pore size and large specific surface area [32]. Permeability measurements at the core and regional scales consistently show that the increase in clay content could result in up to eight orders of magnitude of decrease in permeability [210]. For shale or mudstones that are rich in clay minerals, their permeability is largely controlled by the pore size and connectivity of clay pore structures. As reviewed in Chapter 2, because of the negatively charged surface as a result of cation exchange, clay particles are usually associated with water, either in the form of CBW or capillary-bound water. The thickness of the water layers is a function of clay mineral type, CEC, salinity of the formation water, relative humidity, and stress conditions [210]. The presence of partially-saturated water affects the adsorption capacity of methane, which is the main component of shale gas [213, 214], and reduces the flow capacity [215]. Therefore, understanding the microstructure of clay, and the quantity, distribution, and connectivity of connate water in clay is essential for hydraulic properties estimation.

Clay minerals are commonly associated with unsaturated water with varying in-situ saturations. CBW and capillary-bound water are the main components of the connate water in clay, due

[1] This chapter is currently under preparation for publication.

to the dominance of micropores and mesopores. Therefore, majority of the water in clay is immobile at normal capillary pressure conditions. Common ways of determining the amount of CBW or capillary-bound water and size of the pores these water reside in have been critically reviewed in Chapter 2. The major limitation of available methods is that although the volume/mass of water can be determined, the spatial distribution and connectivity is not very well characterized, nor is the effective PSD and connectivity of the remaining pore space, both of which significantly affect the subsequent methane flow capacity.

The surface properties of clay can also be very complex, characterized by a surface wettability distribution. Clay minerals are commonly covered by a thin film of water under in-situ conditions, making them preferentially water-wet. On the other hand, the presence of asphaltene and natural polar components (acids and bases) soluble in heavy hydrocarbons or kerogen might alter the surface wettability of clay to oil-wet [216], despite the presence of a thin film of water on clay surfaces [217]. Ionic and colloidal interactions are two main mechanisms for wettability alteration with the presence of water films. Adsorption by acid/base and ion binding interactions can create a wide range of wetting conditions, and the wetting outcome of ionic interactions depends on the compositions of oil, brine, clay, as well as on temperature and aging time [218]. colloidal interactions through precipitation of asphaltene from crude oil can also contribute to wettability alteration, which depends on pressure, temperature, and oil composition [217,218]. Water adsorption experiments have been used to determine the surface wettability of different minerals at dry or wet conditions before and after wettability alteration using stearic acid, N, N-dimethyldodecylamine and asphaltene, and the larger the area under the measured adsorption curve, the more water-wet the surface is [216]. The presence of a water film on quartz and kaolinite surfaces was found to enhance the adsorption of stearic acid and N, N-dimethyldodecylamine, thus making the surfaces more water-nonwet than dry surfaces, but reduces asphaltene adsorption [216]. Micro-CT evidence of wettability alteration in clay-rich sandstone is emerging as well, and clay and calcite are found to be preferentially altered to an oil-wet state after treated with crude oil (private communication with G. Garfi and S. Krevor of Imperial College London, paper in review). Fig. 6.1 shows three SEM images where different wettability conditions are directly observed for clay minerals. For pure clay

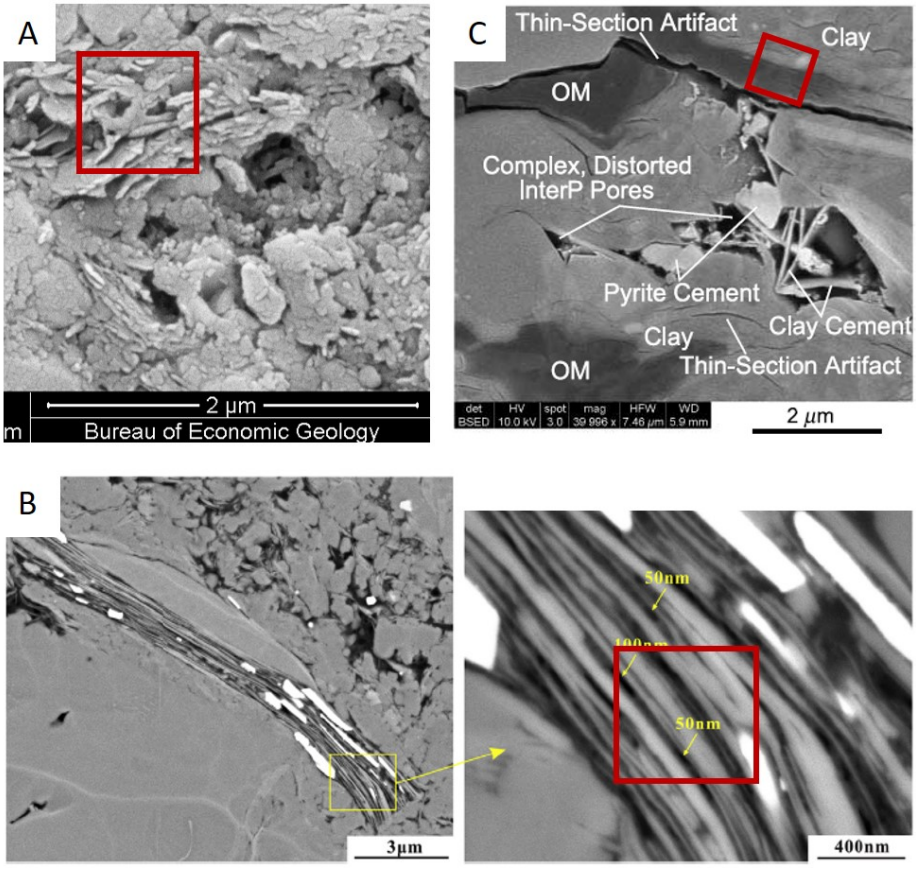

Figure 6.1: SEM images of clay particles that correspond to three wettability conditions which will be used in water adsorption simulations. (A) Water-wet clay (Case 1) which is most commonly observed; (B) Water-nonwet clay that is associated with OM; (C) Mixed-wet clay where a sharp interface between the wetting and nonwetting zones can be observed. The regions outlined in red boxes are of the same size as our simulation domain in 2D (600^2 nm^2) which will be discussed in Section 6.4. (A) is reproduced from Landry *et al.* [15]. (B) is reproduced from Tang *et al.* [4], and (C) is reproduced from Loucks *et al.* [1].

minerals as shown in Fig. 6.1 (A), they are naturally water-wet in the absence of hydrocarbon deposits. On the other hand, as show in Fig. 6.1 (B), clay platelets might be modified by OM, making their surface water-nonwet. Less commonly observed as is shown in Fig. 6.1 (C), clay minerals are partially occupied by OM, with a sharp interface between the water-wet and water-nonwet regions, creating a mixed-wet surface condition. It is not very well understood how the inhomogeneous wettability of clay surfaces affects the water adsorption, distribution, and subsequent methane flow capacity.

The hydraulic conductivity of clay materials has been studied extensively. Neuzil [219] compared the laboratory-derived permeability versus porosity for a variety of natural argillaceous

media, ranging from recently deposited marine clays to mildly metamorphosed argillite, and found that a log-linear relation between permeability and porosity exists over a wide range of consolidation states. Further comparison with field data with permeability and porosity estimated from inverse analysis shows striking agreement, which indicates that permeability in argillaceous media is scale independent up to kilometer scale. Therefore, the flow capacity is largely controlled by the low permeability units observed at the core scale. Vangpaisal and Bouazza [17] conducted a series of gas permeability tests on four partially hydrated geosynthetic clay liners. They found that the gas permeability decreased as gravimetric moisture content and volumetric water content increased, with variation of up to 5–7 orders of magnitude for the conditions investigated. The differences in clay structures and the form of bentonite (granular or powdered) have a significant effect on the variation of gas permeability. Experimental data on permeability measurements of clay are limited with regard to the parameter spaces explored (*e.g.* porosity, water saturation, clay types, surface chemistry), and are sensitive to minute artifacts as a result of the low permeability [220–222]. Therefore, microscale models are often used to explore the hydraulic and mechanical properties of clay.

Bayesteh and Mirghasemi [223] studied the microstructural alteration of clay particles under confining stress using a discrete element method (DEM) approach, considering the mechanical force, diffuse double-layer repulsion, and vdW attraction as the inter-particle interactions. Water-saturated permeability was calculated and DEM results were shown to agree well with experimental data. However, only fully water-saturated media were considered and the clay particles were assumed to be suspended in the solution. Furthermore, MD or Monte Carlo simulations on pairs of clay particles in liquid water [224–227] or coarse-grained simulations with interparticle interaction potentials derived from MD simulations or DLVO theory [228–230] have been used to understand the clay-swelling behavior and the resulting alteration of microstructure and hydraulic properties. Most of these simulations focused on completely water-saturated state, which might not represent the in-situ water saturation. Very few studies have attempted to model the pore scale distribution of water at under-saturated conditions while honoring the actual complex clay pore structure, and to study the resulting gas hydraulic properties as a function of water saturation.

In this study, we used the D3Q19 LBGK LBM model incorporated with mKM EOS intro-

duced in Chapter 5 to study the adsorption, condensation, and distribution of unsaturated water in clay, which has not been probed before using LBM. We first investigated the effect of surface wettability on water adsorption in a 3D clay microstructure reconstructed based on BIB-SEM images analysis. Three wettability conditions were explored including completely water-wet, completely water-nonwet, and mixed-wet. The distribution, size, and connectivity of the water/vapor phases at different saturation stages were studied and compared in detail. This is the first time that microscale distribution and connectivity of the unsaturated water have been studied and visualized using LBM on an image-based 3D reconstruction of clay pore structure with consideration of complex surface wettability.

A MRT LEV D3Q19 LBM model developed by Landry *et al.* [9] was then used to study supercritical methane transport in the reconstructed clay pore structure with the presence of unsaturated water and complex surface wettability. In this model, nanoscale flow physics were incorporated including second-order slip BC to capture the slip velocity near the wall. The novelty of this model was the consideration of local viscosity variation as a function of the local distance to the pore wall, which has been shown to be able to capture flow within the Knudsen layer [9]. Here we took advantage of this MRT LEV D3Q19 LBM model to calculate the velocity field and apparent permeability of supercritical methane flow and compared the simulation results (gas relative permeability curve) to available experimental data measured on clay. In this work, LBM was used as a novel tool to study thermodynamic and hydrodynamic behavior consistently, without having to switch methods, thus avoiding cumbersome mesh regeneration, parameters recalibration, and results reinterpretation.

6.2 Numerical methods

6.2.1 Water adsorption modeling using LBGK D3Q19 LBM model

The LBGK D3Q19 LBM model incorporated with mKM-EOS as introduced in Chapter 5 was used in this study to model water adsorption at reservoir temperature (400 K). Since water and nitrogen sorption occurs at similar reduced temperature ($T_r = 0.61$), we follow the same sorption

modeling methodology as introduced in Chapter 5. In the simulation, the pore spaces are initialized with a uniform density of 0.5 (all the parameters hereafter are in lattice units unless specified otherwise). The adsorption process is simulated by gradually increasing the system density by a fraction of 2×10^{-5} until bulk condensation occurs when the average density of the system reaches 3 (liquid water density). The water saturation S_w at each equilibrium state is determined to be the number of liquid water voxels normalized by the number of pore space voxels.

6.2.2 Methane flow modeling using MRT LEV D3Q19 LBM model

For supercritical methane flow modeling, we used the MRT LEV D3Q19 LBM model developed by Landry *et al.* [9]. MRT was preferred over LBGK in this case due to its superior stability over LBGK for at lower values of relaxation times (*e.g.* high Kn flow as expected in micropores and mesopores) [139, 182, 193]. Furthermore, stability issues induced by the high density ratios across the phase interface are not expected for supercritical methane flow simulations, since there will not be phase separation. For MRT LBM models, the relaxation time is not a constant value for all the hydrodynamic moments as in LBGK models. By allowing each hydraulic or kinetic moment to relax at its own rate, MRT models provides more degrees of freedom to tune the relaxation rates for stability purposes, and the computational error and convergence time significantly decrease compared to LBGK models [183]. The governing equation for MRT LBM models is written as:

$$f(\mathbf{x} + \mathbf{e}\Delta t, t + \Delta t) - f(\mathbf{x}, t) = -M^{-1}\hat{S}(m(\mathbf{x}, t) - m^{eq}(\mathbf{x}, t)), \tag{6.1}$$

where $\hat{S}$ is the diagonal collision matrix, $\hat{S} = \text{diag}(s_0, s_1, \ldots, s_N)$, and $s_i (i = 0, 1, \ldots, N)$ is the corresponding relaxation rate. m are the moments converted from the distribution functions f by a transformation matrix M, and $m = Mf$. The transformation matrix M is determined by orthogonalizing the polynomials of the velocity vectors by the standard Gram–Schmidt procedure, and the detailed expression can be found in [183]. for the D3Q19 lattice, the moment space m is defined to be:

$$|m\rangle = (\rho, e, \varepsilon, j_x, q_x, j_y, q_y, j_z, q_z, 3p_{xx}, 3\pi_{xx}, p_{ww}, \pi_{ww}, p_{xy}, p_{yz}, p_{xz}, m_x, m_y, m_z)^T, \tag{6.2}$$

where ρ is the mass density, e is the kinetic energy, $\varepsilon = e^2$, j is the momentum, q is the energy flux, p and π are the viscous stress tensors, and m is a third-order moment. The equilibrium expressions for these moments and the expression for the transformation matrix M can be found in [183]. The diagonal collision matrix $\hat{S}$ is:

$$\hat{S} = \text{diag}(0, s_1, s_2, 0, s_4, 0, s_4, 0, s_4, s_9, s_{10}, s_9, s_{10}, s_{13}, s_{13}, s_{13}, s_{16}, s_{16}, s_{16}), \tag{6.3}$$

and here we use the same relaxation parameters as in [9] which were optimized for stability purposes.

The flow simulation is initiated by applying a pressure gradient of 0.1 MPa/m which is a typical value for shale gas production. This is achieved in LBM simulations by applying a constant external acceleration (4.3556×10^{-11} in lattice units) to the fluid phase. In the simulation, the condensed water phase is assumed to be immobile or has negligible mobility compared to methane, therefore it is treated as a part of the solid phase.

The force arising from the pressure gradient is then incorporated into the MRT LBM model using the forcing scheme proposed by Guo *et al.* by adding an extra forcing term into the governing equation (Eq. 6.1), considering both the discrete lattice effect and the contributions of the body force to the momentum flux:

$$f(\mathbf{x}+\mathbf{e}\Delta t, t+\Delta t) - f(\mathbf{x}, t) = -M^{-1}\hat{S}(m(\mathbf{x}, t) - m^{eq}(\mathbf{x}, t)) + M^{-1}\left(I - \frac{1}{2}\hat{S}\right) m_f(\mathbf{x}, t), \tag{6.4}$$

where m_f is a similar mapping of the discrete force components to the moment space, and $m_f = MF$, where F_i for the ith direction is defined as:

$$F_i = \omega_i \left[\frac{\mathbf{e}_i - \mathbf{v}}{c_s^2} + \frac{(\mathbf{e}_i \cdot \mathbf{v})}{c_s^4}\mathbf{e}_i\right] \mathbf{F}, \tag{6.5}$$

where ω_i is the weighting factor for each velocity direction:

$$\omega_i = \begin{cases} \frac{1}{3} & i = 0 \\ \frac{1}{18} & i = 1, 2, \ldots, 6 \\ \frac{1}{36} & i = 7, 8, \ldots, 18 \end{cases} \tag{6.6}$$

and $\mathbf{F}$ is the external pressure gradient and $\mathbf{F} = \rho\mathbf{a}$, where $\mathbf{a}$ is the resulting acceleration to be input into the simulation, $\mathbf{v}$ is the particle velocity which is defined as:

$$\rho\mathbf{v} = \sum_i \mathbf{e}_i f_i + \frac{\Delta t}{2}\mathbf{F} \tag{6.7}$$

Slip boundary conditions

At the solid nodes, no-slip BC for liquid flow in conventional rocks is achieved by applying simple bounce-back of the particle distribution functions, namely the distribution functions arriving at the solid node are reversed in the direction and streamed back to the incoming nodes [143]. For high Kn flows ($Kn > 0.001$), slip velocity at the wall should be considered which increases the overall permeability in tight rocks. Slip BC in the MRT LEV LBM model is achieved by using a combined diffusive and bounce-back scheme [9]:

$$f_a(\mathbf{x} + \mathbf{e}_a\Delta t, t + \Delta t) = (1 - \sigma) f_a^R(\mathbf{x}_s, t) + \sigma f_a^D(\mathbf{x}_s, t), \tag{6.8}$$

where $\mathbf{x}_s$ is the location of the solid nodes, and σ is a weighting coefficient determined by Chai *et al.* [144] to ensure the second-order accuracy:

$$\sigma = \frac{2C_1}{\sqrt{\frac{6}{\pi} + C_1}}, \tag{6.9}$$

where C_1 is a tuning parameter fitted to the solutions of linearized Boltzmann equation, and $C_1 = 1.11$ [144]. f_a^R and f_a^D are the contributions of bounce-back and diffusive boundary conditions

respectively:

$$f_a^R(\mathbf{x}_s, t) = f_{-a}(\mathbf{x}_s, t), \tag{6.10}$$

$$f_a^D(\mathbf{x}_s, t) = \omega_i' \rho'(\mathbf{x}_s, t), \tag{6.11}$$

where ω_i is the weight of the incoming f_i, and $\omega_i' = \omega_i / \sum_i \omega_i$; $\rho'(\mathbf{x}_s, t)$ is the sum of f_i at the solid node.

Local effective viscosities

For MRT LBM models, the relaxation time s_v defining kinematic viscosity (ν_0) is:

$$\nu_0 = \frac{1}{3}\left(\frac{1}{s_v} - \frac{1}{2}\right) \tag{6.12}$$

The unbound kinematic viscosity of a gas is related to its unbound mean free path (λ_0):

$$\lambda_0 = \nu_0 \sqrt{\frac{3\pi}{2}} \tag{6.13}$$

Therefore, s_v can be written as a function of mean free path λ_0:

$$s_v = \left(\frac{1}{2} + \sqrt{\frac{2}{3\pi}}\lambda_0\right)^{-1} \tag{6.14}$$

For the LEV LBM model used here, the viscosity is defined locally as a function of the corrected mean free path to account for the increasing frequency of gas/wall collisions near the solid boundaries which affects the viscosity of the gas:

$$\lambda_e(\mathbf{x}) = \lambda_0 \Phi(\mathbf{x}), \tag{6.15}$$

where $\Phi(\mathbf{x})$ is the locally defined correction function for the mean free path, which takes the fol-

lowing form according to Landry *et al.* [9]:

$$\Phi\left(\frac{d_i}{\lambda_0}\right) = \left[1 - \exp((d_i + d_{-i})/\lambda_0) + \frac{d_i + d_{-i}}{\lambda_0^2}\exp((d_i + d_{-i})/\lambda_0)\right]\frac{2}{\pi}\tan^{-1} A\sqrt{2}\left(\frac{d_i}{\lambda_0}\right)^B, \tag{6.16}$$

where d_i is the distance of a fluid particle to the wall along the velocity direction i, and A and B are fitting parameters which are tuned during model validation, and were set to $A = B = 1$ according to [9].

Simulation setup

The flow simulations were conduced at 12 MPa and 400 K with a pressure gradient of 0.1 MPa/m representing reservoir conditions. For convenience, the condensed water phase after the adsorption simulation is assumed to be immobile (either in the form of CBW or capillary-bound water). Therefore, it is segmented as a part of the solid phase, and methane only flows within the connected pore spaces that are occupied by the gas phase. Non-periodic boundary conditions are applied in x and y directions by adding a bounce-back solid layer, and two blank layers (full fluid nodes) are added at the inlet and outlet of z direction to minimize the boundary effect, and periodic boundary conditions are applied. The pore system is initialized with methane of uniform density at 12 MPa and 400 K, and external forces are applied to generate a pressure gradient of 0.1 MPa/m. The relevant physical parameters and corresponding values in lattice units are shown in Table 6.1. The simulation is terminated until the velocity variation every 2,000 time steps drops below a certain threshold. The equilibrium velocity profile is then recorded and the average flow velocity in z direction v_z is used to calculate the apparent permeability based on the following equation:

$$v_z = -\frac{k_a}{\mu\phi}\nabla_z P, \tag{6.17}$$

where k_a is the apparent permeability of methane, μ is the bulk dynamic viscosity, ϕ is the porosity, $\nabla_z P$ is the pressure gradient in z direction.

Table 6.1: Simulation parameters of supercritical methane flow in physical and lattice units

Parameter	Symbol	value in physical unit	value in lattice unit
Characteristic length	L	20 nm	10
Mean free path	λ	0.7 nm	0.35
Knudsen number	Kn	0.0175	0.0175
Kinematic viscosity	ν	$2.67 \times 10^{-7}\ \mathrm{m}^2/\mathrm{s}$	0.4843
Time	t	7.255×10^{-12} s	1
Methane density	ρ_g	$60.7\ \mathrm{kg}/\mathrm{m}^3$	0.95
Pressure gradient	ΔP	0.1 MPa/m	4.11×10^{-11}

6.3 Model calibration and validation

Here we establish the correlation between ρ_s and contact angle θ for water adsorption on surfaces of different wettability. Macroscopically, after phase condensation occurs, the condensed liquid phase either spreads onto the solid surface or accumulates as a droplet, depending on the wettability of the surface. The contact angle θ is therefore the macroscopic result of microscale solid-fluid interactions. It should be mentioned that unlike nitrogen sorption, water sorption on clay minerals may be affected by the chemisorption process through the formation of hydrogen bonds, and charged surfaces of clay particles may further strengthen the surface forces via electrostatic interactions. Here all these forces are adsorbed into a single parameter ρ_s that determines the strength of surface-fluid interactions, and we attribute all these forces to the macroscopic result of the contact angle of a liquid water droplet residing on the clay surface. Previous studies have defined similar surface force configurations as we used in this study for subcritical fluids to model the wettability effect [137, 231, 232], and it was found that setting ρ_s to the equilibrium liquid density ρ_l leads to completely wetting surfaces (contact angle $\theta = 0^\circ$), whereas setting ρ_s to the equilibrium gas density ρ_g leads to completely non-wetting surfaces (contact angle $\theta = 180^\circ$). Values in between lead to partially-wetting surfaces with finite contact angles between 0° and 180°. However, for SCMP LBM models, the correlation between ρ_s and θ varies in all aspects from the lattice structure, density ratio, EOS used, to the forcing schemes. Therefore no established correlation is available in the literature for our specific LBM model. Herein, we establish such correlation systematically by studying the equilibrium liquid configurations on a flat surface with different wettability (ρ_s). It

should be mentioned that contact angle (or wettability) is the result of setting different values of ρ_s in LBM simulations. Here we aim to find the correlation between ρ_s and θ, so that different wettability conditions can be reproduced by setting corresponding values of ρ_s.

The simulations were initiated by setting up a cubic liquid zone $\rho_l = 3$ surrounded by the gas phase $\rho_g = 0.02$ in contact with a flat solid surface with ρ_s setting to a series of values ranging from 0.5 to 3. Fully periodic BC were used. The simulations were terminated until a stable gas/liquid interface configuration is observed. The resulting 3D configurations of four cases with $\rho_s = 2, 1.5, 1, 0.5$ are shown in Fig. 6.2, and corresponding 2D slices across the center of the equilibrium liquid phase are shown in Fig. 6.3, labeled with corresponding contact angle values determined by image analysis codes available on Github (https://github.com/jesantos/MultiphasePorousMediaPalabos). We observe that larger ρ_s leads to smaller contact angles due to the stronger attractive surface force exerted by the wall. By calibrating ρ_s to contact angle θ using a second order polynomial (see Fig. 6.4), we obtain the correlation shown in Eq. 6.18 ($R^2 = 0.99$). This correlation can then be used to guide the simulation setup based on contact angle measurements on shale core samples (*e.g.* using the sessile drop method).

$$\theta = 19.44\rho_s^2 - 118.5\rho_s + 180 \tag{6.18}$$

Finally, for supercritical methane flow simulations in nanopores, the MRT LEV D3Q19 model we used here was already validated elsewhere against the solutions of linearized Boltzmann equation [9] over a wide range of Kn numbers. Therefore, we do not perform further validations here, and readers shall refer to Fig. 8 in [9] for details.

6.4 Clay pore structure reconstruction

Fig. 6.5 shows a schematic of the typical grain structure of a argillaceous rock. Clusters of clay particles are dispersed between a pack of larger silt grains (*e.g.* quartz, calcite, feldspar). The hydraulic properties of the system is dominated by the microstructure of the clay particles. The zoom-in shows a schematic of the clay platelets structure observed by SEM images, where both

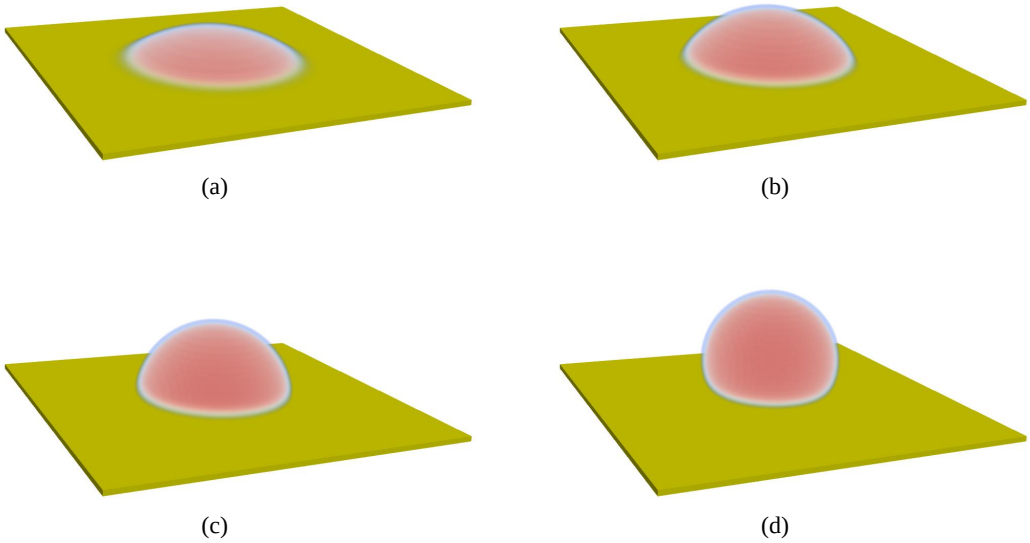

(a) (b)

(c) (d)

Figure 6.2: The equilibrium liquid configurations on a flat solid surface with different wettability (ρ_s) visualized using the ParaView software. The liquid is in red, and the solid is in yellow. (a) – (d) corresponds to $\rho_s = 2, 1.5, 1, 0.5$. Note that completely wetting and completely nonwetting cases are not shown here with $\rho_s = 3$ and 0.018.

micropores (<2 nm) and mesopores (2 – 50 nm) are present as a result of the nonuniform packing of the clay clusters [6]. Here we focus on a cluster of clay platelets between two large grains, which was reconstructed honoring the direct observations of a shale sample via BIB-SEM imaging. The reconstruction was taken from Landry *et al.* [15] and here we present a brief introduction of the reconstruction workflow.

First the shale core sample is prepared for thin section analysis with a field of view of approximately 1.5 in, which is used for targeting regions of interest. Then the core plug is subsampled with guidance from thin-section imaging and prepared for high-resolution SEM imaging by BIB milling. Large-area high-resolution SEM mosaics are acquired, stitched, segmented, and used to measure the pore size and shape characteristics (see Fig. 6.6 and 6.7 for example). Two dominant pore systems (OM and clay pores) are analyzed separately. Here we focus on clay pore system where in-situ water is most likely to reside. A process-based reconstruction process is conducted by placing ellipsoids of different length (assuming constant aspect ratio) and tilt measured by image

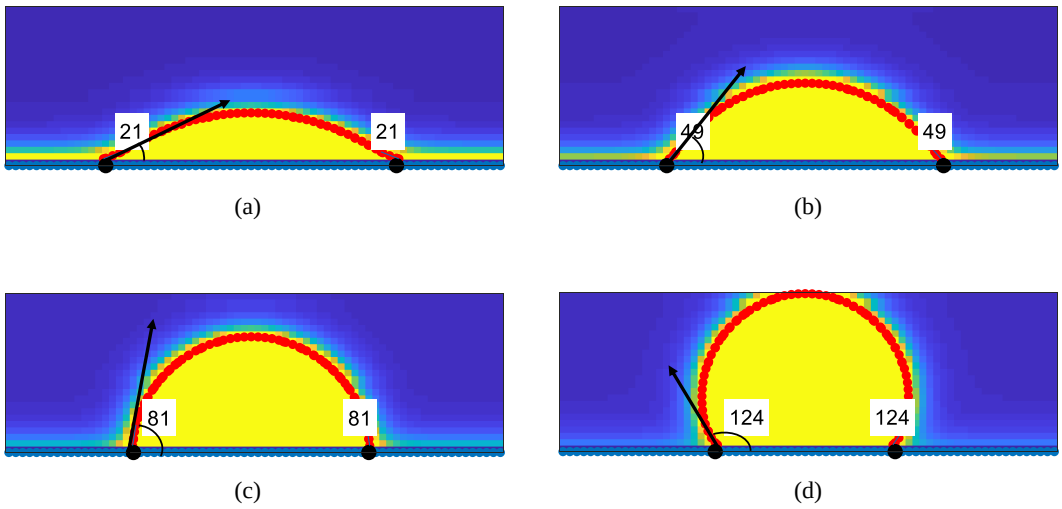

Figure 6.3: 2D slices of the equilibrium liquid/gas density distribution on a flat solid surface with different wettability (ρ_s) and corresponding contact angles determined by image analysis. The liquid is in yellow, and the gas is in deep blue. The bottom layer is the solid. The red dots outline the liquid/gas interface. (a) – (d) corresponds to $\rho_s = 2, 1.5, 1, 0.5$. Note that completely wetting and completely nonwetting cases are not shown here with $\rho_s = 3$ and 0.018.

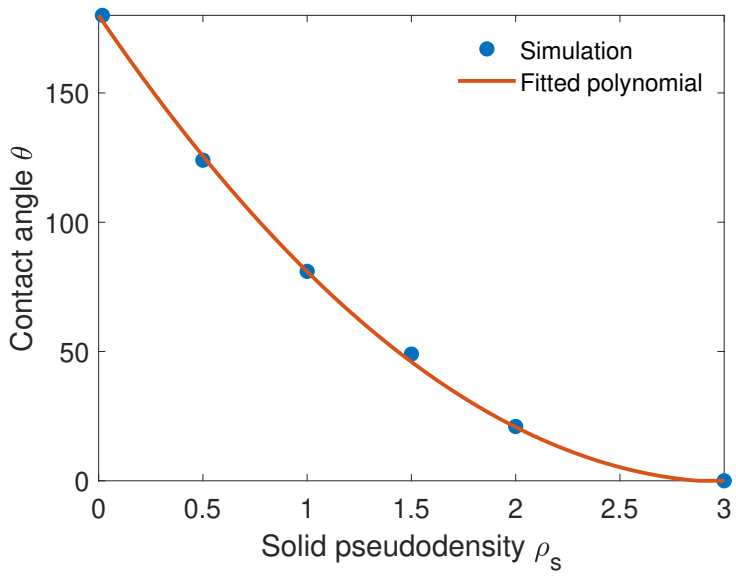

Figure 6.4: Relationship between solid pseudodensity ρ_s defined in LBGK D3Q19 LBM model and contact angle θ as shown in Fig. 6.3.

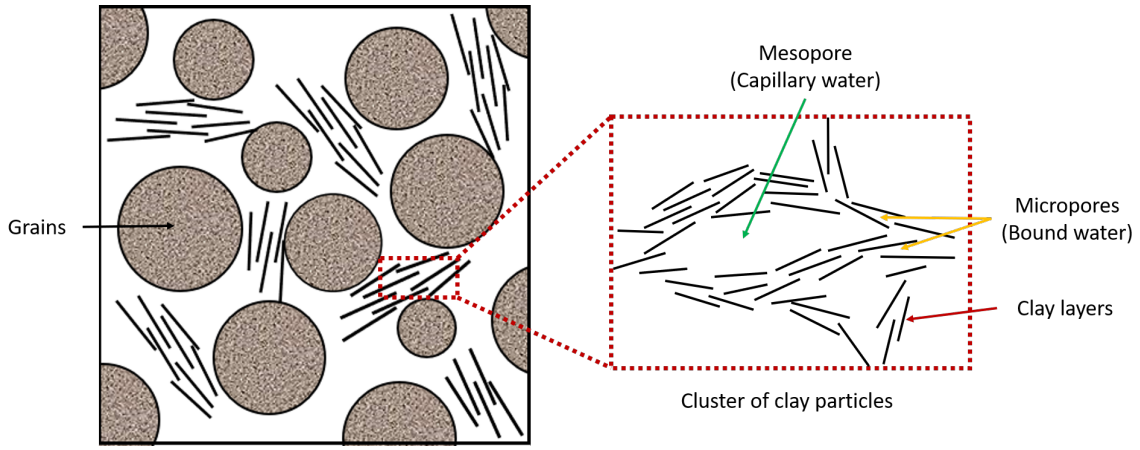

Figure 6.5: Schematic of the shale grain structure in which clusters of clay platelets are dispersed within the interP pore spaces between large silt grains. Also shown is a zoom-in of the clay cluster which shows the existence of both micropores (<2 nm) and mesopores (2 – 50 nm) as a result of the nonuniform packing of the clay platelets.

analysis into a cubic void domain. The ellipsoids are simplified representations of clay platelets. The porosity, pore size and shape distributions measured from BIB-SEM imaging are then compared to those measured from 2D cross-sections of the 3D reconstructions. The parameters of the reconstructions are then tuned to match the 2D pore statistics. This workflow is the first of its kind by calibrating 2D slices of 3D reconstructions to image-based 2D statistics, without having to make certain assumptions of the pore space connectivity. Furthermore, BIB-SEM images at millimeter scale is more likely to achieve REA than FIB-SEM images commonly below 20 μm in size, according to a comprehensive REA/REV study by Kelly *et al.* [79]. The final 3D reconstructions of size 300^3 with lattice resolution of 2 nm/lu and total porosity of 25% is shown in Fig. 6.8, along with three orthogonal 2D slices that show the internal pore structure.

6.5 Results and discussion

6.5.1 Water adsorption and distribution in clay with different surface wettability

We first performed water adsorption and condensation simulations at 400 K (reservoir temperature) within the reconstructed clay pore system using the LBGK D3Q19 LBM model. Three wettability conditions were explored here, including a water-wet case (Case 1) with contact angle

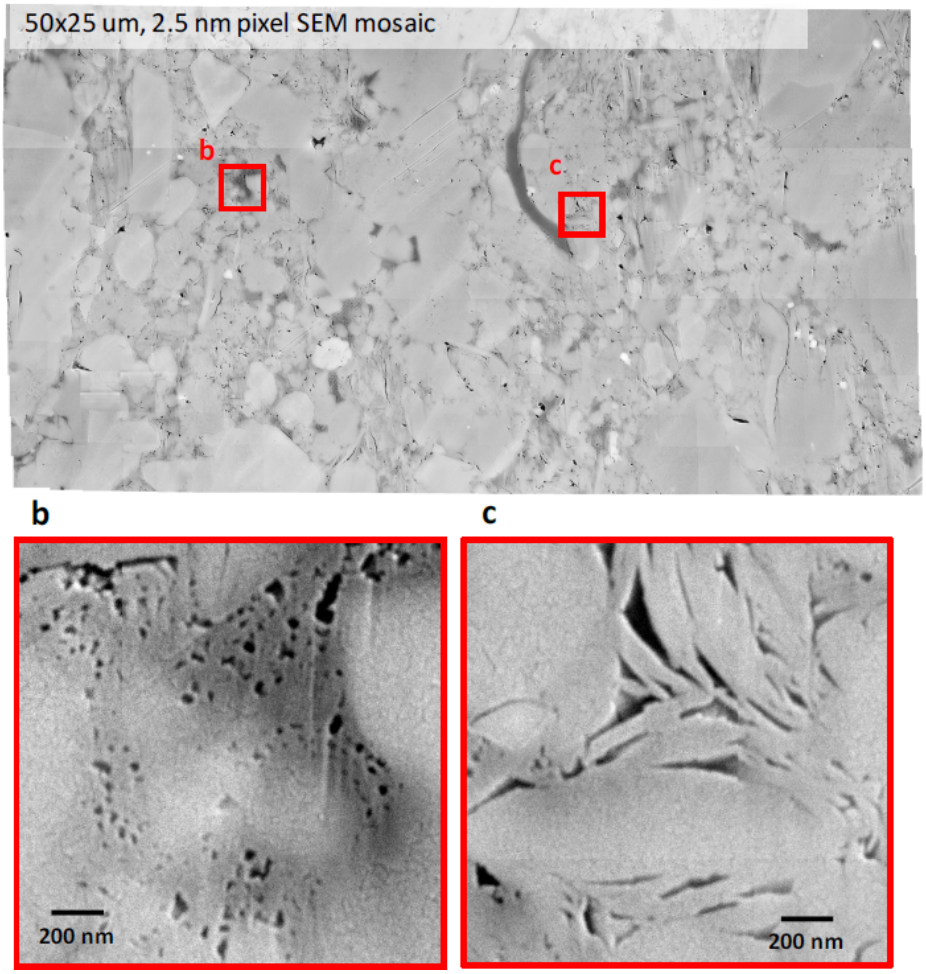

Figure 6.6: The BIB SEM image taken for the shale sample. a) Large-area mosaic with size indicated and two component pore systems, b) OM pores, c) clay pores. The figure is reproduced from Landry *et al.* [15].

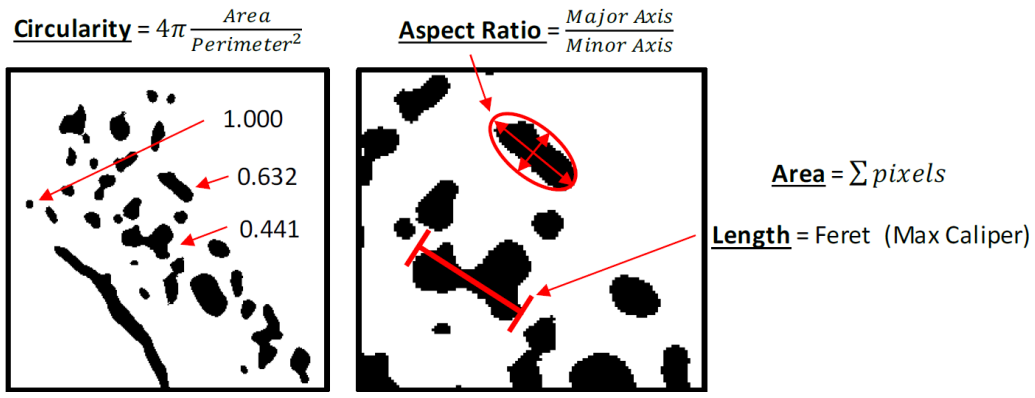

Figure 6.7: Examples of segmented SEM images. Dark spots are pore spaces and white regions are solids. The pore size parameters (area, length) and pore shape parameters (circularity, aspect ratio) are quantified from the segmented images. The figure is reproduced from Landry *et al.* [15].

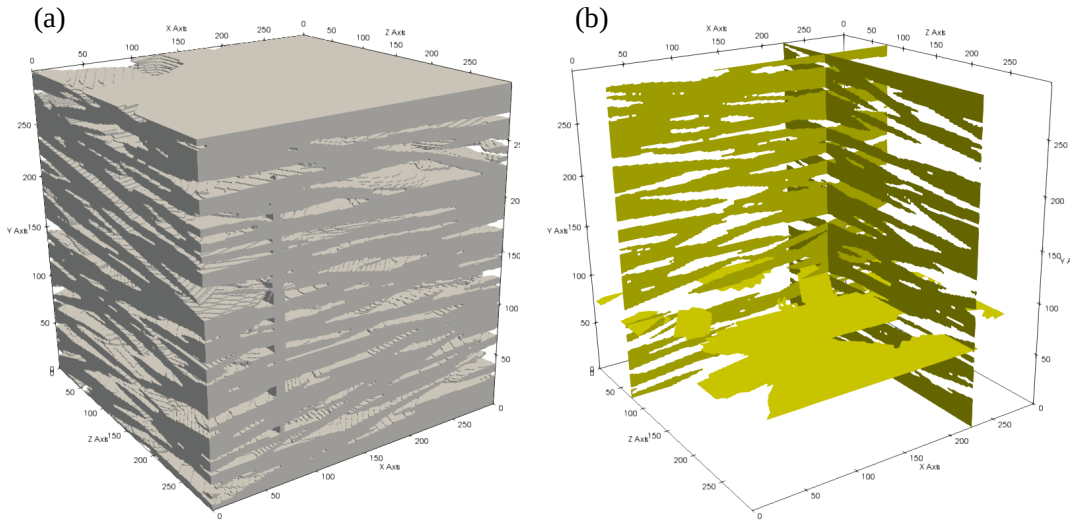

Figure 6.8: (a) Reconstructed 3D clay pore system of size 300^3 voxels with lattice resolution of 2 nm/voxel and total porosity of 25%. The gray regions are clay particles. (b) Three orthogonal 2D slices of the 3D clay pore system which show the internal pore structure. The yellow regions are clay particles.

$\theta = 10^\circ$ ($\rho_s = 2.5$), a water non-wet case (Case 2) with contact angle $\theta = 124^\circ$ ($\rho_s = 0.5$), and a mixed-wet case (Case 3) where the simulation domain is equally split into two wetting and non-wetting regions existing in parallel to the flow direction z, and the corresponding contact angles of the two regions are the same as the two individual wetting (Case 1) and nonwetting (Case 2) cases. These three wettability cases correspond to SEM observations as shown in Fig. 6.1, and the red boxes in Fig. 6.1 are drawn to scale to demonstrate the size of the clay reconstructions in 2D.

The equilibrium 3D distributions of the condensed water phase for the three cases at three water saturations ($S_w = 0.18, 0.37, 0.51$) are shown together in Fig. 6.9, and three orthogonal 2D slices of the corresponding 3D distributions that reveal the internal pore structure and fluid distributions are shown in Fig. 6.10. For Case 1, water adsorbs on the surfaces of clay particles and condenses around the corners of the pore spaces where surface attractive forces are the strongest. Pores with smaller apertures are filled with the liquid water before those with larger apertures. The center of large pores remain unfilled even at high water saturations.

For Case 2, we observe that condensed water accumulates at the center of the pores, forming

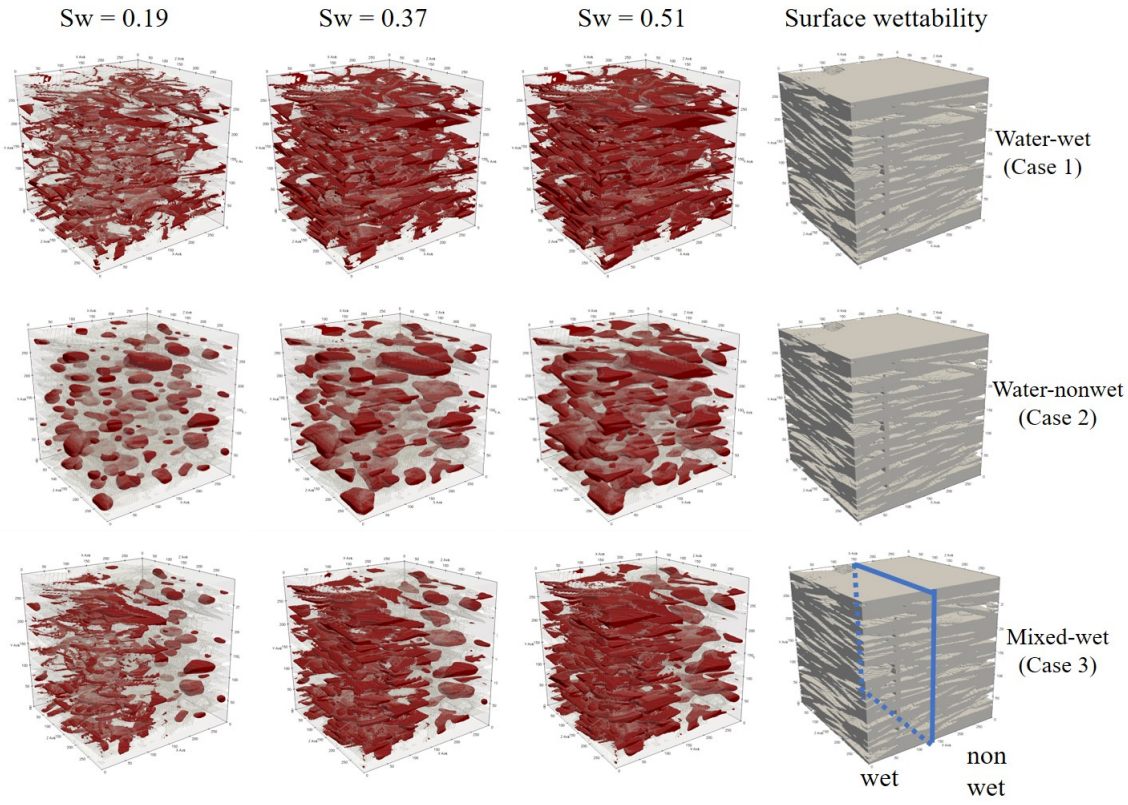

Figure 6.9: The equilibrium 3D distributions of condensed liquid water phase at 400 K in the clay pore system for the three wettability cases (Case 1: water-wet, Case 2: water-nonwet, Case 3: mixed-wet) at three water saturations $S_w = 0.18, 0.37, 0.51$. Red indicates the condensed liquid water, and the clay particles are shown in semi-transparent gray for easier visualization of the condensed phase. The surface wettability of the three cases is shown in the last vertical track.

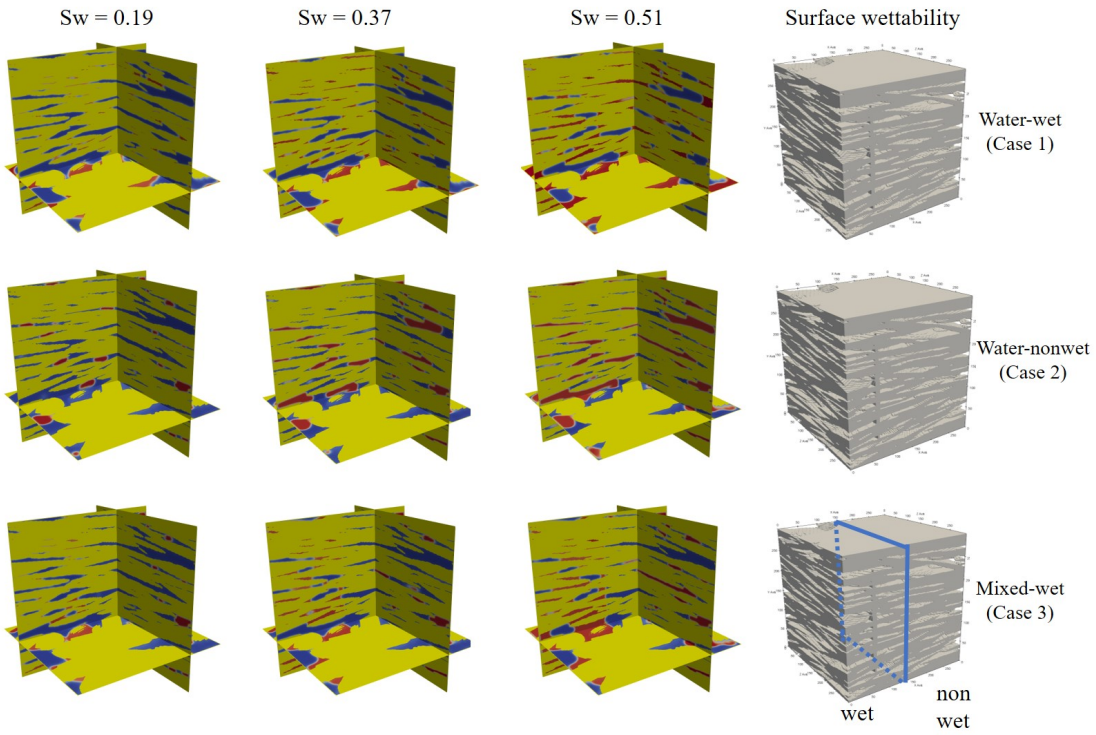

Figure 6.10: The equilibrium 2D distributions of condensed liquid water phase at 400 K in the clay pore system for the three wettability cases (Case 1: water-wet, Case 2: water-nonwet, Case 3: mixed-wet) at three water saturations $S_w = 0.18, 0.37, 0.51$. Red indicates the condensed liquid water, blue indicates the remaining pore space, and yellow indicates the clay particles. The surface wettability of the three cases is shown in the last vertical track.

near-spherical interfaces with vapor water, which is due to the much smaller attractive force exerted by the clay particles. As water saturation increases, the condensed phase merges and grows in size, yet still occupies the center of the pore space. Even at high water saturations, pores with small apertures remain unfilled.

By comparing the distribution of condensed water at the same water saturation for Case 1 and 2, we observe that for Case 2 the liquid water is much more easily distinguishable than Case 1. For Case 1, water exists in the form of thin films in large mesopores, and condenses preferentially at the corners of the pore spaces and in micropores, both of which are usually below the resolution of the SEM images. Our simulations provide a possible explanation of the controversy between two separate cryo-SEM observations on clay samples from the same location by Desbois *et al.* [104, 106], in which they observed in-situ water in clay pores associated with OM, but did not observe as much water as in pure clay pores where no OM is present. Desbois *et al.* [106] attributed the lack of observable water at SEM resolutions to the volume expansion of samples after coring that expels the in-situ water, and the drying by vacuum when preserving and packing the samples. However, such explanations contradict the fact that they did observe in-situ water in samples from the same location where OM was found to be associated with clay [104]. Based on our simulations, a more credible explanation would be the difference in the surface wettability of the observed clay particles in their two studies.

For Case 3, the water distribution within the individual wetting and nonwetting zone follow the specific behavior we observed for Case 1 and 2. Spatially heterogeneous and inhomogeneous distribution of water introduces higher degree of complexity into the connectivity of the vapor/liquid phases, and the flow behavior of methane, as will be shown later.

We then characterize at each water saturation stage the PSD of the remaining pore spaces that are not occupied by the liquid water, namely where vapor water exists. These pore spaces are extracted by thresholding and each individual connected component ('pore') is labeled, and their volumes (number of voxels) and effective pore sizes (maximum inscribed sphere radius) are calculated using the BoneJ particle analyzer plugin [16] in ImageJ software. The pore size bins range from 0 to 48 nm with bin width of 4 nm, and the corresponding pore volume is normalized by

the total pore volume of the clay pore system where no water is present. The resulting PSDs of the three wettability cases are shown in Fig. 6.11. For Case 1, condensed water preferentially occupies smaller pores followed by larger ones. As a result, the average effective pore size gradually increases with water saturation. However, at low water saturations ($S_w = 0.18$), a noticeable peak of pore size below 20 nm exists, which is due to the water wetting the surfaces of mesopores, therefore reducing the effective pore sizes of such pores before filling them completely. On the other hand, a completely reverse trend is observed for Case 2, where the average pore size gradually decreases with water saturation. This is because water preferentially condenses in larger pore bodies and extends to the corner of the pore space. The breadth of PSD is much narrower than Case 1. For Case 3 roughly a bimodal PSD is observed for each water saturation stage, indicating a mixture behavior of the former two cases. The average effective pore size remains almost unchanged. The trends of pore size variation as a function of water saturation for Case 1 and 3 are consistent with experimental measurements by Li *et al.* [30] of water adsorption in a water-wet pure clay (montmorillonite) sample and a mixed-wet shale sample.

Not only the size of the pore space controls flow capacity, but also the connectivity of the pore network. We then calculated the connectivity of the vapor and liquid phases across z direction, which was taken as the flow direction as will be discussed in Section 6.5.2. Here the connectivity is defined as the volume of the connected phase across z direction normalized by the total pore volume, and we name this term 'connected saturation' of a specific phase. Fig. 6.12 shows a comparison of the connected saturation of the vapor and liquid phases as a function of water saturation for the three cases. To guide the eye, we also show two black lines ($y = x$ and $y = 1 - x$) which indicate the maximum connected saturation for the two phases, assuming complete connectivity. For Case 1, the isolated liquid phases at the corner and surface of the pore spaces just begin to form connectivity at $Sw = 0.2$, and for $S_w > 0.42$, almost all liquid phases are connected in the flow direction. On the other hand, the connectivity of the gas phase dramatically decreases with water saturation, and the gas phase almost completely loses connectivity when $S_w > 0.42$ due to the snap-off effect and liquid water bridging at the narrow pore throat regions. For Case 2, since the condensed liquid phase accumulates at the center of the pore spacing forming isolated droplets, it only forms connectivity

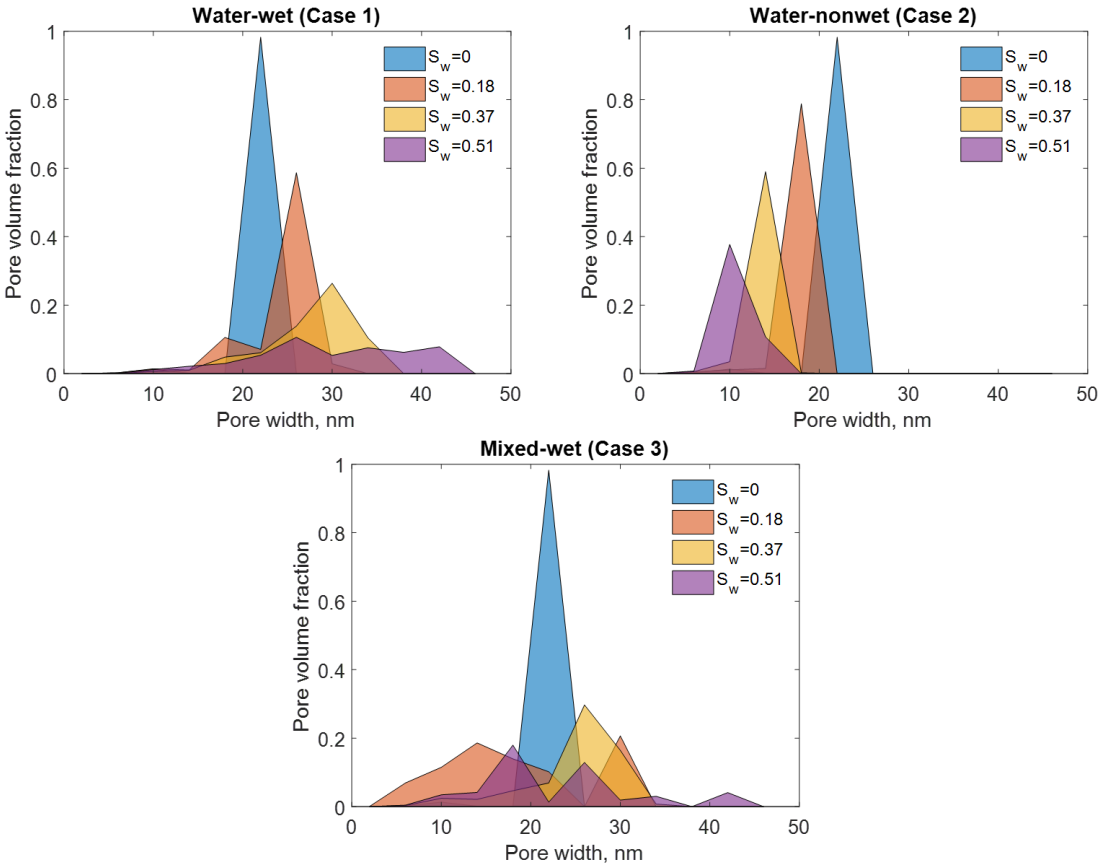

Figure 6.11: PSDs of the remaining pore spaces that are not occupied by the liquid water for the three wettability cases. The vapor water phase is extracted after the water adsorption simulation as the pore spaces, and their volumes (number of voxels) and effective pore sizes (maximum inscribed sphere radius) are calculated using the BoneJ plugin [16] in ImageJ software. The pore size bins range from 0 to 48 nm with bin width of 4 nm, and the corresponding pore volume is normalized by the total pore volume of the clay pore system where no water is present.

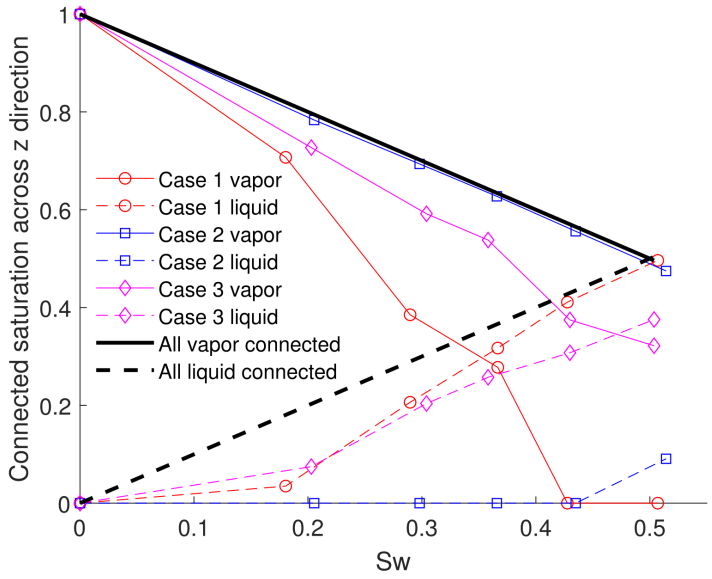

Figure 6.12: The connected saturation (defined as the volume of the connected phase across the flow direction normalized by the total pore volume assuming connectivity of 6) of the vapor and liquid phases as a function of water saturation for the three wettability cases. The black lines are used to guide the eyes, representing situations where either phase is assumed to be fully connected across the flow direction.

when $S_w > 0.42$. However, the gas phase remains high connectivity even at high water saturations. For Case 3, the connectivity of the vapor and liquid phases is bounded by the limits given by Case 1 and 2. The slight deviation from this trend for liquid phase connectivity at $Sw < 0.2$ is an artifact due to the limited data points obtained from the simulations.

6.5.2 Methane flow simulation at different water saturations and wettability

For comparison, we first simulated methane flow in the original clay pore system where no liquid water is present, and the 'intrinsic' permeability assuming no-slip BC and constant viscosity is calculated. The equilibrium velocity profiles of the clay pore system assuming Darcy flow or with consideration of slip BC are shown in Fig. 6.13 (a) and (b) respectively. For either case, three dominant flow pathways across the flow direction are observed. The largest flow velocity occurs at the outlet where apertures are relatively large. When considering the slip flow and variation of viscosity within the pore space, the velocity magnitude is larger as shown by the more intensive streamlines. The average flow velocity for this case is about 44% larger than the case assuming

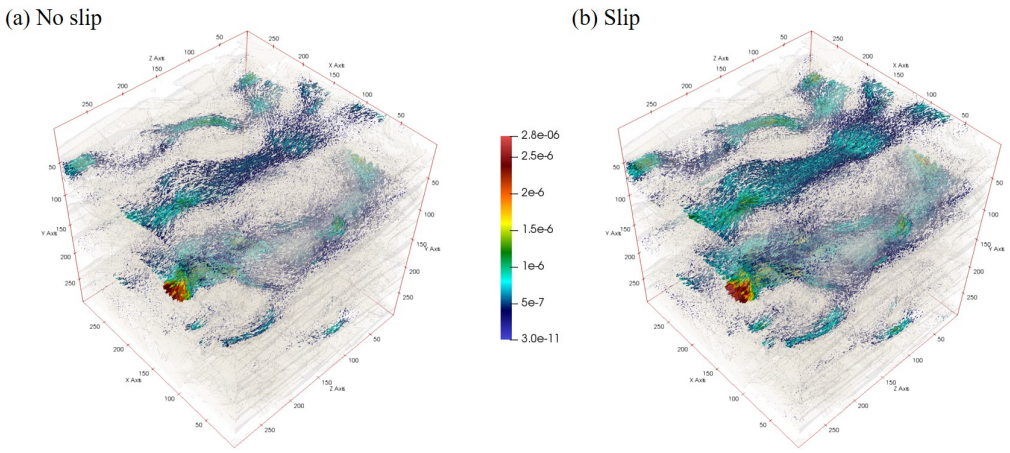

Figure 6.13: The simulated velocity profiles of methane at 400 K and 12 MPa with pressure gradient of 0.1 MPa/m in the original clay pore system without water. Solid is in light gray and the size and direction of the arrows represent the local velocity magnitude and direction. (a) Assuming no-slip flow and viscosity is constant (Darcy flow); (b) Considering slip flow and variation of viscosity as a function of the distance to the pore wall (LEV).

Darcy flow. The calculated intrinsic permeability using Eq. 6.17 is 1.132 μD, and the apparent permeability with consideration of slip flow and variation of viscosity within the pore spaces is 1.592 μD, which is about 40% larger than the intrinsic permeability. This is as expected since the Kn used in the flow simulation is about 0.0175 (see Table 6.1) and the slip flow regime dominates. Therefore, slip velocity at the pore wall can not be ignored.

The calculated methane apparent permeability k_a as a function of water saturation S_w for the three cases is shown in Fig. 6.14. In general, k_a decreases with S_w. $S_w = 0.37$ separates two regions of gas permeability curves, before which k_a follows Case 1 $>$ Case 3 $>$ Case 2 and after which Case 3 $>$ Case 2 $>$ Case 1. To better illustrate the change in flow capacity and pathways before and after $S_w = 0.37$, we show in Fig. 6.15 and 6.16 the equilibrium flow velocity profiles for the three wettability cases at $S_w = 0.30$ and $S_w = 0.43$ respectively.

For $S_w < 0.37$, k_a of methane for the water-wet case is the largest, which is as expected since in this case methane flows across the center of the pore space with larger effective pore sizes. Even though the pore space connectivity for this case is the lowest among the three cases (see Fig. 6.12), the connected pore space is the largest in size (see Fig. 6.11, therefore providing two preferential flow pathways for methane as shown in Fig. 6.15 (a). For $S_w < 0.37$, the water-

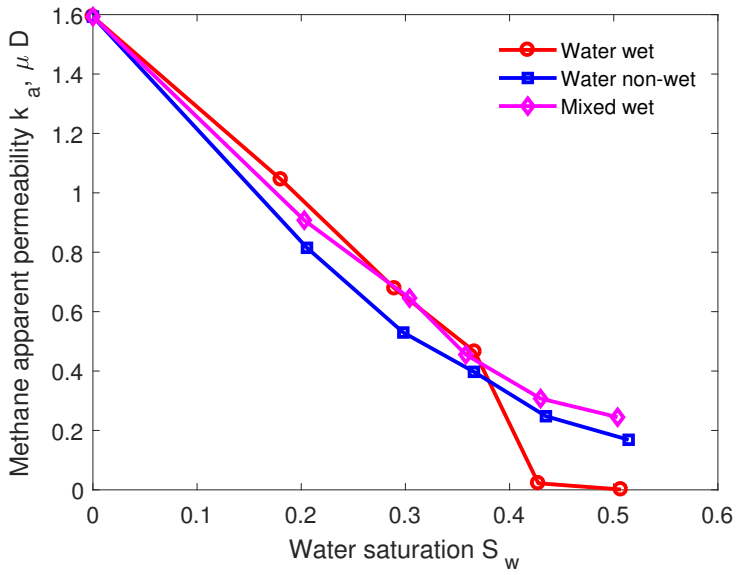

Figure 6.14: The calculated methane apparent permeability as a function of in-situ water saturation at 12 MPa and 400 K for the clay pore system at three wetting cases.

nonwet case has the lowest k_a since methane flows around the corners of the original pore space, resulting in narrower and more tortuous flow pathways and much smaller flow velocities (see Fig. 6.15 (b)) even though the connectivity of the pore space is the largest among the three cases. The mixed-wetting case results in k_a bounded by the wetting and nonwetting cases. However, when $0.28 < S_w < 0.37$, k_a of the mixed-wetting case is almost the same as the wetting case, indicating that the apparent permeability of methane is dominantly controlled by the pore structure of the water wet region.

When $S_w > 0.37$, k_a for the wetting case drops dramatically. This is because the liquid water phase merges at the narrow pore throat regions and the connectivity of pore space drops significantly as shown in Fig. 6.12, approaching zero connectivity for $S_w > 0.4$. As shown in Fig. 6.16 (a), the velocity is hardly noticeable and only one dominant flow pathway exists. For $S_w > 0.37$, k_a of the mixed wetting case is the largest among the three cases. Comparing the velocity profiles in Fig. 6.16, we observe two dominant flow pathways with much larger velocity in the water-nonwet region, together with a less prominent flow pathway in the wetting region. Obviously, the mixed wettability significantly alters the distribution characteristics of the condensed

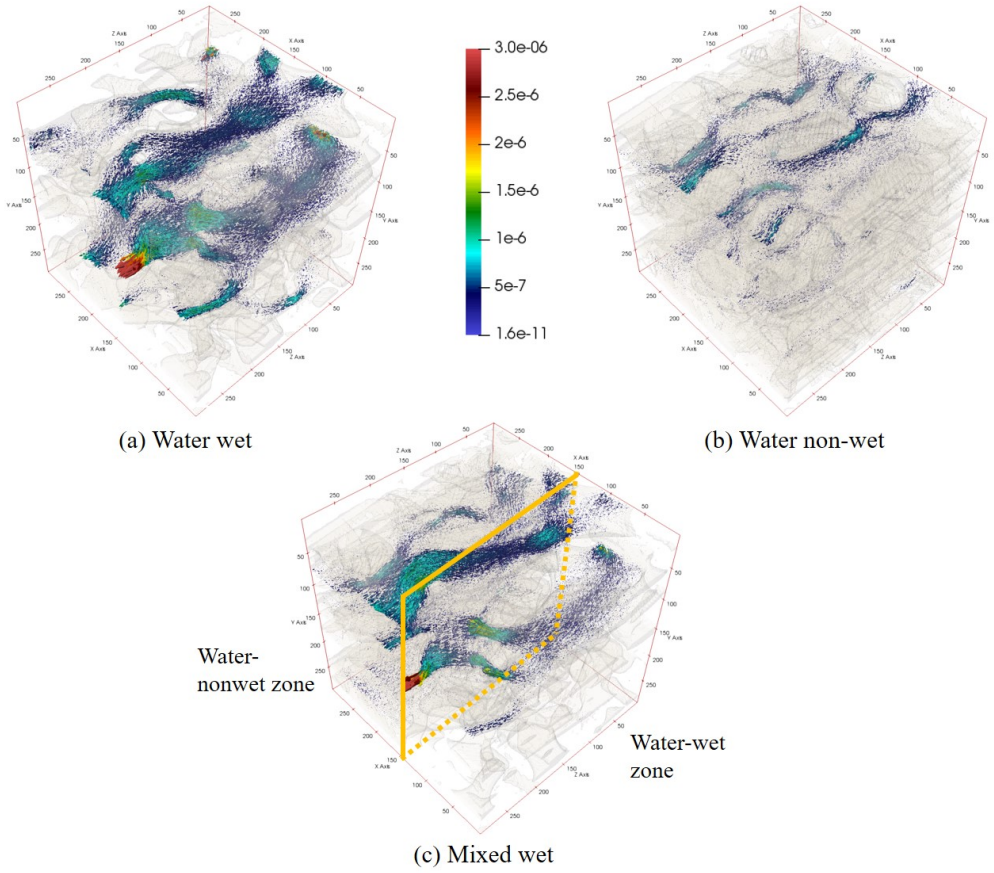

(a) Water wet

(b) Water non-wet

(c) Mixed wet

Figure 6.15: The equilibrium methane flow velocity profiles at $S_w = 0.30$. The remaining open pore spaces are shown in semi-transparent light gray, and the size and direction of the arrows indicate the magnitude and direction of the local velocity vectors. The colorbar shows the magnitude of the velocity in $\mathrm{m/s}$.

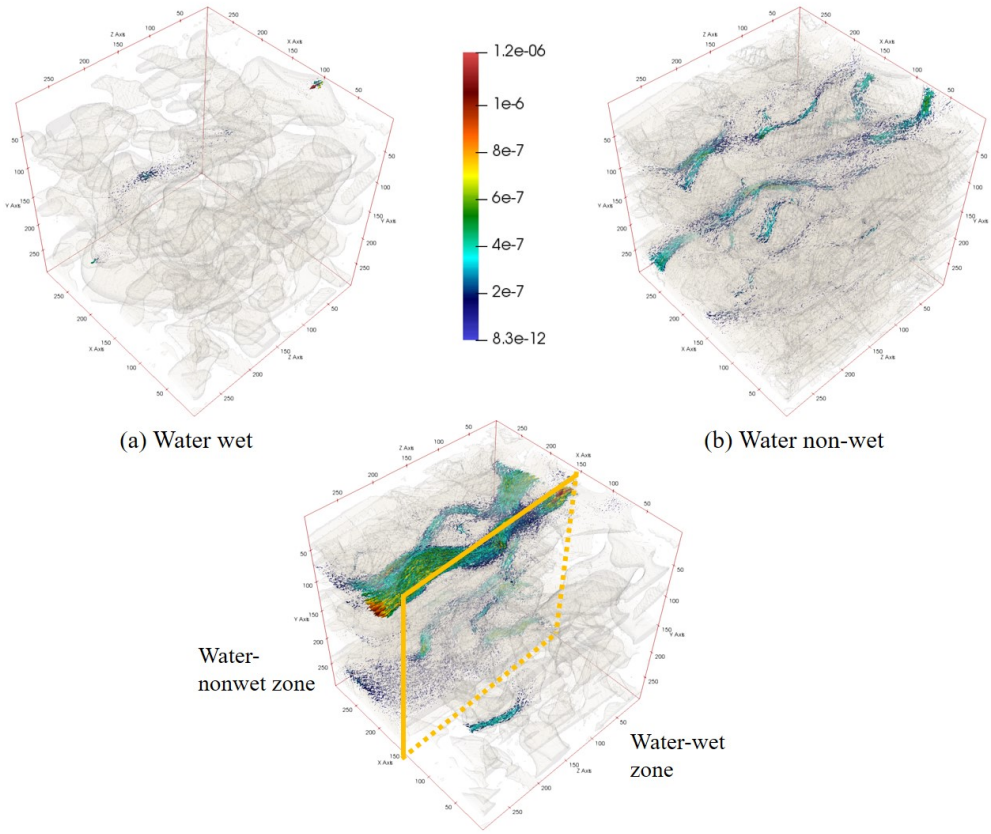

Figure 6.16: The equilibrium methane flow velocity profiles at $S_w = 0.43$. The remaining open pore spaces are shown in semi-transparent light gray, and the size and direction of the arrows indicate the magnitude and direction of the local velocity vectors. The colorbar shows the magnitude of the velocity in $\mathrm{m/s}$.

water. In this case, water condenses preferentially in the water-wet region, while majority of the flow pathways are only slightly affected as shown in Fig. 6.10, which explains the occurrence of the highest methane apparent permeability. The pore space connectivity of about 0.3 at $S_w = 0.37$ can therefore be treated as the percolation threshold of methane in this particular pore structure, which is consistent with common values of percolation threshold observed in sandstones [60]. Above this connectivity value, methane permeability is controlled by the pore size, whereas below this value, methane permeability is controlled by the pore space connectivity.

We then compare in Fig. 6.17 the calculated methane relative permeability (k_a normalized by the maximum permeability at zero water saturation) with experimental data from Vangpaisal and Bouazza [17]. The experimental data represent the measured gas permeability at different water saturation states of four partially hydrated geosynthetic clay liners (GCL) (GCL1, GCL2, GCL3, and GCL4). All GCLs consisted of essentially dry bentonite powder or granular sandwiched between geotextile layers. A normal stress of 20 kPa was applied during the hydration process to minimize the clay swelling effect, which is also assumed negligible in our simulation. In this case, the clay particles are completely water-wet. We observed good agreement between the permeability for the water-wet case by our simulation and the experimental data when plotted in semi-log scale. The dramatic decrease in k_a around $S_w = 0.4 - 0.5$ was captured precisely by the simulation, indicating: 1) the pore structure reconstructed in this study is representative of the actual microstructure of clay; 2) the spatial water distribution and size and connectivity of the remaining pore space as a function of S_w characterized by our simulations are in reasonable agreement with the experimental results (at least for the water-wet case), thus the LBGK D3Q19 LBM model we developed could be used to reproduce water adsorption and distribution in complex geometries; 3) the MRT LEV LBM model provides reasonable estimation of the gas flow properties of tight porous media.

6.5.3 Error and uncertainty assessment

The size of the simulation domain used in this study is 600 nm^3. Even though the size is below REV, the 2D pore structure statistics (pore length, area, aspect ratio, circularity) are informed by BIB-SEM images (mm in size) taken at the REA scale, and the 3D pore structure is reconstructed

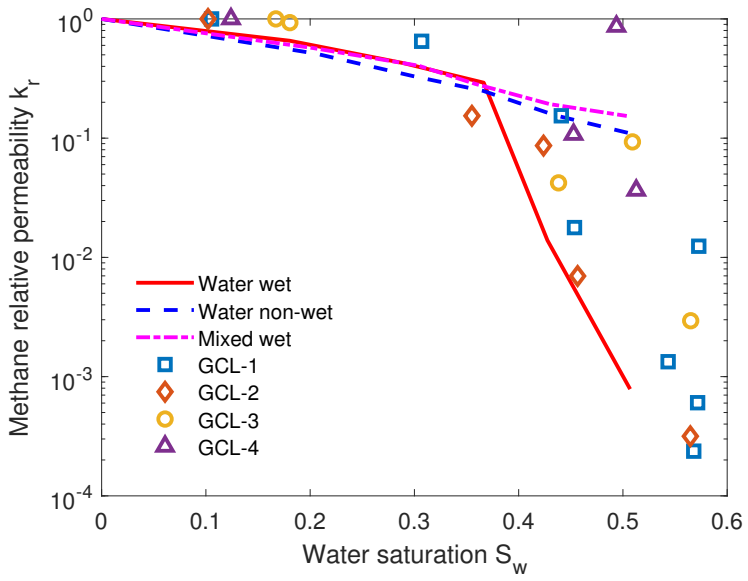

Figure 6.17: The calculated methane apparent permeability as a function of in-situ water saturation at 12 MPa and 400 K for the clay pore system at three wetting cases (lines), in comparison with experimental data on four clay samples (GCL-1, GCL-2, GCL-3, and GCL-4) at different hydration states reported by Vangpaisal and Bouazza [17].

based on a statistically process-based approach. Therefore, it is reasonable to conclude that the 3D simulations performed in this study are representative of clay properties at least for the region of interest where BIB-SEM images are taken.

In this study we assumed that clay surfaces of either the wetting or the non-wetting region can be characterized by a uniform contact angle for the sake of simplicity. However, different clay minerals, CEC, PVT properties, or salinity of the water might interact together to result in different contact angles, even within the same wettability region [210]. The basal surfaces or edges of clay platelets might also have different wettability conditions [32]. It is possible to incorporate complex spatial distribution of wettability as long as it can be characterized in some way.

The coupled adsorption and flow simulations were conducted here in a successive manner, by first simulating the adsorption process using the LBGK 3D LBM model, followed by simulating the flow process using the MRT LEV 3D LBM model. When performing flow simulations, the condensed water phase is assumed to be immobile and therefore treated as the solid phase, and the existence of vapor water in the pore space is neglected. No further interactions between methane and

vapor water are considered since we used a single component LBM with a single set of particle distribution function. Such simplifications might lead to uncertainties in the permeability calculations, which might explain the slight deviation from experimental data.

6.6 Conclusions

In this study, we used LBGK D3Q19 LBM models incorporated with mKM EOS to study water adsorption and distribution in a 3D reconstructed clay pore system based on BIB-SEM image analysis. Three cases with different surface wettability conditions are explored. Results show that water tends to accumulate at the corners and surfaces of the hydrophilic pore walls, while for hydrophobic surfaces, water condenses in the center of the pore space, forming quasi-spherical vapor/liquid interfaces as a result of the force balance among surface tensions. The average size of the effective pore space increases with water saturation for the water-wet case, and decreases with water saturation for the water-nonwet case. A bimodal PSD is observed for the mixed-wet case, indicating the complex water distribution characteristics due to the interplay between the water-wet and water-nonwet zones. The connectivity of the remaining pore space for the water-wet case decreases dramatically and connectivity is almost lost for $S_w > 0.37$. On the other hand, the connectivity of the remaining pore space for the water-nonwet case is the highest, and almost all of the pore spaces are connected. The connectivity for the mixed-wetting case is bounded by the former two cases.

The subsequent methane flow simulations at reservoir conditions shows that the apparent permeability of methane with consideration of slip flow and variation of viscosity in the original dry clay is about 40% larger than the intrinsic permeability calculated assuming Darcy flow. When in-situ water is considered, generally we observe lower apparent permeability for higher water saturation. When comparing the three wettability cases, two different trends are observed with the cutoff $S_w = 0.37$. For $S_w < 0.37$, the apparent permeability of methane is the highest for the water-wet case, and the lowest for the water-nonwet case. However, when $S_w > 0.37$, the apparent permeability of methane for the water-wet case drops up to three orders of magnitude because of the snap-off of the connected pore space by the condensed water phase. The apparent permeability of the mixed-wetting case is the highest, mainly because of the preferential condensation of the wa-

ter phase within the water-wet region, leaving well-connected flow pathways with large apertures within the water-nonwet region. In general, we observe that mixed wettability existing in parallel to the flow direction is beneficial for enhancing the flow capacity with the existence of in-situ water in clay, compared with uniform wettability conditions. This could explain to some extent the unexpectedly higher flow capacities either measured in the lab or in the field, compared with the numerical simulation results assuming uniformly wetting surfaces. The calculated relative permeability for the water-wet case agrees well with experimental data measured at different hydration states on water-wet GCLs, and the relative permeability curve accurately predicts the inflection point for S_w around 0.4 after which the permeability begins to drop dramatically. This validates the representativeness of our clay structure reconstruction, the reliability of the simulated water adsorption and distribution characteristics, and subsequent gas flow behavior, at least for the water-wet case.

Chapter 7: Conclusions

7.1 Summary of contribution

Thermodynamic and hydrodynamic properties characterization of fluid confined in nanopores in shale matrix remains a nontrivial problem, which requires a detailed understanding of the pore structure, surface properties, availability and applicability of experimental or simulation tools, and relevant physics that govern the fundamental processes at the pore scale. The work done in this thesis improves the understanding and solving of this problem to some extent. This problem was approached using two types of methods integrating experimental analysis with numerical simulations.

The first method used PNMs which simplify the pore structure of a porous material as a network of pore bodies connected by pore throats. To reconstruct the PNM that honors the pore structure of shale dominant with nanopores ($<$200 nm), nitrogen sorption experiments and SEM observations were combined to obtain a statistical estimation of pore shape, size, and pore throat connectivity of shale samples, via calibrating the simulated nitrogen sorption curves using PNM and LDFT to experimental measurements. This was the first time that LDFT had been integrated with PNM to estimate sorption behavior with dual-scale PSD, varying pore shapes, and inhomogeneous pore throat connectivity. Pore network effect and cavitation effect were explicitly considered to reproduce the open and forced closure of hysteresis loops. The effect of pore shape on sorption isotherms interpretation was analyzed in detail, which was not paid enough attention to previously. We found that the use of different pore shapes has significant impact on the pore structure interpretation, and the resulting average pore size and connectivity vary up to an order of magnitude. The use of PNMs with a combination of pore shapes informed by SEM image analysis reduced the uncertainty and nonuniqueness of the interpretation. The reconstructed PNM can then be used for estimation of flow properties under a variety of working conditions, which is nontrivial and time-consuming if not at all impossible to characterize by flow experiments. Advection and diffusion,

which are the two main mechanisms for gas flow in shale, were simulated using the reconstructed PNMs. It was found that under reservoir pressure (10 – 50 MPa) and temperature (300 – 400 K) the contribution of diffusion to transport capacity was negligible (orders of magnitude smaller) compared with advection except within micropores and small mesopores ($<$10 nm) at high Kn conditions. We also found that for estimation of single phase flow properties (permeability, diffusivity), PNMs with uniform cylindrical/slit pore shape predict results fairly close to PNMs using a combination of pore shapes informed by SEM images. Since PNMs with cylindrical pore shape lead to lower error and uncertainty when calibrating to experimental sorption curves (contrasting the step feature observed by slit pores), we suggested the choice of cylindrical pore shape for single phase steady state flow capacity estimation, without having to turn to SEM image analysis for detailed pore shape characterization.

We argue that PNMs are cost-efficient simulation tools for the estimation of single phase flow properties via building a statistical reconstruction of the pore structure with simplified assumption of pore shapes and connectivity. However, for multiphase adsorption/flow problems in which the evolution of the phase interface highly depends on the detailed morphology and topology of the pore space as well as the surface properties of the solid matrix, PNMs become deficient although certain simplification can be made. Therefore, we explored in this thesis a second method by performing direct numerical simulations on SEM image-based 3D reconstruction of the nanoporous media. LBM was used instead of PNM since it is easily applicable to complex geometries via simple treatment of the boundary conditions. Microscale interactions between fluid-fluid and fluid-solid molecules can be accounted for by adding pairwise mesoscale phenomenological interparticle forces. Via incorporating realistic EOS and two forms of surface forces for subcrtical and supercritical gases, we showed for the first time a strict validation of LBM against LDFT, GCMC, and experimental sorption data. The major advantage of this method compared to molecular scale approaches (such as GCMC or MD) is its relatively low computational cost (highly parallelizable due to the local nature of streaming and collision processes), the feasibility to simulate in much larger domains (up to two orders of magnitude larger in linear sizes), and most importantly, the possibility of coupling thermodynamic and hydrodynamic processes which makes it suitable for probing a

wide variety of problems. Using the developed LBM models, we studied nitrogen sorption behavior in both 2D and 3D reconstructions of interP and intraP pores, which are two common types of pore systems in shale matrix. We found that subcritical gas adsorption in complex nanoporous media can no longer be simplified as a layer-by-layer process. The curvature of the pore space not only affects the shape of the nitrogen adsorption curve, but also results in different types of sorption hysteresis loops as defined by IUPAC. On the other hand, supercritical gas adsorption is less sensitive to pore shape, but controlled by the surface area since the thickness of the adsorbed layer usually does not extend extend more than three layers of molecules. These simulations provide insight into the detailed adsorption and phase separation behavior at the pore sale, and are critical for understanding fluid distributions in shale, which helps with reserve estimation, production forecasting, and possible EOR design.

Another application of our model was to simulate water adsorption and condensation in clay, the microstructure of which was reconstructed via a process-based approach with critical pore structure properties informed by BIB-SEM image analysis. The spatial distribution, size, and connectivity of condensed water phase was characterized in detail as a function of water saturation and surface wettability. The subsequent supercritical methane flow was simulated and the apparent permeability as a function of water saturation and wettability was calculated and compared to available experimental data. We have shown for the first time the spatial characterization of partially-saturated water in clay with different surface wettability. The resulting gas relative permeability curve for the water-wet case agreed well with experimental measurements on water-wet geosynthetic clay liners. Our simulations suggested that wettability inhomogeneity provides reasonable explanations for the seemingly controversial cryo-SEM observations of in-situ water distribution in clay [104, 106].

7.2 Future work

For PNM work, we used a dual-scale model to account for the coexistence of macroscale interP porosity and microscale intraP porosity, both of which are commonly observed in shale matrix. For computational efficiency, we simplified the microporosity as a bundle of tubes characterized by an average pore size ignored the interconnectivity. Further improvement of the model accuracy

can be made by considering these microporosities explicitly, which requires significant amount of code optimization and parallelization to reduce the computational cost. However, it will be worth the effort to improve or rewrite the codes, so that both pore-filling and grain-filling microporosities can be considered within the same PNM, honoring a more representative pore structure in shale. Furthermore, more advanced image analysis workflow shall be developed to characterize the size, shape, and distribution of these microporosities to guide the reconstruction of PNMs.

For LBM work, we incorporated the pairwise interparticle forces necessary to reproduce the correct phase behavior. We focused on thermodynamic studies of single-component-two-phases (vapor and liquid) problems in this thesis. However, it is possible and straightforward to incorporate more components by adding more sets of particle distribution functions. The interactions between these components can be modeled by adding appropriate interparticle forces calibrated to inter-component interaction strength (*e.g.* in the form of interfacial intension or contact angle). However, adding more sets of particle distribution functions require more advanced structuring of the codes (in terms of domain decomposition, processor communication, and speed optimization). The development of efficient codes that could incorporate more than one set of particle distribution functions (multi-component) while honoring the complex thermodynamic and hydrodynamic physics will enable the model to probe a much wider variety of physical problems, including but not limited to competitive adsorption modeling of supercritical CO_2 and CH_4 for CO_2 sequestration and enhanced gas recovery purposes, multi-component capillary condensation and transport study of shale gas when heavy components such as propane and butane are present and may condense in micropores and small mesopores under reservoir conditions, and more complex coupling between adsorbed water and methane for understanding methane adsorption capacity with connate water and methane transport properties with the existence of adsorbed gas.

Either PNM or LBM (or any other pore scale modeling tools) is constrained by the size of the simulation domain (about 5 μm for PNMs and 600 nm for LBM in this thesis) to balance the computational cost. Upscaling simulation results to REV or core scale is an essential next step in future work. For PNMs reconstruction, nitrogen sorption tests can be performed on isolated organic-rich (kerogen) and inorganic regions respectively to guide the reconstruction of two PNMs

representative of these two pore systems, based on which corresponding flow properties can be obtained. A mixture model (*e.g.* effective medium theory [233, 234]) based on the volume fraction of kerogen by XRD or EDS analysis [235] can then be used to upscale the pore scale results to the core scale. Continuous time random walks approach [48] can also be considered for upscaling purposes, using a generalized network model representation of the porous medium, where the the transport between sites can be described by a transit-time probability distribution derived from simulation at a smaller scale. For LBM, we focused on the reconstruction of clay microstructure in this thesis by analyzing BIB-SEM images. Similarly, OM pore structure can be reconstructed following this workflow [15]. LBM calculations of gas permeability can be obtained on these two pore systems. A mixture model similar to PNMs can be used for upscaling predictions. Another possible upscaling pathway can be explored by assembling the LBM-calculated permeabilities of OM and clay-rich regions into a 2D simulation domain using the Monte Carlo sampling method [129], and matching the TOC informed by BIB-SEM image analysis. The REA-scale permeability can then be determined using a finite difference approach.

List of acronyms

(with page numbers where first introduced)

AFM atomic force microscopy. 15

BC boundary condition. 37

BET Brunauer-Emmett-Teller. 12

BIB broad-ion-beam. 14

BJH Barret-Joyner-Halenda. 12

BSE back scattered electron. 14

CBW clay-bound water. 24

CDF cumulative density function. 51

CEC cation exchange capacity. 25

CT computerized tomography. 9

D2Q9 two dimensional nine velocity. 83

D3Q19 three dimensional 19 velocity. 113

DEM discrete element method. 135

DFT density functional theory. 23

DGM dusty gas model. 33

DLVO Derjaguin—Landau—Verwey—Overbeek. 27

DSMC direct simulation Monte Carlo. 41

EDM exact difference method. 114

EDS energy dispersive spectroscopy. 8

EOR enhanced oil recovery. 1

EOS equation of state. 39

FIB focused-ion-beam. 14

GCL geosynthetic clay liner. 159

GCMC grand canonical Monte Carlo. 24

HK Horvath–Kawazoe. 12

interP interparticle. 5

intraP intraparticle. 5

IUPAC International Union of Pure and Applied Chemistry. 5

LBGK lattice Bhatnagar–Gross–Krook. 83

LBM lattice Boltzmann method. 3

LDFT lattice density functional theory. 24

LEV local-effective-viscosity. 38

MD molecular dynamics. 37

MICP mercury intrusion capillary pressure. 9

mKM modified Kaplun-Meshalkin. 116

MRT multi-relaxation time. 83

NLDFT nonlocal density functional theory. 12

NMR nuclear magnetic resonance. 9

OM organic matter. 5

PDF probability density function. 50

PNM pore network model. 3

PR Peng-Robinson. 86

PSD pore size distribution. 1

REA representative elementary area. 15

REV representative elementary volume. 15

SANS small-angle neutron scattering. 5

SCMP single component multiphase. 39

SE secondary electron. 14

SEM scanning electron microscopy. 1

SR specular reflection. 37

TEM transmission electron microscopy. 5

TMAC tangential momentum accommodation coefficient. 38

TOC total organic carbon. 1

USANS ultra-small-angle neutron scattering. 5

vdW van der Waals. 19

XRD X-ray diffraction. 5

References

[1] Loucks, R. G, Reed, R. M, Ruppel, S. C, and Hammes, U. Spectrum of pore types and networks in mudrocks and a descriptive classification for matrix-related mudrock pores. *AAPG Bulletin*, 96(6):1071–1098, June 2012.

[2] Loucks, R. G, Reed, R. M, Ruppel, S. C, and Hammes, U. Preliminary classification of matrix pores in mudrocks. *Gulf Coast Association of Geological Societies Transactions*, 60:435–441, 2010.

[3] Josh, M, Esteban, L, Delle Piane, C, Sarout, J, Dewhurst, D. N, and Clennell, M. B. Laboratory characterisation of shale properties. *Journal of Petroleum Science and Engineering*, 88-89:107–124, June 2012.

[4] Tang, X, Jiang, Z, Jiang, S, and Li, Z. Heterogeneous nanoporosity of the Silurian Longmaxi Formation shale gas reservoir in the Sichuan Basin using the QEMSCAN, FIB-SEM, and nano-CT methods. *Marine and Petroleum Geology*, 78:99–109, December 2016.

[5] Thommes, M, Kaneko, K, Neimark, A. V, Olivier, J. P, Rodriguez-Reinoso, F, Rouquerol, J, and Sing, K. S. Physisorption of gases, with special reference to the evaluation of surface area and pore size distribution (IUPAC Technical Report). *Pure and Applied Chemistry*, 87(9-10):1051–1069, July 2015.

[6] Sondergeld, C. H, Ambrose, R. J, Rai, C. S, and Moncrieff, J. Micro-structural studies of gas shales. SPE Unconventional Gas Conference, January 2010.

[7] Pallatt, N and Thornley, D. The role of bound water and capillary water in the evaluation of porosity in reservoir rocks. *Advances in Core Evaluation: Accuracy and Precision in Reserves Estimation*, pages 21–23, 1990.

[8] Javadpour, F. Nanopores and apparent permeability of gas flow in mudrocks (shales and siltstone). *Journal of Canadian Petroleum Technology*, 48(08):16–21, August 2009.

[9] Landry, C. J, Prodanović, M, and Eichhubl, P. Direct simulation of supercritical gas flow in complex nanoporous media and prediction of apparent permeability. *International Journal of Coal Geology*, 159:120–134, April 2016.

[10] Wang, J, Chen, L, Kang, Q, and Rahman, S. S. The lattice Boltzmann method for isothermal micro-gaseous flow and its application in shale gas flow: A review. *International Journal of Heat and Mass Transfer*, 95:94–108, April 2016.

[11] Qajar, A, Daigle, H, and Prodanović, M. The effects of pore geometry on adsorption equilibrium in shale formations and coal-beds: Lattice density functional theory study. *Fuel*, 163:205–213, January 2016.

[12] Mehmani, A and Prodanović, M. The effect of microporosity on transport properties in porous media. *Advances in Water Resources*, 63:104–119, January 2014.

[13] Zhang, T, Ellis, G. S, Ruppel, S. C, Milliken, K, and Yang, R. Effect of organic-matter type and thermal maturity on methane adsorption in shale-gas systems. *Organic Geochemistry*, 47:120–131, June 2012.

[14] Fan, C, Zeng, Y, Do, D. D, and Nicholson, D. A molecular simulation study of adsorption and desorption in closed end slit pores: Is there a hysteresis loop? *Chemical Engineering Science*, 121:313–321, January 2015.

[15] Landry, C. J, Prodanović, M, Reed, R. M, Eichhubl, P, and Mohanty, K. Estimating oil-water relative permeability curves using digital rock physics. Unconventional Resources Technology Conference, July 2017.

[16] Doube, M, Kłosowski, M. M, Arganda-Carreras, I, Cordelières, F. P, Dougherty, R. P, Jackson, J. S, Schmid, B, Hutchinson, J. R, and Shefelbine, S. J. BoneJ: Free and extensible bone image analysis in ImageJ. *Bone*, 47(6):1076–1079, December 2010.

[17] Vangpaisal, T and Bouazza, A. Gas permeability of partially hydrated geosynthetic clay liners. *Journal of Geotechnical and Geoenvironmental Engineering*, 130(1):93–102, January 2004.

[18] Baihly, J. D, Malpani, R, Altman, R, Lindsay, G, and Clayton, R. Shale gas production decline trend comparison over time and basins-revisited. Unconventional Resources Technology Conference, July 2015.

[19] Milliken, K. L, Rudnicki, M, Awwiller, D. N, and Zhang, T. Organic matter-hosted pore system, Marcellus Formation (Devonian), Pennsylvania. *AAPG Bulletin*, 97(2):177–200, February 2013.

[20] Kuila, U and Prasad, M. Specific surface area and pore-size distribution in clays and shales. *Geophysical Prospecting*, 61(2):341–362, March 2013.

[21] Clarkson, C. R, Solano, N, Bustin, R. M, Bustin, A. M. M, Chalmers, G. R. L, He, L, Melnichenko, Y. B, Radliński, A. P, and Blach, T. P. Pore structure characterization of North American shale gas reservoirs using USANS/SANS, gas adsorption, and mercury intrusion. *Fuel*, 103:606–616, January 2013.

[22] Loucks, R. G, Reed, R. M, Ruppel, S. C, and Jarvie, D. M. Morphology, genesis, and distribution of nanometer-scale pores in siliceous mudstones of the Mississippian Barnett shale. *Journal of Sedimentary Research*, 79(12):848–861, 2009.

[23] Wu, Y, Fan, T, Jiang, S, Yang, X, Ding, H, Meng, M, and Wei, D. Methane adsorption capacities of the lower Paleozoic marine shales in the Yangtze Platform, South China. *Energy Fuels*, 29(7):4160–4167, July 2015.

[24] Sing, K. S. W and Williams, R. T. The use of molecular probes for the characterization of nanoporous adsorbents. *Particle & Particle Systems Characterization*, 21(2):71–79, August 2004.

[25] Sing, K. The use of nitrogen adsorption for the characterisation of porous materials. *Colloids and Surfaces A: Physicochemical and Engineering Aspects*, 187-188:3–9, August 2001.

[26] Seaton, N. A. Determination of the connectivity of porous solids from nitrogen sorption measurements. *Chemical Engineering Science*, 46(8):1895–1909, January 1991.

[27] Thommes, M. Physical adsorption characterization of nanoporous materials. *Chemie Ingenieur Technik*, 82(7):1059–1073, June 2010.

[28] Murray, K. L, Seaton, N. A, and Day, M. A. Use of mercury intrusion data, combined with nitrogen adsorption measurements, as a probe of pore network connectivity. *Langmuir*, 15(23):8155–8160, November 1999.

[29] Wu, K, Chen, Z, Li, J, Li, X, Xu, J, and Dong, X. Wettability effect on nanoconfined water flow. *PNAS*, 114(13):3358–3363, March 2017.

[30] Li, J, Li, X, Wu, K, Wang, X, Shi, J, Yang, L, Zhang, H, Sun, Z, Wang, R, and Feng, D. Water sorption and distribution characteristics in clay and shale: effect of surface force. *Energy Fuels*, 30(11):8863–8874, November 2016.

[31] Li, J, Li, X, Wang, X, Li, Y, Wu, K, Shi, J, Yang, L, Feng, D, Zhang, T, and Yu, P. Water distribution characteristic and effect on methane adsorption capacity in shale clay. *International Journal of Coal Geology*, 159:135–154, April 2016.

[32] Rotenberg, B. Water in clay nanopores. *MRS Bulletin*, 39(12):1074–1081, December 2014.

[33] Li, Z, Jin, Z, and Firoozabadi, A. Phase behavior and adsorption of pure substances and mixtures and characterization in nanopore structures by density functional theory. *SPE Journal*, 19(06):1,096–1,109, December 2014.

[34] Bui, B. T, Liu, H.-H, Chen, J, and Tutuncu, A. N. Effect of capillary condensation on gas transport in shale: a pore-scale model study. *SPE Journal*, 21(02):601–612, April 2016.

[35] Chalmers, G. R, Bustin, R. M, and Power, I. M. Characterization of gas shale pore systems by porosimetry, pycnometry, surface area, and field emission scanning electron microscopy-/transmission electron microscopy image analyses: Examples from the Barnett, Woodford, Haynesville, Marcellus, and Doig units. *AAPG Bulletin*, 96(6):1099–1119, June 2012.

[36] Labani, M. M, Rezaee, R, Saeedi, A, and Hinai, A. A. Evaluation of pore size spectrum of gas shale reservoirs using low pressure nitrogen adsorption, gas expansion and mercury porosimetry: A case study from the Perth and Canning Basins, Western Australia. *Journal of Petroleum Science and Engineering*, 112:7–16, December 2013.

[37] Seaton, N. A, Walton, J. P. R. B, and quirke, N. A new analysis method for the determination of the pore size distribution of porous carbons from nitrogen adsorption measurements. *Carbon*, 27(6):853–861, January 1989.

[38] Sing, K. S. W. Reporting physisorption data for gas/solid systems with special reference to the determination of surface area and porosity (Recommendations 1984). *Pure and Applied Chemistry*, 57(4):603–619, 1985.

[39] Jarvie, D. M, Hill, R. J, Ruble, T. E, and Pollastro, R. M. Unconventional shale-gas systems: The Mississippian Barnett Shale of north-central Texas as one model for thermogenic shale-gas assessment. *AAPG Bulletin*, 91(4):475–499, 2007.

[40] Landry, C. J, Eichhubl, P, Prodanović, M, and Wilkins, S. Nanoscale grain boundary channels in fracture cement enhance flow in mudrocks. *Journal of Geophysical Research: Solid Earth*, 121(5):3366–3376, 2016.

[41] Heath, J. E, Dewers, T. A, McPherson, B. J. O. L, Petrusak, R, Chidsey, T. C, Rinehart, A. J, and Mozley, P. S. Pore networks in continental and marine mudstones: Characteristics and controls on sealing behavior. *Geosphere*, 7(2):429–454, April 2011.

[42] Engelder, T, Lash, G. G, and Uzcategui, R. S. Joint sets that enhance production from Middle and Upper Devonian gas shales of the Appalachian Basin. *AAPG Bulletin*, 93(7):857–889, 2009.

[43] Gale, J. F. W, Reed, R. M, and Holder, J. Natural fractures in the Barnett Shale and their importance for hydraulic fracture treatments. *AAPG Bulletin*, 91(4):603–622, 2007.

[44] Woodruff, W. F and Revil, A. CEC-normalized clay-water sorption isotherm. *Water Resources Research*, 47(11), 2011.

[45] Ambrose, R. J, Hartman, R. C, Diaz Campos, M, Akkutlu, I. Y, and Sondergeld, C. New pore-scale considerations for shale gas in place calculations. SPE Unconventional Gas Conference, January 2010.

[46] Sulucarnain, I. D, Sondergeld, C. H, and Rai, C. S. An NMR study of shale wettability and effective surface relaxivity. SPE Canadian Unconventional Resources Conference, January 2012.

[47] Bai, B, Elgmati, M, Zhang, H, and Wei, M. Rock characterization of Fayetteville shale gas plays. *Fuel*, 105:645–652, March 2013.

[48] Blunt, M. J, Bijeljic, B, Dong, H, Gharbi, O, Iglauer, S, Mostaghimi, P, Paluszny, A, and Pentland, C. Pore-scale imaging and modelling. *Advances in Water Resources*, 51:197–216, January 2013.

[49] Dixit, A. B, Buckley, J. S, McDougall, S. R, and Sorbie, K. S. Empirical measures of wettability in porous media and the relationship between them derived from pore-scale modelling. *Transport in Porous Media*, 40(1):27–54, July 2000.

[50] Purcell, W. R. capillary pressures - their measurement using mercury and the calculation of permeability therefrom. *Journal of Petroleum Technology*, 1(02):39–48, February 1949.

[51] Rose, W and Bruce, W. A. Evaluation of capillary character in petroleum reservoir rock. *Journal of Petroleum Technology*, 1(05):127–142, May 1949.

[52] Washburn, E. W. Note on a method of determining the distribution of pore sizes in a porous material. *Proceedings of the National academy of Sciences of the United States of America*, 7(4):115–116, April 1921.

[53] Curtis, M. E, Ambrose, R. J, and Sondergeld, C. H. Structural characterization of gas shales on the micro- and nano-scales. Canadian Unconventional Resources and International Petroleum Conference, January 2010.

[54] Comisky, J. T, Santiago, M, McCollom, B, Buddhala, A, and Newsham, K. E. Sample size effects on the application of mercury injection capillary pressure for determining the storage capacity of tight gas and oil shales. Canadian Unconventional Resources Conference, January 2011.

[55] Sigal, R. F. Mercury capillary pressure measurements on Barnett core. *SPE Reservoir Evaluation & Engineering*, 16(04):432–442, August 2013.

[56] Sondergeld, C. H, Newsham, K. E, Comisky, J. T, Rice, M. C, and Rai, C. S. Petrophysical considerations in evaluating and producing shale gas resources. SPE Unconventional Gas Conference, January 2010.

[57] Coates, G. R, Xiao, L, and Prammer, M. G. *NMR logging: principles and applications*. Haliburton Energy Services, 1999.

[58] Mullen, J. Petrophysical characterization of the Eagle Ford Shale in South Texas. Canadian Unconventional Resources and International Petroleum Conference, January 2010.

[59] Fleury, M and Romero-Sarmiento, M. Characterization of shales using T1–T2 NMR maps. *Journal of Petroleum Science and Engineering*, 137:55–62, January 2016.

[60] Daigle, H and Johnson, A. Combining mercury intrusion and nuclear magnetic resonance measurements using percolation theory. *Transport in Porous Media*, 111(3):669–679, February 2016.

[61] Kuila, U and Prasad, M. Application of nitrogen gas-adsorption technique for characterization of pore structure of mudrocks. *The Leading Edge*, 32(12):1478–1485, December 2013.

[62] Li, T, Tian, H, Chen, J, and Cheng, L. Application of low pressure gas adsorption to the characterization of pore size distribution of shales: An example from Southeastern Chongqing area, China. *Journal of Natural Gas Geoscience*, 1(3):221–230, June 2016.

[63] Brunauer, S, Emmett, P. H, and Teller, E. Adsorption of gases in multimolecular layers. *Journal of the American Chemical Society*, 60(2):309–319, February 1938.

[64] Horváth, G and Kawazoe, K. Method for the calculation of effective pore size distribution in molecular sieve carbon. *Journal of Chemical Engineering of Japan*, 16(6):470–475, 1983.

[65] Barrett, E. P, Joyner, L. G, and Halenda, P. P. The determination of pore volume and area distributions in porous substances. I. Computations from nitrogen isotherms. *Journal of the American Chemical Society*, 73(1):373–380, January 1951.

[66] Evans, R, Marconi, U. M. B, and Tarazona, P. Capillary condensation and adsorption in cylindrical and slit-like pores. *Journal of the Chemical Society, Faraday Transactions 2: Molecular and Chemical Physics*, 82(10):1763–1787, January 1986.

[67] Neimark, A. V and Ravikovitch, P. I. Capillary condensation in MMS and pore structure characterization. *Microporous and Mesoporous Materials*, 44-45:697–707, April 2001.

[68] Landers, J, Gor, G. Y, and Neimark, A. V. Density functional theory methods for characterization of porous materials. *Colloids and Surfaces A: Physicochemical and Engineering Aspects*, 437:3–32, November 2013.

[69] Liu, H, Zhang, L, and Seaton, N. A. Sorption hysteresis as a probe of pore structure. *Langmuir*, 9(10):2576–2582, October 1993.

[70] Liu, X, Xiong, J, and Liang, L. Investigation of pore structure and fractal characteristics of organic-rich Yanchang formation shale in central China by nitrogen adsorption/desorption analysis. *Journal of Natural Gas Science and Engineering*, 22:62–72, January 2015.

[71] Afsharpoor, A, Javadpour, F, Wu, J, Ko, L, and Liang, Q. Network modeling of liquid flow in Yanchang shale. *Interpretation*, 5(2):SF99–SF107, February 2017.

[72] Zhang, L, Xiong, Y, Li, Y, Wei, M, Jiang, W, Lei, R, and Wu, Z. DFT modeling of CO2 and Ar low-pressure adsorption for accurate nanopore structure characterization in organic-rich shales. *Fuel*, 204:1–11, September 2017.

[73] Bustin, R. M, Bustin, A. M. M, Cui, A, Ross, D, and Pathi, V. M. Impact of shale properties on pore structure and storage characteristics. SPE Shale Gas Production Conference, January 2008.

[74] Prodanović, M, Lindquist, W. B, and Seright, R. S. Porous structure and fluid partitioning in polyethylene cores from 3d X-ray microtomographic imaging. *Journal of Colloid and Interface Science*, 298(1):282–297, June 2006.

[75] Ketcham, R. A and Carlson, W. D. Acquisition, optimization and interpretation of X-ray computed tomographic imagery: applications to the geosciences. *Computers & Geosciences*, 27(4):381–400, May 2001.

[76] Wildenschild, D, Vaz, C. M. P, Rivers, M. L, Rikard, D, and Christensen, B. S. B. Using X-ray computed tomography in hydrology: systems, resolutions, and limitations. *Journal of Hydrology*, 267(3):285–297, October 2002.

[77] Xiong, Q, Baychev, T. G, and Jivkov, A. P. Review of pore network modelling of porous media: Experimental characterisations, network constructions and applications to reactive transport. *Journal of Contaminant Hydrology*, 192(Supplement C):101–117, September 2016.

[78] Wu, S, Zhu, R, Cui, J, Cui, J, Bai, B, Zhang, X, Jin, X, Zhu, D, You, J, and Li, X. Characteristics of lacustrine shale porosity evolution, Triassic Chang 7 Member, Ordos Basin, NW China. *Petroleum Exploration and Development*, 42(2):185–195, April 2015.

[79] Kelly, S, El-Sobky, H, Torres-Verdin, C, and Balhoff, M. T. Assessing the utility of FIB-SEM images for shale digital rock physics. *Adv. Water Resour.*, 95:302–316, September 2016.

[80] Okabe, H and Blunt, M. J. Pore space reconstruction using multiple-point statistics. *Journal of Petroleum Science and Engineering*, 46(1):121–137, February 2005.

[81] Gu, X, Cole, D. R, Rother, G, Mildner, D. F. R, and Brantley, S. L. Pores in Marcellus Shale: a neutron scattering and FIB-SEM study. *Energy Fuels*, 29(3):1295–1308, March 2015.

[82] Tang, D and Spikes, K. Segmentation of shale SEM images using machine learning. SEG International Exposition and 87th Annual Meeting, October 2017.

[83] Curtis, M. E, Sondergeld, C. H, Ambrose, R. J, and Rai, C. S. Microstructural investigation of gas shales in two and three dimensions using nanometer-scale resolution imaging. *AAPG Bulletin*, 96(4):665–677, 2012.

[84] Shabro, V, Kelly, S, Torres-Verdin, C, Sepehrnoori, K, and Revil, A. Pore-scale modeling of electrical resistivity and permeability in FIB-SEM images of organic mudrock. *Geophysics*, 79(5):D289–D299, October 2014.

[85] Aranovich, G. L and Donohue, M. D. Adsorption of supercritical fluids. *Journal of Colloid and Interface Science*, 180(2):537–541, June 1996.

[86] Aranovich, G. L and Donohue, M. D. Predictions of multilayer adsorption using lattice theory. *Journal of Colloid and Interface Science*, 189(1):101–108, May 1997.

[87] Myers, A. L and Monson, P. A. Adsorption in porous materials at high pressure: theory and experiment. *Langmuir*, 18(26):10261–10273, December 2002.

[88] Halsey, G. Physical adsorption on non-uniform surfaces. *The Journal of Chemical Physics*, 16(10):931–937, October 1948.

[89] Langmuir, I. The adsorption of gases on plane surfaces of glass, mica and platinum. *Journal of the American Chemical Society*, 40(9):1361–1403, September 1918.

[90] Lastoskie, C, Gubbins, K. E, and Quirke, N. Pore size distribution analysis of microporous carbons: a density functional theory approach. *The Journal of Physical Chemistry*, 97(18):4786–4796, May 1993.

[91] Ono, S and Kondo, S. Molecular theory of surface tension in liquids. In *Structure of Liquids/Struktur der Flüssigkeiten*, Encyclopedia of Physics / Handbuch der Physik, pages 134–280. Springer, 1960.

[92] Salazar, R and Gelb, L. D. Application of the Bethe-Peierls approximation to a lattice-gas model of adsorption on mesoporous materials. *Physical Review E*, 71(4):041502, April 2005.

[93] Bakhshian, S, Shi, Z, Sahimi, M, Tsotsis, T. T, and Jessen, K. Image-based modeling of gas adsorption and deformation in porous media. *Scientific Reports*, 8(1):8249, May 2018.

[94] Coasne, B and Pellenq, R. J.-M. Grand canonical Monte Carlo simulation of argon adsorption at the surface of silica nanopores: Effect of pore size, pore morphology, and surface roughness. *The Journal of Chemical Physics*, 120(6):2913–2922, February 2004.

[95] Hill, H. J, Klein, G. E, Shirley, O. J, Thomas, E. C, and Waxman, W. H. Bound water in shaly sands - its relation to Q and other formation properties. *The Log Analyst*, 20(03), May 1979.

[96] Davis, D. D, Horton, R, Heitman, J. L, and Ren, T. Wettability and hysteresis effects on water sorption in relatively dry soil. *Soil Science Society of America Journal*, 73(6):1947–1951, November 2009.

[97] Michot, L. J, Villieras, F, Francois, M, Yvon, J, Le Dred, R, and Cases, J. M. The structural microscopic hydrophilicity of talc. *Langmuir*, 10(10):3765–3773, October 1994.

[98] Rotenberg, B, Patel, A. J, and Chandler, D. Molecular explanation for why talc surfaces can be both hydrophilic and hydrophobic. *Journal of the American Chemical Society*, 133(50):20521–20527, December 2011.

[99] Testamanti, M. N and Rezaee, R. Determination of NMR T2 cut-off for clay bound water in shales: A case study of Carynginia Formation, Perth Basin, Western Australia. *Journal of Petroleum Science and Engineering*, 149:497–503, January 2017.

[100] Newman, A. C. D. *Chemistry of clays and clay minerals*. Wiley, August 1987.

[101] Heijs, A. W. J, de Lange, J, Schoute, J. F. T, and Bouma, J. Computed tomography as a tool for non-destructive analysis of flow patterns in macroporous clay soils. *Geoderma*, 64(3):183–196, January 1995.

[102] De Boever, W, Diaz, A, Derluyn, H, De Kock, T, Van Stappen, J, Dewanckele, J, Bultreys, T, Boone, M, De Schryver, T, Skjønsfjell, E. T. B, Holler, M, Breiby, D. W, and Cnudde, V. Characterization of composition and structure of clay minerals in sandstone with ptychographic X-ray nanotomography. *Applied Clay Science*, 118:258–264, December 2015.

[103] Yuan, W, Li, X, Pan, Z, Connell, L. D, Li, S, and He, J. Experimental investigation of interactions between water and a lower Silurian Chinese shale. *Energy Fuels*, 28(8):4925–4933, August 2014.

[104] Desbois, G, Urai, J. L, and Kukla, P. A. Morphology of the pore space in claystones - evidence from BIB/FIB ion beam sectioning and cryo-SEM observations. *eEarth Discussions*, 4:1–19, February 2009.

[105] Desbois, G, Urai, J. L, Pérez-Willard, F, Radi, Z, Offern, S, Burkart, I, Kukla, P. A, and Wollenberg, U. Argon broad ion beam tomography in a cryogenic scanning electron microscope: a novel tool for the investigation of representative microstructures in sedimentary rocks containing pore fluid. *Journal of Microscopy*, 249(3):215–235, 2013.

[106] Desbois, G, Urai, J. L, Hemes, S, Brassinnes, S, De Craen, M, and Sillen, X. Nanometer-scale pore fluid distribution and drying damage in preserved clay cores from Belgian clay formations inferred by BIB-cryo-SEM. *Engineering Geology*, 179:117–131, September 2014.

[107] Toumelin, E and Torres-Verdín, C. Object-oriented approach for the pore-scale simulation of DC electrical conductivity of two-phase saturated porous media. *Geophysics*, 73(2):E67–E79, February 2008.

[108] Qajar, A, Daigle, H, and Prodanović, M. Methane dual-site adsorption in organic-rich shale-gas and coalbed systems. *International Journal of Coal Geology*, 149:1–8, September 2015.

[109] Chen, J.-H, Zhang, J, Jin, G, Quinn, T, Frost, E, and Chen, J. Capillary condensation and NMR relaxation time in unconventional shale hydrocarbon resources. SPWLA 53rd Annual Logging Symposium, June 2012.

[110] Chen, J.-H, Mehmani, A, Li, B, Georgi, D, and Jin, G. Estimation of total hydrocarbon in the presence of capillary condensation for unconventional shale reservoirs. SPE Middle East Oil and Gas Show and Conference, March 2013.

[111] Wang, L, Wang, S, Zhang, R, Wang, C, Xiong, Y, Zheng, X, Li, S, Jin, K, and Rui, Z. Review of multi-scale and multi-physical simulation technologies for shale and tight gas reservoirs. *Journal of Natural Gas Science and Engineering*, 37:560–578, January 2017.

[112] Wang, J, Chen, L, Kang, Q, and Rahman, S. S. Apparent permeability prediction of organic shale with generalized lattice Boltzmann model considering surface diffusion effect. *Fuel*, 181:478–490, October 2016.

[113] Yu, H, Chen, J, Zhu, Y, Wang, F, and Wu, H. Multiscale transport mechanism of shale gas in micro/nano-pores. *International Journal of Heat and Mass Transfer*, 111:1172–1180, August 2017.

[114] Wu, K, Chen, Z, Li, X, Guo, C, and Wei, M. A model for multiple transport mechanisms through nanopores of shale gas reservoirs with real gas effect–adsorption-mechanic coupling. *International Journal of Heat and Mass Transfer*, 93:408–426, February 2016.

[115] Mason, E. A and Malinauskas, A. P. *Gas transport in porous media: the dusty-gas model*. Elsevier, 1983.

[116] Sakhaee-Pour, A and Bryant, S. Gas permeability of shale. *SPE Reservoir Evaluation & Engineering*, 15(04):401–409, August 2012.

[117] Brown, and DiNardo,. The flow of gases in pipes at low pressures. *Journal of Applied Physics*, 17(10):802–813, October 1946.

[118] Beskok, A and Karniadakis, G. E. Report: a model for flows in channels, pipes, and ducts at micro and nano scales. *Microscale Thermophysical Engineering*, 3(1):43–77, February 1999.

[119] Roy, S, Raju, R, Chuang, H. F, Cruden, B. A, and Meyyappan, M. Modeling gas flow through microchannels and nanopores. *Journal of Applied Physics*, 93(8):4870–4879, March 2003.

[120] Shabro, V, Torres-Verdin, C, and Javadpour, F. Numerical simulation of shale-gas production: from pore-scale modeling of slip-flow, Knudsen diffusion, and Langmuir desorption to reservoir modeling of compressible fluid. North American Unconventional Gas Conference and Exhibition, January 2011.

[121] Fatt, I. The network model of porous media. *Petroleum Transactions, AIME*, January 1956.

[122] Blunt, M. J. Flow in porous media — pore-network models and multiphase flow. *Current Opinion in Colloid & Interface Science*, 6(3):197–207, June 2001.

[123] Afsharpoor, A and Javadpour, F. Liquid slip flow in a network of shale noncircular nanopores. *Fuel*, 180:580–590, September 2016.

[124] Reeves, P. C and Celia, M. A. A functional relationship between capillary pressure, saturation, and interfacial area as revealed by a pore-scale network model. *Water Resources Research*, 32(8):2345–2358, 1996.

[125] Jivkov, A. P, Hollis, C, Etiese, F, McDonald, S. A, and Withers, P. J. A novel architecture for pore network modelling with applications to permeability of porous media. *Journal of Hydrology*, 486:246–258, April 2013.

[126] Mehmani, A and Prodanović, M. The application of sorption hysteresis in nano-petrophysics using multiscale multiphysics network models. *International Journal of Coal Geology*, 128–129:96–108, August 2014.

[127] Dong, H and Blunt, M. J. Pore-network extraction from micro-computerized-tomography images. *Physical Review E*, 80(3):036307, September 2009.

[128] Song, W, Yao, J, Ma, J, Sun, H, Li, Y, Yang, Y, and Zhang, L. Numerical simulation of multiphase flow in nanoporous organic matter with application to coal and gas shale systems. *Water Resources Research*, 54(2):1077–1092, 2018.

[129] Wang, D, Yao, J, Chen, Z, Song, W, and Sun, H. Image-based core-scale real gas apparent permeability from pore-scale experimental data in shale reservoirs. *Fuel*, 254:115596, October 2019.

[130] Bryant, S and Blunt, M. Prediction of relative permeability in simple porous media. *Physical Review A*, 46(4):2004–2011, August 1992.

[131] Bryant, S. L, King, P. R, and Mellor, D. W. Network model evaluation of permeability and spatial correlation in a real random sphere packing. *Transport in Porous Media*, 11(1):53–70, April 1993.

[132] Bryant, S. L, Mellor, D. W, and Cade, C. A. Physically representative network models of transport in porous media. *AIChE Journal*, 39(3):387–396, 1993.

[133] Finney, J. L. Random packings and the structure of simple liquids. I. The geometry of random close packing. *Proceedings of the Royal Society of London. A. Mathematical and Physical Sciences*, 319(1539):479–493, November 1970.

[134] Øren, P.-E, Bakke, S, and Arntzen, O. J. Extending predictive capabilities to network models. *SPE Journal*, 3(04):324–336, December 1998.

[135] Øren, P.-E and Bakke, S. Process based reconstruction of sandstones and prediction of transport properties. *Transport in Porous Media*, 46(2):311–343, February 2002.

[136] Mehmani, A, Prodanović, M, and Javadpour, F. Multiscale, multiphysics network modeling of shale matrix gas flows. *Transport in Porous Media*, 99(2):377–390, September 2013.

[137] Chen, S and Doolen, G. D. Lattice Boltzmann method for fluid flows. *Annual Review of Fluid Mechanics; Palo Alto*, 30:329, 1998.

[138] Sukop, M. C and Thorne, D. T. *Lattice Boltzmann modeling: an introduction for geoscientists and engineers*. Springer, 2006.

[139] Verhaeghe, F, Luo, L.-S, and Blanpain, B. Lattice Boltzmann modeling of microchannel flow in slip flow regime. *Journal of Computational Physics*, 228(1):147–157, January 2009.

[140] Ren, J, Guo, P, Guo, Z, and Wang, Z. A lattice Boltzmann model for simulating gas flow in kerogen pores. *Transport in Porous Media*, 106(2):285–301, January 2015.

[141] Zhang, X.-L, Xiao, L.-Z, Guo, L, and Xie, Q.-M. Investigation of shale gas microflow with the Lattice Boltzmann method. *Petroleum Science*, 12(1):96–103, March 2015.

[142] Lim, C. Y, Shu, C, Niu, X. D, and Chew, Y. T. Application of lattice Boltzmann method to simulate microchannel flows. *Physics of Fluids*, 14(7):2299–2308, May 2002.

[143] Tao, S and Guo, Z. Boundary condition for lattice Boltzmann modeling of microscale gas flows with curved walls in the slip regime. *Physical Review E*, 91(4):043305, April 2015.

[144] Chai, Z, Shi, B, Guo, Z, and Lu, J. Gas flow through square arrays of circular cylinders with Klinkenberg effect: a lattice Boltzmann study. *Communications in Computational Physics*, 2010.

[145] Zhu, L, Tretheway, D, Petzold, L, and Meinhart, C. Simulation of fluid slip at 3d hydrophobic microchannel walls by the lattice Boltzmann method. *Journal of Computational Physics*, 202(1):181–195, January 2005.

[146] Zhou, L, Qu, Z. G, Chen, L, and Tao, W. Q. Lattice Boltzmann simulation of gas–solid adsorption processes at pore scale level. *Journal of Computational Physics*, 300:800–813, November 2015.

[147] Zou, Q and He, X. On pressure and velocity boundary conditions for the lattice Boltzmann BGK model. *Physics of Fluids*, 9(6):1591–1598, June 1997.

[148] Gunstensen, A. K, Rothman, D. H, Zaleski, S, and Zanetti, G. Lattice Boltzmann model of immiscible fluids. *Physical Review A*, 43(8):4320–4327, April 1991.

[149] Shan, X and Chen, H. Lattice Boltzmann model for simulating flows with multiple phases and components. *Phys. Rev. E*, 47(3):1815–1819, March 1993.

[150] Shan, X and Chen, H. Simulation of nonideal gases and liquid-gas phase transitions by the lattice Boltzmann equation. *Physical Review E*, 49(4):2941–2948, April 1994.

[151] Swift, M. R, Osborn, W. R, and Yeomans, J. M. Lattice Boltzmann simulation of nonideal fluids. *Physical Review Letters*, 75(5):830–833, July 1995.

[152] Swift, M. R, Orlandini, E, Osborn, W. R, and Yeomans, J. M. Lattice Boltzmann simulations of liquid-gas and binary fluid systems. *Physical Review E*, 54(5):5041–5052, November 1996.

[153] Chen, L, Kang, Q, Mu, Y, He, Y.-L, and Tao, W.-Q. A critical review of the pseudopotential multiphase lattice Boltzmann model: Methods and applications. *International Journal of Heat and Mass Transfer*, 76:210–236, September 2014.

[154] Nourgaliev, R. R, Dinh, T. N, Theofanous, T. G, and Joseph, D. The lattice Boltzmann equation method: theoretical interpretation, numerics and implications. *International Journal of Multiphase Flow*, 29(1):117–169, January 2003.

[155] Yuan, P and Schaefer, L. Equations of state in a lattice Boltzmann model. *Physics of Fluids*, 18(4):042101, April 2006.

[156] Sukop, M. C and Or, D. Lattice Boltzmann method for modeling liquid-vapor interface configurations in porous media. *Water Resources Research*, 40(1), January 2004.

[157] Guo, L, Xiao, L, Shan, X, and Zhang, X. Modeling adsorption with lattice Boltzmann equation. *Scientific Reports*, 6:srep27134, June 2016.

[158] Zhao, J, Yao, J, Zhang, L, Sui, H, and Zhang, M. Pore-scale simulation of shale gas production considering the adsorption effect. *International Journal of Heat and Mass Transfer*, 103:1098–1107, December 2016.

[159] Ning, Y, Jiang, Y, Liu, H, and Qin, G. Numerical modeling of slippage and adsorption effects on gas transport in shale formations using the lattice Boltzmann method. *Journal of Natural Gas Science and Engineering*, 26:345–355, September 2015.

[160] Wang, S, Javadpour, F, and Feng, Q. Molecular dynamics simulations of oil transport through inorganic nanopores in shale. *Fuel*, 171:74–86, May 2016.

[161] Wang, S, Javadpour, F, and Feng, Q. Fast mass transport of oil and supercritical carbon dioxide through organic nanopores in shale. *Fuel*, 181:741–758, October 2016.

[162] Wu, H, Chen, J, and Liu, H. Molecular dynamics simulations about adsorption and displacement of methane in carbon nanochannels. *The Journal of Physical Chemistry C*, 119(24):13652–13657, June 2015.

[163] Li, Z.-Z, Min, T, Kang, Q, He, Y.-L, and Tao, W.-Q. Investigation of methane adsorption and its effect on gas transport in shale matrix through microscale and mesoscale simulations. *International Journal of Heat and Mass Transfer*, 98:675–686, July 2016.

[164] Barisik, M and Beskok, A. Surface–gas interaction effects on nanoscale gas flows. *Microfluid Nanofluid*, 13(5):789–798, November 2012.

[165] Cranston, R. W and Inkley, F. A. 17 the determination of pore structures from nitrogen adsorption isotherms. In Farkas, A, editor, *Advances in Catalysis*, volume 9 of *Proceedings of the International Congress on Catalysis*, pages 143–154. Elsevier, January 1957.

[166] Yin, Y, Qu, Z. G, and Zhang, J. F. Multiple diffusion mechanisms of shale gas in nanoporous organic matter predicted by the local diffusivity lattice Boltzmann model. *International Journal of Heat and Mass Transfer*, 143:118571, November 2019.

[167] Tarazona, P. Free-energy density functional for hard spheres. *Physical Review A*, 31(4):2672–2679, April 1985.

[168] Aranovich, G. L and Donohue, M. D. Surface compression in adsorption systems. *Colloids and Surfaces A: Physicochemical and Engineering Aspects*, 187-188:95–108, August 2001.

[169] Groen, J. C, Peffer, L. A. A, and Pérez-Ramírez, J. Pore size determination in modified micro- and mesoporous materials. Pitfalls and limitations in gas adsorption data analysis. *Microporous and Mesoporous Materials*, 60(1–3):1–17, June 2003.

[170] Xu, C and Torres-Verdín, C. Pore system characterization and petrophysical rock classification using a bimodal Gaussian density function. *Mathematical Geosciences*, 45(6):753–771, August 2013.

[171] Karniadakis, G. E, Beskok, A, and Aluru, N. *Microflows and nanoflows: fundamentals and simulation*. Springer Science & Business Media, 2005.

[172] Song, W, Yao, J, Wang, D, Li, Y, Sun, H, and Yang, Y. Dynamic pore network modelling of real gas transport in shale nanopore structure. *Journal of Petroleum Science and Engineering*, 184:106506, January 2020.

[173] Mi, L, Jiang, H, and Li, J. The impact of diffusion type on multiscale discrete fracture model numerical simulation for shale gas. *Journal of Natural Gas Science and Engineering*, 20:74–81, September 2014.

[174] Kim, C, Jang, H, and Lee, J. Experimental investigation on the characteristics of gas diffusion in shale gas reservoir using porosity and permeability of nanopore scale. *Journal of Petroleum Science and Engineering*, 133:226–237, September 2015.

[175] Speedy, R. J. Diffusion in the hard sphere fluid. *Molecular Physics*, 62(2):509–515, October 1987.

[176] Guo, Y, He, X, Huang, W, and Wang, M. Microstructure effects on effective gas diffusion coefficient of nanoporous materials. *Transport in Porous Media*, 126(2):431–453, January 2019.

[177] Pollard, W. G and Present, R. D. On gaseous self-diffusion in long capillary tubes. *Physical Review*, 73(7):762–774, April 1948.

[178] Krishna, R and van Baten, J. M. Investigating the validity of the Bosanquet formula for estimation of diffusivities in mesopores. *Chemical Engineering Science*, 69(1):684–688, February 2012.

[179] Centeno, T. A and Stoeckli, F. The assessment of surface areas in porous carbons by two model-independent techniques, the DR equation and DFT. *Carbon*, 48(9):2478–2486, August 2010.

[180] Shi, H. Activated carbons and double layer capacitance. *Electrochimica Acta*, 41(10):1633–1639, June 1996.

[181] Qian, Y. H, D'Humières, D, and Lallemand, P. Lattice BGK models for Navier-Stokes equation. *EPL*, 17(6):479, 1992.

[182] Ginzburg, I. Equilibrium-type and link-type lattice Boltzmann models for generic advection and anisotropic-dispersion equation. *Advances in Water Resources*, 28(11):1171–1195, November 2005.

[183] d'Humières, D, Ginzburg, I, Krafczyk, M, Lallemand, P, and Luo, L.-S. Multiple-relaxation-time lattice Boltzmann models in three dimensions. *Philosophical Transactions: Mathematical, Physical and Engineering Sciences*, 360(1792):437–451, 2002.

[184] Lu, J. H, Lei, H. Y, and Dai, C. S. An optimal two-relaxation-time lattice Boltzmann equation for solid-liquid phase change: The elimination of unphysical numerical diffusion. *International Journal of Thermal Sciences*, 135:17–29, January 2019.

[185] Kuzmin, A and Mohamad, A. A. Multirange multi-relaxation time Shan–Chen model with extended equilibrium. *Computers & Mathematics with Applications*, 59(7):2260–2270, April 2010.

[186] Guo, Z, Zheng, C, and Shi, B. Discrete lattice effects on the forcing term in the lattice Boltzmann method. *Physical Review E*, 65(4):046308, April 2002.

[187] Huang, H, Krafczyk, M, and Lu, X. Forcing term in single-phase and Shan-Chen-type multiphase lattice Boltzmann models. *Phys. Rev. E*, 84(4):046710, October 2011.

[188] Sandler, S. I. *Chemical, biochemical, and engineering thermodynamics*. John Wiley & Sons, April 2017.

[189] Sangwichien, C, Aranovich, G. L, and Donohue, M. D. Density functional theory predictions of adsorption isotherms with hysteresis loops. *Colloids and Surfaces A: Physicochemical and Engineering Aspects*, 206(1):313–320, July 2002.

[190] Prodanović, M, Lindquist, W. B, and Seright, R. S. 3d image-based characterization of fluid displacement in a Berea core. *Advances in Water Resources*, 30(2):214–226, February 2007.

[191] Mei, R, Luo, L.-S, and Shyy, W. An accurate curved boundary treatment in the lattice Boltzmann method. *Journal of Computational Physics*, 155(2):307–330, November 1999.

[192] Lallemand, P and Luo, L.-S. Theory of the lattice Boltzmann method: Dispersion, dissipation, isotropy, Galilean invariance, and stability. *Physical Review E*, 61(6):6546–6562, June 2000.

[193] Guo, Z and Zheng, C. Analysis of lattice Boltzmann equation for microscale gas flows: Relaxation times, boundary conditions and the Knudsen layer. *International Journal of Computational Fluid Dynamics*, 22(7):465–473, August 2008.

[194] He, X and Doolen, G. D. Thermodynamic foundations of kinetic theory and lattice Boltzmann models for multiphase flows. *Journal of Statistical Physics*, 107(1-2):309–328, April 2002.

[195] Kupershtokh, A. L, Medvedev, D. A, and Karpov, D. I. On equations of state in a lattice Boltzmann method. *Computers & Mathematics with Applications*, 58(5):965–974, September 2009.

[196] Qajar, A, Peer, M, Rajagopalan, R, Liu, Y, Brown, C, and Foley, H. C. Surface compression of light adsorbates inside microporous PFA-derived carbons. *Carbon*, 60:538–549, August 2013.

[197] Finney, J. Finney packing of spheres. `http://www.digitalrocksportal.org/projects/47`, 2016.

[198] Herring, A. L, Harper, E. J, Andersson, L, Sheppard, A, Bay, B. K, and Wildenschild, D. Effect of fluid topology on residual nonwetting phase trapping: Implications for geologic CO2 sequestration. *Advances in Water Resources*, 62:47–58, December 2013.

[199] Fisher, L. R and Israelachvili, J. N. Experimental studies on the applicability of the Kelvin equation to highly curved concave menisci. *Journal of Colloid and Interface Science*, 80(2):528–541, April 1981.

[200] Ally, J, Molla, S, and Mostowfi, F. Condensation in nanoporous packed beds. *Langmuir*, 32(18):4494–4499, May 2016.

[201] Xu, R, Prodanović, M, and Landry, C. J. Simulation of gas adsorption and capillary condensation in shale nanopores using lattice Boltzmann modeling. Unconventional Resources Technology Conference, August 2018.

[202] Xu, R, Prodanović, M, and Landry, C. J. Study of subcritical and supercritical gas adsorption behavior in different nanopore systems in shale using lattice Boltzmann method. *International Journal of Coal Geology*, 212:103263, August 2019.

[203] Hecht, M and Harting, J. Implementation of on-site velocity boundary conditions for D3q19 lattice Boltzmann simulations. *Journal of Statistical Mechanics: Theory and Experiment*, 2010(01):P01018, 2010.

[204] Bhatnagar, P. L, Gross, E. P, and Krook, M. A model for collision processes in gases. I. Small amplitude processes in charged and neutral one-component systems. *Physical Review*, 94(3):511–525, May 1954.

[205] Zhang, R and Chen, H. Lattice Boltzmann method for simulations of liquid-vapor thermal flows. *Physical Review E*, 67(6):066711, June 2003.

[206] Bojan, M. J and Steele, W. A. Computer simulation of physical adsorption on stepped surfaces. *Langmuir*, 9(10):2569–2575, October 1993.

[207] Bojan, M. J and Steele, W. A. Computer simulations of the adsorption of xenon on stepped surfaces. *Molecular Physics*, 95(3):431–437, October 1998.

[208] Xu, R and Prodanović, M. Effect of pore geometry on nitrogen sorption isotherms interpretation: A pore network modeling study. *Fuel*, 225:243–255, August 2018.

[209] Guo, B, Ma, L, and Tchelepi, H. A. Image-based micro-continuum model for gas flow in organic-rich shale rock. *Advances in Water Resources*, 122:70–84, December 2018.

[210] Bourg, I. C and Ajo-Franklin, J. B. Clay, water, and salt: controls on the permeability of fine-grained sedimentary rocks. *Accounts of Chemical Research*, 50(9):2067–2074, September 2017.

[211] Bourg, I. C. Sealing shales versus brittle shales: a sharp threshold in the material properties and energy technology uses of fine-grained sedimentary rocks. *Environmental Science & Technology Letters*, 2(10):255–259, October 2015.

[212] Mazurek, M, Alt-Epping, P, Bath, A, Gimmi, T, Niklaus Waber, H, Buschaert, S, Cannière, P. D, Craen, M. D, Gautschi, A, Savoye, S, Vinsot, A, Wemaere, I, and Wouters, L. Natural tracer profiles across argillaceous formations. *Applied Geochemistry*, 26(7):1035–1064, July 2011.

[213] Ross, D. J. K and Marc Bustin, R. The importance of shale composition and pore structure upon gas storage potential of shale gas reservoirs. *Marine and Petroleum Geology*, 26(6):916–927, June 2009.

[214] Gasparik, M, Bertier, P, Gensterblum, Y, Ghanizadeh, A, Krooss, B. M, and Littke, R. Geological controls on the methane storage capacity in organic-rich shales. *International Journal of Coal Geology*, 123:34–51, March 2014.

[215] Pan, Z, Connell, L. D, Camilleri, M, and Connelly, L. Effects of matrix moisture on gas diffusion and flow in coal. *Fuel*, 89(11):3207–3217, November 2010.

[216] Alipour Tabrizy, V, Denoyel, R, and Hamouda, A. A. Characterization of wettability alteration of calcite, quartz and kaolinite: Surface energy analysis. *Colloids and Surfaces A: Physicochemical and Engineering Aspects*, 384(1):98–108, July 2011.

[217] Buckley, J. S and Liu, Y. Some mechanisms of crude oil/brine/solid interactions. *Journal of Petroleum Science and Engineering*, 20(3):155–160, June 1998.

[218] Buckley, J. S. Wetting alteration of solid surfaces by crude oils and their asphaltenes. *Revue de l'Institut Français du Pétrole*, 53(3):303–312, May 1998.

[219] Neuzil, C. E. How permeable are clays and shales? *Water Resources Research*, 30(2):145–150, February 1994.

[220] Best, M. E and Katsube, T. J. Shale permeability and its significance in hydrocarbon exploration. *The Leading Edge*, 14(3):165–170, March 1995.

[221] Kwon, O, Herbert, B. E, and Kronenberg, A. K. Permeability of illite-bearing shale: 2. Influence of fluid chemistry on flow and functionally connected pores. *Journal of Geophysical Research: Solid Earth*, 109(B10), 2004.

[222] Keller, L. M, Schuetz, P, Erni, R, Rossell, M. D, Lucas, F, Gasser, P, and Holzer, L. Characterization of multi-scale microstructural features in Opalinus Clay. *Microporous and Mesoporous Materials*, 170:83–94, April 2013.

[223] Bayesteh, H and Mirghasemi, A. A. Numerical simulation of porosity and tortuosity effect on the permeability in clay: Microstructural approach. *Soils and Foundations*, 55(5):1158–1170, October 2015.

[224] Ebrahimi, D, Whittle, A. J, and Pellenq, R. J.-M. Mesoscale properties of clay aggregates from potential of mean force representation of interactions between nanoplatelets. *The Journal of Chemical Physics*, 140(15):154309, April 2014.

[225] Sun, L, Hirvi, J. T, Schatz, T, Kasa, S, and Pakkanen, T. A. Estimation of montmorillonite swelling pressure: a molecular dynamics approach. *The Journal of Physical Chemistry C*, 119(34):19863–19868, August 2015.

[226] Meyer, S, Levitz, P, and Delville, A. Influence of the relative orientation of two charged anisotropic colloidal particles on their electrostatic coupling: a (N,V,T) Monte Carlo study. *The Journal of Physical Chemistry B*, 105(43):10684–10690, November 2001.

[227] Hu, H, Xing, Y, and Li, X. Molecular modeling on transportation of CO2 in montmorillonite: Diffusion and permeation. *Applied Clay Science*, 156:20–27, May 2018.

[228] Dijkstra, M, Hansen, J.-P, and Madden, P. A. Statistical model for the structure and gelation of smectite clay suspensions. *Physical Review E*, 55(3):3044–3053, March 1997.

[229] Kutter, S, Hansen, J.-P, Sprik, M, and Boek, E. Structure and phase behavior of a model clay dispersion: A molecular-dynamics investigation. *The Journal of Chemical Physics*, 112(1):311–322, December 1999.

[230] Anandarajah, A and Amarasinghe, P. Discrete-element study of the swelling behaviour of Na-montmorillonite. *Géotechnique*, 63(8):674–681, June 2013.

[231] Yiotis, A. G, Psihogios, J, Kainourgiakis, M. E, Papaioannou, A, and Stubos, A. K. A lattice Boltzmann study of viscous coupling effects in immiscible two-phase flow in porous media. *Colloids and Surfaces A: Physicochemical and Engineering Aspects*, 300(1–2):35–49, June 2007.

[232] Huang, H and Lu, X.-y. Relative permeabilities and coupling effects in steady-state gas-liquid flow in porous media: A lattice Boltzmann study. *Physics of Fluids*, 21:092104–092104, September 2009.

[233] Sayar, P and Torres-Verdin, C. Using anisotropic effective medium theories to quantify elastic properties of sandstone-shale laminated rocks. *Geophysics*, 81(4):D315–D333, May 2016.

[234] Ghanbarian, B and Javadpour, F. Upscaling pore pressure-dependent gas permeability in shales. *Journal of Geophysical Research: Solid Earth*, 122(4):2541–2552, March 2017.

[235] Bai, B, Sun, Y, and Liu, L. Petrophysical properties characterization of Ordovician Utica gas shale in Quebec, Canada. *Petroleum Exploration and Development*, 43(1):74–81, February 2016.